Nuno Manuel Gonçalves Vilhena

M.Sc. in Electrical and Computer Engineering

Contribution for the Study of the Integration of Inductive Superconducting Fault Current Limiters in Electrical Distribution Grids

Dissertation to obtain the degree of Doctor of Philosophy in
Electrical and Computer Engineering

Supervisor: João Miguel Murta Pina, Assistant Professor
Universidade NOVA de Lisboa, Portugal

Co-supervisors: Anabela Monteiro Gonçalves Pronto, Assistant Professor
Universidade NOVA de Lisboa, Portugal

Alfredo Álvarez García, Associate Professor,
Universidad de Extremadura, Spain

Evaluation board:

President: Doctor João Carlos da Palma Goes, FCT NOVA

Opponents: Doctor Antonio Morandi, University of Bologna

Doctor Guilherme Gonçalves Sotelo, Universidade Federal Fluminense

Members: Doctor Alexander Polasek, Eletrobras Cepel

Doctor João Miguel Murta Pina, FCT NOVA

Doctor João Francisco Alves Martins, FCT NOVA

FACULDADE DE CIÊNCIAS E TECNOLOGIA
UNIVERSIDADE NOVA DE LISBOA

November 2020

Contribution for the Study of the Integration of Inductive Superconducting Fault Current Limiters in Electrical Distribution Grids

To my family and friends

Acknowledgements

I would like to express my gratitude to all the people who contributed directly or indirectly to this thesis.

First of all, I would like to thank my supervisors, professor João Murta Pina and professor Anabela Pronto, for having accepted to be my supervisors, since my master's degree, and showed me the interesting world of superconductivity, and thanks to professor Alfredo Álvarez for agreeing to be my supervisor as well. Thank you for your support, guidance, for sharing your knowledge, for encouraging me in the final stretch which helped me to get here!

I would like to thank the Departamento de Engenharia Electrotécnica e de Computadores da NOVA School of Science and Technology, Universidade NOVA de Lisboa (DEEC-FCT-UNL), and research centre Centre of Technology and Systems (CTS-UNINOVA) for providing me the conditions for developing this research work.

I also acknowledge the indispensable financial support provided by Fundação para a Ciência e Tecnologia (FCT) under the research grant SFRH/BD/92010/2012.

I also would like to thank all members of my research group, especially professor João Martins, for having believed in me and my skills, invited me to collaborate with the research group, and for always encouraging me to finish this thesis.

To the secretariat staff of the DEEC, I want to thank you for all the support they have given me, with special thanks to Helena Inácio, that without her help I would not have reached this final stage.

I am thankful to my colleagues Nuno Amaro, Pedro Arsénio and Fábio Januário, for the friendship and for the support and all the help I needed during my lab work. Thanks, Arsénio, for your help in revising this document. Thanks to the other colleagues and co-workers of my research group.

To all my friends who were always present, for sharing good moments, good talks, for travelling together, for friendship above all. A special thanks to Bruno Galveia, Ricardo Silva and Eva Marques, my brother Bruno Vilhena and finally Gonçalo Santos, that without them this long journey would have been much more difficult, mainly in the final stretch. Thank you to all my friends from Grupeta Team, for all the past moments lived together. Thank you, Quim Inverno, for your indispensable help in revising this thesis.

Finally, I would like to thank all my family for their incentive, support and always being there when I needed. Thanks to my uncles Jorge and Sónia, for the great friendship we have. Thanks to my brother for supporting me in good and bad times, I know you have always been there! And the greatest thanks to my parents who made the person I am today…

Thank you all!

Abstract

A wider adoption of distributed generation sources and an increased interconnection of networks tend to increase the complexity of electric power grids, thus causing a surge in failures, especially short-circuits. The conventional solution against short-circuit currents, for example, the construction of new substations, splitting of busbars, even updating the technology of the existing current limiters may prove either economically or technically unfeasible. Fault current limiters, mainly the superconducting fault current limiters, have already demonstrated their viability in electric power grids. Fault current limiter devices at normal operation are invisible to the grid, acting almost instantly upon a fault, returning to their normal state upon its correction.

To disseminate these technologies, the development of straightforward design tools is required. These tools must consider the properties of the available constitutive elements of the devices. Behind these design tools, the integrity of the fault current limiter should be assured during its operation. Problems regarding the electrodynamic forces developed under short-circuit events must be properly characterized because they can damage windings, causing device breakage and affecting the power grid.

In this thesis, a design methodology that intends to model and optimise saturated cores superconducting fault current limiters is presented. This methodology considers the characteristics of each constitutive element of the limiter while addressing utility requirements and power grid characteristics. Genetic algorithms are used both to optimise the constitutive elements of the limiter and its performance in the power grid. In order to validate the present methodology, a three-phase superconducting fault current limiter is designed/optimised, built and tested. The electrodynamic forces analysis developed in superconducting tapes of an inductive transformer type superconducting fault current limiter, under short-circuit conditions is performed.

Keywords: Fault Current Limiters, Saturated Cores Fault Current Limiter, Modelling, Optimisation, Genetic Algorithms, Transformer Type Fault Current Limiter, Mechanical Stresses, Superconducting Devices.

Resumo

A crescente adoção de fontes de geração distribuída e o aumento das ligações internas entre redes de energia levou ao aumento da complexidade das redes elétricas, causando um provável aumento do número de falhas, especialmente os curto-circuitos. Soluções convencionais para lidar com curto-circuitos, como por exemplo, a construção de novas subestações, a divisão dos barramentos, ou a atualização tecnológica dos limitadores de corrente existentes, podem se mostrar muito dispendiosas ou tecnicamente inviável. Os limitadores de corrente de defeito, principalmente os dispositivos supercondutores, têm vindo a demostrar a sua viabilidade em redes de energia elétrica. Estes dispositivos são considerados invisíveis para a rede, quando em operação normal. Quando uma falha na rede ocorre, estes agem instantaneamente, retornando ao seu estado normal após a falha terminar.

De modo a disseminar estas tecnologias, é necessário o desenvolvimento de ferramentas de projeto e modelação, de fácil uso. Essas ferramentas devem considerar as propriedades dos elementos que constituem os dispositivos de proteção. Por detrás dessas ferramentas de projeto, a integridade do limitador deve ser assegurada durante todo o seu funcionamento. Problemas relacionados com forças eletrodinâmicas desenvolvidas sob eventos de curto-circuito devem ser devidamente caracterizados, pois podem danificar os enrolamentos, e por sua vez o equipamento e afetar a rede elétrica.

Nesta tese, é apresentada uma metodologia de projeto, que visa modelar e otimizar limitadores de corrente de defeito supercondutores, do tipo núcleos saturados. Esta metodologia considera as características de cada elemento constitutivo do limitador enquanto aborda os requisitos da concessionária da rede de distribuição de energia e as características da rede elétrica. Algoritmos genéticos são usados para otimizar os o limitador e o seu desempenho na rede elétrica. A fim de validar a metodologia atual, um limitador trifásico é projetado/otimizado, construído e ensaiado. É ainda realizada a

análise das forças eletrodinâmicas desenvolvidas em fitas supercondutoras de um limitador de corrente de defeito, do tipo transformador, em condições de curto-circuito.

Palavras-chave: Limitadores de Corrente de Defeito, Limitadores de Corrente de Defeito de Núcleos Saturados, Projeto de Dispositivos de Potência, Otimização de Dispositivos de Potência, Algoritmos Genéticos, Limitador de Corrente de Defeito do tipo Transformador, Tensões Mecânicas, Dispositivos Supercondutores.

List of Contents

List of Figures

List of Tables

List of Symbols

$\boldsymbol{B}$	Magnetic flux density (T)
D	Depth of the Core (m)
f	Frequency (Hz)
$\vec{f}$	Lorentz Force Vector (N/m^3)
$F_{m\,AC}$	Magnetomotive Force due to AC coil (At)
$F_{m\,DC}$	Magnetomotive Force due to DC coil (At)
$g_j(x)$	Inequality Constraint Function
g_1	Coefficient Associated with the Requirements for the SFCL Optimisation
g_2	Coefficient Associated with the Requirements for the SFCL Optimisation
$GOAL_{VALUE}$	Fitness Value Obtained in Each Genetic Algorithm Iteration
$\boldsymbol{H}$	Magnetic Field (A/m).
H	Height of Each Core (m)
H_e	
H_c	Critical Magnetic Field (A/m)
$h_k(x)$	Equality Constraint Function
i_{AC}	AC Line Current (A)
I_{AC1}	AC Bias Current Amplitude of Coil 1 (A)
I_{AC2}	AC Bias Current Amplitude of Coil 2 (A)
$I_{AC\,max}$	Maximum AC current for the Range of i_{AC} (A)
$I_{AC\,inc}$	Increment Step of $I_{AC\,max}$ (A)
I_c	Critical Current (A)
I_{DC}	DC Bias Current (A)

i_{knee}	Current Value Related to the Operation Point C in Figure 2.14 (A)
i_{line}	AC Line Current (A)
i_{max}	Maximum Current Vaule Related to the Operation Point D in Figure 2.14 (A)
i_{ss}	Current Steady-state Response (A)
i_{trans}	Current Transiente Response (A)
$\boldsymbol{J}$	Current Density (A/m^2)
J_c	Critical Current Density (A/m^2)
L	Windings Inductance (H)
l_n	Mean Length of the Flux Path n (m)
l_y	Mean Length of the yoke (m)
l_l	Mean Length of the limb (m)
L_{SFCL}	Variable Inductance (H)
$\boldsymbol{M}$	Magnetization Field (A/m)
M_{an}	Anhysteretic Magnetization (A/m)
Max_Goal_{VALUE}	Maximum Fitness Value Obtained During the Optimised Process
N	Number of Turns
N_{AC}	Number of Turns of Coil AC
N_{DC}	Number of Turns of Bias Coil DC
$P(x)$	Penalty Function for Genetic Algorithm
$Penalized_{VALUE}$	Penalized Value for Genetic Algorithm
P_{Load}	Load Active Power (W)
Q_{load}	Load Reactive Power (Var)
R_{SFCL}	Resistance of the SFCL (Ω)
S_{AC}	Cross-sections area of AC limb (m^2)
S_n	Cross-Section Area of Flux Path n (m^2)
S_y	Cross-sections area of core yoke (m^2)
S_{DC}	Cross-sections area of DC limb (m^2)
t	Time (s)
T_c	Critical Temperature (K)
T_{AC}	Thickness of AC Limbs (m)
T_{DC}	Thickness of DC Limbs (m)

T_y	Thickness of Yokes (m)
U_S	Voltage Source (V)
u_{SFCL}	Voltage Drop of the SFCL (V)
W	Width of Each Core (m)
V_{LL}	Line to Line Voltage Source (V)
x_{iU}	Upper Bounds
x_{iL}	Lower Bounds
Z_{LOAD}	Load Impedance (Ω)
Z_{Line}	Source and Line Impedance (Ω)
$\bar{Z}_{SFCL}$	Impedance of the SFCL (Ω)
Z_S	Source Impedance (Ω)
Λ_1	Permeances of Half-Moon Magnetic Flux Tubes (Corners) (H)
Λ_2	Permeances of Half-Moon Magnetic Flux Tubes (Edges) (H)
Λ_3	Permeances of Circular cross-section Coil (H)
Λ_4	Permeances of Hollow Semi-circular Magnetic Flux Tubes (H)
Λ_5	Permeances of Hollow Semi-circular Magnetic Flux Tubes (H)
$\Re_c$	Reluctance of the Open-Cores (H^{-1})
$\Re_y$	Reluctance Associated With the Flux Paths Between the Two AC Coils (H^{-1})
$\Re_a$	Reluctance of the Flux Paths That Link the Inner AC Loop with the Other Paths (H^{-1})
$\Re_i$	Reluctance of the Remaining Flux Paths Inside the DC Bias Coil (H^{-1})
$\Re_0$	Reluctance of the Flux Paths Outside the DC Bias Coil (H^{-1})
$\Re_n$	Reluctance of the Flux Paths n (H^{-1})
$\Re_{01}$	Reluctance associated with the Leakage Flux Path of AC Coil 1 (H^{-1})
$\Re_{02}$	Reluctance associated with the Leakage Flux Path of AC Coil 2 (H^{-1})
$\boldsymbol{\mu_0}$	Vacuum permeability ($4 \times \pi \times 10^{-7}$ H/m)
μ_n	Permeability of Flux Path n (H/m)
τ	Time constant (s)
$\boldsymbol{\phi}$	Magnetic Flux (Wb)
ϕ_n	Magnetic Flux passing through the surface n (Wb)
$\boldsymbol{\Psi}$	Linked Magnetic Flux (Wb)
ψ_{AC}	Linked Magnetic Flux with AC Coil (Wb)

ψ_{DC}	Linked Magnetic Flux with DC Coil (Wb)
Ψ_{SFCL}	Linked Magnetic Flux of the Fault Current Limiter (Wb)
$\boldsymbol{\omega}$	Angular Frequency (rad/s)
α	Constant from Jiles-Atherton Hysteresis Model
$\boldsymbol{\varepsilon}$	Tensile Strain
$\boldsymbol{\sigma}$	Stress (mechanics) (Pa)
$\boldsymbol{E}$	Young's Modulus (Pa)

List of Acronyms

(RE)BCO	Alloy of rare-earth element with barium-copper-oxide
1G	Superconducting material of first generation
2G	Superconducting material of second generation
AC	Alternating current
Bi-2212	$Bi_2Sr_2CaCu_2O_{8+x}$
Bi-2223	$(Bi,Pb)_2Sr_2Ca_2Cu_3O_{10-x}$
BSCCO	Bismuth strontium calcium copper oxide
CB	Circuit Breaker
CF	Cost Function
CRIEPI	Central Research Institute of the Electric Power Industry
DC	Direct Current
DV	Decision Variable
FCL	Fault Current Limiter
FEM	Finite Elements Method
GA	Genetic Algorithm
GTO	Gate Turn-Off thyristor
GUI	Graphical User Interface
HFCL	Hybrid type FCL
HTS	High Temperature Superconducting
HV	High Voltage
IGCT	Integrated Gate Commutated Thyristor
IGBT	Insulated Gate Bipolar Transistor

KVL	Kirchhoff's Voltage Law
MOO	Multi-Objective Optimisation
MOSFET	Metal–Oxide–Semiconductor Field-Effect Transistor
mmf	Magnetomotive Force
MV	Medium Voltage
R&D	Research and Development
SC	Short-Circuit
SFCL	Superconducting Fault Current Limiter
SC-SFCL	Saturated Cores Superconducting Fault Current Limiter
TT-SFCL	Transformer Type Superconducting Fault Current Limiter
SS-FCL	Solid-state Fault Current Limiter
THD	Total Harmonic Distortion
YBCO	Yttrium Barium Copper Oxide

1

Introduction

1.1 Background and Motivation

An increase in electrical energy consumption, as well as the necessity of improving energy efficiency, have been pushing the adoption of smart grid concept. In fact, the consumption of energy was estimated to increase 75% by the year 2020 (compared to the year 2000) *(Garrity, 2008)*. Simultaneously, in order to cope with this trend, there has been a growth in distributed generation, which leads to an increase in network interconnections, therefore increasing the complexity of current electrical grids as well as the number of failures, namely the ones resulting from short-circuit currents.

The conventional solution for dealing with short-circuit currents, such as the construction of new power substations, splitting of grids or splitting of busbars, even updating the circuit-breakers or other equipment may prove either economically or technically unfeasible *(Schmitt et al., 2003)*.

In order to obtain a solution for these problems, superconducting fault current limiters (SFCL) have been studied and developed to improve grid protection systems and optimise recovery time under a failure, thus improving the reliability of electrical grids. Such devices as the saturated cores SFCL (SC-SFCL) type or the transformer type have an inherent and passive ability to limit short-circuit levels *(Moriconi et al., 2011)*.

The saturated cores topology originally proposed in *(Raju et al., 1982)*, involves the use of highly saturated magnetic cores. This is achieved by a DC current that flows in a high-temperature superconducting coil in order to maintain two magnetic cores saturated (in its single-phase configuration). When the line current exceeds normal

operation limits, e.g. due to a fault, the inductance increases abruptly, limiting the current through an inductive voltage drop.

The transformer type SFCL (TT-SFCL) (also referred to as shielded iron core type SFCL) topology acts as a power transformer with its secondary winding short-circuited. In normal operation regime, magnetomotive force (*mmf*), created by the primary coil, is nullified by the superconducting secondary winding. Therefore, magnetic flux changes in the core are almost null and the voltage drop at the terminals of the limiter is negligible. However, when a fault occurs, the AC current in the primary coil increases abruptly and the secondary windings reach their limit ability to nullify the *mmf* created by the primary. Thus, a change in magnetic flux occurs in the core, abruptly increasing the line impedance and causing current limitation.

For the advent of these devices and technology, the development of straightforward design tools that allow simulating them in electrical power grids with different voltage ratings and characteristics are required by utilities. (for example, for simulation of scenarios, to study better materials and equipment, mitigation of investment risks, etc).

Finite elements method (FEM) software packages are often used to simulate the performance of these devices *(Shahbazi et al., 2011)*. However, simulating an SFCL with FEM software can take a considerable amount of time, from several hours to days or weeks, even when considering simple devices in very simple grids.

In order to reduce simulation times even for integration in complex grids, it is necessary to develop methods that can be applied to perform fast dynamic simulations.

Integration of SFCL devices in power grids depends also on developing adequate tools to model and simulate them under different conditions. This work aims to contribute to such developments.

1.2 Research Question and Hypothesis

1.2.1 Problem Statement

The growing energy demand and the increase of renewable sources due to environmental and economic purposes have been shifting the power grid to a distributed generation model based on smart grid concept *(F. Li et al., 2010)*, also to improve voltage profile, voltage stability and to minimize power losses. The increase of faults in power grids (namely short-circuits) is directly related to the increase of dispersed generation

systems, such as wind power generation *(Akhmatov & Eriksen, 2007; Sung-Hun Lim & Jae-Chul Kim, 2012)*.

In the last years, research and development of SFCLs have been under significant progress due mainly to the capability of the latter to offer superior technical performance in comparison with conventional power devices with the same functionality. The saturated cores topology is one of the SFCL types that has been studied the most and some projects have been developed in order to achieve a commercial product (Nelson et al., 2011; Pellecchia et al., 2017; Xin et al., 2013). This type of limiter is characterized by having the superconducting coil operating under DC current. Therefore the superconductor does not quench, which allows an immediate system recovery after a fault event *(Mathias Noe & Steurer, 2007)*. However, the operation principle of this type of FCL is not dependent on superconducting materials, nevertheless, the Joule losses would make it unfeasible. A problem to be taken into account in this type of limiter is the magnetic coupling between the AC and DC coils due to the induced voltage in the DC coil, which can damage it. In general, SC-SFCL satisfies the main requirements of an ideal limiter which are: fast and effective current limitation, quick and passive recovery, or low AC losses.

On the other hand, and in the specific case of the TT-SFCL, the short-circuit events induce high mechanical forces in their superconducting windings (Takao et al., 2007; van der Laan et al., 2010), that could compromise the integrity of the device, leading to its destruction. Therefore, the study of electromechanical forces developed on the superconducting materials is essential in order to ensure their integrity and that of the devices where they are used. This work contributes to evaluate the robustness and best geometry of this transformer type limiters.

All SFCL technologies need to achieve some maturity in order to demonstrate their robustness, thus fast design tools must be developed, allowing the simulation of those devices on electric power grids with different characteristics. The development of such tools needs to take into account the constitutive parts of the limiter in order to optimise its operation regime and ensure its integrity, for instance, considering electromechanical forces experienced by the HTS materials, making this the main focus of this work.

1.2.2 Research Questions

The main research questions chosen to guide this work are the following:

Q1 Are there available methodologies and simulation tools of Saturated Cores Fault Current Limiters, allowing for the analysis of its performance in power grids with different degrees of complexity, and thus contributing to sustained advent of technologies based on superconducting materials?

Q2 Is it possible to optimise Saturated Cores Fault Current Limiters under specific requisites of electrical grids?

Q3 Can electromechanical forces developed under short-circuit events compromise the integrity of Fault Current Limiters?

1.2.3 Hypothesis and Approaches

Proposed hypotheses to address research questions are:

H1 Simulation models and design tools for Saturated Cores Fault Current Limiters can be developed based on its electromagnetic characteristics, as well as taking into account its constructive parts, which will allow utilities, R&D centres, electrical equipment manufacturers, and other entities, to consider and evaluate its performance to maintain safe short-circuit levels in power grids.

H2 A Saturated Cores Fault Current Limiter can be optimized by genetic algorithms using as decision variables the constructive parameters of the device which allows for the prediction of its behaviour.

H3 Electromechanical forces developed in the superconducting material, under short-circuit conditions, can be measured using strain gauges and compared with the mechanic limits of the respective material.

1.3 Objectives

The following research goals were defined as objectives for this thesis:

- Study the design and modelling of the saturated cores fault current limiters;
- Development of an optimisation and simulation tool for the saturated cores fault current limiters, based on genetic algorithms;
- Study and analysis of the electromagnetic force intensities on tapes of an SFCL, under fault conditions;
- Study of transient effects in the DC bias coil, under a fault event;
- Build and test laboratory-scale fault current limiters of saturated cores type and transformer type in order to validate proposed methodologies and carry out the study of such devices.

1.4 Structure of the Document

This document is structured into six chapters. A brief description of them is given as follows:

- Chapter 1 – Introduction.

  This chapter presents a brief overview of the SC-SFCL, its advantages and requirements concerning its design tools and addresses the research questions as well as the hypotheses that support them.

- Chapter 2 - Literature Review.

  A literature review about concepts and projects of SC-SFCLs is addressed in this chapter as well as some modelling methods. It is also presented a brief overview of electric power system failures and typical measures to mitigate them, high-temperature superconducting materials and electromechanical forces developed on superconducting tapes. Lastly, a brief review of optimisation techniques is presented, focusing on genetic algorithms.

- Chapter 3 - Saturated Cores Superconducting Fault Current Limiter: Modelling, Simulation and Test.

In this chapter, the constitutive parts of the SC-SFCL are presented. The baseline to conduct this work is the SFCL modelling and simulation, therefore three different methodologies are presented. The first methodology is based on the magnetic characteristic of the SFCL and it is used to simulate the behaviour of the limiter, either in single-phase or three-phase power grids. The second methodology is based on a reluctance method approach, which is used to model the limiter, through its constitutive parts and return its magnetic characteristic. The last methodology is based on FEM simulator and it is used to return the magnetic characteristic of the limiter, from its constitutive parts and dimensions.

- Chapter 4 - Saturated Cores Superconducting Fault Current Limiter: Design Optimisation.

  The optimisation process of the SFCL is presented, based on genetic algorithms. The degrees of freedom and objectives are outlined. The constitutive parts of the limiter are considered decision variables by the algorithm, taking into account the power grid for which the SFCL is designed. A three-phase SFCL is designed and built, and its performance is analysed.

- Chapter 5 - Transformer Type Superconducting Fault Current Limiter: Analysis of the Electromechanical Forces Developed Under Faults.

  In this chapter, the developed electromechanical forces in superconducting windings are measured and the integrity and performance of the SFCL under fault are evaluated and compared. The single-phase and three-phase topologies are tested. For the three-phase SFCL, a traditional core type and a shell type are tested under some of the most common fault conditions (asymmetric and symmetric).

- Chapter 6 - Conclusions and Future Work.

  Conclusions of the performed work are present in this chapter, as well as future work.

1.5 Original Contributions

The original contributions of this work are:

- Development of a simulation methodology for transient simulation, based on the magnetic characteristic of the SFCL. The simulation tool was implemented in Simulink/MATLAB and allows fast simulations comparing with other tools, e.g. FEM method.
- Development of a modelling methodology, based on a reluctance approach, allows the obtention of an approximated magnetic characteristic of the SFCL from the constitutive parts and dimensions of the limiter.
- Development of a design optimisation tool, based on genetic algorithms, for the SC-SFCL, which allows optimising the limiter for a specific power grid, meeting some requirements, for example, the maximum limited fault current ability of the limiter. The tools return the optimal constitutive parts and dimensions of the SFCL.
- Prototyping and test a three-phase laboratory-scale SFCL, previously optimised. The most common types of faults were caused to the SFCL and their effects were analysed. Testing the prototype allows for the validation of the optimisation tool.
- Development of a measurement procedure to measure the mechanical stresses developed in the HTS coils of the TT-SFCL, using strain gauges. A Rogowski coil, to measure the current in the short-circuited HTS coils, was also developed and built.
- Experimental testing of a single-phase and a three-phase TT-SFCL to analyse the effect of the mechanical forces developed in the HTS coils.

2

Literature Review

When a fault occurs in a section of the electrical power grid, it could damage equipment such as power transformers, causing a blackout of that section or the entire network. In this chapter, a comprehensive analysis of the effects of faults in the power grid and their effects are shown as well as typical measures to mitigate these events. Fault current limiter technologies are introduced in this chapter. The topic regarding high-temperature superconductor materials, used in the superconducting fault current limiters, are addressed. Following, the classification, operation principles and the state of the art of fault current limiters are presented. The mechanical forces developed in these devices are also referred. Lastly, the optimisation techniques and methods are discussed, focusing on the optimisation using genetic algorithms.

2.1 Faults in Electric Power Grids

Modern electric power systems have become more complex mainly due to the increasing of demand.

The growth of renewable energy sources, as well as the liberalization of energy markets, have forced power systems to observe a higher level of flexibility in production, in order to accommodate the increase of distributed generation and its variability. However, the latter leads to a higher probability of occurrence failures in the electric power system.

Actually, high power quality is also imperative pushing to the development of special protection devices (such as SFCL) and procedures in order to avoid damages to the electrical power system *(Mathias Noe & Steurer, 2007)*.

2.1.1 Faults and Their Effects

Most failures on the power system occur in overhead lines and cables due to atmospheric phenomena or contact with external elements (birds, trees). On the other hand, either in underground cables or power transformers, the main problems occur due to high temperatures and high electric fields that cause their degradation as a result of overcurrents and short-circuits.

A short-circuit (SC) event can be characterized by its duration, origin and location, as can be seen in FIGURE 2.1. Concerning its duration, short-circuits are usually classified as self-extinguishing; transient or steady-state. Relatively to its origin, a short-circuit can be caused by mechanical issues, such as breaking of a conductor or accidental electrical contact between two conductors, internal or atmospheric overvoltages and insulation breakdown due to heat, humidity or a corrosive environment *(Metz-Noblat et al., 2005)*.

Short-circuits can be symmetrical or asymmetrical. Symmetrical faults simultaneously affect all phases of the electrical system. Otherwise, asymmetrical faults are phase-to-ground, phase-to-phase and phase-phase-to-ground faults.

Single phase-to-earth faults are the most common fault occurring in about 80% of the cases; phase-to-phase is 15% of total faults (this type of fault often degenerates into a three-phase fault) and three-phase in only 5% of initial faults *(Metz-Noblat et al., 2005; Sung-Hun Lim et al., 2009)*. These different short-circuit currents are presented in FIGURE 2.2.

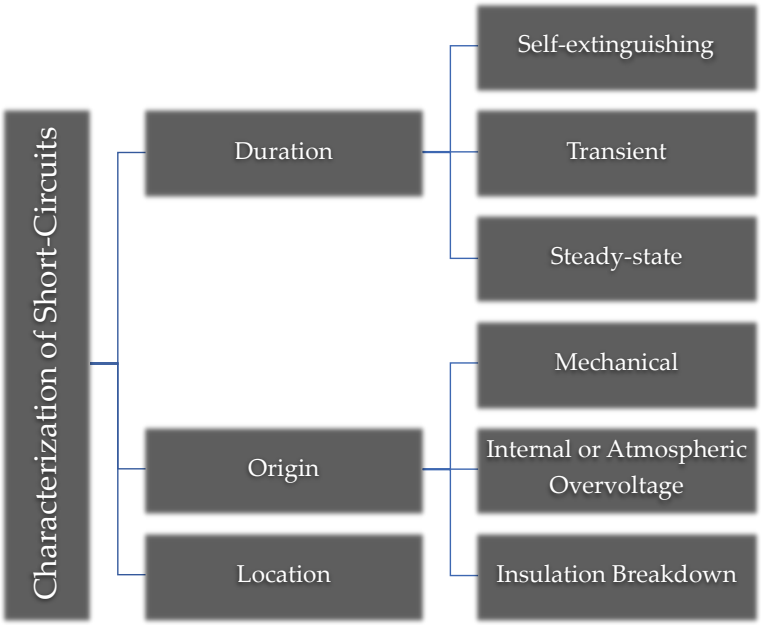

Figure 2.1 - Characterization of short-circuits (adapted of *(Metz-Noblat et al., 2005)*).

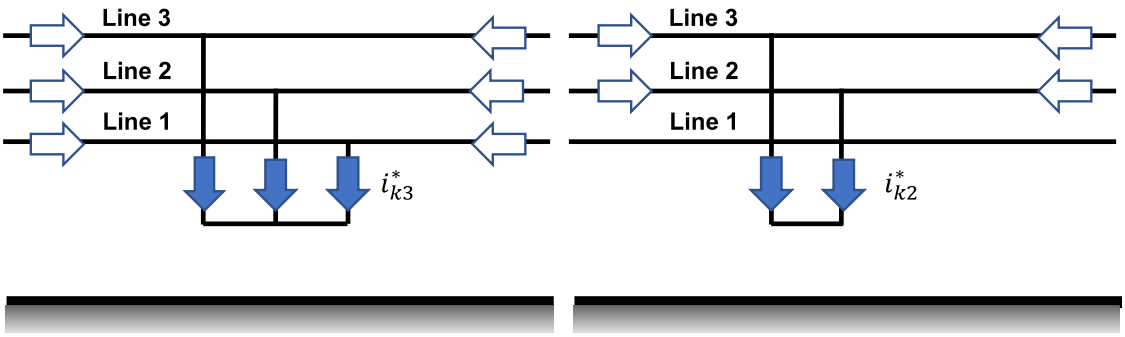

(a) Three-phase short-circuit

(b) Phase-to-phase short-circuit

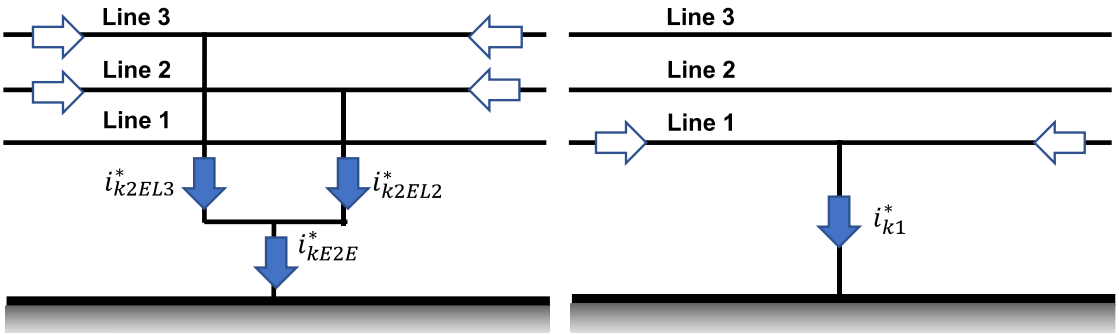

(c) Phase-to-phase-to-ground short-circuit

(d) Phase-to-ground short-circuit

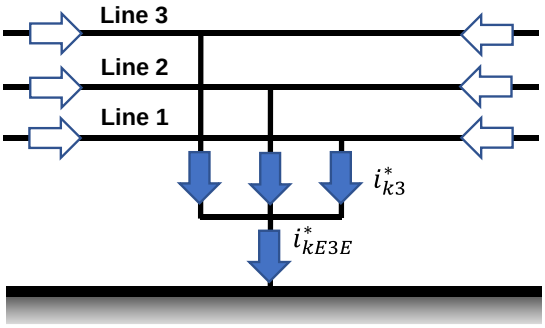

(e) Three-phase-to-ground short-circuit

Figure 2.2 - Different types of short-circuits and their currents (adapted of *(Metz-Noblat et al., 2005)*).

The consequences of short-circuit events are represented in FIGURE 2.3.

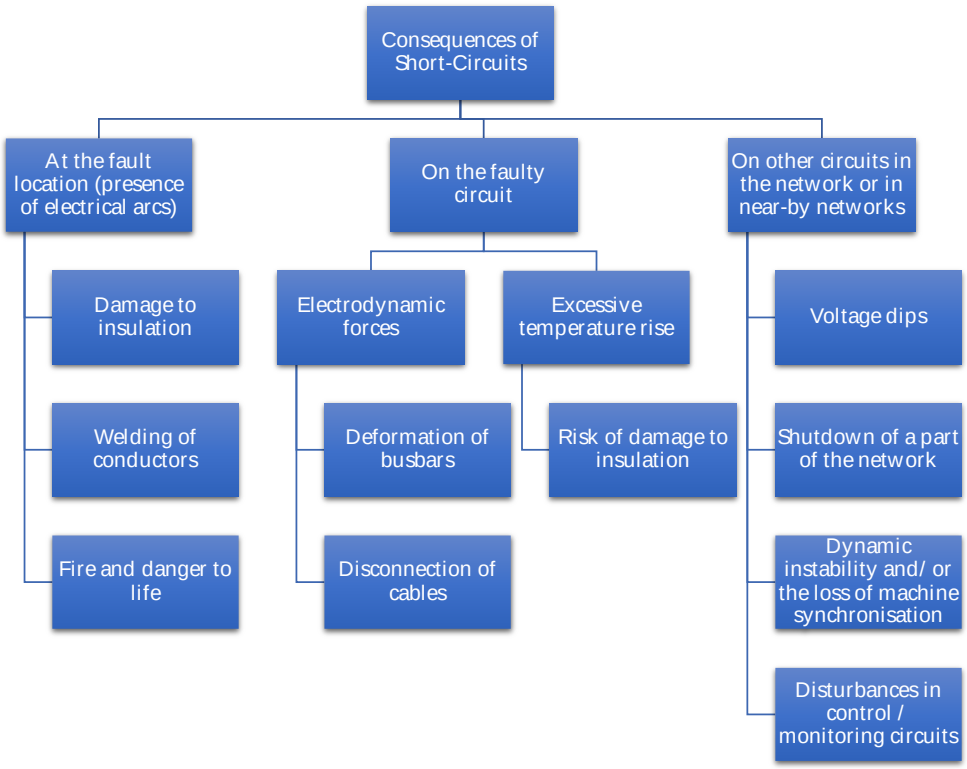

Figure 2.3 - Consequences of short-circuit events (adapted of *(Metz-Noblat et al., 2005)*).

2.1.2 Protections for Power Grids

The increase of SC events is also accompanied by an increase in the SC current levels due to the growth in the grid power (for instance, with the introduction of more renewable generation). The SC current levels may exceed the limits of the installed protection devices. Some typical solutions to protect the power grid and prevent and/or reduce the effects of short-circuit currents due to a failure in the transmission voltage level are described in TABLE 2.1.

Instead of using conventional solutions, a fault current limiter may be a good solution to limit short-circuit currents, which has been receiving much attention recently *(Mathias Noe & Steurer, 2007)*.

These devices have an inherent ability to limit fault current levels, allowing postponing or avoiding costly investments of e.g. upgrading grid protections.

In general, the requirements of an FCL can be described as is follow *(Leung et al., 1997)*:

- High reliability.
- Safe and fail-safe operation.

- Compatible with existing protection.
- Automatic insertion (less than one cycle) upon fault detection.
- Fault current reduction of at least 50%.
- Low voltage drop during normal operation.
- Conformance to utility industry equipment standards.

Table 2.1 - Conventional solutions to prevent and reduce the effects of short-circuit currents due to a failure (adapted from *(Kovalsky et al., 2005)*).

Solution	Advantage	Disadvantage	Relative Expense
Construction of new substations	Provides for future growth	Expensive and slow to install	Most expensive solution
Busbar splitting	Separates sources of fault current	Separates sources of load current from load centres and undermines system reliability.	High, if split busbar is not already installed
Circuit-breaker upgrades	Most direct solution with no adverse side effect	Difficult to schedule outages; Busbar work reinforcement also required	High to medium, depending on number of circuit-breakers
Current limiting reactors and high impedance transformers	Easy to install	Voltage drop and power losses; potentially cause instability	Medium to low
Sequential breaker tripping	No major hardware installation involved.	Expands impact of fault to wider range of the system	Low
Fuses and Pyrotechnic breakers	Fast interrupting the short-circuit current.	Needs to be replaced after a fault.	Medium to low

Concerned to its application, an FCL can be applied in an electric power system in different positions and different voltage levels, either in distribution and transmission networks, as can be seen in FIGURE 2.4.

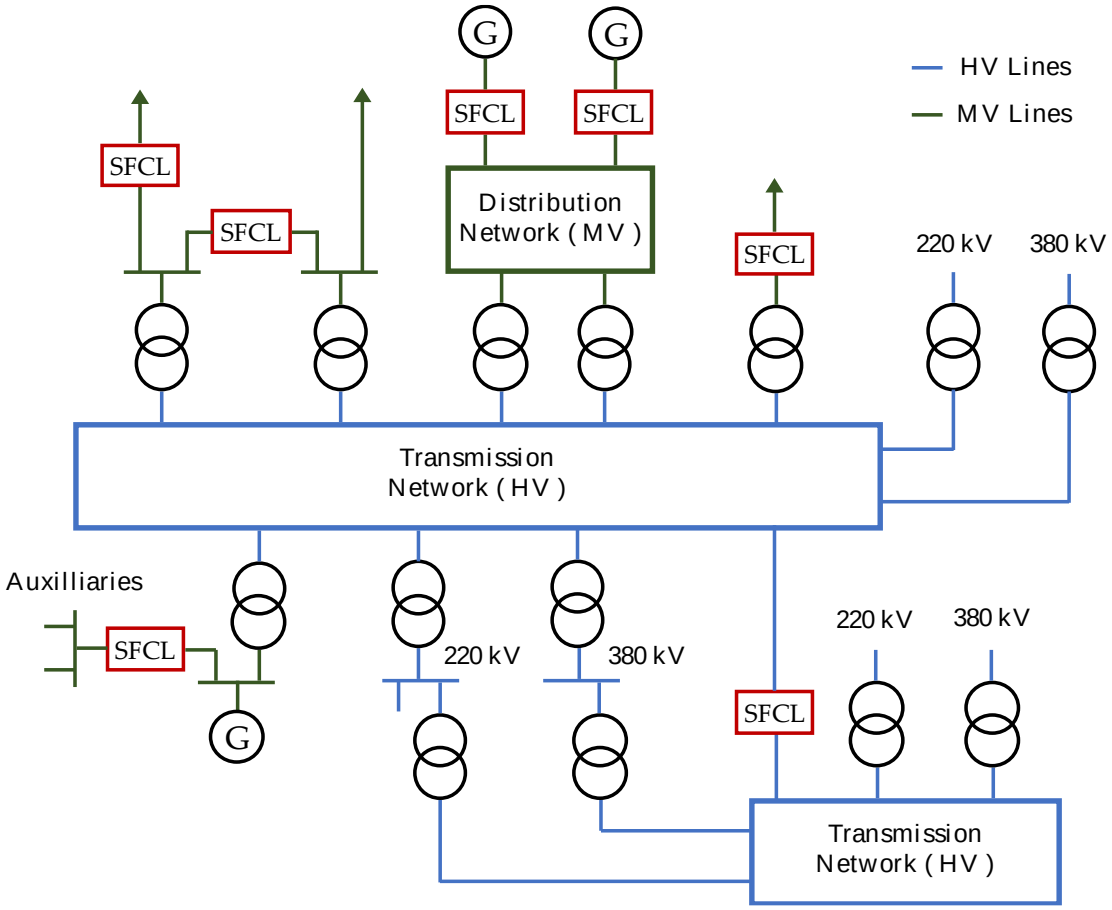

Figure 2.4 – Possible practical applications for SFCLs on HV and MV networks (adapted of *(Morandi, 2013)*).

The most important installations of SFCL are the following *(Morandi, 2013)*:

• Interconnection of Medium Voltage busbars – At normal operation, the busbars are connected in parallel and during a fault, the SFCL will decouple them automatically.

• Protection against voltage dips induced by disturbing customers – The SFCL protects the healthy part of the electrical system from the effect of a fault produced by disturbing customers.

• Grid integration of distributed generation – Using an SFCL, new generation sources can be directly connected to the medium voltage level instead of connecting them to high voltage level through a high voltage transformer.

2.1.3 Fault Current Limiter Principles

FCLs have been intensely studied and investigated in the academic and also industrial circles, resulting in different topologies of FCL, however, the principle is the same: insertion of resistive impedance or/and reactive impedance (through an inductor, with or without a capacitor) into the power line under protection.

FIGURE 2.5 shows an equivalent single-phase power grid circuit with the FCL connected in series with the line. This circuit is composed of a voltage source (U_S), a source impedance ($Z_S = R_L + j\omega L_L$), the FCL ($Z_{FCL} = R_{FCL} + j\omega L_{FCL}$), the load ($Z_{LOAD}$) and the circuit breaker (CB).

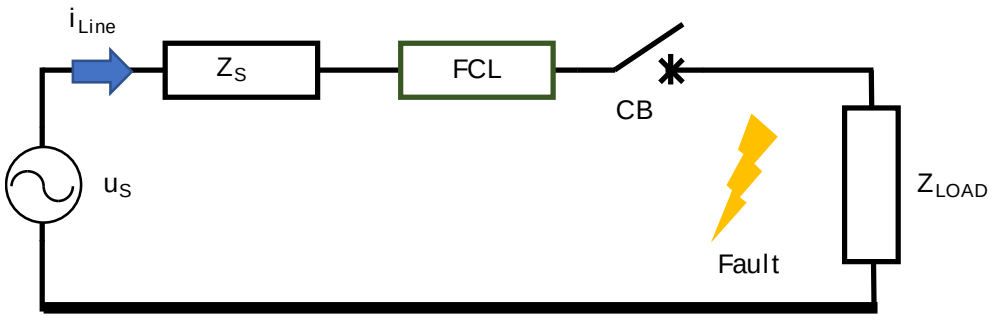

Figure 2.5 - Equivalent circuit of a single-phase power grid with an FCL.

Considering that the voltage source is sinusoidal, applying KVL to the circuit in FIGURE 2.5 gives the EQUATION (2.1) that can characterize the system.

$$L_{eq}\frac{di}{dt} + R_{eq}i = U_m \cos(\omega t + \phi) \tag{2.1}$$

where L_{eq} is the equivalent inductance of the circuit and R_{eq} is the equivalent resistance.

The fault current due to a single-phase to ground fault can be obtained by solving the first-order equation (2.1) and it is described in two terms, the transient response (i_{tr}) which eventually "settles down" to the steady-state value (i_{ss}).

$$i(t) = i_{tr}(t) + i_{ss}(t) \tag{2.2}$$

The transient response is given by:

$$i_{tr}(t) = Ae^{-t/\tau} \tag{2.3}$$

The steady-state is given by:

$$i_{ss}(t) = B\cos(\omega t + \phi - \theta) \tag{2.4}$$

where the magnitude B and the phase shift θ are respectively:

$$B = \frac{U_m}{\sqrt{R_{eq}^2 + \omega^2 L_{eq}^2}} \tag{2.5}$$

$$\theta = \tan^{-1}\left(\frac{\omega L_{eq}}{R_{eq}}\right) \tag{2.6}$$

If $i(t = 0) = 0$, the parameter A is given by:

$$A = -B\cos(\phi - \theta) \tag{2.7}$$

The time constant of the line depends on the FCL installed in the line. For a Resistive FCL, the time constant is given by

$$\tau_{R\_FCL} = \frac{L_{eq}}{R_{eq}} = \frac{L_L}{R_L + R_{FCL}} \tag{2.8}$$

And for an Inductive FCL:

$$\tau_{L\_FCL} = \frac{L_{eq}}{R_{eq}} = \frac{L_L + L_{FCL}}{R_L} \tag{2.9}$$

The resistive FCL shows a lower first peak fault current than the inductive FCL, for the same FCL impedance.

FIGURE 2.6 shows a typical total fault current versus time that includes both transient and steady-state contributions. The sub-transient current, as a consequence of the sudden reduction of the synchronism reactance in the generators, that appears during a first cycle or so after the fault, is not considered.

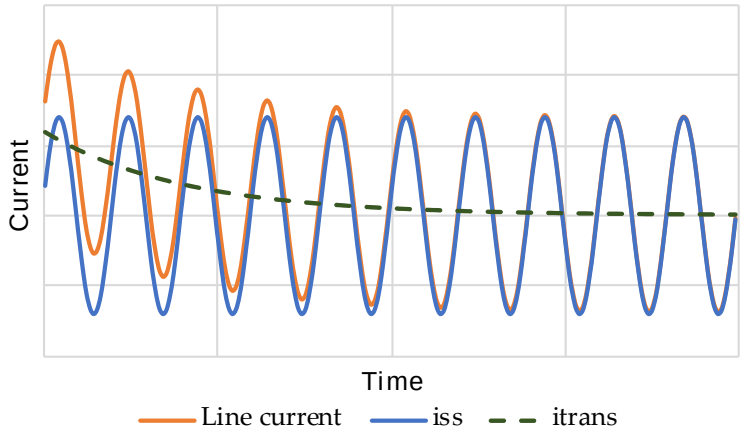

Figure 2.6 - Total fault current (the steady-state in blue; the transient in dashed green and the total fault line current in orange).

2.2 High Temperature Superconductors

The phenomenon of superconductivity was discovered in 1911 as the result of straightforward research to investigate the electrical resistance of metals at low temperatures among other properties. Heike Kamerlingh Onnes, from the University of Leiden, Netherlands, led in 1911 the famous experiment to observe the behaviour of resistance with decreasing temperature, towards absolute zero, using the metallic element mercury. He concluded that mercury resistance did not decrease linearly with temperature, instead, a sudden drop to null values below 4.2 K was observed. Onnes stated it as evidence of a new state of matter which he called "superconductivity" *(Buckel & Kleiner, 2004)*.

Since the discovery of the phenomenon of superconductivity in mercury, many other materials were tested in order to verify its superconducting properties. However, until 1986, all new superconductors discovered were low-temperature superconductors (LTS), where the temperature is usually well below 30 K. This scenario changed in 1986 upon the discovery of cuprates based high-temperature superconductors (HTS) by Georg Bednorz and Alexander Müller *(Bednorz & Müller, 1986)* in the ceramic compound of Ba-La-Cu-O. Other HTS superconducting materials have been discovered, mostly based on copper and oxygen (cuprates), such as bismuth strontium calcium copper oxide (BSCCO) and yttrium barium copper oxide (YBCO).

FIGURE 2.7 presents the summarized timeline with the most important discoveries about superconductivity.

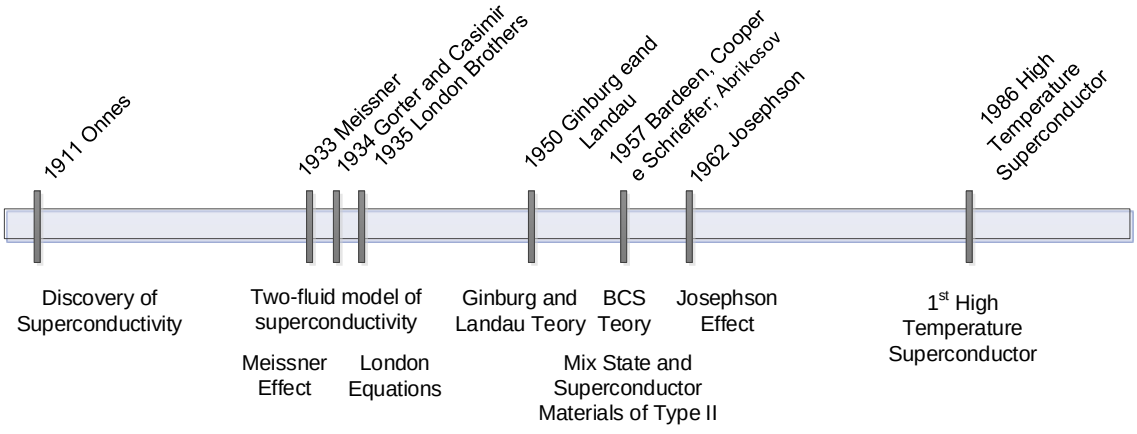

Figure 2.7 - Timeline of the most important historic milestones about the superconductivity.

The HTS materials, either YBCO or BSCCO, can appear commercially on two types (bulks or tapes).

2.2.1 Physical shape: Bulks and Tapes

HTS materials are commercially available either as bulks or tapes.

HTS bulk materials can be made with one of the hundreds of HTS compounds existing but the majority of bulks are made of YBCO. Bulks can be single crystal or polycrystalline depending on their fabricating process.

HTS tapes were developed and optimised for being flexible and carrying as much current as possible. They are ceramic compounds, and they will only bend without breaking if their thickness is sufficiently small. For mechanical robustness and texture reasons, most of superconducting tapes have a thin layer (from 1 to 4 μm) of HTS material, and the others are stabilizer and buffer layers.

First-generation tapes (1G tape) are made of BSCCO, specifically Bi-2212 and Bi-2223. Differences between those superconductors are that Bi-2223 has a higher critical temperature (110 K) than Bi-2212 (90 K) as well as higher critical current density and Bi-2212 has less degradation of its properties in the presence of magnetic field. These tapes consist of BSCCO filaments embedded in a silver matrix which brings them mechanical robustness and flexibility *(Subramanyam & Boolchand, 2001)*.

Second Generation Tapes (2G tape), also called coated conductors, are made mostly of YBCO. More recently, rare earth-based HTS materials ((RE)BCO) have been developed and used to made also HTS tapes. The most frequently rare earths elements are Yttrium, Samarium and Gadolinium. Tapes of second-generation offer some performance benefits such as operation at higher temperatures and less degradation of performance under magnetic fields. FIGURE 2.8 shows a diagram representing the SuperPower® SCS4050 HTS coated conductor. The technique used to manufacture this kind of tape consists of a continuous process using thin film deposition techniques in order to deposit HTS material on a substrate *(Hazelton et al., 2009)*.

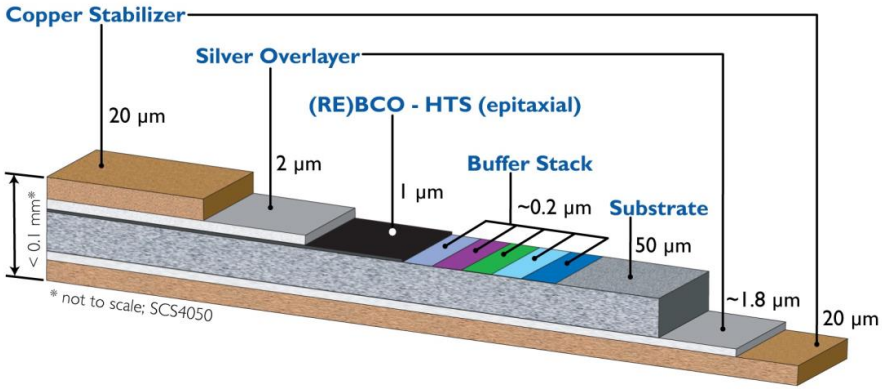

Figure 2.8 - SuperPower® SCS4050 HTS coated conductor (from *(Superpower, 2016)*).

2.3 Fault Current Limiters

Fault current limiters are devices with the ability of limiting short-circuit currents in the power lines where they are installed. There are different topologies with different working principles, which are reviewed below.

2.3.1 Classification of Fault Current Limiters

FCLs can be classified as follow *(Schmitt et al., 2003)*:

- Passive FCL: increase of impedance at nominal and fault conditions.
- Active FCL: increase their impedance quickly at fault conditions and present a small impedance at nominal conditions.

Examples of passive FCLs are the high impedance transformers, which show a short-circuit current value higher than an ordinary transformer *(Y. Li et al., 2019)*, and the fault current limiting air coil reactors, which are connected in series with generators leads, installed between bus sections and in feeders and ties in order to reduce the magnitude of the current faults. This device is an inductive coil with a large inductive reactance comparing with their resistance that change the system impendence, limiting the current fault (Razzaghi & Niayesh, 2011).

Regarding the active FCLs, these devices can be divided into three major categories *(M Noe et al., 2008)*:

2.3.1.1 Superconducting Fault Current Limiters

In a SFCL, superconductor material is used due to its magnetic and electrical proprieties, which are in general, zero resistivity below a critical current (I_C), magnetic field (H_C) and temperature (T_C) and if these limits are surpassed, the resistivity of the

material increases rapidly. These materials also present a perfect diamagnetism, expelling all magnetic fields due to the Meissner effect.

The resistive type SFCL uses the superconductor electrically connected with the line under protection and its behaviour is similar to a variable resistor (FIGURE 2.9). The sudden transition between the superconducting state (almost zero resistance) and the normal state (high resistance), by exceeding the critical current of the superconductor, is used to limit the fault current *(Dalessandro et al., 2007; Didier et al., 2015)*.

The inductive type SFCL (FIGURE 2.10), unlike the resistive type, limits the fault current through an inductive reactance inserted into the grid. The shielded magnetic core type (also called transformer type) is composed of a magnetic core, a primary coil (normal conducting) and a superconducting cylinder placed concentrically with the primary and between this and the core. If the induced current in the superconductor is lower than the critical current, the superconducting cylinder acts as a perfect magnetic shield to the primary coil. In a fault condition, the superconductor loses its proprieties ceasing to be able to shield the magnetic core, thus the magnetic flux penetrates it and a high impedance is inserted in the power line. The operational principle is similar to a transformer with its secondary coil short-circuited (represented by the superconductor) *(Arsenio et al., 2013; J. Kozak et al., 2005).* Another approach is to use short-circuited rings made of superconducting tape, for the secondary coil *(Arsénio et al., 2014; Murta-Pina et al., 2018)*. The saturated-cores type is another inductive SFCL that is composed of two magnetic cores embraced by a superconducting DC bias coil which saturates deeply the cores (FIGURE 2.11). The primary coil (connected in series with the line) is wound in both cores but in magnetic opposition direction. In normal state both cores remain saturated, leading to low impedance and no limitation. When a fault occurs, the cores are driven out of saturation alternately and the impedance rises, limiting the fault current *(JW Moscrop & Hopkins, 2009; Raju et al., 1982; Vilhena et al., 2018)*. Other design for this type of SFCL is also possible.

The bridge type SFCL, shown in FIGURE 2.12, is composed of a full-bridge rectifier, a superconducting coil and a current source. In normal operation, the amplitude of the line current is lower compared with the DC current, therefore the line current bypasses the inductance because all diodes are in the conduction region. In this operation mode, the losses and the voltage drop are from the power electronics. If a fault occurs, the line current amplitude exceeds the DC current leading the diodes to be arrested alternately,

for each half cycle of the AC line current, limiting the fault current by the inductance *(Boenig & Paice, 1983; Yazawa et al., 2001)*.

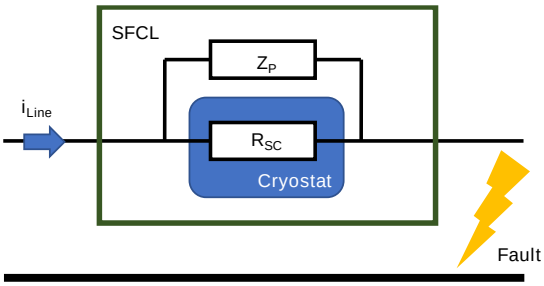

Figure 2.9 - Resistive Type FCL.

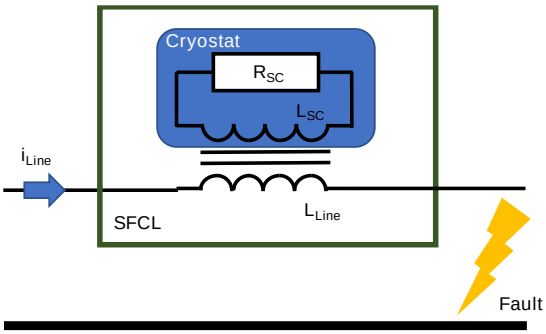

Figure 2.10 - Inductive Type SFCL.

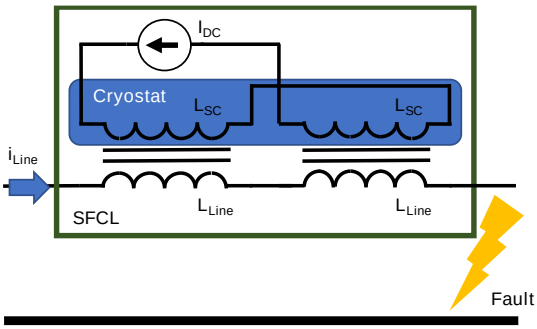

Figure 2.11 - Saturated-cores type SFCL.

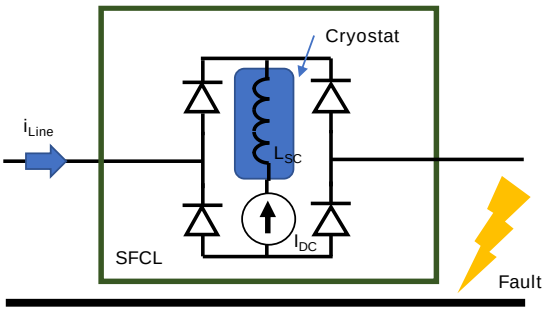

Figure 2.12 - Bridge type SFCL.

2.3.1.2 Solid-State Fault Current Limiter

A solid-state FCL (SS-FCL) use high-power semiconductor switches in order to insert an impedance in the path of the fault current, within a few milliseconds fowling fault inception, limiting the current. Self-commutated solid-state switches, such as IGBT (insulated bipolar transistor), IGCT (integrated gate-commutated thyristor), GTO (gate turn-off thyristor), Power MOSFET (metal–oxide–semiconductor field-effect transistor), are used for this purpose. These devices can act very fast, however, some disadvantages are the possible high-power losses in normal operation, related with the power electronics, the possible increase in the total harmonic distortion (THD) due to the switching devices and the need for an external trigger for operation *(Abramovitz & Ma Smedley, 2012)*.

Many topologies are using solid-state components, therefore these devices can be divided into three major categories. The serial type SS-FCL is composed of a bidirectional semiconductor switch and a bypass path. The bypass path contains a normal state bypass, which is used in normal operation in order to reduce the losses and distortion (it is usually an electromechanical fast switch); a fault current bypass which limits the fault

current; and an over-voltage protection and snubber bypass used to protect the limiter from high voltage levels *(Chen et al., 2006; Meyer et al., 2004)*. The bridge type SS-FCL, in which the operational principle is similar to the bridge-type SFCL, is implemented by a full bridge of power diodes or thyristors and a DC current source in the rectifier zone *(Zhengyu Lu et al., 2003)*. The resonance type SS-FCL uses a switch to change between the normal state to the fault state, reconfiguring its resonant network. Under normal operation, the resonant circuit is tuned in order to achieve near-zero series impedance, however during a fault, the impedance increase due to the shift out of resonance condition *(Karady, 1992)*.

2.3.1.3 Hybrid type and Other Fault Current Limiters

A hybrid FCL (HFCL) consists of a combination of different modules, each responsible for a certain task related to the device operation. Basically, the HFCL is a mix between the SS-FCL, the SFCL or another topology. In *(Hoshino et al., 2005)* was proposed a non-inductive HFCL that uses two superconducting coils connected in parallel and in opposite direction and placed in the rectifier part of a full-bridge circuit. The fault current is limited when the trigger coil loses its superconductivity leading the total flux inside the reactor is no longer zero, the equivalent impedance of both coils increased, and the fault current is limited.

Examples of other technologies are the Liquid-metal FCL, which limits the fault current through the pinch effect *(He et al., 2018)* and the PTC-resistor FCL which is a combination of the advantages of a fuse and a circuit breaker, showing a fast current limitation and can be used more than one time. These devices change their resistivity upon temperature increase *(Strumpler et al., 1999)*.

2.3.2 Saturated Cores Superconducting Fault Current Limiter

Several different geometries of the SC-SFCL have been proposed since its first description in *(Raju et al., 1982)*. However, the basic operation principle remains the same.

2.3.2.1 Operation Principle and Topology

The basic elements of a single-phase SC-SFCL are shown in FIGURE 2.13. This device is composed of two magnetic cores placed side by side and embraced by an HTS bias coil which carries a DC current, for core saturation. The outer limbs of the cores are wound by conventional AC coils, which are connected in series with the line under protection. It is necessary to wound the AC coils in opposite directions considering the

flux generated by the DC coil. This design protects each half cycle of the AC line current under a fault.

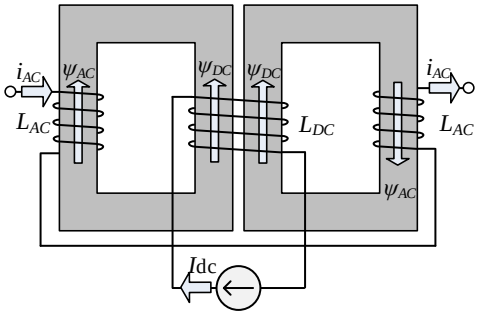

Figure 2.13 - Conceptual diagram of a SC-SFCL. i_{AC} is the line current, I_{DC} represent the DC bias current, L is the windings inductance and ψ represent the magnetic flux through cores.

The operation principle of the limiter is described considering the relation between linked flux with AC coil (ψ_{AC}) and *mmf*. FIGURE 2.14 shows $\psi_{AC} - mmf$ characteristic of each AC coil. When the cores are biased by a DC current, the operation point of each AC coil will be point B. Due to the way that AC coils are wound on each core, in opposite directions, *mmf* due to AC current will lead one of the cores to a deep saturation (region in the right of B point) and the other core out of saturation (region in the left of B point).

Under normal operation (nominal line current), AC current in the windings creates a magnetic flux that is not enough to lead the cores out of magnetic saturation. In this situation, the operation point will oscillate between points A and C making the impedance of the device negligible. In other words, the cores are saturated and thus the limiter has small inductance only due to the leakage magnetic flux, so it is nearly invisible to the grid.

However, when a fault occurs, the AC current in the windings increases abruptly, exceeding the normal operation limits, leading the cores out of magnetic saturation alternately (between point B and D). This increases line inductance steeply and allows current limitation by limiting the current through an inductive voltage drop developed at SFCL terminals.

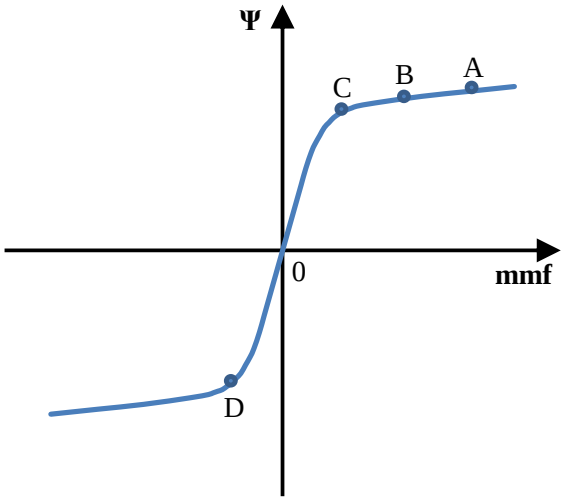

Figure 2.14 - Magnetic characteristic associated with each AC coil of the SC-SFCL.

FIGURE 2.15 shows the magnetic characteristics of each AC coil as well as the device characteristic. Current i_{knee} is related to the operation point C while $i_{max}$is related to the operation point D. If the AC current increase above i_{max}, core reach saturation state again and device impedance decrease to low values. Therefore, i_{knee}define the current value for which the limiter starts limiting and i_{max} define the current value for which the limiter loses the capability to limit.

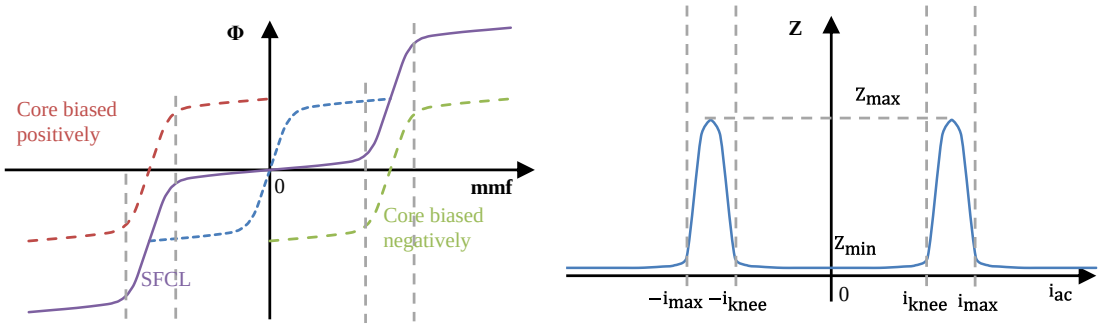

Figure 2.15 - At left: Magnetic characteristic of each AC core and of the SC-SFCL. At right: SC-SFCL inductance as a function of line current.

2.3.2.2 DC Magnetisation System

Most SC-SFCL require a DC magnetization system, composed of a DC bias coil and a current source that can supply high current to magnetise the cores. However, a big concern is regarding the high induced voltage in the DC coil, as a short-circuit fault takes place, because this may damage any element of this system.

The magnetisation circuit may consist of a non-adjustable or phase-controlled bridge rectifier, or a switched power supply. The main advantage of using a controlled power supply is to be able to control the operating point of the limiter, by adjusting the bias current.

In *(Hong et al., 2009)*, the authors have presented a DC magnetization system, based on a controlled switched voltage power source, consisted of a superconducting DC coil, a DC power rectifier, high-speed switches, and an energy release device (FIGURE 2.16). When a fault occurs and it is detected, the high-speed switch (Switch) will open, and the energy release circuit will release the magnetic energy stored in the cores. Piezoresistors (Energy Release Circuit) will suppress the high induced voltage surged in the DC coil due to the quick disconnection of the circuit. This option chosen by the authors is an effective solution to protect the DC system, breaking the DC circuit and releasing the magnetic energy stored in less than 5 ms, however when the fault disappears, the magnetic cores are desaturated and the system needs to supply energy to saturated them quickly. In this system, the re-magnetization takes around 800 ms.

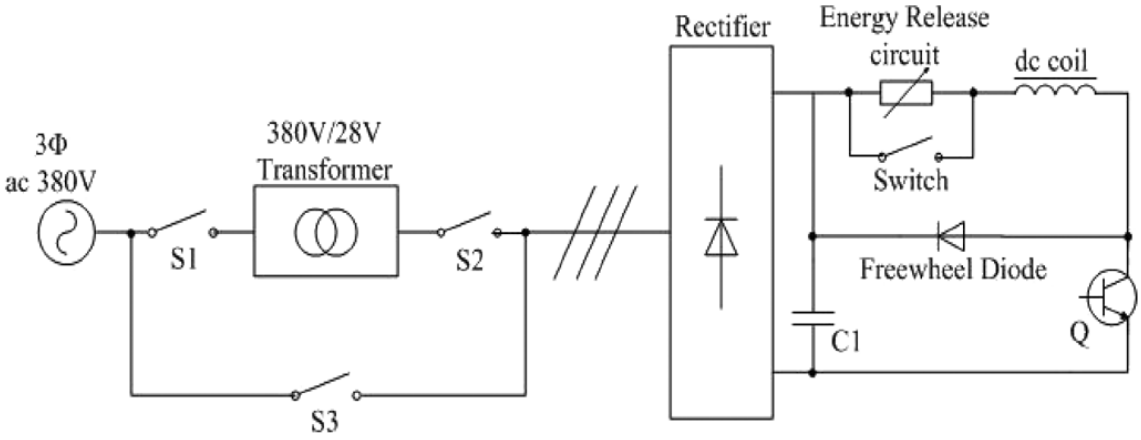

Figure 2.16 – DC magnetization system for a 35 kV SC-SFCL (from *(Hong et al., 2009)*)

A different approach was proposed by *(Xin et al., 2010)*. A non-superconducting winding of a few turns was wound around the DC coil column and electrically connected in parallel with the superconducting DC winding, as shown in FIGURE 2.17 (A). In the normal state, the DC bias current travels through the superconducting winding due to its zero resistivity. In fault conditions, the voltage at the terminals of the two parallel windings is determined by the low number of turns of the auxiliary winding so that the voltage that appears at the DC coil terminals is effectively reduced. The disadvantage of this method is that, although the voltage at the coil terminals is low, the induced AC

voltage, because the windings act as a transformer, contributes to increasing the current in the DC circuit.

Another idea was proposed in *(Oberbeck et al., 1979)*. In order to protect the DC coil from induced voltages due to the AC magnetic flux, a short-circuited winding was added to the column containing the DC coil, FIGURE 2.17 (B). This short-circuited winding does not affect the DC flow created by the polarisation coil however, it reacts to the AC magnetic flux. The current that arises by induction in the short-circuited winding tends to reduce the unwanted AC flow in the DC coil column. This appears to be an optimal solution to this problem however, the author does not provide any experimental reports on the effectiveness or limitations of this method.

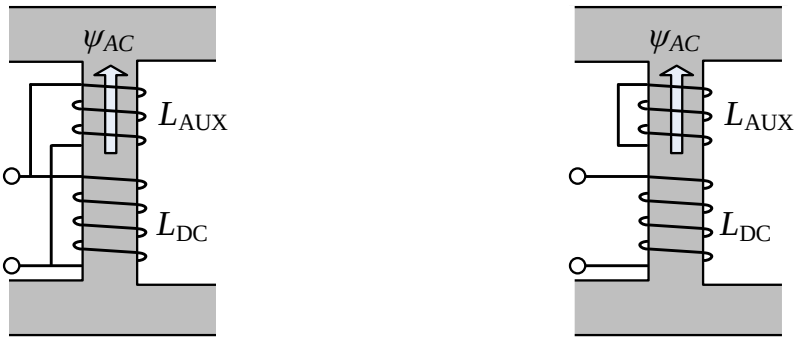

(a) (b)

Figure 2.17 - Overvoltage suppressor windings. (a) In parallel *(Xin et al., 2010)*. (b) Shorted *(Oberbeck et al., 1979)*.

In a SC-SFCL, assuring that, in normal operation, DC and AC limbs of the magnetic cores are deeply saturated making the impedance of the limiter negligible, and in fault conditions, the DC limb remains saturated, is essential to assure the best performance of the limiter and avoiding problems of overvoltage in the magnetization system. In *(J. W. Moscrop, 2013),* the author has concluded that the ratio between the DC and AC limb cross-sections areas is a critical design parameter and the most optimal ratio is 1:0.75. The choice of an adequate DC bias current is also an important factor for the design process. The optimal DC bias point is when both DC and AC limbs achieve the same magnetic induction value for a given DC current *(J. W. Moscrop, 2013)*.

2.3.2.3 State of the Art

A single-phase SC-SFCL was presented and patented in early 1980 by Raju *(Raju et al., 1982)* with the same operation principle that was described previously. Some years

later, with the discovery of the HTS materials, SC-SFCLs employing HTS materials were developed.

The most important concepts on SC-SFCL are presented below.

A. SC-SFCL Concept by Raju

The conceptual diagram of the single-phase SC-SFCL presented by Raju and his team in early 1980, is shown in FIGURE 2.18. The SC-SFCL was composed of two EI type magnetic cores. Each core has two coils wound in the centre limb. DC coils were made of superconducting tape and fed by a low voltage, high current DC source supply. AC coils were connected in series and in opposite direction with the line under protection.

The main advantages of this approach compared to other types of limiters are the simple and symmetrical core design and ruggedness of its constitutive parts. However, the big disadvantage is the core design that makes it difficult to implement a 3-phase SC-SFCL since it is necessary a pack of six cores placed side by side with a safe clearance, making the cryogenics design also a challenge. Another problem with this design is the magnetic coupling between AC and DC coils, which can cause destruction to the DC power supply due to the large induced voltage in the DC coil.

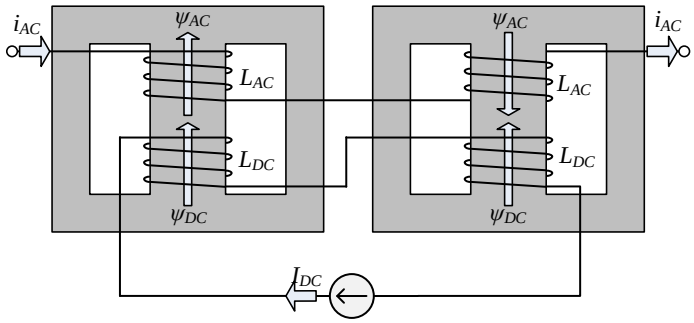

Figure 2.18 - Conceptual diagram of saturated cores SFCL used by Raju.

B. Saturated Open Core SFCL Concept by Rozenshtein

A new approach of a SC-SFCL was proposed in *(Rozenshtein et al., 2007)* and its structure is shown in FIGURE 2.19. The main difference of this SFCL is that it uses only one core per phase. The DC coil is wound around the narrow segment of the UI type core. It provides a closed magnetic path for the DC bias flux that will allow an easy saturation of the core due to its high permeability. The AC coil is wound around the core in order to

embrace both elongated vertical limbs of the core. Thus, it appears as an open core for the AC coil.

The operation principle of this limiter remains the same. DC flux flows in a closed path and in opposite directions through the two limbs embraced by the AC coil. The AC magnetic flux reinforces the DC magnetic flux in one of the limbs and counteracts in the other limb. At normal operation, the induced AC magnetic flux is low so, the limbs remain saturated causing a low inductance of the AC coil. When a fault occurs, the high AC current is capable to lead, the limb with counteract magnetic flux, out of magnetic saturation. Therefore, AC coil experiences an increase in inductance, limiting the fault current.

The main advantage of this limiter compared with the previous one is that only one magnetic core and one AC coil are used, per phase. This design enables decreasing the volume and mass of the limiter. Another important feature is the decreased magnetic coupling between AC and DC coils.

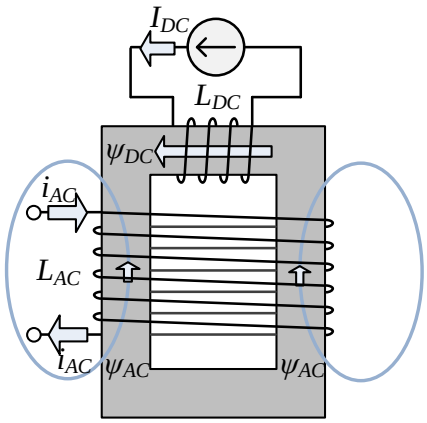

Figure 2.19 - Conceptual diagram of SC-SFCL used by Rozenshtein.

C. Double Storey Three-Phase SFCL Concept by Wolfus

A novel three-phase SC-SFCL was proposed in *(Wolfus et al., 2014)*. The SFCL is composed of two parallel planes of rectangular magnetic cores (AC planes), where the AC coils are wound and connected in series with the power line. There are two perpendicular core limbs between AC planes, connecting them. The DC coils are wound in those limbs allowing the saturation of the AC planes. FIGURE 2.20 (A) shows the core with AC and DC coils mounted on it.

This SFCL is a three-phase device, thus it is composed of three AC coils corresponding to R, S and T phases. Each AC coil is split in four and mounted on the AC limbs inversely connected in series across opposing limbs. FIGURE 2.20 (B) shows schematically the connection of the four R-phase AC coils where a similar connection is also used for the S and T phases. The magnetic flux caused by AC current in the coils 35R1 and 35R3 will be in opposite direction to the magnetic flux caused by the DC bias coils while magnetic flux caused by the AC current in the remaining AC coils will be in the same direction that magnetic flux caused by the DC bias coils, in the same half cycle of AC current. The main advantage of this design is the magnetic circuit for flux caused by AC coils (35R1, 35R2 and 35R3, 35R4) and DC coils (34a and 34b) appear as closed magnetic paths. The magnetic coupling between AC and DC circuits will be negligible due to the respective *mmf* of each AC coil pairs are in opposite directions.

The main feature of this concept is the asymmetry between phase coils and it is achieved by varying the phase coil diameter, number of turns and/or the position of the coil along the limb. This asymmetry is needed to guarantee in a three-phase symmetrical fault event that the sum of the resulting magnetic field is not null and its value is sufficient to drive the AC limb out of saturation.

In general, to achieve asymmetrical magnetic impedance, the AC coils need to satisfy the following requirements:

- The AC coils are wound with different numbers of turns.
- The AC coils are disposed on different portions of the AC circuit limbs.
- The AC coils have different geometries.
- A respective decoupling loop is wound on each of the AC circuit limbs in order to partially inhibit flux transfer between the AC coils. These decoupling loops serve as short-circuit coils, allowing the control of mutual impedance between AC coils.

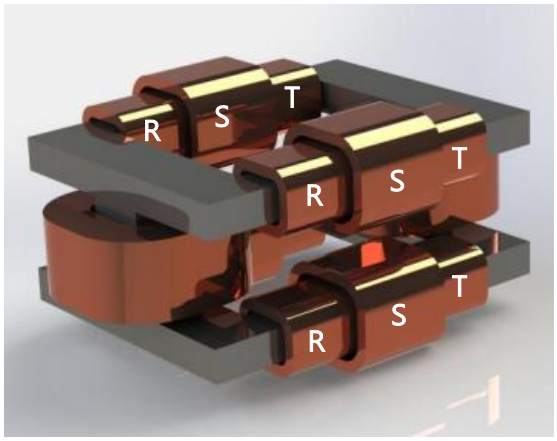

(a)

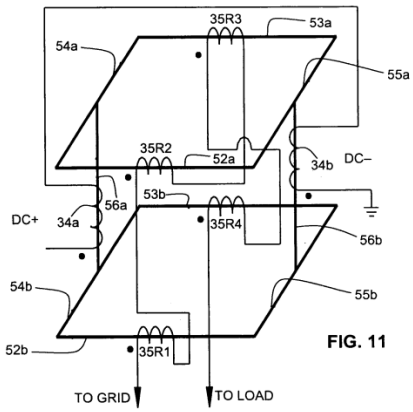

(b)

Figure 2.20 - Conceptual diagram of SC-SFCL used by Wolfus. (a) CAD model of the SC-SFCL (from *(Wolfus et al., 2014)*). (b) Diagram of connection of R-phase AC coils (from *(Shuki et al., 2011)*).

FIGURE 2.21 shows the open-closed three-phase SFCL design proposed by the same author *(Nikulshin et al., 2016)*. This design applied the asymmetric concept of the previous limiter for the project presented in subchapter B.

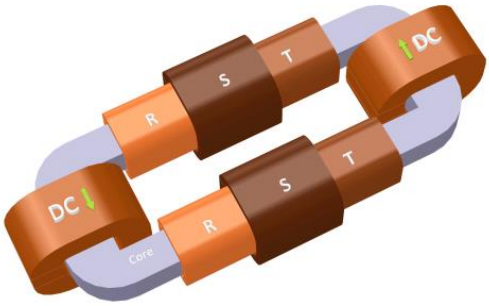

Figure 2.21 - CAD model of the open-closed 3-phase SFCL design (from *(Nikulshin et al., 2016)*).

D. Zenergy Power Project

Zenergy Power was a U.K. superconductor energy technology company with three operating subsidiaries in Germany, the USA and Australia. The Zenergy commercial focus was the innovation and production of clean energy superconductor solutions in the field of renewable and efficient energy technologies. In 2012, Applied Superconductor Company (ASL) acquired Zenergy Power, a company that went bankrupt a year later. The know-how and patents of Zenergy Power were later acquired by ASG Power Systems, a subsidiary of ASG Superconductors Company.

Zenergy developed SC-SFCLs between 2006 and 2012. As can be seen in FIGURE 2.22, Zenergy had designed and tested three main different devices.

(a) 1º Generation Prototype – the spider design.

(b) 2º Generation Prototype – Rectangular Compact SFCL.

(c) Commercial Product – Round Compact SFCL.

Figure 2.22 - Different devices designed by Zenergy. (a) is the first generation SFCL that was tested, installed and used in the grid, to prove its performance and reliability. (b) is the rectangular compact SFCL that was built and tested to validate a smaller and more efficient SFCL. (c) is the round compact SFCL for distribution-class applications.

The first-generation prototype was a three-phase SFCL composed of combining six rectangular cores arranged in a "spider" configuration, which allows wounding a single HTS coil in the centre of the device that saturates all cores. The AC coils are arranged radially around the device (in the outer limbs) *(JW Moscrop & Hopkins, 2009)*. This device had the big test on March 9, 2009, with the support of the California Energy Commission (CEC) and the U. S. Department of Energy (DOE). It became the first SFCL in service in the U.S.A when it was installed in the Avanti Circuit in the Southern California Edison Company's Shandin Substation in San Bernardino, California. This device, known as CEC FCL, was a 12 kV three-phase SFCL with a fault limiting capability of 20% in a three-phase-to-ground fault type *(Moriconi, Koshnick, et al., 2010)*.

The success of the CEC FCL led Zenergy to investigate new design options for its limiter with the objective of reducing the size and weight of the device.

The new concept became known as the Compact HTS FCL and it still works with the same operation principle as the spider concept but presenting a new design. On this concept, the magnetic cores with AC coils are involved by the HTS coil, as can be seen in FIGURE 2.23. The Compact HTS FCL is approximately 1/3 of the volume and weight for equivalent performance. This was achieved mainly because of the new SFCL design as well as a new cryogen-free design and Oil-Filled Dielectric Design. Four prototypes of this limiter were built and tested and two of them were three-phase devices *(Moriconi, De La Rosa, et al., 2010)*.

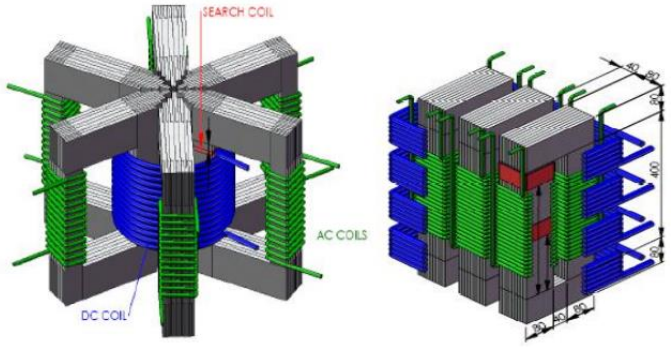

Figure 2.23 - Spider and Compact FCL Design Concepts (from *(Moriconi, De La Rosa, et al., 2010)*).

Due to the successful testing of the Compact FCL, in January 2010, Zenergy received a contract to design and build a 15 kV Compact FCL, 1.25 kA of nominal current, 50 Hz, capable of limiting a 3 s fault and reducing it by at least 30%. The limiter was tested in a CE Electric substation in the UK by Applied Superconductor Ltd. As can be seen in Figure 2.24, this new device has a round design, composed of six open cores wounded each one by an AC coil and two HTS bias coil disposed of axially aligned, constituting a Helmholtz coil, and involving all cores. It also uses "dry-type" cryogenics to conductively cool the HTS coil without liquid nitrogen *(Nelson et al., 2011)*.

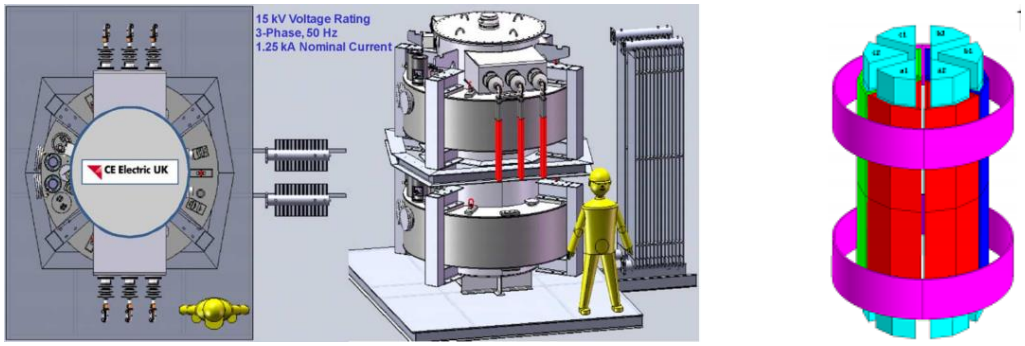

(a) (b)

Figure 2.24 - Round Compact FCL prototype (from *(Nelson et al., 2011)*). (a) Design and layout of commercial 15 kV-class FCL installed in a CE Electric substation in early 2011. (b) CAD model of the prototype.

A new SFCL (with 33 kV / 45 MVA rating) was developed by ASG Power Systems in 2016 *(Pellecchia et al., 2017)*.

E. Innopower Project

Innopower has been developing a saturated magnetic core type SFCL since 2004. The reason to choose the SC-SFCL type was to avoid the quenching effect of the superconductor coils during fault current limiting, which results in long recovery time after a fault and complicated protection requirements *(Ying Xin et al., 2007)*.

Innopower developed a 35 kV/90 MVA SC-SFCL and in January 2008 the limiter was installed in a transmission network at Puji Station of China Southern Power Grid. This device is similar in design and operation principle to Zennergy Spider concept. As can be seen in FIGURE 2.25 (A), the device is composed of six UI type magnetic cores disposed of in a hexagonal configuration. The HTS coil is installed inside the cryostat involving the inner limbs of the cores. The AC coils are wound in the outer limbs of each core *(Yin Xin et al., 2009)*.

Due to the success of the 35 kV SC-SFCL, Innopower designed and manufactured a new device from January 2008 to March 2011. The new device was a 220 kV SC-SFCL (FIGURE 2.25 (B)), which was installed at Shigezhung Substation of the State Grid in Tianjin at the end of 2011. This device followed the same design as the last one *(Xin et al., 2013)*. TABLE 2.2 shows the main characteristics of 35 kV and 220 kV SC-SFCL.

(a) (b)

Figure 2.25 - Prototypes developed by Innopower (from *(Yin Xin et al., 2009)* and (Xin et al., 2013)). (a) 35 kV SC-SFCL prototype. (b) 220 kV SC-SFCL prototype.

Table 2.2 - Main characteristics of the two prototypes developed by Innopower.

	35 kV SC-SFCL	220 kV SC-SFCL
*Rated Voltage (*kV*)*	35	220
*Rated Current (*kA*)*	1.5	0.8
*Max. Prospective Current (*kA*)*	41	50
*Max. Limited Current (*kA*)*	25	30
Max. Line Voltage Drop (%)	<1	<1.25
*Fault Detection Time (*ms*)*	<1	
*Reaction Time (*ms*)*	<5	none
*Restoration Time (*ms*)*	<800	<500

2.3.2.4 Methodologies to Simulate Saturated Cores Superconducting Fault Current Limiters

There are methodologies, generally simplified representations, that can be used to predict the behaviour of the FCL in order to simulate and analyse the device's behaviour in a real electrical grid.

A. Nonlinear Reluctance Model

A nonlinear reluctance model of a single-phase SC-FCL was proposed in *(Commins & Moscrop, 2013)*, *(Gunawardana et al., 2015)*. This analytic model describes the nonlinear magnetic operation of the limiter through an equivalent magnetic circuit of reluctances that includes all significant magnetic flux paths. Two different geometries of the limiter were analysed. Initially, an air-core geometry was examined, then extended to an open-core arrangement, as can be seen in FIGURE 2.26 (A). This arrangement consists of two AC coils wounded in two open-cores placed side by side and embraced by a DC bias coil. FIGURE 2.26 (B) shows the equivalent magnetic circuit of the significant magnetic flux paths, where $\Re_c$ represents the reluctance of the open-cores, $\Re_y$ represents the reluctance associated with the flux paths between the two AC coils. The reluctances of the magnetic cores are nonlinear, therefore, $\Re_c$ and $\Re_y$ are nonlinear variables. $\Re_a$ represents the reluctance of the flux paths that link the inner AC loop with the other paths, $\Re_i$ represents the reluctance of the remaining flux paths inside the DC bias coil

and $\Re_0$ represents the reluctance of the flux paths outside the DC bias coil. $N \cdot I_{DC}$, $N \cdot I_{AC1}$ and $N \cdot I_{AC2}$ are the *mmf* due to the DC bias coil and the AC coils respectively.

In order to obtain the parameter values of the equivalent magnetic circuit is necessary to carry out either a FEM simulation or real experimentation following the next test conditions:

- Test 1: $N \cdot I_{DC}$ is varied, while $N \cdot I_{AC1} = N \cdot I_{AC2} = 0$
- Test 2: $N \cdot I_{DC} = 0$, while $N \cdot I_{AC1} = N \cdot I_{AC2}$ (varied)
- Test 3: $N \cdot I_{DC} = 0$, while $N \cdot I_{AC1} = -N \cdot I_{AC2}$ (varied)

During the tests, the range of applied *mmf* must be sufficient in order to saturate the magnetic cores.

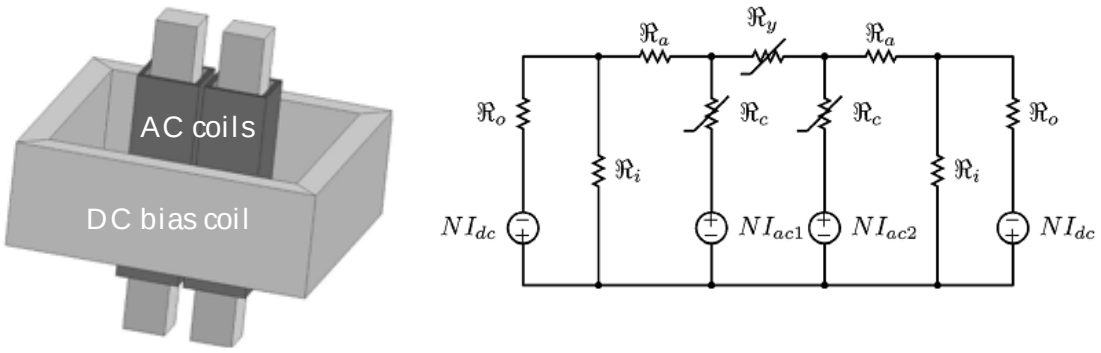

(a) (b)

Figure 2.26 - FCL used to design the analytical nonlinear reluctance model (from *(Gunawardana et al., 2015)*). (a) Single-phase open-core arrangement. (b) Equivalent open-core magnetic circuit.

Test 1 and Test 2 are used to calculate the constant values of $\Re_i$ and $\Re_0$ by EQUATION (2.10) and EQUATION (2.11). ϕ_{01} and ϕ_{02} represent the magnetic flux through $\Re_0$, obtained by tests 1 and 2 respectively. ϕ_{c1} and ϕ_{c2} represent the magnetic flux through $\Re_C$, obtained also by test 1 and 2 respectively (as can be seen in FIGURE 2.27).

$$\Re_i = \frac{NI_{dc}}{\phi_{o1} - \phi_{c1} - \frac{\phi_{o1}}{\phi_{o2}}(\phi_{o2} - \phi_{c2})} \tag{2.10}$$

$$\Re_o = \frac{NI_{dc}}{\phi_{o1} - \phi_{o2}\frac{\phi_{o1} - \phi_{c1}}{\phi_{o2} - \phi_{c2}}} \tag{2.11}$$

$\Re_{ca}$ is the series combination of $\Re_c$ and $\Re_a$ and,

$$\Re_{ca} = \frac{\Re_i(\phi_{o2} - \phi_{c2}) + NI_{ac1}}{\phi_{c2}} \tag{2.12}$$

$\Re_p$ is the parallel combination of $\Re_i + \Re_0$

$$\Re_p = \frac{\Re_i \Re_o}{\Re_i + \Re_o} \tag{2.13}$$

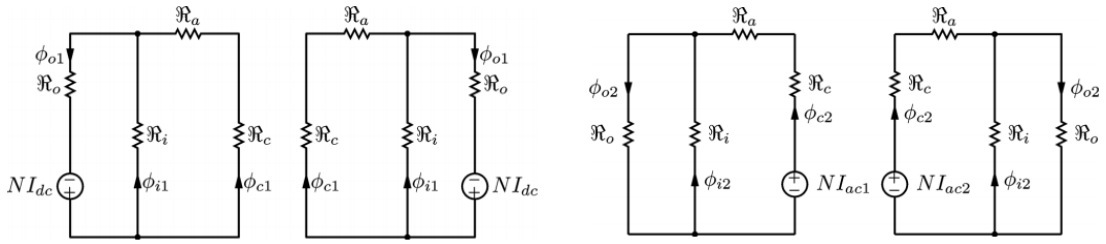

(a) (b)

Figure 2.27 - (a) equivalent circuit for Test 1 and (b) equivalent circuit for Test 2 (from *(Gunawardana et al., 2015)*).

Test 3 is used to calculate the individual values of $\Re_a$ and $\Re_c$, along with $\Re_y$ by EQUATIONS (2.14), (2.15) and (2.16) (the equivalent circuit is shown in Figure 2.28).

$$\Re_a = \frac{\Re_{ca}\phi_{c3} + \Re_p(\phi_{c3} - \phi_{y3}) - NI_{ac1}}{\phi_{y3}} \tag{2.14}$$

$$\Re_c = \Re_{ca} - \Re_a \tag{2.15}$$

$$\Re_y = \frac{(\phi_{c3} - \phi_{y3})}{\phi_{y3}}(\Re_a + \Re_p) \tag{2.16}$$

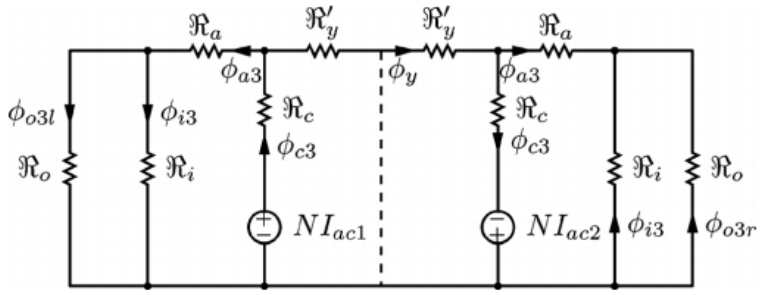

Figure 2.28 - Equivalent circuit for Test 3 (from *(Gunawardana et al., 2015)*).

In order to determine reluctance values of the equivalent model magnetostatic simulations are carried out using a FEM software. After determining the reluctance values, the performance of the analytical model is compared with FEM transient simulation, where the resulting flux linkage values for the analytical model is calculated using a numerical computing environment such as Matlab software.

B. Jiles-Atherton Hysteresis Model

In *(Zhang Xuhong et al., 2005)* was proposed an analytic method based on Jiles-Atherton hysteresis model to describe the dynamic differential equations of a circuit comprising a single-phase SC-SFCL and using a numerical computing software to carry out simulations of the voltage drop across the AC coils and the limited current under a fault.

FIGURE 2.29 (A) represents the SC-SFCL schematic used to apply this analytic method. The SFCL is a single-phase limiter, composed of two separated magnetic cores, which are saturated by a single DC bias coil. FIGURE 2.29 (B) represents the electrical schematic of a simplified network comprising SFCL.

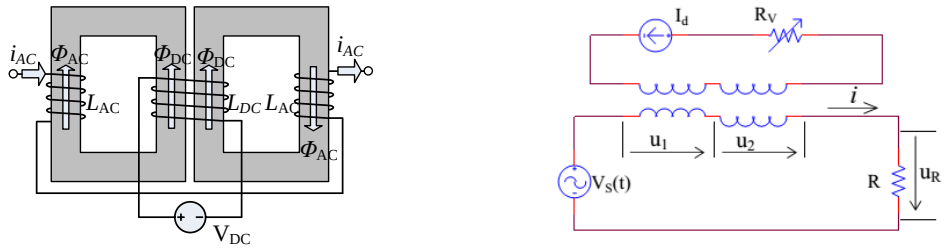

(a) (b)

Figure 2.29 - The diagram of SC-SFCL used and the electrical network simulated. (a) The SC-SFCL diagram adopted. (b) Principle diagram of a simplified network comprising SC-SFCL (from (ZHANG XUHONG ET AL., 2005)).

In 1986, D. C. Jiles and D. L. Atherton presented a mathematical model of the ferromagnetic hysteresis, which the magnetic susceptibility is a function of the magnetization M and the applied magnetic field H, as shown in equation (2.17) *(Jiles & Atherton, 1984)*.

$$\frac{dM(H)}{dH} = \frac{1}{1+c} \cdot \frac{M_{an}(H_e) - M}{\delta k - \alpha[M_{an}(H_e) - M]} + \frac{c}{1+c} \cdot \frac{dM_{an}(H_e)}{dH} \qquad (2.17)$$

where H_e is an effective field given by:

$$H_e = H + \alpha M \tag{2.18}$$

$M_{an}(H_e)$ is the anhysteretic magnetization, which can be expressed by a modified Langevin function and M_s is the saturation magnetization.

$$M_{an}(H_e) = M_s \left[\coth\frac{H_e}{a} - \frac{a}{H_e}\right] \tag{2.19}$$

And δ takes the value +1 or -1 if H increasing in the positive direction or increasing in the negative direction respectively.

The model parameters can be obtained from experimental values, thus the hysteresis model of each magnetic core could be simulated in a numerical computing software with an excellent agreement with the measured curves *(Jiles & Thoelke, 1989)*.

In order to apply this model, a mathematical formulation of the simplified power grid comprising an SFCL showed in FIGURE 2.29 (B), was done.

According to Ampère's Law:

$$N_{dc}I_{dc} - N_{ac}i = H_1 l \tag{2.20}$$

$$N_{dc}I_{dc} + N_{ac}i = H_2 l \tag{2.21}$$

and:

$$\vec{B} = \mu_0(\vec{H} + \vec{M}) \tag{2.22}$$

From Faraday's Law, it can be obtained the voltage drop of AC coil 1, which is given by:

$$u_1 = -e_1 = L\frac{di}{dt}\left(1 + \frac{dM_1}{dH_1}\right) \tag{2.23}$$

The voltage drop of AC coil 2 is given by:

$$u_2 = -L\frac{di}{dt}\left(1 + \frac{dM_2}{dH_2}\right) \tag{2.24}$$

Analysing the circuit based on Kirchhoff's law:

$$\frac{di}{dt} = \frac{U_s(t) - iR}{L\left(\frac{dM_1}{dH_1} - \frac{dM_2}{dH_2}\right)} \tag{2.25}$$

Therefore, through numerical computing software, such as MATLAB, if the current i is given, it is possible to obtain the voltage drop of each AC coil from EQUATIONS (2.17),

(2.20), (2.21), (2.23) and (2.24). It is also possible to obtain the line current from EQUATIONS (2.17), (2.20), (2.21) and (2.25).

C. Model Based on $\boldsymbol{\Psi - i}$ Characteristic

The methodology presented in *(Vilhena, Arsenio, et al., 2015)* is based on the SC-SFCL characteristic, which allows simulating the behaviour of the limiter in electrical power grids with different voltage ratings and characteristics.

This magnetic characteristic, which relates to line current, i and the linked flux of the device (total linked flux by the two AC coils), Ψ_{SFCL}, allows to determine the electromagnetic behaviour of the limiter and it is directly related to the inductive voltage drop developed at the terminals of the limiter that is given by:

$$u_{SFCL}(t) = R_{SFCL} i + \frac{d\Psi_{SFCL}(t)}{di} \cdot \frac{di(t)}{dt} \tag{2.26}$$

The first step of the methodology consists of determining the magnetic characteristic of the limiter and describing it analytically. Therefore, the behaviour of the limiter can be predicted by a simple mathematic model and simulated in numerical computation software such as MATLAB.

The magnetic characteristic of the limiter can be modelled by:

$$\Psi_{SFCL}(i) = \frac{p_1 i^5 + p_2 i^4 + p_3 i^3 + p_4 i^2 + p_5 i + p_6}{i^4 + q_1 i^3 + q_2 i^2 + q_3 i + q_4} \tag{2.27}$$

where $p_k, k = 1 \dots 6$, and $q_m, m = 1 \dots 4$, are parameters determined by fitting of a characteristic curve obtained by simulation or real experiments.

The equation of the circuit in FIGURE 2.30 is given by:

$$u_g = R_{line} i + \left(R_{SFCL} i + \frac{d\Psi_{SFCL}}{di} \cdot \frac{di}{dt} \right) + R_{load} i \tag{2.28}$$

by manipulation equation (2.28) leads to:

$$\frac{di}{dt} = \frac{1}{\frac{d\Psi_{SFCL}}{di}} \cdot \left(u_g - R_{line} i - R_{SFCL} i - R_{load} i \right) \tag{2.29}$$

Equation (2.29) allows determining line current and thus simulating the SFCL.

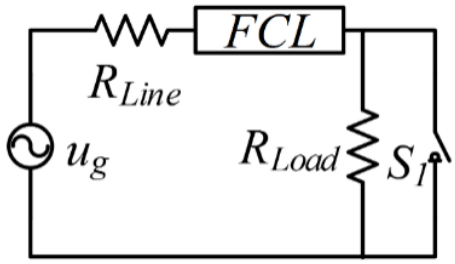

Figure 2.30 – Circuit used to simulate the FCL.

2.3.3 Transformer Type Superconducting Fault Current Limiter

2.3.3.1 Operation Principle

A TT-SFCL is basically a transformer with its secondary coil short-circuited. The basic elements of a single-phase TT-SFCL are shown in FIGURE 2.31. This device is composed of a magnetic core (open or closed configuration) where it is wound a primary coil, connected in series with the line under protection. The secondary coil is short-circuited and made of superconducting material (superconducting tape).

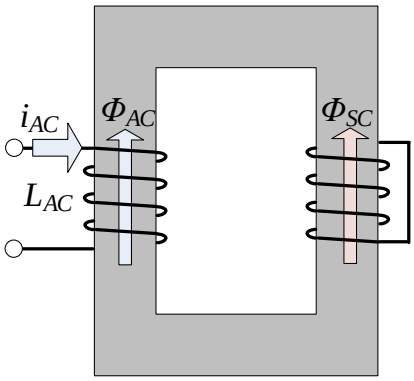

Figure 2.31 - Conceptual diagram of a TT-SFCL. i_{AC} is the line current, L_{AC} is the inductance of the coil connected with the power line, Φ_{AC} represents the magnetic flux through the core induced by the AC coil and Φ_{SC} represent the opposite magnetic flux through the core induced by the short-circuited coil.

During normal operation, the *mmf* developed by the AC coil is cancelled through the opposite *mmf* developed by the short-circuited coil, ensuring a very low impedance of the AC coil and in turn, a negligible voltage drop of the FCL. In a fault event, the line current rises abruptly which induces high currents in the short-circuited coil, quenching it, and failing to cancel primary *mmf*, in totally. Therefore, the line inductance also increases, limiting the fault current *(Wojtasiewicz et al., 2014)*.

FIGURE 2.32 shows the excursion in the $\Psi - i$ (linked flux versus line current) plane of the TT-SFCL under normal (the small excursion in the centre) and fault conditions (for different prospective fault currents). During normal regime, the excursion looks like a horizon path, showing almost no variation of the magnetic flux in the core, which leads to a negligible impedance. Contrariwise, during a fault event, the variation in the magnetic flux leads to a brutally increase in the line impedance.

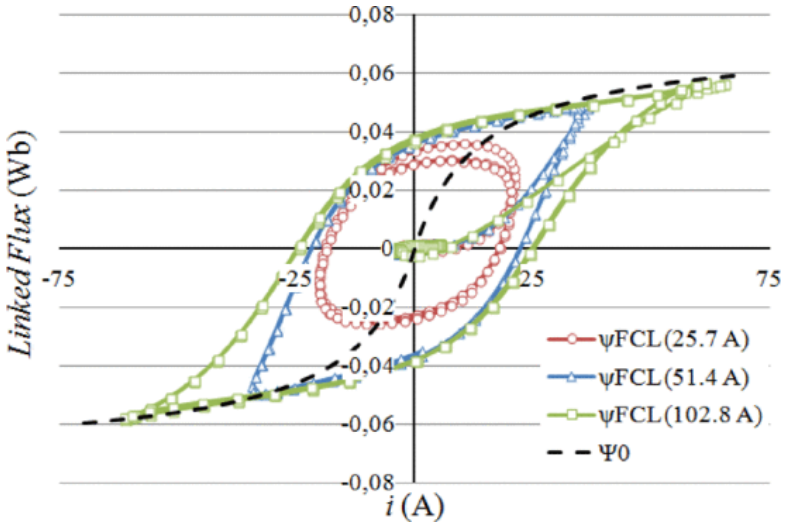

Figure 2.32 – Excursion in $\Psi - i$ plane of the TT-SFCL under a fault, for different peak prospective fault currents (from *(Arsenio et al., 2013)*).

2.3.3.2 State of the Art

The inductive type SFCL has experienced a high development in the last years. In the beginning, the inductive type SFCL used the superconducting material in bulks format and low-temperature superconductors. One of this type of limiter, probably the first one, was patented in 1987 *(Bekhaled, 1987)*. With the discovery of high-temperature superconductors, the R&D related to this type of SFCL has increased due to the low cost of the cooling system required for this technology, for instance. TABLE 2.3 shows some projects that were developed.

The project from Hydro-Quebec started in 1992 and a 100 kVA SFCL prototype was built and tested. The SFCL was composed of an EI magnetic core with the primary coil placed in the inner limb of the core and a superconducting bulk between the primary and the core, shielding it. Two key issues identified was heat management and the difficulty of obtaining homogeneous superconducting properties *(Cave et al., 1999)*.

The project from ABB consisted of a three-phase SFCL prototype, with a power rate of 1.2 MVA. The limiter used superconducting bismuth-based ceramic rings (Bi-2212),

where each phase utilized a tube composed of 16 rings. The prototype was installed in 1996 and tested for one year, in the NOK hydropower plant Kraftwerk am Lontsch in Switzerland. During the test period, no faults occurred, and also the superconducting ceramic was not degraded *(Paul & Chen, 1998)*.

Table 2.3 - Summary of some projects of Inductive Type SFCL.

Project Owner	Country	Power Rating	HTS Material
Hydro-Quebec	Canada	100 *kVA*	Bi-2212 – Bulk
ABB	Switzerland	1.2 *MVA*	Bi-2212 – Bulk
CRIEPI	Japan	66 *kV*, 1 *kA*	Bi-2212 – Thick film Bi-2223 – Bulk
Nagoya University	Japan	2 *MVA*	YBCO – Tape Bi-2223 – Tape
Bruker	Germany	40 *MVA*	YBCO – Tape
IEL	Poland	6 *kV*, 0.6 *kA*	YBCO – Tape

The SFCL developed by Central Research Institute of the Electric Power Industry (CRIEPI) used two different shielding cylinders, a Bi2223 bulk cylinder and a Bi2212 thick film cylinder. The reason for using a thick film cylinder is because it is easier to make large-scale cylinders. This was a 66 kV/ 1 kA prototype that was tested in a laboratory environment. The authors have concluded that using a thick film cylinder is better for limiting performance purpose *(Ichikawa & Okazaki, 1995)*.

Researchers at Nagoya University have developed and tested a three-phase SFCL Transformer with the functionality of a transformer in steady-state and an SFCL in fault conditions. The last prototype developed had a power rating of 2 MVA and uses a hybrid structure of HTS coils using YBCO, YBCO/Cu tapes (for the low voltage coil) and Bi2223 tapes (for the high voltage coil). The final tests showed that the devices exhibited an excellent current limitation (around 34% of the prospective current) and no-load, short-circuit and partial-load tests verified that the device exhibited the fundamental performance for this type of device *(Kojima et al., 2011)*.

Bruker High-Temperature Superconductor had developed a three-phase 40 MVA SFCL together with Schneider Electric and Alstom Grid, so-called iSFCL, since 2010. In this

limiter, the superconductor is arranged in a stack of rings made of YBCO tape. It is placed between the magnetic core and the primary coil, concentrically *(Bäuml & Kaltenborn, 2012)* .

IEL developed a single-phase coreless SFCL of 6 kV / 0.6 kA in 2012, compared with other solutions, it has the advantage of reduced weight of the device and also a reduced of the primary copper coil. *(Janusz Kozak et al., 2012)*

2.3.3.3 Electromechanical Stresses

Electromechanical forces developed under short-circuit events must be well characterized, as they can compromise the integrity of electric power systems, especially power transformers or other devices, such as SFCL. These forces can destroy windings causing devices failure and affecting power grid operation.

During fault conditions when currents can increase up to several times their rated values, SFCL windings experience substantial forces. The consequences of these forces can be the destruction of windings, particularly if they are made of HTS material, which is less mechanically robust than copper windings. To ensure the integrity of HTS windings, the mechanical design must be carefully defined in order to avoid windings permanent deformations or fractures resulting from applied stresses *(Soika et al., 2007)*.

Stress tests performed on YBCO tapes have shown that these show excellent mechanical resistance due to their axial strength, allowing the maintenance of superconducting performance under these types of forces *(Osamura et al., 2010)*.

The effects of transverse stresses on the performance of the YBCO tape has been studied showing that critical current of YBCO tapes degrades significantly under transverse stress before delamination, causing low delamination strength of less than 15 MPa *(Laan et al., 2007; Takao et al., 2007)*.

Since tape joints are crucial to superconducting power applications, YBCO tape lap joints submitted to mechanical stresses have also been tested showing good results for their strength and electrical resistance *(Duckworth et al., 2010)*.

Therefore, the study of electromechanical forces developed on the superconducting materials is essential in order to ensure their integrity.

A. Axial and Radial Forces

When a conductor carrying an electric current is placed in a magnetic field, it will experience a force. This is the case of the windings of an SFCL under operating conditions. Due to the interaction between the magnetic field and the winding current, the windings will experience electromagnetic forces.

The Lorentz force law shows that the force density (force per unit of volume) generated in the windings depends on the induction magnetic field and current density *(Heydari & Faghihi, 2010)*,

$$\vec{f} = \vec{J} \times \vec{B} \ (\mathrm{N/m^3}) \tag{2.30}$$

FIGURE 2.33 shows the Lorentz force vector *F* experienced by a wire carrying an electrical current of density *J* and submerged in a magnetic flux density *B*.

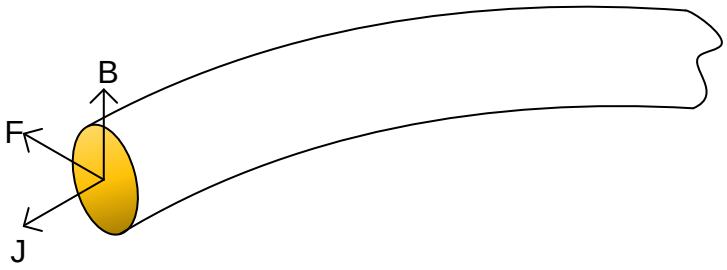

Figure 2.33 - Vector diagram resulting from Lorentz's Law.

In an inductive SFCL, electromagnetic forces experienced by HTS windings will be developed in axial or radial directions depending on the direction of magnetic field vectors.

An TT-SFCL composed of single turns of HTS tapes *(Arsenio et al., 2013)* is affected by radial and axial forces, which are related to axial and radial flux density directions, respectively. The axial force tends to compress the single turn axially whereas the radial force causes compressive and bending stresses or tensile stress (hoop stress) acting over the length of the single turn, as can be seen in FIGURE 2.34. The hoop stress is compressive or tensile depending on whether the radial pressure acts radially inward or outward, respectively *(Vecchio et al., 2010)*.

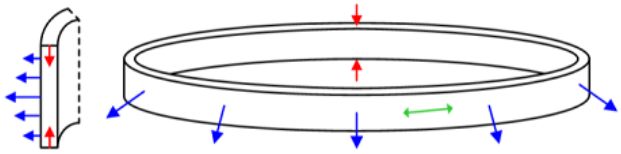

Figure 2.34 - Forces exerted on a single turn: Radial forces are represented in blue and the hoop stress caused by radial forces is represented in green. The axial forces are red.

2.3.3.4 Methodology to Measure Electromechanical Forces

It is important to quantify the forces developed in SFCL devices in order to minimize the effects of those forces during the project phase. Using FEM simulation software packages (such as Cedrat Flux2D® and COMSOL Multiphysics®), it is possible to estimate the magnitude of those forces on an SFCL previously modelled by FEM. However, a method that allows measuring those forces is required.

A method to quantify those forces can be based on strain gauges. Using a resistive electric strain gauge (FIGURE 2.36 (A)) it is possible to measure the strain in the HTS tape in operation conditions.

When a material is submitted to a tensile force P (or compressive force), it corresponds to a stress σ which is the force per unit of area, as is represented in FIGURE 2.35 (A). Depending on the stress, the cross-section contracts (elongates) and the length elongates (contracts) by ΔL (FIGURE 2.35 (B)).

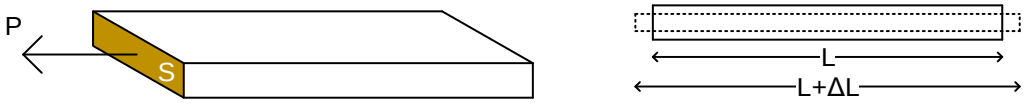

(a) (b)

Figure 2.35 - Material submitted to a tensile force P. (a) Tensile force P applied on a surface S. (b) Mechanical deformation when a tensile force is applied.

The relation between the original length L, and the change in length ΔL, is called tensile strain and is expressed as follows:

$$\varepsilon = \frac{\pm \Delta L}{L} \tag{2.31}$$

Taking into account Hooke's law, equation (2.32) shows the relation between stress and strain initiated in a material where E is its Young's modulus.

$$\sigma = E \cdot \varepsilon \ (Pa) \tag{2.32}$$

A typical mechanical characteristic of a material is shown in FIGURE 2.36 (B). There are two main regions, elastic region and plastic region. The elastic region is the region where the material preserves its mechanical properties, and it can return to the undeformed state after removing the applied force. The plastic region is the region where the material deforms permanently. In the elastic region, the material presents a proportional ratio between stress and strain, thus it is possible to use the Hooke's law in this region.

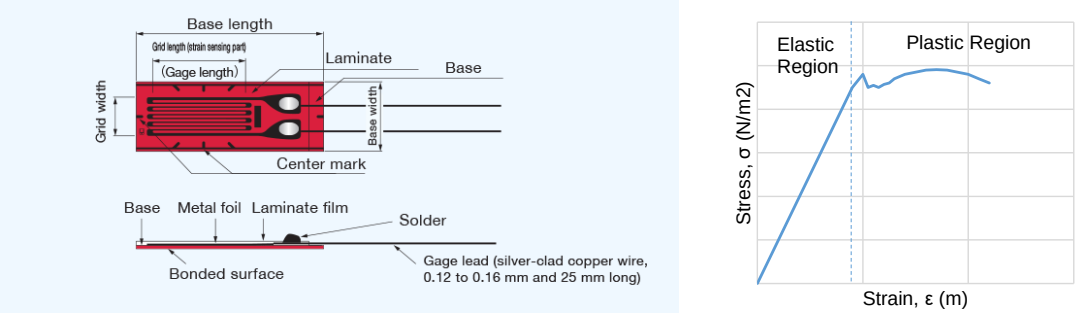

(a) (b)

Figure 2.36 – (a) Example of a strain gauge (from *(Kyowa, 2016)*) and (b) Example of a mechanical characteristic of a material.

The strain gauges are devices able to measure deformations on a material, such as HTS tapes. By knowing the material characteristic, it is possible to derive the mechanical stress applied to the material, by interpolation of that curve.

FIGURE 2.37 shows the mechanical characteristic of YBCO coated conductor made by Superpower. Yield stress (77 K) is 970 MPa at 0.92 % of strain i.e., from this value the material starts to deform permanently. However, the stress limit is 700 MPa in order to maintain its electrical properties, namely the critical current of the material *(Hazelton, 2011)*.

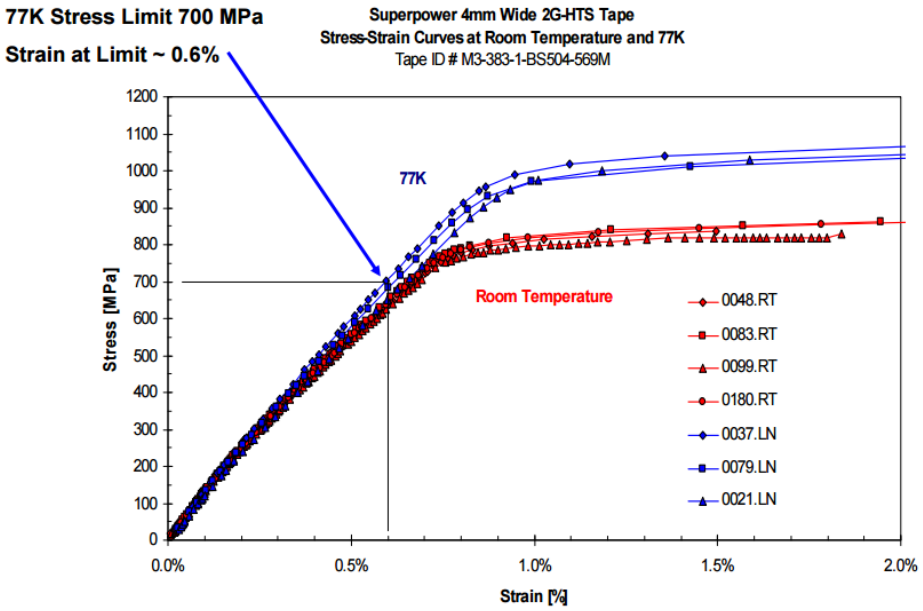

Figure 2.37 - Mechanical characteristic of YBCO coated conductor (from *(Hazelton, 2011)*). RT stands for room temperature, while LN means liquid nitrogen temperature.

2.4 Optimisation Techniques and Methods

Mathematical optimisation is a branch of applied mathematics and aims to find the best solution to a problem. It can be useful in different fields, like engineering, mechanics, economics, marketing, manufacturing, production, transportation, finance, policy modelling, etc.

A basic optimisation problem consists of *(Amaran et al., 2016; Venter, 2010)*:

- The Cost Function (CF), $f(x)$, is the function or system that describes the problem in optimisation and whose maximum or minimum is to be determined.
- Decision Variables (DV), x_1, x_2, x_n, (where x refers to DV as a group) are the independent variables of the cost function. Different combinations of x lead to a different solution to the search range defined.
- Constraints are equations that place limits for the relation between DVs or the founded solutions in order to eliminate infeasible solutions or penalise the CF. $g_j(x)$ refers to an inequality constraint and $h_k(x)$ an equality constraint function.
- Upper, x_{iU}, and Lower Bounds, x_{iL}, are the limits allowed for the DV and represents the searchable domain for the DV.

- An optimal point is a point in the searchable domain where the CF is maximum or minimum.

Optimisation techniques could be classified into two categories:

- Linear methodologies

  The problem in optimisation can be modelled using linear combinations of their decision variables and constraints, using simple methods of linear programming in order to obtain the optimal point. This is a straightforward technique because there is only a unique solution for the linear optimisation problem. Some techniques are the direct method, recursive method, iterative method, etc *(Bertsimas & Tsitsiklis, 1997)*.

- Non-linear methodologies

  When the cost function of a problem in optimisation or their constraint shows a non-linear characteristic, as usually in engineering problems, non-linear methodologies must be used. These techniques are complex and sophisticated because a non-linear problem has local optimal points which could lead the algorithm to them instead of the global and unique solution. These methods may have a deterministic characteristic where the same solution is achieved if starting from the same initial decision variables values, or a stochastic characteristic where is not assured the same solution when starting from the same initial point, due to the aleatory behaviour of the method *(Ramachandran et al., 2019; Zobolas et al., 2008)*.

  Classical and conventional algorithms are deterministic, for example, the gradient-based algorithms (Newton-Raphson algorithm is gradient-based). However, if the cost function shows some discontinuity, it does not work well.

  For stochastic problems, the decision variables are random generated, which involve random cost function or random constraints. Stochastic search methods have been shown more efficient in solving large problems in a way that is not possible when using deterministic algorithms. Another advantage is relatively easy to implement these algorithms on complex problems. A subgroup of the stochastic techniques is the heuristic method which means “to find” or “to

discovery" the solution by trial and error. Even so, feasible and quality solutions to a tough optimisation problem can be achieved in a limited amount of time, but no guarantee of the founded solution is the optimal one. This is not important in problems where the best solution is not necessary but rather good solutions which are reachable easily. Artificial neural networks are an example of a heuristic method. Another subgroup is the meta-heuristic algorithms that have a small difference compared to the previous one, it is the second generation of heuristic methods and can be used for more complex problems. In general, their performance is better than simple heuristics due to the use of certain trade-off of randomization and local search, mainly inspired by natural phenomena, which improves the domain search for the optimal solution. Genetic algorithms are an example of meta-heuristics *(Kunche & Reddy, 2016)*.

In FIGURE 2.38 is shown a classification schematic of the optimisation technics and some optimisation methods used in optimisation problems.

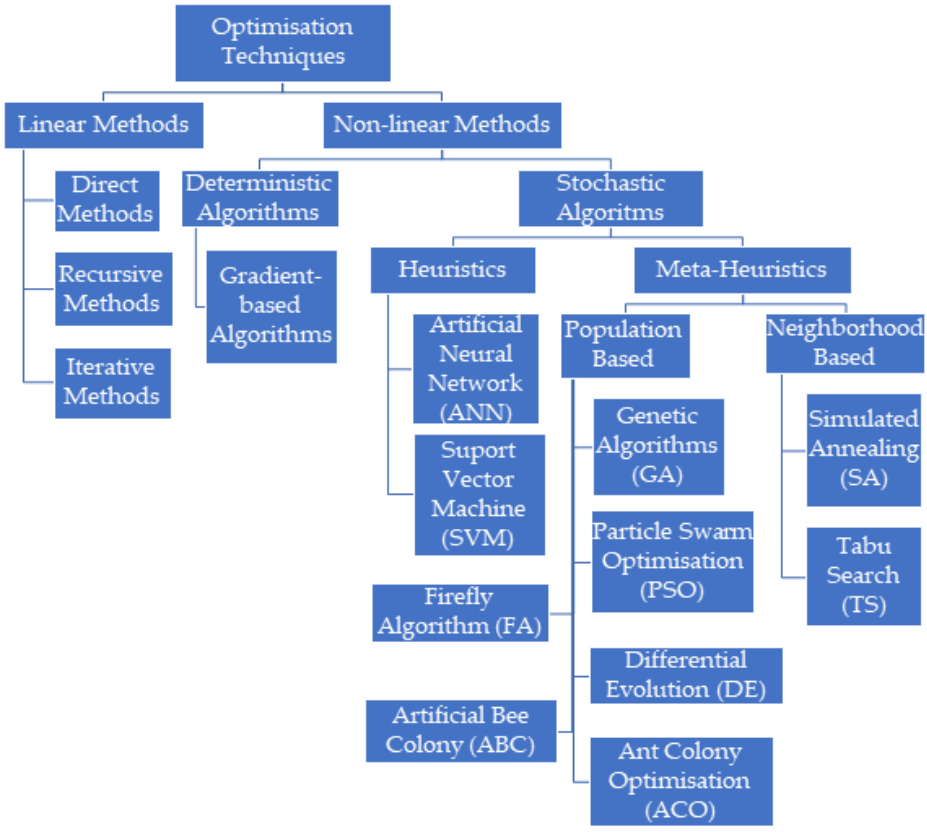

Figure 2.38 – Classification diagram of optimisation algorithms.

The standard form for a single-objective, non-linear, constrained optimisation problem could be described by EQUATION (2.33) *(Amaran et al., 2016; Venter, 2010)*.

$$\begin{gathered} \text{Minimize:} \\ f(x) \\ \text{Subject to:} \\ g_j(x) \leq 0;\ j = 1, m \\ h_k(x) = 0;\ k = 1, p \\ x_{iL} \leq\ x_i \leq x_{iH}; i = 1, n \end{gathered} \tag{2.33}$$

For nonlinear optimisation and depending on the chosen algorithm, the optimisation process could return a local optimal solution instead of a global optimal solution. This happens when the problem in optimisation has more than one optimal solution, thus the algorithm converges to a locally optimal point, which is a point where no better feasible solutions can be found in the immediate neighbourhood of the given solution. That means other local optimal solution may, or may not, exist with better values. FIGURE 2.39 shows a plot of the cost function $y(x)$ for values of x with bound limits between 0 and 6. All the 3 points identified in the figure are minimum local optimal points, however only the last point at the right side is the global optimal point for this problem because it is the lowest feasible value.

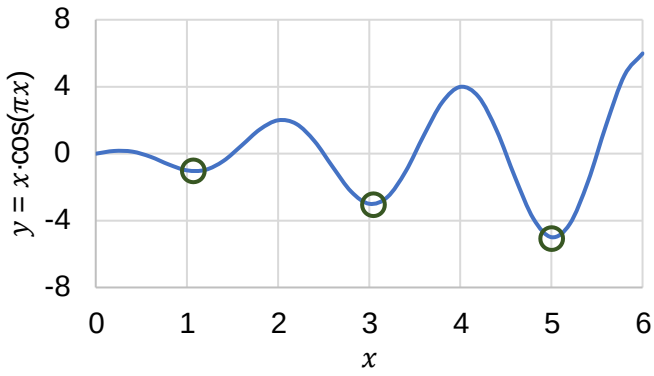

Figure 2.39 - Graph of function $y = x \cdot cos(\pi x)$.

2.4.1 Optimisation Using Genetic Algorithms

Evolutionary algorithms, inspired by Darwinian theory of evolution, are search heuristic algorithms that mimic the natural process of evolution through genetic operators as are crossover and mutation. It uses iterative progress, such as growth in a population, in order to achieve a population where the individuals tend to the optimal

solution *(Fleming & Purshouse, 2002)*. Genetic algorithms (GA) are a subclass of evolutionary algorithms, proposed by John Holland in 1975 *(Holland, 1992)*, which are more robust than other methods and they have been chosen for optimisation of hard problems quickly, accurately and reliably *(Malhotra et al., 2011; Sivanandam & Deepa, 2008)*.

GA perform a parallel search in the domain of the decision variables manipulating them (that are the variables to be optimised) in order to achieve an optimal solution and concatenate them into so-called chromosomes. It starts from an initial population of solutions (for instance by random generation) and gauges the performance of each individual using a fitness function where the most efficient chromosomes have a higher probability to reproduce. The process of reproduction is done using natural operators such as crossover and mutation creates a new generation of solutions. Therefore, a growing improvement of the solutions given over generations is expected. GA can be used to solve constrained and unconstrained problems, including problems where the Cf is discontinuous, non-differentiable, stochastic, or highly non-linear.

2.4.1.1 Basic Genetic Algorithm

GA uses the following terminology:

1) Fitness Function: also known as cost function, is the function in optimisation in order to find its minimum.
2) Individuals: It is any point in the domain of the problem for where the cost function is applied, and a score is given. An individual can be referred to as a genome that is composed of genes.
3) Population: A population is a group of individuals.
4) Generation: Each successive population generated in each iteration when the GA is applied in the current population, is called as a new generation.
5) Diversity: It is the average distance between individuals inside the population. This is an important parameter because allows the GA to increase or decrease its search space.
6) Fitness Value: It is the value given to each individual by the fitness function for that individual.
7) Parents and Children: Parents are the selection of certain individuals in the current population. The parents are used to create individuals in the next

generation, called children. Parents with better fitness values are more likely to be selected.

In GA, three main rules are used in each iteration to create the next generation from the current population.

- Selection Rules: Selection of the individuals (the parents) that will generate the next generation
- Crossover Rules: Combination of two parents to create children for the next generation.
- Mutation Rules: Random changes are applied to individual parents used to create children.

In FIGURE 2.40 the basic steps of a GA are shown. Firstly, the initial population is created randomly (within the constraints of the problem). After that, a sequence of new population is created using the individuals in the current generation (called parents) to create the next population of children. The steps to create a new population are:

1) Each individual of the current population is scored through the cost function (sometimes called fitness function) that returns their fitness value.
2) The fitness values are converted into a more usable range of values, the rank value, through the chosen selection function.
3) The parents are selected from the members of the population based on their expectations. The GA usually selects the members that have a better rank as parents.
4) Some of the individuals in the current population are chosen as elite members (a member that has a lower rank). These elite individuals automatically survive to the next generation.
5) Children are produced from their parents either by making random changes through mutations in a single parent or/and combining a pair of parents by crossover.
6) The current population is replaced with the children to form the next generation.

The GA stops when the stopping criteria is met.

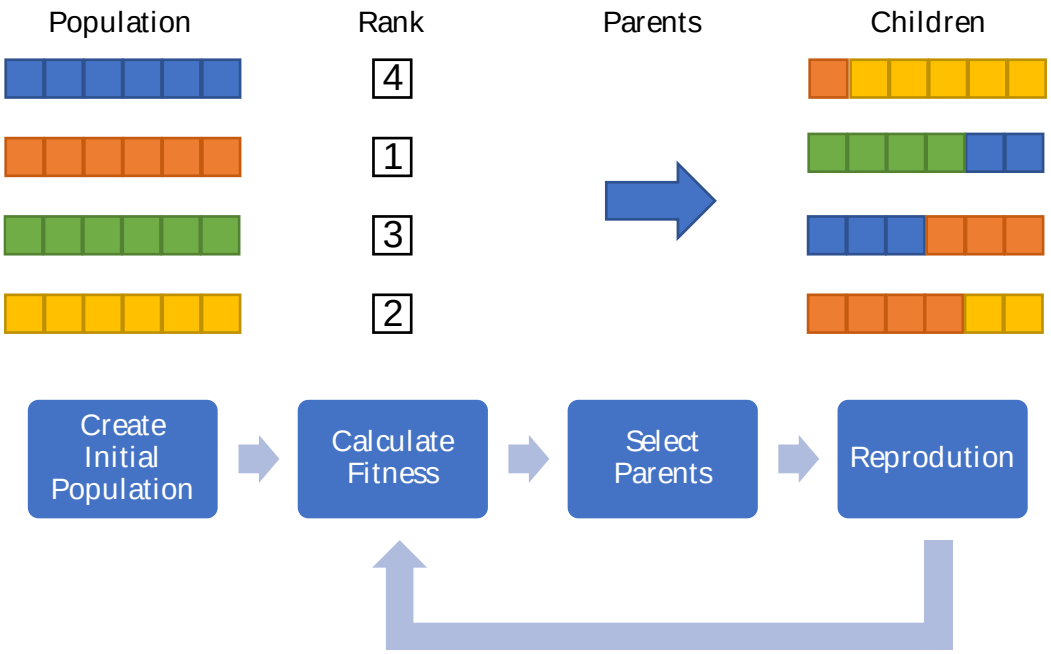

Figure 2.40 – Overview of a classic genetic algorithm. (Adapted from *(Venter, 2010)*)

2.4.1.2 Parameters

1) Population size: This parameter directly affects the overall performance and efficiency of GA. A population with few individuals provides a small coverage of the search domain, reducing the performance of the algorithm. Contrariwise, a high population consumes more time and resources, deteriorating the performance of the algorithm. However, the coverage of the search domain is assured, reducing the probability of the algorithm converges to a local solution instead of a global solution.
2) Generation number: The number of generations is directly related to the execution time available for the algorithm and with the population size.
3) Crossover Rate: High crossover rate values can retain individuals with good skills quickly, otherwise, the algorithm becomes very slow. Typically, this value is between 70% and 87%.
4) Mutation Rate: High mutation rate values makes the convergence of the algorithm complicated due to the search process becomes practically random. Typically, this value is between 1% and 5%, reducing the hypotheses of the algorithm stagnant at a local point.

2.4.1.3 Selection Options

GA uses a selection function to choose the parents for the next generation, based on their scaled fitness value (rank value). An individual can be selected to be a parent more than once, contributing its genes to more than one child.

The Roulette method is one of the functions used to select the parents in the current population. Parents are chosen by simulating a roulette wheel, where is given to each individual a section area of the wheel corresponding to their fitness value. Thus, the higher the fitness of an individual is, the more likely it is to be selected.

Another selection method is the Tournament. In this method, N tournaments are carried out in order to select N parents, involving a specific number of individuals in each tournament, chosen randomly without taking into account their fitness value. In each tournament, the individual with the highest fitness value, compared to its opponents, wins.

Other methods are the Stochastic Uniform method, Remainder method and Uniform method.

2.4.1.4 Genetic Operators

1) Crossover: It is a genetic operator used to recombine the genetic material of the population. Two individuals (or parents) are chosen, and a crossover point is randomly defined. Portions of the chromosome of each parent are combined to produce the new children for the next generation *(Zalzala & Fleming, 1997)*. FIGURE 2.41 shows this process.

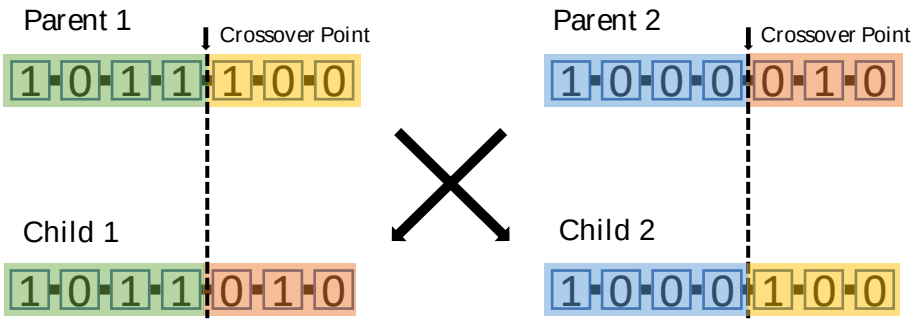

Figure 2.41 – Crossover operation.

2) Mutation: The mutation operator introduces small random changes in the genetic material of some individuals in the population to create mutation children. This operation helps the GA to escape from local minima traps, providing diversity and enables the GA to search a broader space *(Zalzala & Fleming, 1997)*. FIGURE 2.42 shows how this operation is done.

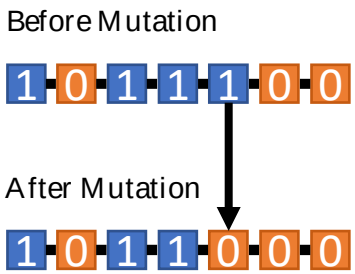

Figure 2.42 – Mutation operation.

3) Elitism: This operator assures that the best individuals (with the best fitness values), in the current generation survive to the next generation without changes. They are called elite children. Therefore, it is expected that the best solutions found so far will not be lost due to the stochastic behaviour of the selection method. It is necessary to be careful because if many elite children survive, they can dominate the population which can make the search less effective.

2.4.1.5 Penalty Functions

When, in a constrained problem, one individual is not feasible violating one or more constraints, it must be penalized in order to be discarded in the next generation. Therefore, using a penalty function (EQUATION (2.34)), the fitness of the inadmissible individuals is penalised proportionally with the number of violated constraints, converting the constrained problem into an unconstrained problem. For example, a problem with the following constraints: a driver cannot drive above 50 km/h, can be turned into an unconstrained problem if the driver is allowed to drive above 50 km/h but charge it 10 € per extra km/h of speed or award 5 € for driving below the 50 km/h.

Minimize:

$$F(x) = \begin{cases} f(x), & x \in feasible\ region \\ f(x) + P(x), & x \notin feasible\ region \end{cases}$$

The penalty function is:

$$P(x) = k \sum_{i=1}^{m} d_i(x) \tag{2.34}$$

Where k is the penalty parameter, m the number of constraints to be penalized and $d(x)$ is the metric function describing the distance between the unfeasible point to the admissible region.

2.4.1.6 Stopping Criteria

There are two main criteria that cause the algorithm to terminate, either the algorithm has reached some maximum runtime, or the algorithm has reached some threshold on its performance. If it happened, the final solution is selected and returned as the optimal solution.

The criteria related to maximum runtime are:

1) Maximum generation reached.
2) Maximum times allowed for the algorithm to be running achieved.
3) Maximum stall time limit achieved which means no improvement in the best fitness value for a defined interval of time.

The criteria related to the GA performance are:

1) Fitness limit value reached is less or equal to the defined fitness limit.
2) Maximum stall generation is achieved which means the average relative change in the best fitness value over stall generations is less than a specified tolerance.

2.4.1.7 Multi-objective Optimisation Problems

Many engineer design problems involve more than one objective in optimisation therefore a single-objective optimisation is not feasible. For example, in an FCL device, its volume, its ability to reduce the fault current and its cost can be used as goals to be optimised. In this case, a Multi-Objective Optimisation (MOO) must be considered because a single solution is hardly the optimal solution for all objectives simultaneously. In FIGURE 2.43 is shown the dominated solutions, in the problem domain, of a MOO for

two objective goals. Each point, in the feasible design domain, is called Pareto optimal solution if there is no other point that minimized at least one objective goal without increasing another one. The Pareto optimal front curve is always on the boundary of these feasible criterion space *(Chang, 2015)*.

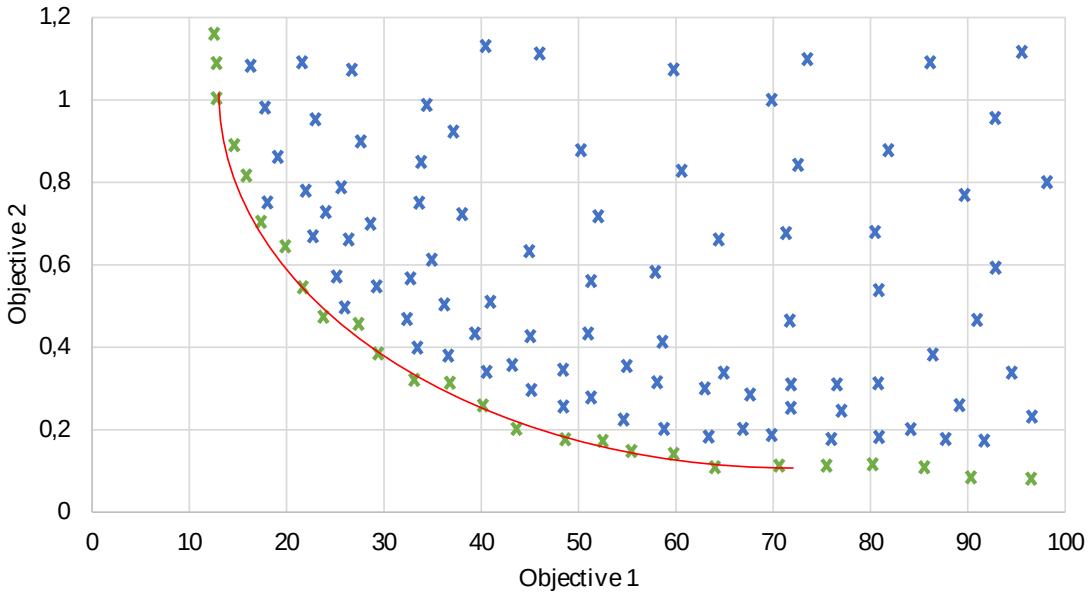

Figure 2.43 – Pareto optimal front curve of a MOO. The points represent the dominated solutions of the problem where the green points trace the pareto curve which represents the pareto optimal solutions.

2.4.2 Optimisation in Superconductivity Devices

The use of optimisation techniques has been increasing as a step in the design process of the superconducting device and regarding its application in the power grid. The following will list some examples of the use of optimisation techniques:

A. Optimisation for the FCL placement in the power grid.

   The FCL are effective devices to limit fault currents and protect the integrity of the power networks. However, the correct placement of the FCL in the grid is an important factor to assure its protection. An optimisation process to

determine the number, location, and impedance of FCLs in the power grid is essential to ensure reliability, power losses reduction and economic benefits. In *(Bahramian Habil et al., 2015)* the authors have used particle swarm optimisation algorithm (a sub-group of the evolutionary algorithms) to find the optimal place and impedance for an FCL in an RBTS bus test system taking into account the minimization od the real power losses, the reliability enhancement and the economical use of the FCL. In *(Hyung-Chul Jo et al., 2013)* a multiobjective optimisation through entropy-based weighting algorithm is used and in *(Yang et al., 2018)* a combination between fuzzy logic decision and particle swarm algorithms are used to find the optimal place of the FCL in the grid. A genetic algorithm method is used to search for the best locations and parameters of FCLs in *(Teng & Lu, 2010)*.

B. Design optimisation of the FCL based on its behaviour and constitutive parts. The performance of the FCT depends on its design, therefore, find the optimal design is very important for satisfactory steady and transient performance. In *(Dey & Choudhury, 2016)* a multi-objective Ga is used for two different approaches, with the aim of finding the optimal solution for the saturated cores superconducting FCL behaviour. In *(Hekmati, 2015)* a shield type superconducting FCL was optimised using a heuristic method, where the parameters with the most impact on the cost, weight and performance were chosen for the optimisation process, such as the volume of the copper, magnetic and superconducting. In *(Magnusson et al., 2014)* was proposed a model that combines transient analysis with an optimisation module to obtain multiple possible design parameter values, to optimise a hybrid FCL. Each constitutive part of the FCL can be optimised individually, to assure the best performance for the FCL operation. In *(Kudymow et al., 2011)* the 2G YBCO tapes was optimised in order to identify the optimal stabilized coated conductor according to the FCL requirements.

2.5 Summary

In this chapter, a review regarding electric power system failures and typical mitigate measures were carried out, as well as an introduction about fault current limiters. A brief overview of the high-temperature superconducting materials is presented. These materials have high importance for the SC-SFCL since they contribute to power losses reduction in the DC magnetization circuit. These materials are also essential for TT-SFCL.

A literature review of concepts and projects regarding SC-SFCLs is also addressed, as well as some modelling and simulation methods. Research and development on SFCL devices have been going on for many years, however, the diversity of concepts is still quite limited. Apparently, most of the effort has been devoted to optimising components, improving efficiency and reducing the costs of a limited number of basic ideas. In all topologies, superconducting coils can be used to saturate cores, depending on the associated costs. The greatest difficulties of the SC-SFCL are predicted with magnetic coupling and, more importantly, the high volume of ferromagnetic cores required, which influences weight. This challenges the commercial viability of these devices.

Electromechanical forces developed on superconducting tapes of these devices should be taken into account due to the fact that they may destroy the SFCL causing disturbances in the power grid. A review of the electromechanical forces is also shown.

Lastly, a brief review of optimisation techniques is presented focusing on genetic algorithms.

3

Saturated Cores Superconducting Fault Current Limiter: Modelling, Simulation and Test

Superconducting fault current limiters have demonstrated their viability in electric power grids. The growth in distributed generation sources and an increased interconnection of networks tend to increase the complexity of electric power grids, increasing the number of failures, especially short-circuits. To develop and disseminate these technologies, the development of straightforward design tools is required. These tools must consider the properties of the available constitutive elements of the devices.

In this chapter, two design methodologies that allow modelling and simulate SC-SFCL are presented. A methodology for simulating the behaviour of saturated cores limiters is presented as an alternative to techniques based on FEM, thereby dramatically reducing computation time. This methodology is based on the magnetic characteristic of those limiters. Another methodology for the modelling of the SC-SFCL through a reduced reluctance approach is presented, in order to obtain the magnetic characteristic of the limiter.

3.1 Constitutive Parts and Behaviour of the Single-phase Superconducting Fault Current Limiter

The topology and working principle of a SC-SFCL have been described in CHAPTER 2.3.2. The basic topology is composed of two magnetic cores placed side by side,

surrounded by a superconducting DC coil in the centre of the device. The DC coil is energized by a high bias current which saturates the magnetic cores. The outer limbs of the cores are wrapped by conventional copper AC coils, which are connected in series with the line under protection. The AC coils are wound in oppositive directions to create antagonistic magnetic flux in each magnetic core in order to allow the protection of each half cycle of the AC line current.

Under normal conditions, AC current in the windings creates low AC magnetic ripple flux when compared to the DC bias magnetic flux, maintaining the magnetic cores saturated and the impedance of the device low, as can be seen in FIGURE 3.1 A). However, when a fault occurs, the AC current in the windings increases to the point where the cores leave the magnetic saturation alternately (FIGURE 3.1 B)), which increases the line impedance rapidly, limiting the AC current.

Since SC-SFCL is an inductive device, the line impedance changes according to the inductive voltage drop in SFCL terminals. In accordance with Faraday's law of induction, EQUATION (3.1).

$$u_{SFCL}(t) = -\frac{d\Psi_{SFCL}(t)}{dt} = -\frac{d\Psi_{SFCL}(t)}{di_{line}} \times \frac{di_{line}(t)}{dt} \tag{3.1}$$

$d\Psi_{SFCL}(t)/di_{line}$ represents the magnetic characteristic of the limiter, which relates to line current, i_{line}, and the linked flux with the split primary, $\Psi_{SFCL}(t)$. This characteristic determines the electromagnetic behaviour of the limiter.

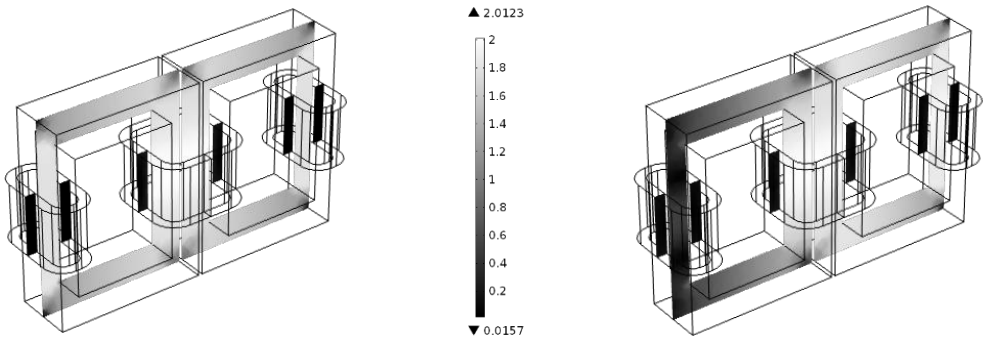

(a) (b)

Figure 3.1 - Flux density of the FCL at normal and fault conditions. (a) In normal operation, both external limbs remain saturated. (b) In case of failure, each external limb drives out of the saturation alternately.

3.2 Methodology for Superconducting Fault Current Limiter Simulation Based on its $\boldsymbol{\Psi - i}$ Characteristic

The proposed methodology is based on the magnetic characteristic of the limiter. The first step of the methodology consists of determining the magnetic characteristic of the limiter and describing it analytically. Therefore, the behaviour of the limiter can be predicted by a simple mathematic model and simulated in numerical computation software such as MATLAB. As a result, the dynamic behaviour of the SFCL can be simulated faster, compared to using FEM software.

SC-SFCL can be defined, generically, by a variable inductance, L_{SFCL}, which represents the non-linear magnetic characteristic of the limiter, in series with a resistance, R_{SFCL}, which represents the resistance of the AC coils, shown in FIGURE 3.2. The inductance of the limiter depends on the operation point at a certain moment, i.e., in normal operation the inductance is very low, but if the line current increases due to a fault, the limiter goes out of the saturation zone, increasing the device inductance and limiting the current, therefore the inductance is a function of the line current. The impedance of the limiter can be given by EQUATION (3.2) and the voltage drop of the limiter, in EQUATION (3.1), can be rewritten as EQUATION (3.3) in order to include the device resistance.

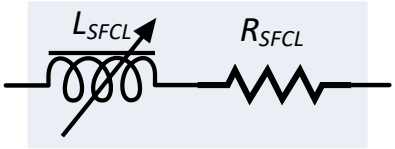

Figure 3.2 – Generic schematic of the SC-SFCL.

$$\bar{Z}_{SFCL}(I_{line}) = j\omega L_{SFCL}(I_{line}) + R_{SFCL} \tag{3.2}$$

$$\begin{aligned} u_{SFCL}(t) &= -\left[\frac{d\Psi_{SFCL}(t)}{dt} + R_{SFCL} \times i_{line}(t)\right] \\ &= -\left[\frac{d\Psi_{SFCL}(t)}{di_{line}} \times \frac{di_{line}(t)}{dt} + R_{SFCL} \times i_{line}(t)\right] \\ &= -\left[L_{SFCL}(i_{line}) \times \frac{di_{line}(t)}{dt} + R_{SFCL} \times i_{line}(t)\right] \end{aligned} \tag{3.3}$$

The SC-SFCL magnetic characteristic is explained in CHAPTER 2.3.2.1 and it is generically shown in FIGURE 3.3 (A). This characteristic has to be mathematically modelled to be used in previous EQUATION (3.3), which can be done using the inverse tangent function (FIGURE 3.3 (B)), due to its similarity with the non-biased characteristic of the

magnetic core. Therefore, the SFCL characteristic can be modelled by EQUATION (3.4) where a, b, c and d are parameters determined by the fitting.

$$\Psi(i_{line}) = a[\tan^{-1}(b \times i_{line} - c) + \tan^{-1}(b \times i_{line} + c)] + d \times i_{line} \quad (3.4)$$

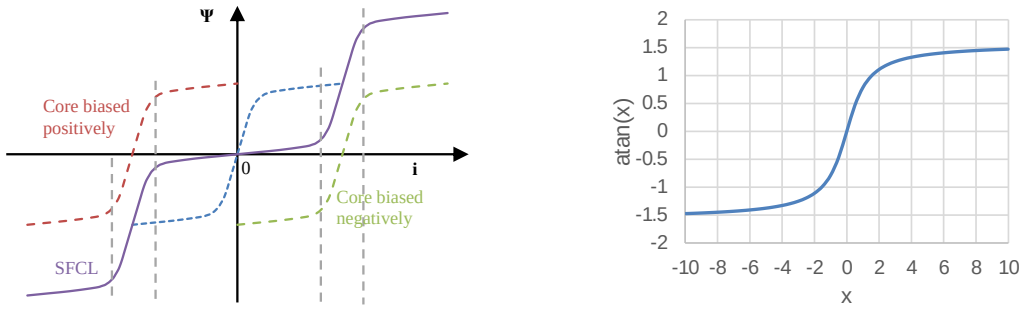

Figure 3.3 – Magnetic characteristic of the SC-SFCL and the inverse tangent function used to model it. (a) Generic SC-SFCL magnetic characteristic. (b) Inverse tangent function.

3.2.1 Model Validation

To validate the proposed methodology, transient simulation of the SC-SFCL was carried out with FEM software. FIGURE 3.4 (A) shows the SFCL's dimensions and FIGURE 3.4 (B) shows the SFCL built-in FEM simulator with its mesh. As can be seen, the magnetic core provides closed magnetic paths for each outer limb. Therefore, to assure that both outer limbs (where are the AC coils are placed) are driven into strong saturation, their cross-sections must be less than 50% of the cross-section of the inner limb (where the DC coil is placed). In the present case, the cross-section of the outer limbs is 40% of the cross-section of the inner limb.

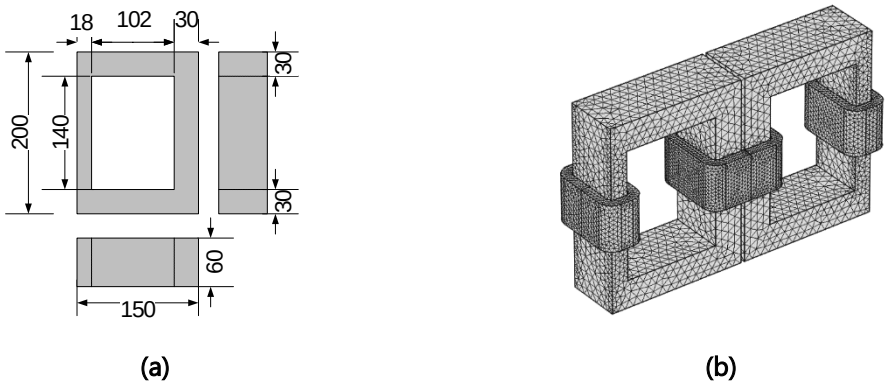

Figure 3.4 - (a) Dimensions of each magnetic core of the SC-SFCL. All dimensions in millimetres; (b) SC-SFCL modelled in FEM software in 3D with two cores and coils. Can be seen the limiter's mesh used in the FEM simulator.

The AC coils are made of copper wire with a 2 mm^2 cross-section, wound with 100 turns each and a resistance value of 0.11 Ω. A DC coil with 40 turns is built using 10 mm-wide superconducting tape with a critical current of 300 A.

The B-H characteristic of the core and the electrical diagram of the SFCL test circuit is shown in FIGURE 3.5. The latter is built by a voltage source u_{grid}, a line impedance Z_{line}, and a load Z_{load}, where a circuit breaker S_1 is used to simulate faults.

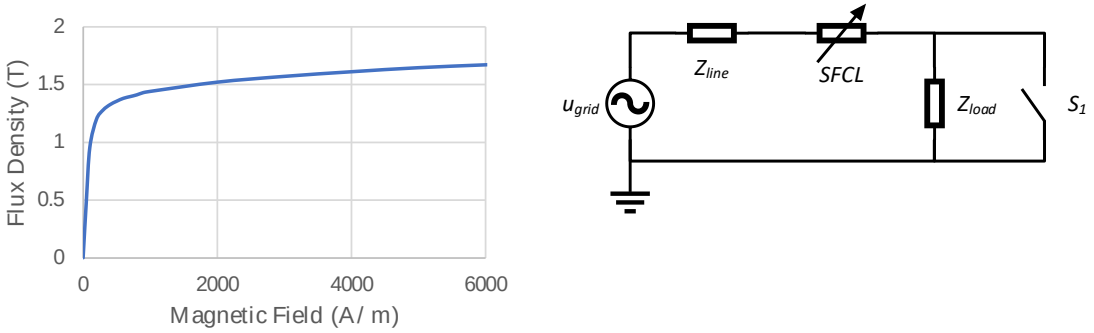

(a) (b)

Figure 3.5 – (a) Magnetic cores B-H characteristic and (b) simulation test grid.

TABLE 3.1 shows the electrical test grid parameters. The limiter must be tested beyond its limit, leading to the point where it saturates once again and loses the ability of current fault limitation, in order to obtain the complete SFCL characteristic. Thus, the oversized value was imposed for the voltage source.

Table 3.1 - Characteristics of simulation test grid.

Parameter	
Voltage source u_g(V$_{rms}$)	Nominal value = 100 Oversized value = 240
Frequency f *(Hz)*	50
Line impedance (Ω)	1+i0
Load impedance (Ω)	25+i0
DC bias current (A)	300

Transient magnetic field simulations coupled with electrical circuit were both solved simultaneously in the FEM simulator. Simulations were carried out using a computer with Intel Core i7 – 4700HQ processor, 16 GB of RAM and Windows 10 64 bits operating system. The total number of nodes was 134.664 and a time step of 0.25 ms was used. Simulation completed four grid voltage cycles (80 ms at 50 Hz).

FIGURE 3.6 shows the AC line current as a function of time. As can be seen in the figure, the current waveform is not sinusoidal during the fault event, which means the magnetic cores achieve the opposite saturation zone and the SFCL lost its ability of current limitation. This behaviour allows obtaining the complete SFCL characteristic.

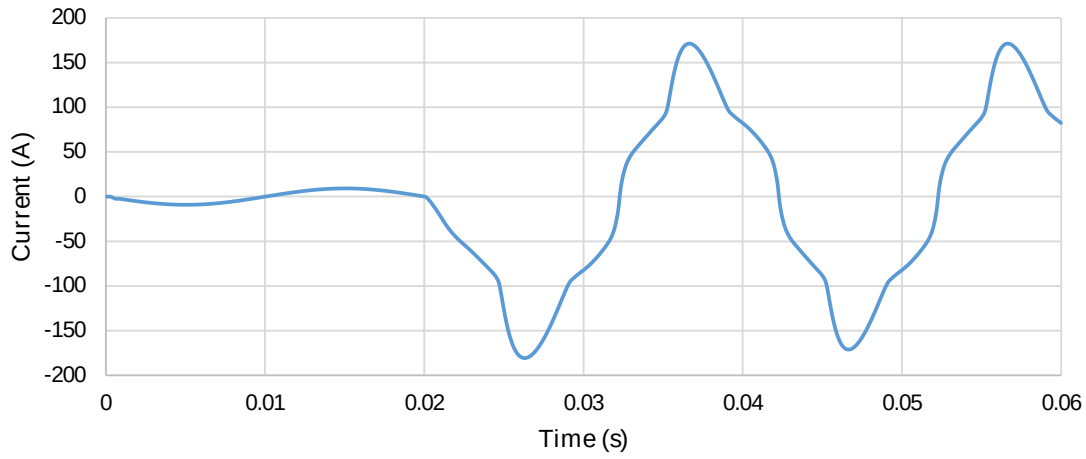

Figure 3.6 - Line current evolution under a fault as a function of time.

3.2.1.1 Determination of the Limiter Characteristic

The $\Psi - i$ characteristic of the SC-SFCL is depicted in FIGURE 3.7, which can be modelled mathematically by EQUATION (3.4). This characteristic was obtained from the previous transient simulations, however, this characteristic could be obtained from a series of magnetostatic simulations rather than a time-domain simulation.

Fitted parameters, determined by MATLAB's cftool function, are shown in TABLE 3.2 and the fitted curve is also shown in FIGURE 3.7. There is a good correlation between the original and the fitted characteristics, with $R_{squared}$ of 0.9997.

Table 3.2 – Fitted parameters of the characteristic of the limiter.

Parameter	Value
a	0.1892
b	0.0463
c	-3.0720
d	-0.0006

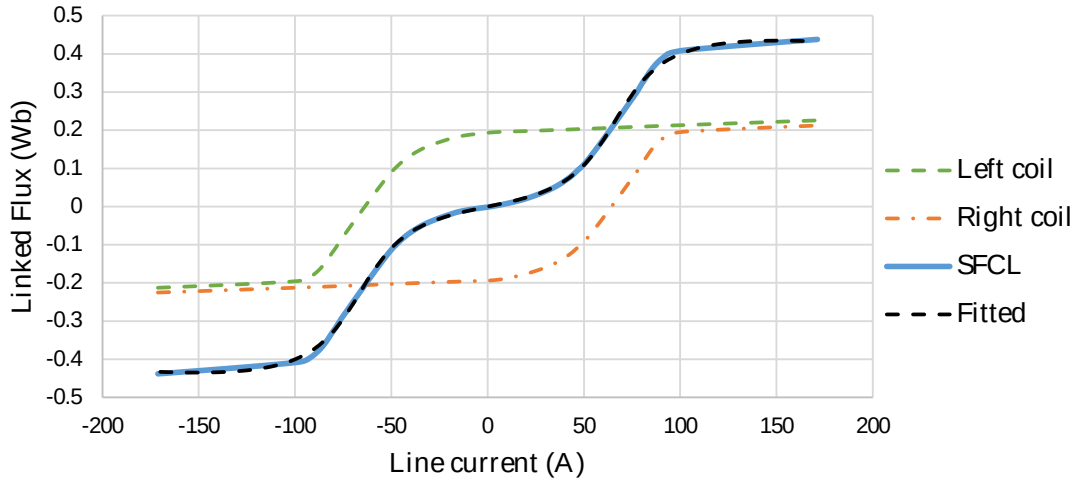

Figure 3.7 - $\Psi - i$ excursion of each coil and SC-SFCL.

3.2.1.2 Methodology for the Dynamic Simulation of the Limiter

FIGURE 3.5 (B) represents the electrical circuit used to determine limiter's dynamic behaviour under a fault. The circuit response is obtained by EQUATION (3.5) which includes the voltage drop of the limiter, given in EQUATION (3.3). It is composed of a pure resistive line impedance and a purely resistive load impedance, which values are presented in TABLE 3.2.

$$u_g(t) = R_{line} \times i_{line}(t) + \left[\frac{d\Psi_{SFCL}(t)}{di_{line}} \times \frac{di_{line}(t)}{dt} + R_{SFCL} \times i_{line}(t)\right] + R_{load} \times i_{line}(t) \tag{3.5}$$

where

$$\frac{di_{line}(t)}{dt} = \frac{1}{\frac{d\Psi_{SFCL}(t)}{di_{line}}}\left(u_g(t) - R_{line} \times i_{line}(t) - R_{load} \times i_{line}(t)\right) \tag{3.6}$$

To obtain current versus time from the differential EQUATION (3.6), the Euler's method can be used to discretize that equation. The line current can be determined using EQUATION (3.7), at time interval $t = (k+1) \times \Delta t, k = [0; N]$, where Δt is the sampling period and N is the number of samples. As can be seen, the value of current at iteration $k+1$ depends on the values of voltage, current and $\frac{d\Psi_{SFCL}(t)}{di_{line}}$ at previous iteration k. Due to the fact the use of a forward/explicit Euler's scheme, in order to prevent some stability problems, a dynamic update of the sample period was implemented.

$$i_{line}^{k+1} = i_{line}^{k} + \frac{1}{\left.\frac{d\Psi_{SFCL}}{di_{line}}\right|_{k}} \times \left(u_g^k - (R_{line} - R_{SFCL} - R_{load}) \times i_{line}^{k}\right) \times \Delta t \tag{3.7}$$

3.2.1.3 Evaluation of the Dynamic Behaviour of the Limiter

The results obtained using the proposed methodology were first compared with FEM simulations in order to validate the presented methodology. A new simulation with $u_g = 100$ V_{rms} was carried out and the methodology was implemented and simulated in MATLAB. A fault was applied at $t = 23$ ms and removed at $t = 72$ ms. Line current obtained by FEM simulation and by the proposed methodology is presented in FIGURE 3.8. Computation time took less than 1 hour in the FEM simulator and some seconds in MATLAB.

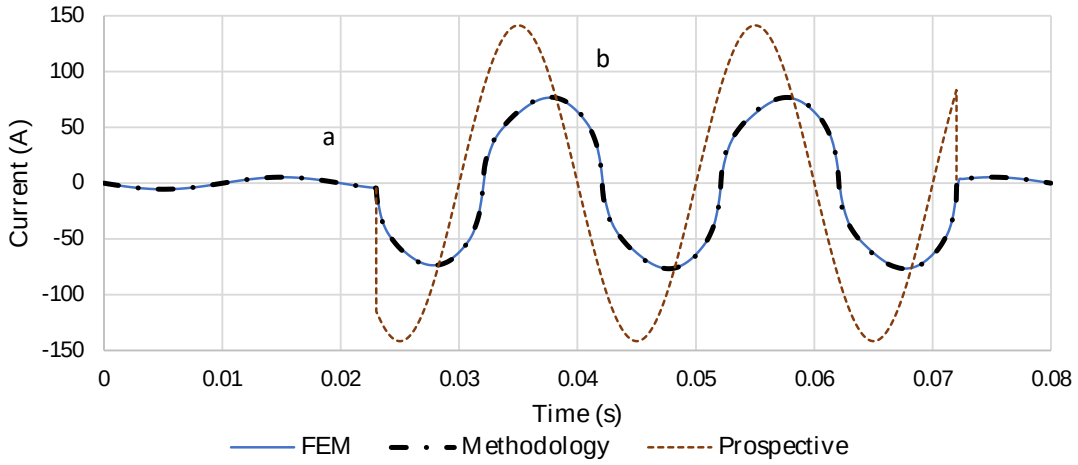

Figure 3.8 - Line current evolution under a fault as a function of time. Comparison between current in the circuit obtained by the present methodology and by FEM simulation.

In fault conditions, fault current was limited to around 55% of the prospective short-circuit value (141 A_{rms}). These results exceed the minimum industry requirement of 50% fault current reduction *(Jeff Moscrop & Darmann, 2009)*. Comparing the methodology with FEM simulation, it shows a good correlation between both methodologies, which can be seen in TABLE 3.3 (where the results and relative errors of the FEM and Methodology simulations at the points "a" and "b" in FIGURE 3.8 are shown).

Table 3.3 – Results at zones "a" and "b" and the relative error between them.

Parameter	a	b
i_{line} *by FEM (A)*	5.39	76.63
i_{line} *by Methodology (A)*	5.39	76.94
Error (%)	0.00	0.40

FIGURE 3.9 shows the SFCL equivalent inductance as a function of the instantaneous line current. The SFCL equivalent inductance shows low inductance at small line current (like an air core reactor) and non-linear increase of inductance at high currents, limiting the fault currents. The green zone shows the non-limitation zone, with a threshold of ±15 A (the normal operating current is 5.44 A). Moreover, a clear interval with flat low inductance is not evident, and there is no sharp transition (a rather smooth increase of the inductance is observed).

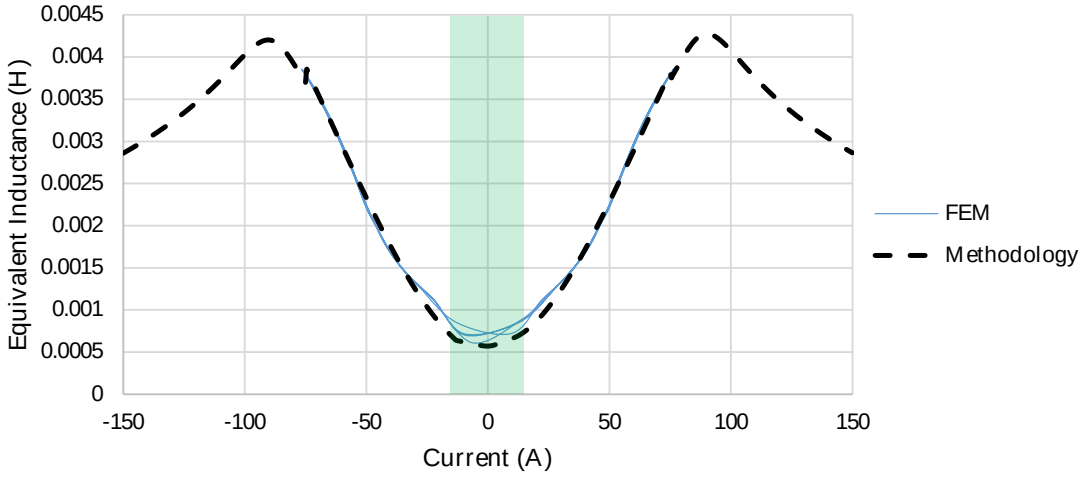

Figure 3.9 - The SFCL equivalent inductance as a function of the line current.

3.2.1.4 Comparison Between the Proposed Methodology and Experimental Results

In order to validate this methodology with experimental results, a laboratory prototype (built in *(Vilhena, 2012)*) was used to carry out experimental measurements, shown in FIGURE 3.10. The dimensions of this prototype are 300x168x60 mm and it is composed of a magnetic EI-type core, 2 AC coils with 40 turns each (placed on the outer limbs) and an HTS DC coil with 60 turns (placed on the inner limb). The internal resistance of the SFCL is $R_{SFCL} = 0.4\ \Omega$. The cryostat is made of XPS material.

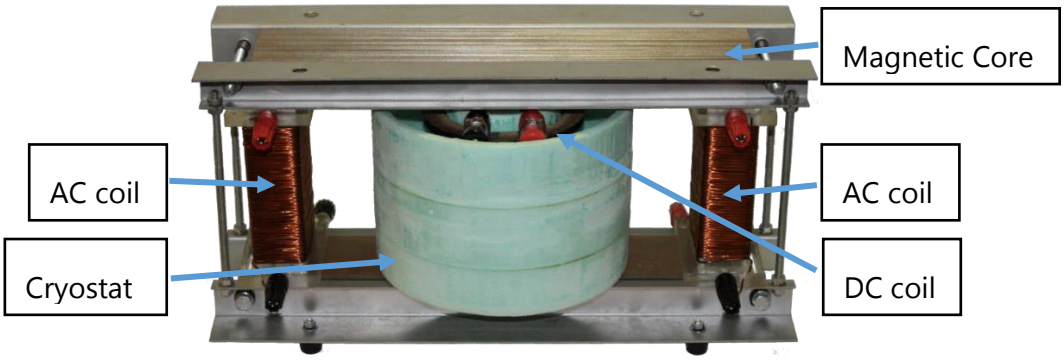

Figure 3.10 – Single-phase prototype of the SC-SFCL.

FIGURE 3.11 shows the experimental apparatus used for the tests where the line current was derived from voltage drop in the line resistor and linked flux was determined by integrating the voltage induced in auxiliary coils wound around primaries. The characteristic of the test grid is depicted in TABLE 3.4.

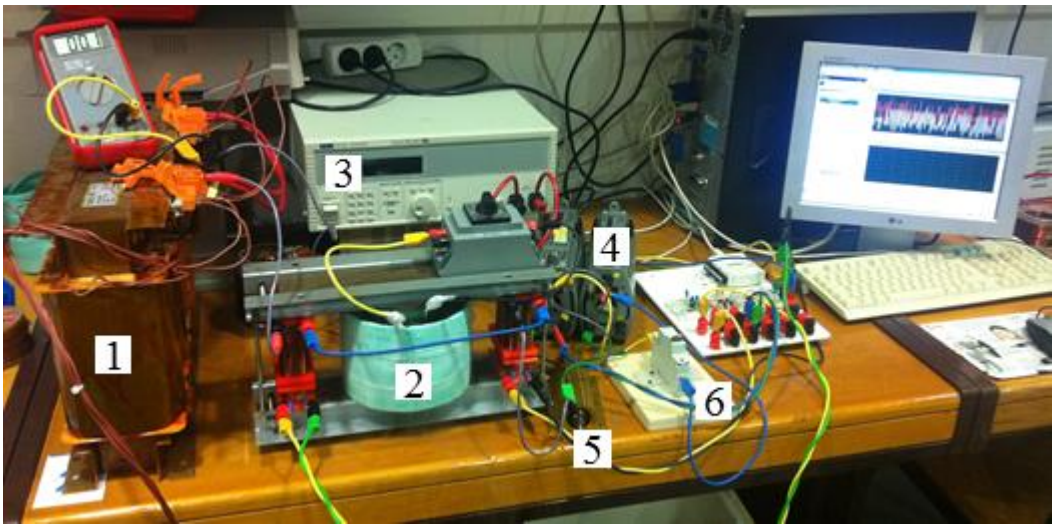

Figure 3.11 - Experimental apparatus: (1) test grid transformer, (2) SFCL, (3) DC supply, (4) load, (5) line resistor, (6) circuit breaker.

Table 3.4 - Characteristics of the test grid.

Parameter	
Voltage source u_g *(*V_{rms}*)*	Nominal value = 50 Oversized value = 100
Nominal current i_{nom} *(*A_{rms}*)*	2.38
Frequency f *(Hz)*	50
Line impedance (Ω)	1+i0
Load impedance (Ω)	20+i0
DC bias current (A)	100

A. Determination of the Limiter Characteristic

The first part of the methodology consists of determining the SFCL characteristic. Both experimental characteristic and characteristic obtained by curve fitting process can be seen in FIGURE 3.12. This curve was obtained by transient test where the current was measured by sensing the voltage drop in the line resistor and the linked magnetic flux was measured through auxiliar windings.

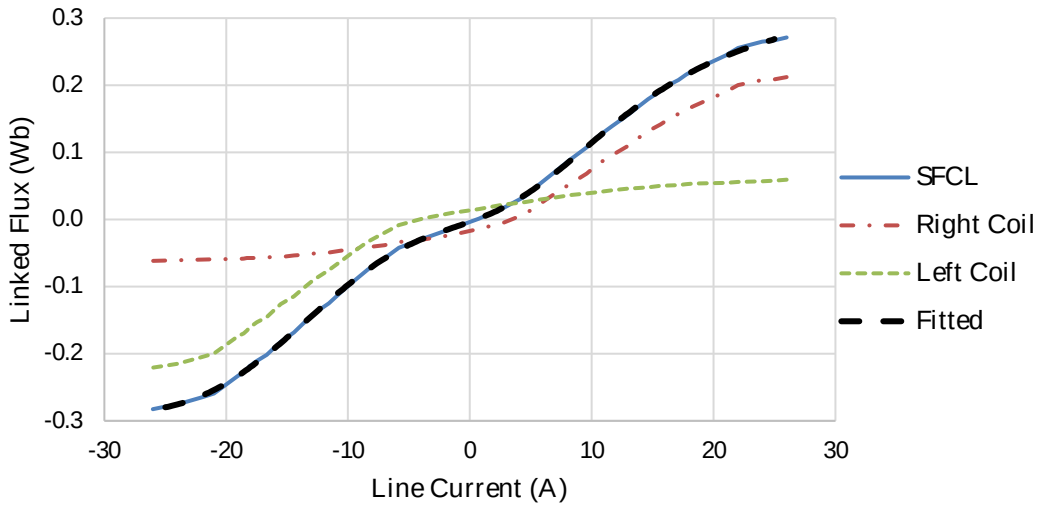

Figure 3.12 - Experimental $\Psi - i$ characteristics of each AC coil and SFCL, and SFCL characteristics obtained by curve fitting process (Fitted).

B. Evaluation of the Dynamic Behaviour of the Limiter

A test was carried out considering $u_g = 50\ V_{rms}$. A short-circuit was applied around 1.49 s. FIGURE 3.13 shows the evolution of current, either measured and predicted by the proposed methodology. Both curves show good agreement. The voltage drop is also shown in FIGURE 3.13. As shown in this figure, when a fault occurs the voltage drop of the SFCL increases, and fault current is thus limited.

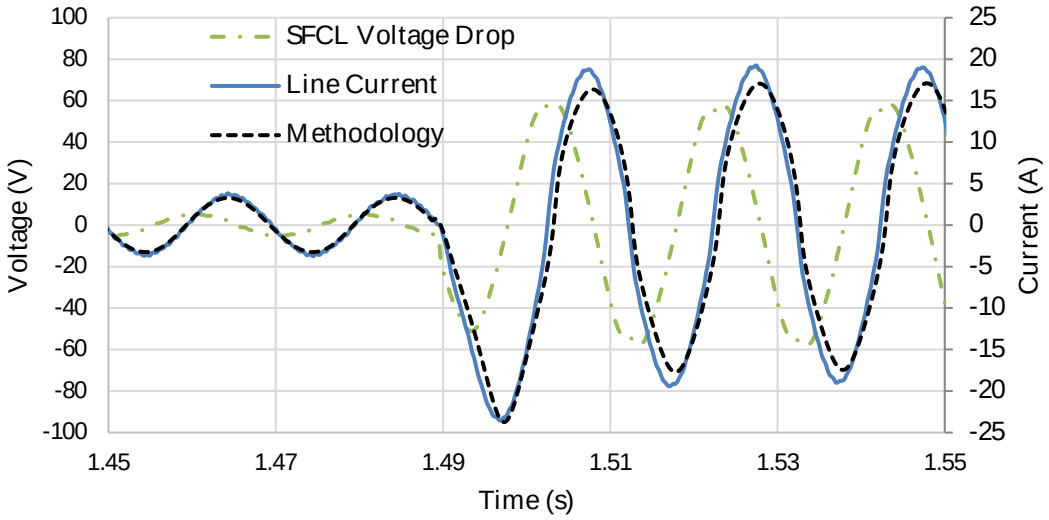

Figure 3.13 - Comparison between measured and predicted currents in the circuit under a fault and measured SFCL voltage drop.

3.2.2 Computational Model for Power System Simulator

EQUATION (3.3) shows the developed voltage drop at the terminals of the SFCL that is directly related to the SFCL characteristic. This characteristic can describe the electromagnetic behaviour of the limiter.

Using the magnetic characteristic of the SFCL, it is possible to develop an adequate computational model for power system simulation software (such as PSCAD or SimPowerSystems/Simulink) that do not rely directly on knowledge of circuit theory, which is practically unfeasible. This computation model was presented in *(Vilhena, Arsénio, et al., 2015)*.

The first step of the methodology consists of determining the magnetic characteristic $\Psi - i$ of the limiter. This characteristic may be determined by real tests. Using the characteristic obtained it is possible to implement the SFCL in Simulink, as a variable inductance.

3.2.2.1 Model for the Dynamic Simulation of the Limiter

A model was built to simulate the SFCL in Simulink, it describes the SFCL behaviour according to EQUATION (3.3). The model was developed with a dependent current source that imposes a specific current in the line, depending on the characteristic of the SFCL. The SFCL characteristic is a function of linked flux and line current, thus if the linked flux is known the current that the SFCL should force is also known. EQUATION (3.8) shows how the linked flux may be calculated, by the integration of the voltage drop over the SFCL, Δu_{SFCL}, and subtraction of the resistive voltage drop over the SFCL, $R_{SFCL} \cdot i_{line}$. FIGURE 3.14 shows the model in Simulink. The model is composed of a set of blocks that compute the linked flux according to EQUATION (3.8), a lookup table block (so-called *Psi-i*) that computes the current according to the linked flux with the primary of the SFCL, and a dependent current source block (so-called Inject SFCL current) which provides the current in the line. A lookup table block maps inputs to output by looking up or interpolating a table of values, by approximating mathematical functions. The lookup table block used approximates one-dimensional function.

$$\begin{aligned} &\Delta u_{SFCL}(t) = R_{SFCL} \cdot i_{line}(t) + \frac{d\Psi_{SFCL}(t)}{dt} \Leftrightarrow \\ &\Leftrightarrow \frac{d\Psi_{FCL}(t)}{dt} = \Delta u_{SFCL}(t) - R_{SFCL} \cdot i_{line}(t) \Leftrightarrow \\ &\Leftrightarrow \Psi_{SFCL}(t) = \int (\Delta u_{SFCL}(t) - R_{SFCL} \cdot i_{line}(t)) \cdot dt \end{aligned} \tag{3.8}$$

An high value shunt resistor is used only to avoid numerical singularities.

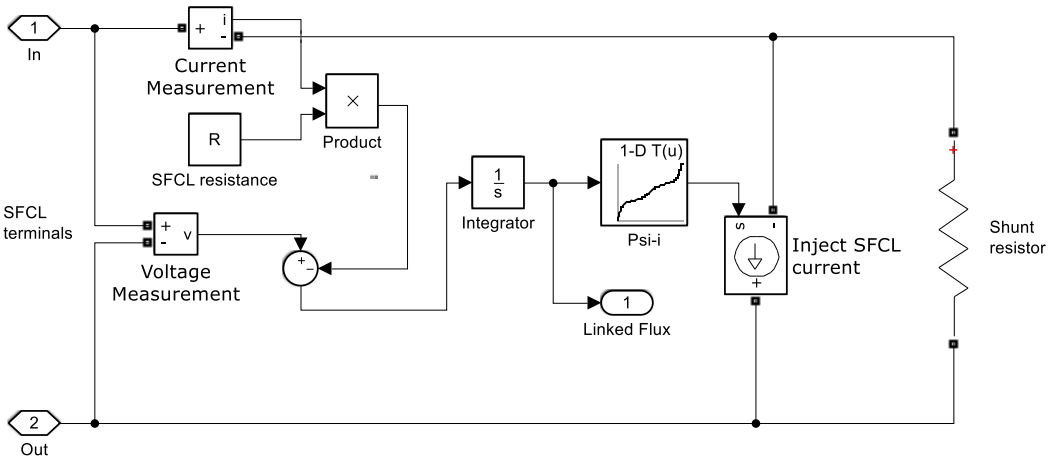

Figure 3.14 - Simulink model for the SFCL implementation.

3.2.2.2 Evaluation of the Dynamic Behaviour of the Limiter

To evaluate the behaviour of the SFCL, a test circuit was also implemented in Simulink. FIGURE 3.15 shows this circuit, in the Simulink environment, which is composed of a voltage source, a line impedance, a load impedance, a circuit breaker and the SFCL.

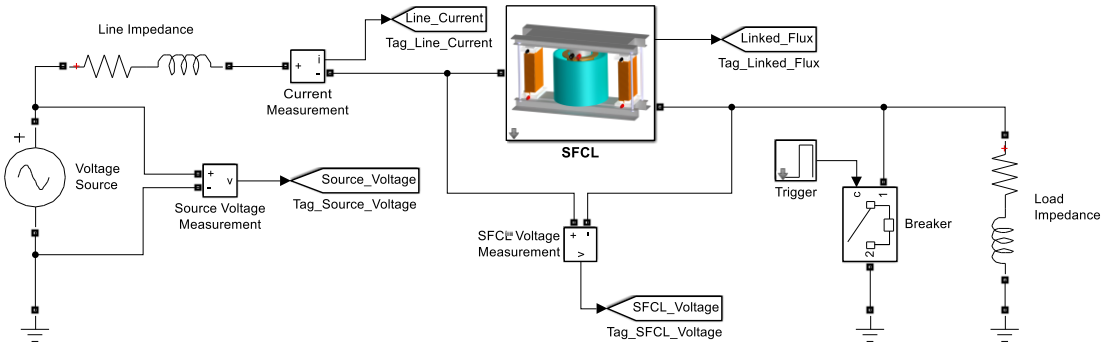

Figure 3.15 - Test grid implemented in Simulink.

A real test was carried out considering the grid parameters and the SFCL $\Psi - i$ characteristic of CHAPTER 3.2.1.4 (to compare the simulation with the real test, the line and load impedances are considered purely resistive). The internal resistance of the SFCL is $R_{SFCL} = 0.4\ \Omega$. A short-circuit was applied around $t = 1.49$ s and cleared around $t = 2.49$ s.

The achieved results from the proposed methodology were compared with real tests. FIGURE 3.16 shows the evolution of the line current as a function of time, measured from a real test and predicted by the proposed methodology. Both curves show similar behaviour and good agreement. The fault current was limited to around 75% of the prospective current.

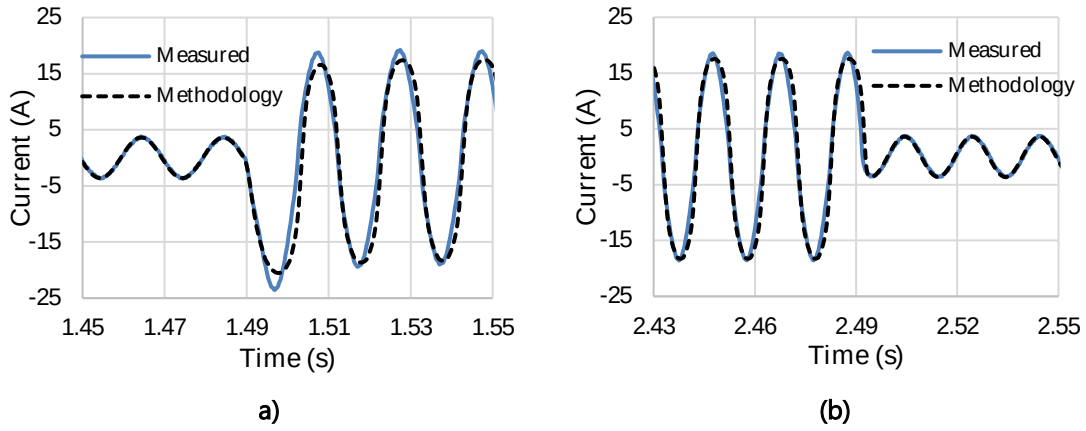

Figure 3.16 - Comparison between measured and predicted currents in the circuit under a fault. (a) At the moment, the fault occurs. (b) At the moment, the fault is removed.

The methodology shows good agreement with experimental measurements. Its main advantage is a drastic decrease in simulation times when compared with FEM software. This allows for the simulation of these devices in complex grids, which is one requisite imposed by utilities.

3.2.2.3 I_{DC} Parameter Included in the Limiter Model

In order to make the model more versatile, the DC current parameter was included, thus it is possible to simulate the SFCL for different DC bias currents, or varying this parameter during the simulation. FIGURE 3.17 shows the Simulink model with the new feature where the *Psi-i* block was replaced by a 2D lookup table. This lookup table block approximates two-dimensional functions.

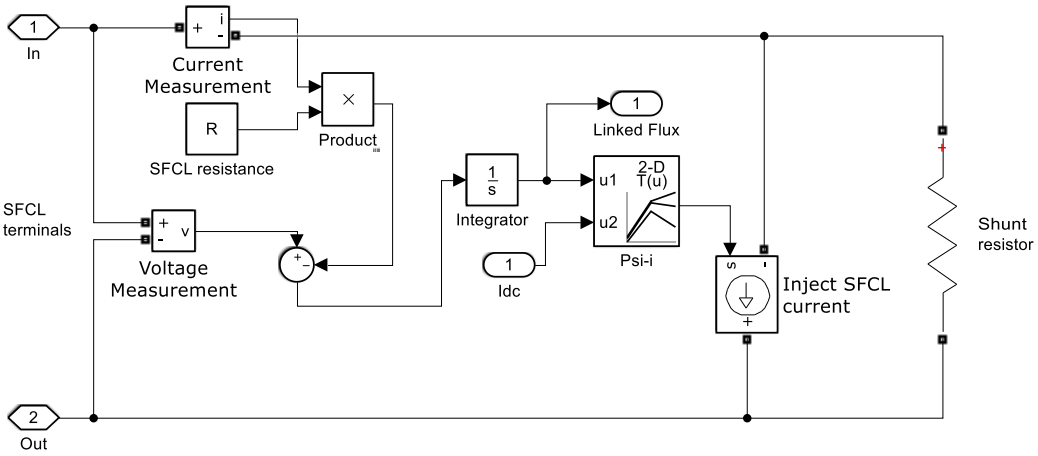

Figure 3.17 - Simulink model for the SFCL implementation with I_{DC} parameter.

The SFCL FEM project described in CHAPTER 3.2.1 was used to carry out simulations in order to obtain the SFCL characteristics for different DC bias current values. Therefore, the SFCL was simulated for I_{DC} values in the interval between 0 A and 300 A, with a step of 20 A. FIGURE 3.18 shows the SFCL magnetic characteristics obtained in previous simulations where the red curve means the SFCL characteristic with no DC bias current applied. The data is computed by the 2D lookup table block previously described, where the inputs are the linked magnetic flux with the AC coils and the DC bias current. The output is the interpolated current value, which is imposed into the AC line.

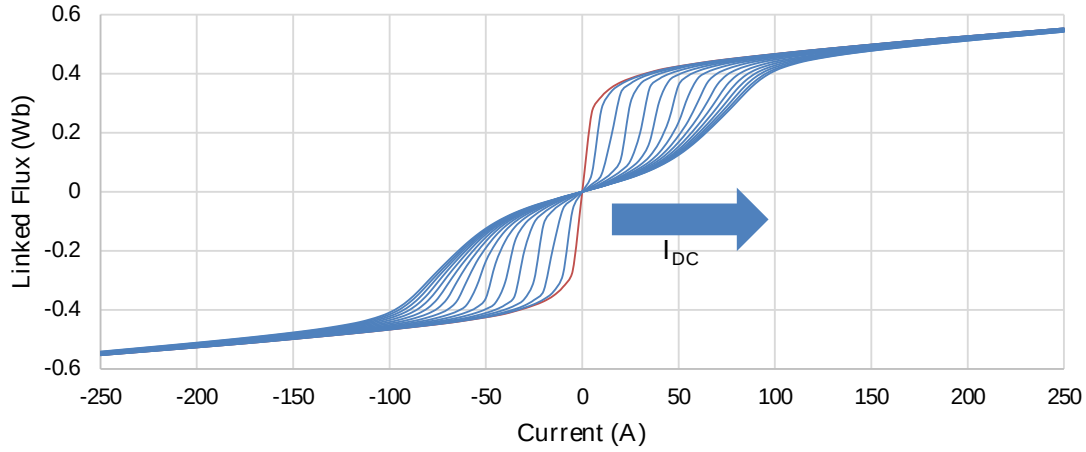

Figure 3.18 – FEM simulated $\Psi - i$ characteristics of the SFCL for different bias current values.

To evaluate the behaviour of the SFCL, the test circuit described in CHAPTER 3.2.2.2 was used. The internal resistance of the SFCL is $R_{SFCL} = 0.4\ \Omega$. A short-circuit was applied around $t = 0.49$ s and cleared around $t = 1.49$ s. The voltage source is $u_g = 60\ V_{rms.}$

For this simulation, the DC bias current is interrupted when the fault is detected, to improve the limitation ability of the SFCL, and after the fault ends, the DC bias current is restored *(Hong et al., 2009)*. The DC bias current is turned off following a ramp function, from the applied DC bias current value to 0 A, in 5 ms, to simulate the release of the magnetic energy stored in the saturated magnetic cores. When the fault is over, the DC bias current is put back in 800 ms, following a ramp function from 0 A to the default value.

In FIGURE 3.19 and FIGURE 3.20 can be seen the line current and linked flux of the SFCL under fault condition, respectively. The prospective fault current is 84.5 A which means the fault current was limited at 94%, only possible when both magnetic cores are desaturated during the fault. The recovery time of the limiter is defined at 800 ms.

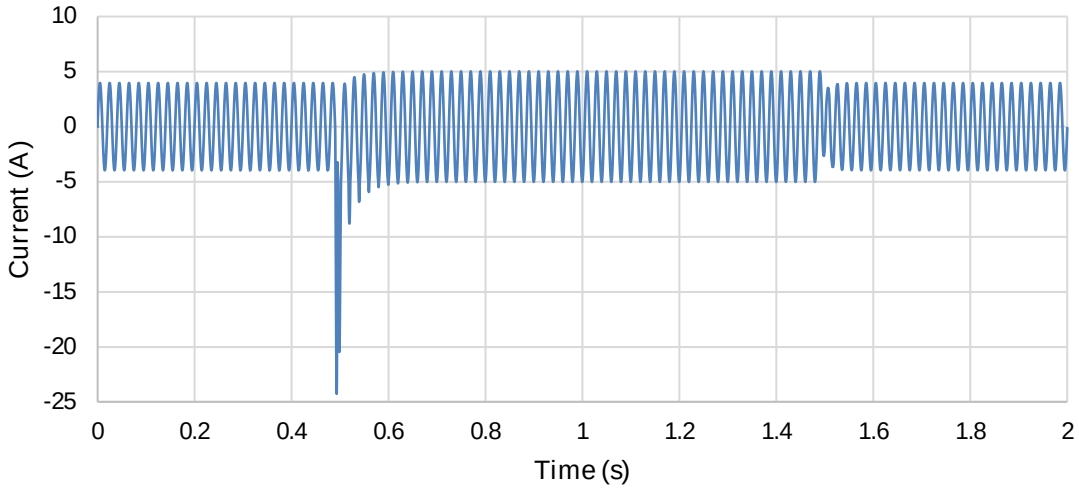

Figure 3.19 – SFCL line current time evolution under fault condition. Fault imposed at 0.49 s with 1 s of duration.

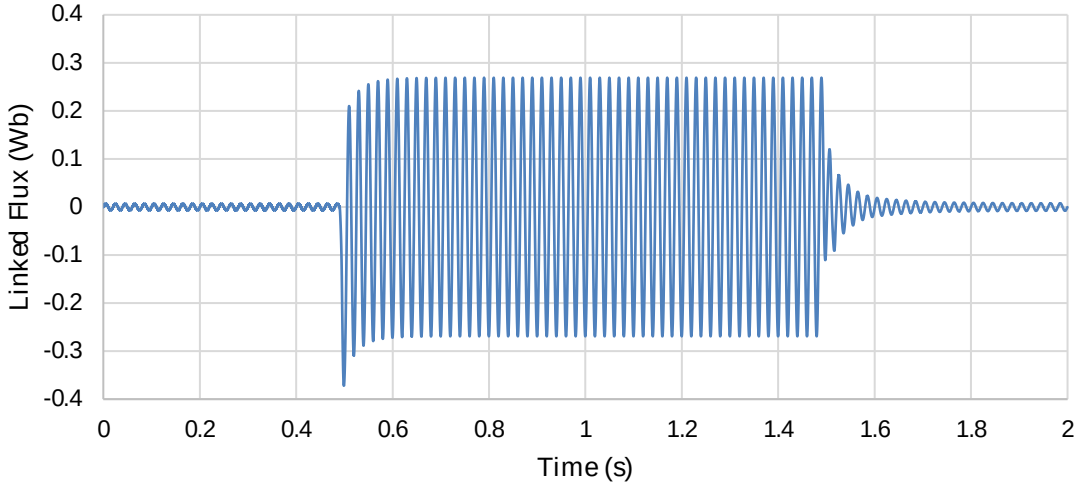

Figure 3.20 - SFCL linked flux time evolution under fault condition. Fault imposed at 0.49 s with 1 s of duration.

3.2.3 The Three-phase Topology

The three-phase SFCL can be built from three single-phase topologies, sharing the same DC bias coil, in a hexagonal arrangement, as can be seen in CHAPTER 2.3.3.2 for the Zenergy Power and Innopower companies. For a first approach, the computational model of a three-phase device can also be built replicating the model previously presented (FIGURE 3.14) three times. However, this approach is not completely according to with

happens because the linked magnetic flux of one phase depends, besides the DC bias current, on the current of the other phases.

The magnetic characteristic of the SFCL in CHAPTER 3.2.1 was used to implement the three-phase limiter. To simulate the three-phase limiter, a 3-bus power grid composed of two generators working at 400 V_{rms}, two lines and two loads was implemented which is depicted in FIGURE 3.21. The SFCL is placed after Bus 3. The characteristic of the power grid is shown in TABLE 3.5.

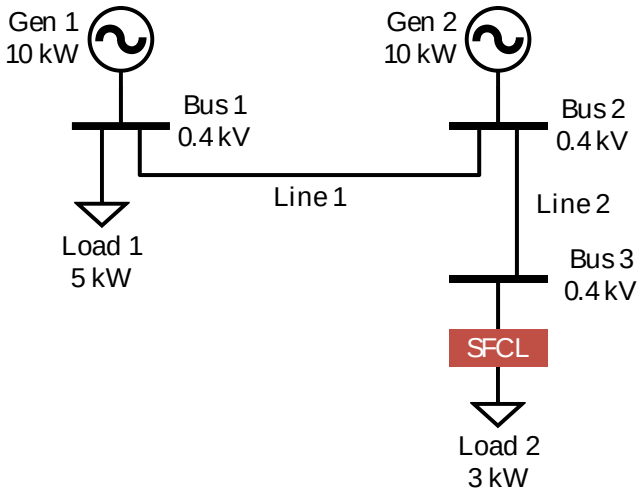

Figure 3.21 – Single line diagram of a 3-bus power grid used for simulations.

Table 3.5 - Characteristics of 3-bus power grid used for simulations.

Parameter	
Generator 1	10 kW / 0.4 V
Generator 2	0.89 + i5.21
Line 1	1 km
Line 2	1.83 + i0.082
Load 1	5.0 + i0.1 kVA
Load 2	3.0 + i0.1 kVA

3.2.3.1 Evaluation of the dynamic behaviour of the three-phase Limiter

The 3-bus power grid was implemented in Simulink as well as the three-phase SFCL topology model. A phase-to-earth fault and a three-phase-to-earth fault were imposed

to the grid in load 2, at 0.04 s until 0.15 s which are shown in FIGURE 3.22 and FIGURE 3.23 respectively. For both simulations, the prospective fault current is approximately 80 A and faults were reduced by 25%. The previously stated value of 25% is due to the fact the magnetic characteristic used for simulations is not optimised for this power grid and was only used to prove the model. As can be seen in FIGURE 3.22, only phase A is affected by the fault, however, depending on the topology of the used SFCL, the healthy phases may be slightly affected due to the magnetic coupling between phases. The proposed model is a first and simplistic approach, not taking these issues into account.

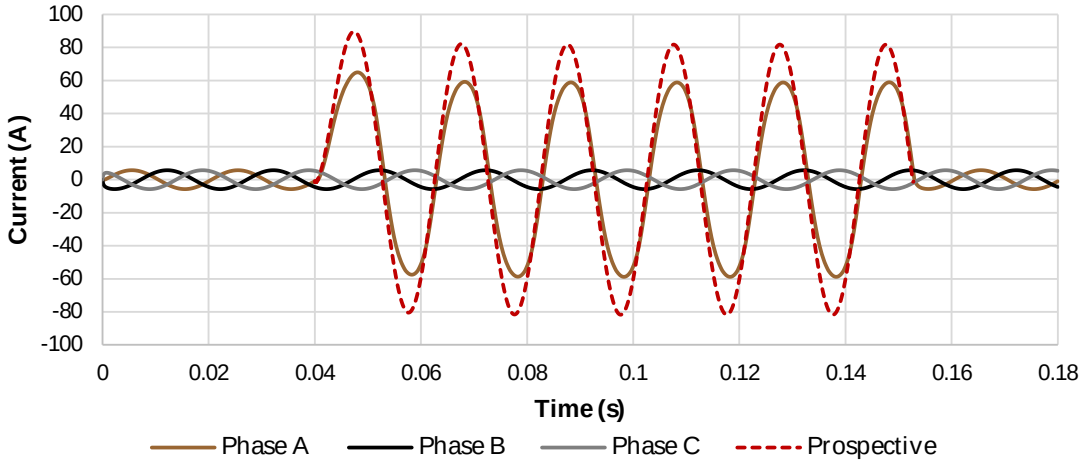

Figure 3.22 - Line current evolutions under a phase-earth fault as a function of time.

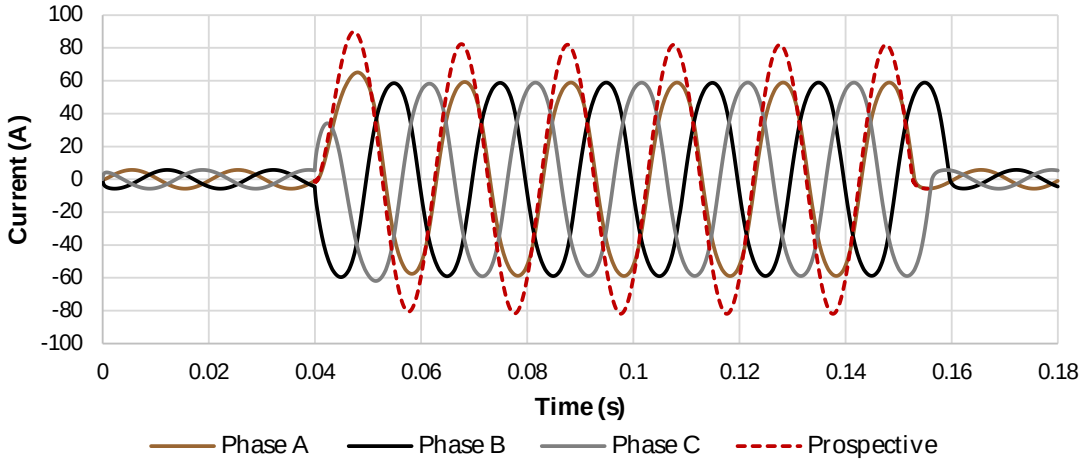

Figure 3.23 – Line current evolutions under a 3-phase-earth fault as a function of time.

3.3 Methodology for Superconducting Fault Current Limiter Modelling Based on Reluctance Method

An analytical methodology describing the nonlinear magnetic properties of the SFCL cores through a reluctance approach is presented in *(Commins & Moscrop, 2013)*. This reluctance equivalent circuit includes all significant magnetic flux paths of the SFCL. However, the values of each parameter are determined by magnetic flux measurements (either by FEM or real tests), which means this model describes the behaviour of a specific SFCL previously designed and/or implemented.

A lumped-element model was developed for the purposes of this thesis, based on reluctances that describe the core segments and *mmf* sources to characterize the coils, in order to provide an approximation of the behaviour of the SFCL. Thus, through this model is possible to obtain the magnetic characteristic of the SFCL, needed for the simulations, where the inputs are the constitutive parts of the limiter as well as some electrical parameters associated with coils.

3.3.1 B-H Curve Parametrisation

When a magnetic field strength, H, is applied into the vacuum, the magnetic field density, B, shows the relation given by EQUATION (3.9), where μ_0 is the magnetic permeability of free space.

$$B = \mu_0 H \tag{3.9}$$

If a ferromagnetic material is placed in the proximity of that magnetic field, the ratio between B and H is not constant but varies with flux density, in other words, the magnetic characteristic of the material shows non-linear behaviour, as can be seen in FIGURE 3.24. By EQUATION (3.10), it can be verified that the magnetic permeability is the slope of the $B - H$ curve.

$$\mu = \frac{B}{H} \tag{3.10}$$

The *B-H* curve is shown to be approximated by the EQUATION (3.11), where k_1, k_2 and k_3 are parameters obtained by fitting *(Brauer, 1975)*.

$$H = (k_1 e^{k_2 \cdot B^2} + k_3) \cdot B \tag{3.11}$$

FIGURE 3.24 also shows the approximated curve in dashed line, where $k_1 = 60$, $k_2 = 1.6$, $k_3 = 300$ and the magnetic saturation started at 1.2 T. The fitted curve shows 95% confidence bounds and $R = 1$.

Analysing EQUATION (3.10) and EQUATION (3.11), it can be seen that magnetic permeability can be obtained by EQUATION (3.12), as a function of the magnetic flux density *B*.

$$\mu(B) = \frac{1}{(k_1 e^{k_2 \cdot B^2} + k_3)} \tag{3.12}$$

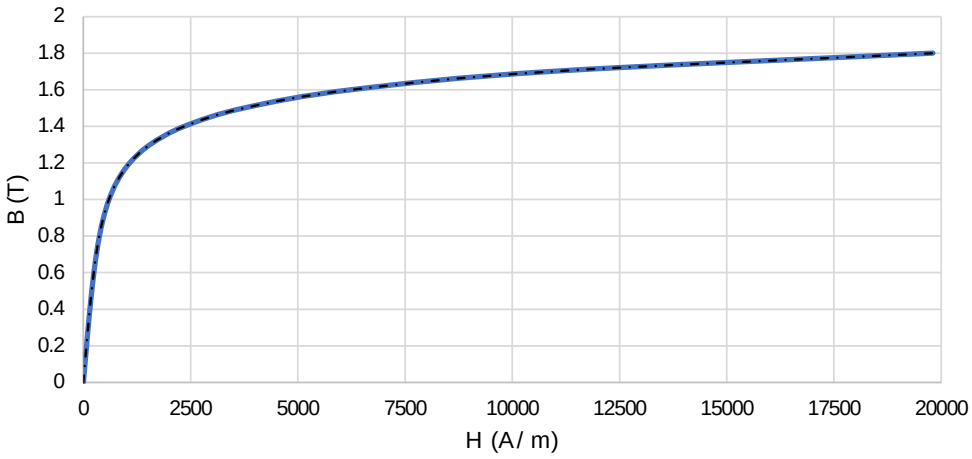

Figure 3.24 – *B-H* magnetization curve of a ferromagnetic material.

3.3.2 Single-phase Equivalent Magnetic Circuit

The main magnetic flux paths associated with each core of the single-phase SFCL, presented in CHAPTER 3.1, are shown in FIGURE 3.25. Straight lines show qualitatively the flux path in the cores and dashed lines represent the main flux path (called flux tubes) of the leakage magnetic flux.

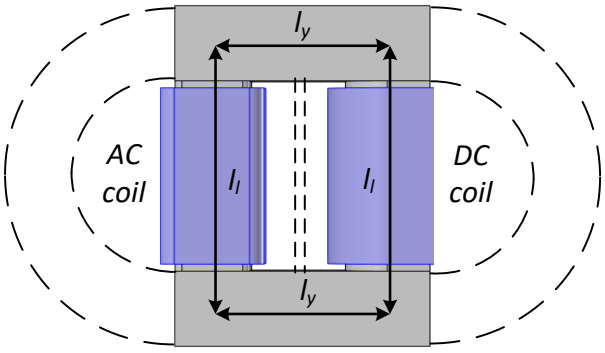

Figure 3.25 - Schematic diagram of magnetic flux paths of cores (straight lines) and leakage magnetic field distribution (dashed lines).

There is an associated magnetic reluctance for each magnetic flux path. Thus, the representation of the magnetic circuit is possible through the resistance-reluctance

model, which draws an analogy between electrical and magnetic circuits. The equivalent magnetic circuit of each core is shown in FIGURE 3.26. $\Re_1$ to $\Re_6$ represent the equivalent reluctance of each magnetic path of the magnetic core. These reluctances show a non-linear dependence of H due to the fact the magnetic core shows a non-linear magnetic characteristic, therefore they are represented as variable reluctances. $\Re_{01}$, $\Re_{02}$ and $\Re_0$ represent the leakage reluctance associated with the coils.

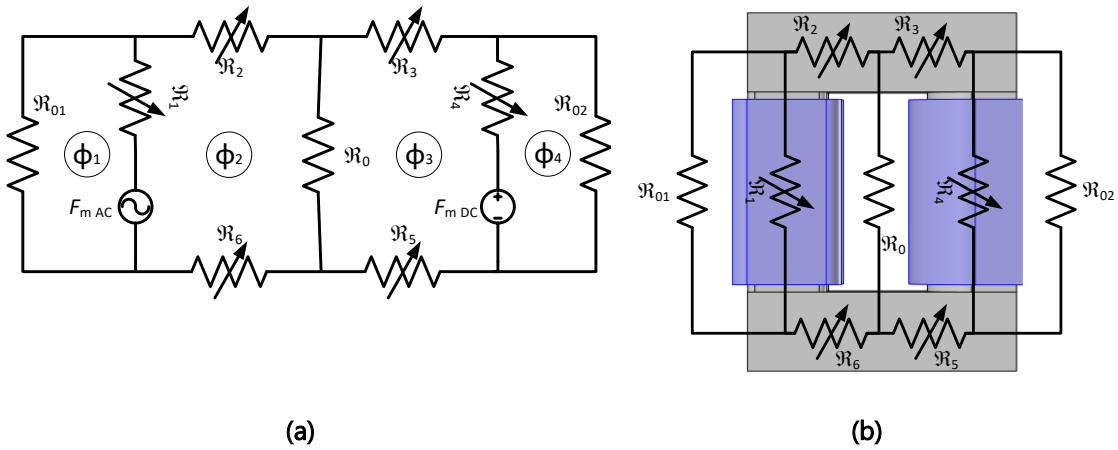

Figure 3.26 - Equivalent reluctance methodology of each SFCL core. $\Re_1$ to $\Re_6$ are the non-linear reluctances of the core segments, and $\Re_{01}$, $\Re_{02}$ and $\Re_0$ means the leakage reluctance. (a) Equivalent reluctance circuit with its imaginary magnetic flux loops. (b) Representation of the reluctance circuit overlapped to the core.

The SFCL is modelled according to the electrical and geometrical parameters depicted in TABLE 3.6, which are the DC bias current, I_{DC}, turn number of AC and DC coil, N_{AC} and N_{DC} respectively, and the magnetic paths of yoke and limb, l_y and l_l respectively and cross-section of AC, DC limbs and yoke, S_{AC}, S_{DC} and S_y respectively.

Table 3.6 – Parameters used for reluctance methodology.

Parameter	
I_{DC}	DC current to bias the SFCL
N_{AC}, N_{DC}	Number of turns of AC and DC coils, respectively
l_y, l_l	Lengths of magnetic paths of yokes and limbs respectively
S_{AC}, S_y, S_{DC}	Cross-sections area of AC limb, yoke and DC limb respectively

3.3.2.1 Limiter dimensions from reluctance model parameters

FIGURE 3.27 depicts the parameters used to obtain the dimensions of an equivalent SFCL design, from the reluctance model parameters, as seen in TABLE 3.6. In FIGURE 3.27 (A) is shown the SFCL constructive parameters used to design the SFCL and in FIGURE 3.27 (B) is depicted the reluctance model parameters.

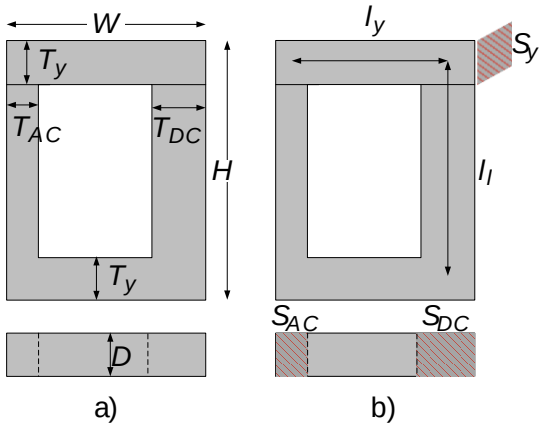

Figure 3.27 – Magnetic cores with the parameters used to parametrise SFCL cores

As described previously, the proposed methodology uses the parameters described in TABLE 3.6.

The SFCL dimensions and electrical characteristics can be defined by parameters shown in TABLE 3.7 which need to be related with parameters in TABLE 3.6 in order to obtain an equivalent SFCL design with the same magnetic properties of the reluctance model. EQUATION (3.13) to EQUATION (3.18) show the conversion between parameters.

Table 3.7 – Parameters used for SFCL cores parametrisation.

Parameter	
I_{DC}	DC current to bias the SFCL
N_{AC}, N_{DC}	Number of turns of AC and DC coils, respectively
W	Width of each core
H	Height of each core
D	Depth of the core
T_{AC}, T_{DC}, T_y	Thickness of AC limbs, DC limbs and yokes, respectively

$$D = \sqrt{S_{DC}} \tag{3.13}$$

$$T_{DC} = D \tag{3.14}$$

$$T_{AC} = S_{AC}/D \tag{3.15}$$

$$T_y = S_y/D \tag{3.16}$$

$$W = l_y + T_{DC}/2 + T_{AC}/2 \tag{3.17}$$

$$H = l_l + T_y/2 + T_y/2 \tag{3.18}$$

3.3.2.2 Magnetomotive Forces

The *mmf* of each coil can be calculated by EQUATION (3.19) and EQUATION (3.20) where i_{AC} is the line current. Variables $F_{m\,AC}$ and $F_{m\,DC}$ correspond, respectively to mmf due to AC coil and mmf due to DC coil. The proposed model uses as an independent variable, the line current i_{AC}.

$$F_{m\,AC} = N_{AC} \cdot i_{AC} \tag{3.19}$$

$$F_{m\,DC} = N_{DC} \cdot I_{DC} \tag{3.20}$$

3.3.2.3 Non-linear magnetic reluctances

The magnetic reluctance of a uniform magnetic circuit, associated with $\Re_1$ to $\Re_6$, can be calculated by EQUATION (3.21), according to Hopkinson's law. l_n is the mean length of the circuit element n, S_n is its cross-section area and μ_n is the magnetic permeability of the element n.

$$\Re_n = \frac{l_n}{\mu_n \cdot S_n} \tag{3.21}$$

Core material shows a non-linear behaviour, that is defined by its $B - H$ curve. Therefore, the magnetic permeability of each segment is not constant, which varies with the saturation state of the cores.

For this model, it is intended to use the magnetic permeability as a function of the magnetic flux through S_n, $\mu(\phi_n)$. Considering the magnetic field density constant, the magnetic flux passing through the surface S_n is given by EQUATION (3.22).

$$\phi_n = B \cdot S_n \tag{3.22}$$

Combining EQUATION (3.11) and EQUATION (3.22), $\mu(\phi_n)$ can be calculated by EQUATION (3.29).

$$\mu(\phi_n) = \frac{1}{(k_1 e^{k_2 \cdot \left(\frac{\phi_n}{S_n}\right)^2} + k_3)} \tag{3.23}$$

3.3.2.4 Magnetic Leakage Reluctances

The magnetic leakage reluctances are represented by $\mathfrak{R}_{01}$, $\mathfrak{R}_{02}$ and $\mathfrak{R}_0$, where the latter are obtained by analyzing the magnetic flux tubes (the path for the leakage magnetic flux) of leakage magnetic flux of each coil *(Leupold & Potenziani, 1996; Q. Li et al., 2012)*.

FIGURE 3.28 (A) AND (B) shows the flux tubes associated with a rectangular cross-section coil and FIGURE 3.28 (C) with a circular cross-section coil. The flux tubes associated with the coil height are shown in blue, these are called half-moon magnetic flux tubes, identified by $\boldsymbol{\Lambda_1}$ and $\boldsymbol{\Lambda_2}$ for corner and edge of the rectangular cross-section coil, respectively, and by $\boldsymbol{\Lambda_3}$ for a circular cross-section coil. The fluxtubes associated with the core height are represented in green and are called hollow semi-circular magnetic flux tubes, identified by $\boldsymbol{\Lambda_4}$ and $\boldsymbol{\Lambda_5}$.

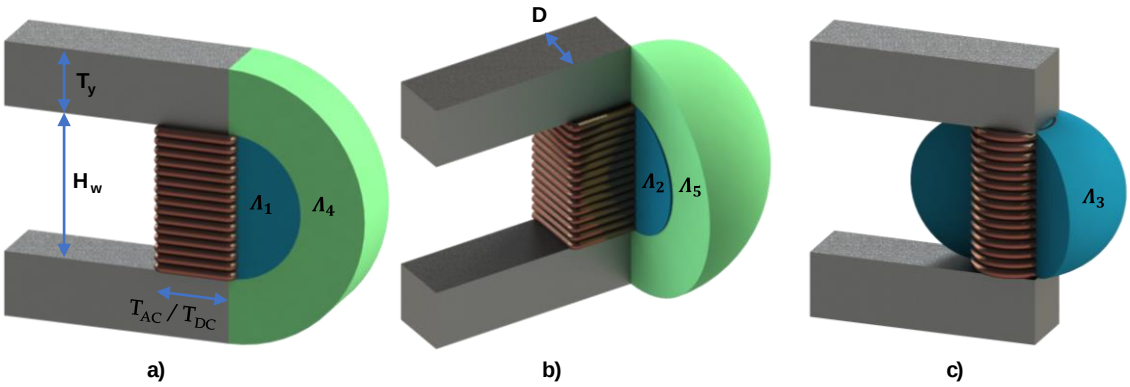

Figure 3.28 – Flux tubes associated to a coil.

Through EQUATION (3.24), EQUATION (3.25) and EQUATION (3.26) is possible to calculate the permeances of half-moon magnetic flux tubes previously described *(Leupold & Potenziani, 1996; Q. Li et al., 2012)*. Parameters *h*, *t* and *d* are depicted in FIGURE 3.28 and represent the windows hight, the yoke thickness and the core depth, respectively. Parameter *c* varies between 0 and 1 where 1 means a complete revolution of flux tube $\boldsymbol{\Lambda_3}$.

$$\Lambda_1 = \mu_0 \times 0.26 \times D \tag{3.24}$$

$$\Lambda_2 = \mu_0 \times 0.08 \times H_w \tag{3.25}$$

$$\Lambda_3 = \mu_0 \times 1.63 \times (D + 0.25 \times H_w) \times c \tag{3.26}$$

Through EQUATION (3.27) and EQUATION (3.28) is possible to calculate the permeances of hollow semi-circular magnetic flux tubes *(Leupold & Potenziani, 1996; Q. Li et al., 2012)*.

$$\Lambda_4 = \mu_0 \times 0.318 \times D \times ln(1 + 2t/H_w) \tag{3.27}$$

$$\Lambda_5 = \mu_0 \times 0.25 \times T_y \tag{3.28}$$

Reluctances $\Re_{01}$ and $\Re_{02}$ are associated with the AC and DC coils respectively, which have rectangular cross-sections. Therefore, they can be calculated by the inverse of the sum of the permeances associated with the fluxes tubes, thus EQUATION (3.29) shows how the leakage reluctances are calculated.

$$\Re_{0n} = \frac{1}{(4 \times \Lambda_1 + 4 \times \Lambda_2) + (3 \times \Lambda_4 + 4 \times \Lambda_5)} \tag{3.29}$$

Reluctances $\Re_0$ is related to the magnetic flux leakage through the core window and can be calculated by EQUATION (3.30), where the cross-section S_0 is the bottom area of the core window.

$$\Re_0 = \frac{h}{\mu_0 \times S_0} \tag{3.30}$$

$$S_0 = d \times \frac{l_{window}}{4}$$

3.3.2.5 Computational model implementation

In EQUATION (3.31) is shown the matrix that described the equivalent magnetic circuit in FIGURE 3.26. The SFCL characteristic can be obtained using numerical software such as MATLAB in order to solve the previous circuit, using line current i_{AC} as independent variable.

$$\begin{vmatrix} \Re_{10} + \Re_1 & -\Re_1 & 0 & 0 \\ -\Re_1 & \Re_1 + \Re_2 + \Re_6 + \Re_0 & -\Re_0 & 0 \\ 0 & -\Re_0 & \Re_3 + \Re_4 + \Re_5 + \Re_0 & -\Re_4 \\ 0 & 0 & -\Re_4 & \Re_4 + \Re_{40} \end{vmatrix} \cdot \begin{vmatrix} \phi_1 \\ \phi_2 \\ \phi_3 \\ \phi_4 \end{vmatrix} = \begin{vmatrix} -N_{AC} i_{AC} \\ N_{AC} i_{AC} \\ -N_{DC} I_{DC} \\ N_{DC} I_{DC} \end{vmatrix} \tag{3.31}$$

Linked magnetic fluxes are calculated by EQUATION (3.32) and EQUATION (3.33). The maximum AC current must be calculated in order to define the range for the independent variable i_{AC}, which can be calculated through EQUATION (3.34).

$$\psi_{AC} = N_{AC}(\phi_1 - \phi_2) \tag{3.32}$$

$$\psi_{DC} = N_{DC}(\phi_3 - \phi_4) \tag{3.33}$$

$$I_{AC\,max} = 2\left(\frac{N_{DC} \times I_{DC}}{N_{AC}}\right) \tag{3.34}$$

Each numerical simulation follows steps in FIGURE 3.29, that is, input parameters are given in order to define magnetic and physical properties of the SFCL and a numerical simulation, which is implemented by EQUATION (3.31), is carried out in order to obtain the magnetic characteristic of the limiter.

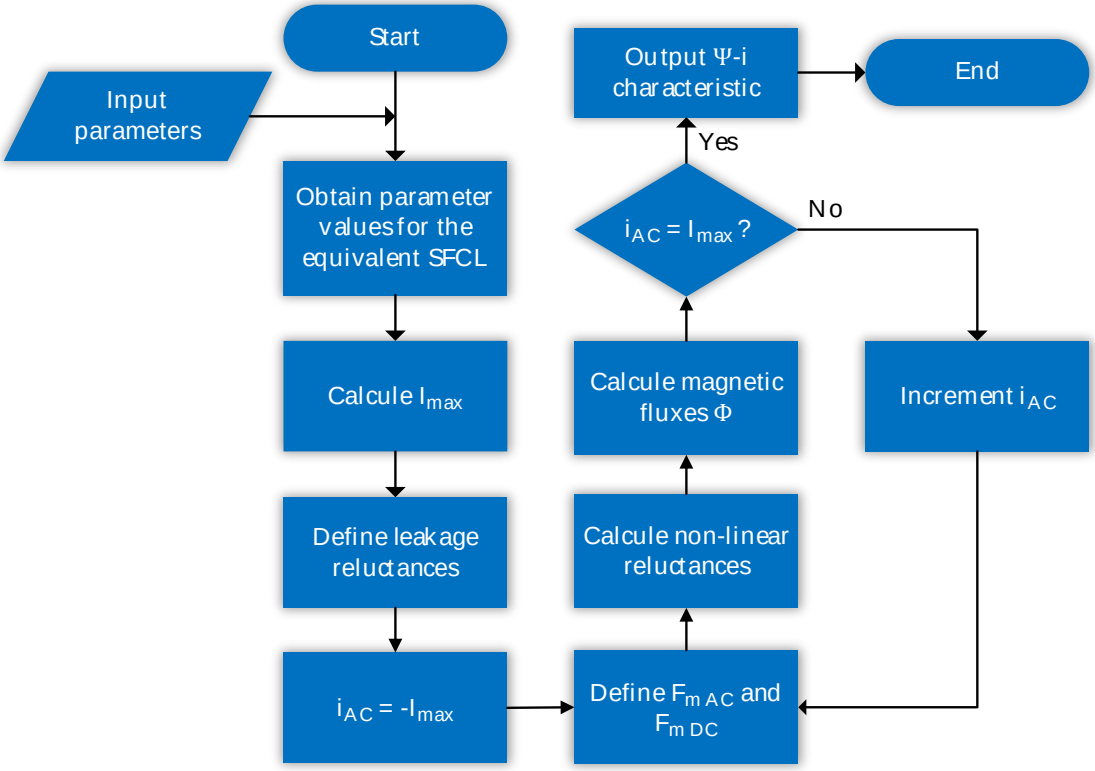

Figure 3.29 - Steps for obtaining characteristic by reluctance model simulation.

3.3.3 Model Validation by FEM Simulations

To validate the proposed methodology, a stationary magnetic field simulation of the SFCL, previously presented in CHAPTER 3.2.1, was carried out to obtain the $\Psi - i$ characteristic of the SFCL and compare it with the characteristic resulting from the present methodology.

FIGURE 3.30 shows the SFCL topology implemented in FEM software with its mesh.

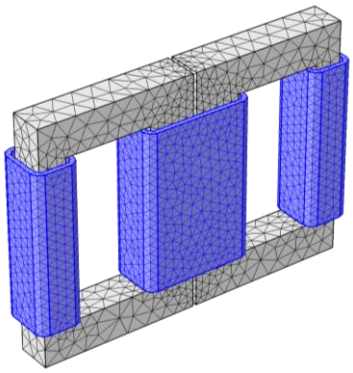

Figure 3.30 – 3D model of the SFCL built-in FEM and its mesh.

As described in CHAPTER 3.3.2.1, the proposed methodology uses the parameters described in TABLE 3.6. For FEM simulations, the SFCL can be correctly defined by parameters shown in TABLE 3.7 which are related by EQUATION (3.13) to EQUATION (3.18). Therefore, it is possible to obtain the SFCL dimensions for FEM simulation using previous equations.

Three distinct designs of SFCL were simulated and their $\Psi - i$ characteristic compared to that which was obtained by the reluctance method. TABLE 3.8 shows their dimensions and electrical characteristics. The main difference between design 1 and 2 are the applied DC bias current, and design 3 has bigger dimensions.

Table 3.8 – The SFCL electrical characteristics and dimensions used in FEM simulations.

Parameter	SFCL 1	SFCL 2	SFCL 3
I_{DC} *(A)*	300	150	300
N_{DC}	40	40	500
N_{AC}	100	100	60
W *(mm)*	198	198	1800
H *(mm)*	260	260	2668
D *(mm)*	60	60	400
T_{AC} *(mm)*	18	18	308
T_{DC} *(mm)*	30	30	513
T_y *(mm)*	24	24	410

3.3.3.1 B-H curve parametrisation

FIGURE 3.31 shows the $B-H$ curve of the magnetic cores used for the simulation, as well as the fitted curve obtained by parametrization, in dashed line, as explained in CHAPTER 3.3.1. The $B-H$ curve shows a knee value of 1.2 T, approximately. The fitted curve, according to EQUATION (3.11), shows 95% confidence bounds and $R = 0.99$ and their parameters are shown in TABLE 3.9.

Table 3.9 – Parameters of the fitted B-H curve.

Parameter	
k_1	4.5
k_2	2.4
k_3	50.0

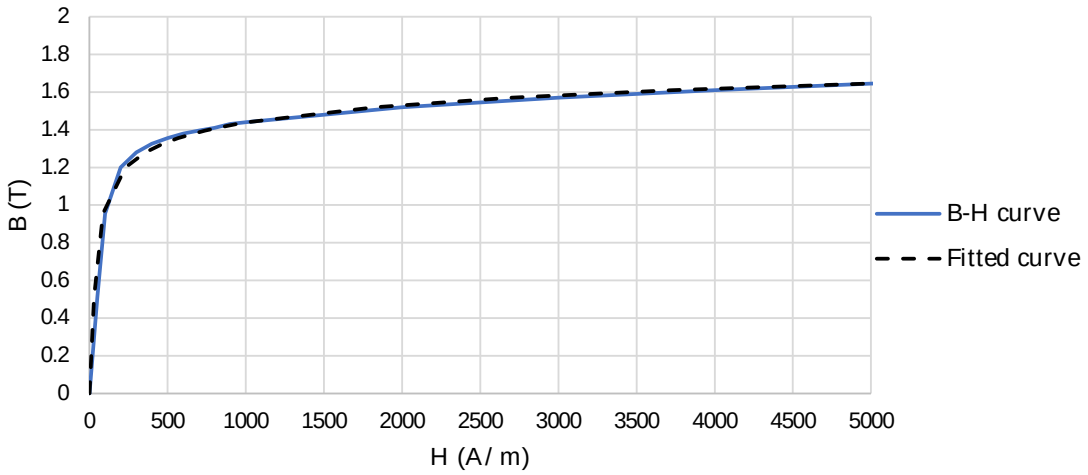

Figure 3.31 – B-H curve and the fitted curve obtained by parametrization.

3.3.3.2 Input parameters

The proposed methodology receives as input the parameters described in TABLE 3.6, which are related to the SFCL parameters used in FEM simulation (shown in TABLE 3.7), by EQUATION (3.13) to EQUATION (3.18). In TABLE 3.10 is shown the dimensions and the electrical characteristics of each SFCL design used in simulations.

Table 3.10 – The SFCL electrical characteristics and dimensions used in the reluctance methodology.

Parameter	SFCL 1	SFCL 2	SFCL 3
I_{DC} *(A)*	300	150	300
N_{DC}	40	40	500
N_{AC}	100	100	60
l_y *(mm)*	118	118	1390
l_l *(mm)*	168	168	2260
S_{DC} *(mm²)*	1600	1600	205200
S_{AC} *(mm²)*	60% of S_{DC}	60% of S_{DC}	60% of S_{DC}
S_y *(mm²)*	80% of S_{DC}	80% of S_{DC}	80% of S_{DC}

3.3.3.3 Comparison between the proposed methodology and FEM simulations

The reluctance method was used to obtain the $\Psi - i$ characteristic of an SFCL, which can approximately describe the SFCL behaviour. To validate the accuracy of the present method, three distinct FEM simulation, based on three different SFCL designs, were carried out and the SFCL characteristic obtained by FEM and by the reluctance method are compared.

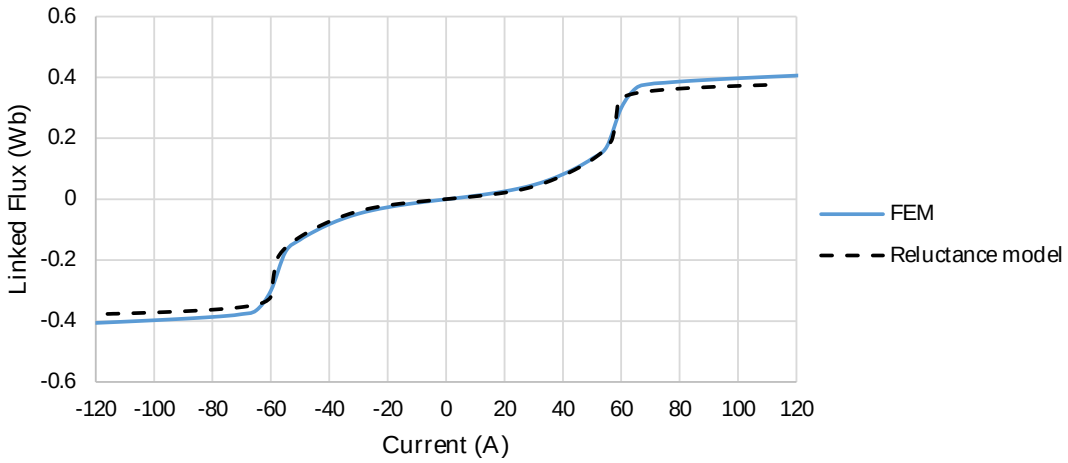

Figure 3.32 - $\Psi - i$ excursion of SFCL by FEM simulation and by proposed reluctance model, for SFCL design 1.

FIGURE 3.32, FIGURE 3.33 and FIGURE 3.34 show the $\Psi - i$ characteristic obtained by both methods, for SFCL design number 1, 2 and 3, respectively. For each case, FEM and reluctance model curves show good correlation, better for the SFCL 3, the biggest limiter.

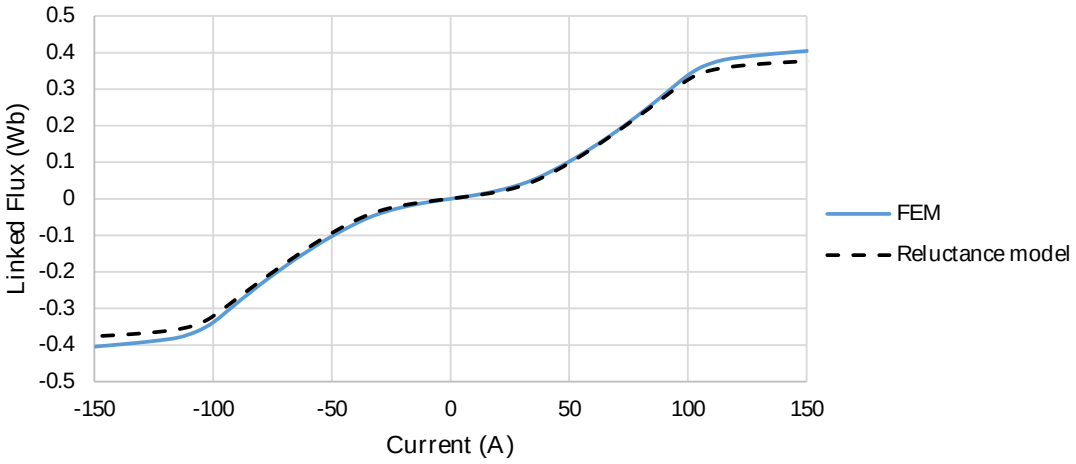

Figure 3.33 - $\Psi - i$ excursion of SFCL by FEM simulation and by proposed reluctance model, for SFCL design 2.

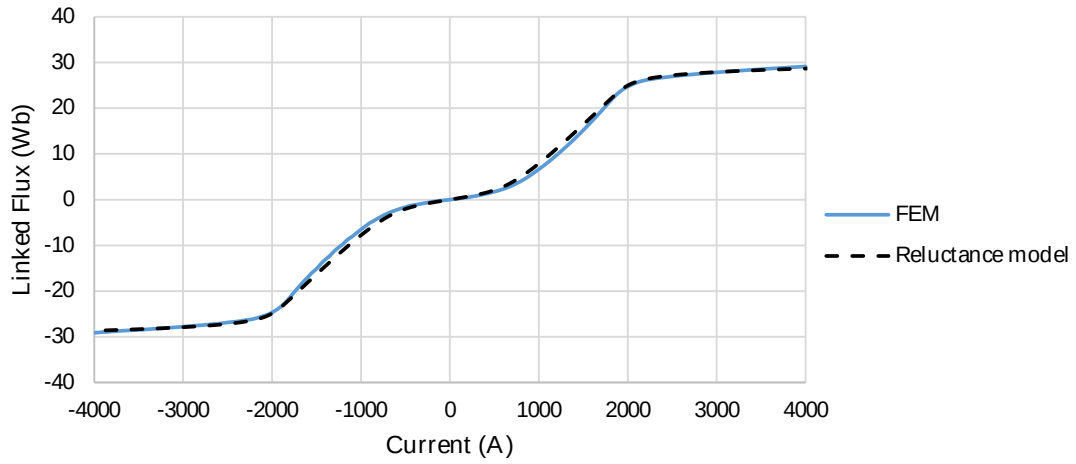

Figure 3.34 - $\Psi - i$ excursion of SFCL by FEM simulation and by proposed reluctance model, for SFCL design 3.

3.4 Methodology for Superconducting Fault Current Limiter Modelling Based on FEM

A FEM project simulation methodology was developed in order to obtain the $\Psi - i$ characteristic of the SFCL by stationary magnetic field simulation. This methodology uses the same constitutive parameters previously described in CHAPTER 3.3.2.1, following the same approach used for the CHAPTER 3.3.3.

FIGURE 3.35 (A) shows a 3D model of the SFCL built-in FEM software and its mesh. The project can be defined by the parameters shown in TABLE 3.11. Parameters related to the dimensions of each core are shown in FIGURE 3.35 (B).

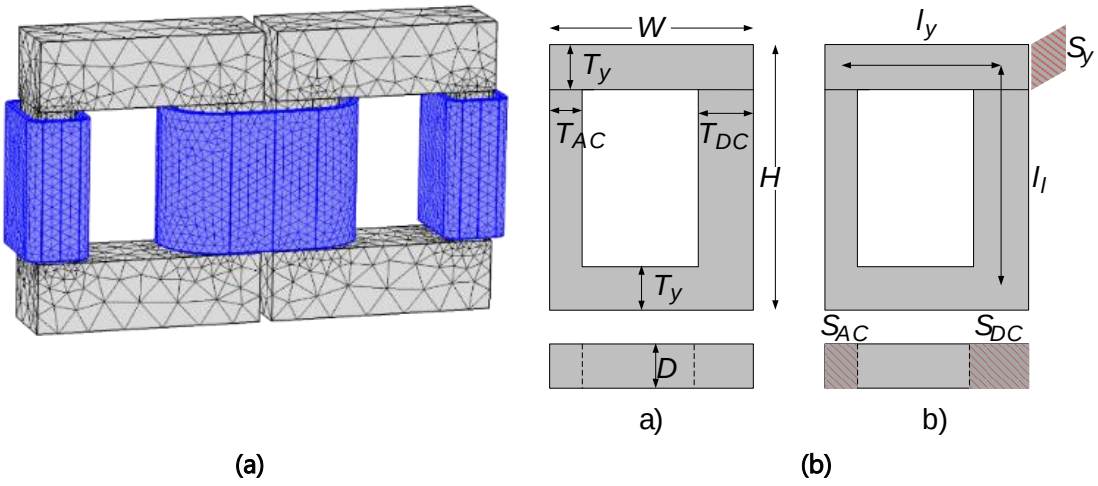

Figure 3.35 - SFCL model in FEM software. a) 3D model of the SFCL built-in FEM and its mesh. b) Parameters used to parametrize SFCL cores.

Table 3.11 – Parameters for reluctance methodology.

Parameter	
I_{DC}	DC current to bias the SFCL
$I_{AC\ max}$, $I_{AC\ inc}$	Maximum AC current and its increment step.
N_{AC}, N_{DC}	Number of turns of AC and DC coils, respectively
W	Width of each core
H	Height of each core
D	Depth of the core
T_{AC}, T_{DC}, T_y	Thickness of AC limbs, DC limbs and yokes, respectively

Each FEM simulation follows steps in FIGURE 3.36, that is, input parameters are given in order to define the dimensions/characteristics of cores and coils, the respective simulations are carried out and the $\Psi - i$ characteristic is obtained.

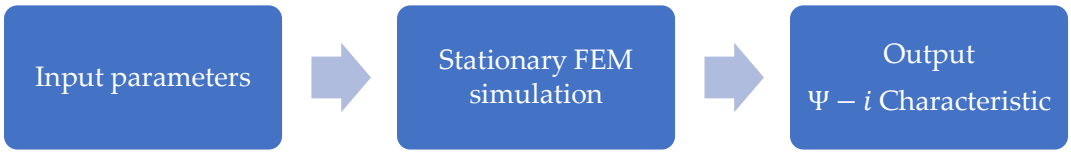

Figure 3.36 - Steps for obtained $\Psi - i$ characteristic by FEM simulation.

The SFCL is parametrised in the FEM software through MATLAB environment that provides it with input parameters, starting the simulation, and finally receives the data from FEM software.

3.4.1 Input Parameters

The input parameters are the constitutive parts of the limiter which are listed in TABLE 3.11. Another input parameter is the $H - B$ curve specified for the magnetic cores. All parameters are sent to the FEM software by a MATLAB script.

3.4.2 Stationary FEM Simulation

A stationary study is defined with an auxiliary sweep and adaptative mesh. This configuration is needed to run the parametric solver, where the line current is chosen as sweep parameter. In order to obtain the $\Psi - i$ characteristic of the limiter, the limits of the current i (associated with the line current) $I_{AC\,max}$ is calculated by EQUATION (3.35), and the respective step incrementation is calculated by EQUATION (3.36).

$$I_{AC\,max} = 2 \times \mathbb{N}\left(\frac{N_{DC} \times I_{DC}}{N_{AC}}\right) \tag{3.35}$$

$$I_{AC\,inc} = 5\%\ of\ I_{AC\,max} \tag{3.36}$$

The I_{AC} parameter is defined in the interval $[-I_{AC\,max}; I_{AC\,max}]$ with a step of $I_{AC\,inc}$. For each value of I_{AC}, FEM software will calculate the correspondent linked magnetic flux with primaries, Ψ_{SFCL}.

3.4.3 Output $\Psi - i$ Characteristic

When the simulation is finished, the obtained $\Psi - i$ characteristic is sent to the MATLAB.

3.5 Summary

Two distinct methodologies for the modelling and simulation of SC-SFCL were presented.

A. Methodology for Superconducting Fault Current Limiter simulation based on its $\Psi - i$ characteristic

A methodology to simulate the dynamic behaviour of the SC-SFCL, in an electrical grid, was presented in this chapter. The methodology shows good agreement with FEM simulations and experimental measurements. Its main advantage is a drastic decrease in simulation times when compared with FEM software. This allows for the simulation of these devices in complex grids, which is one requisite of utilities.

A computational model was developed in MATLAB/SIMULINK. The computation model also includes the DC current specifically in the $\Psi - i$ curve expression, which allows for the change of the DC bias current value during simulation or to perform multiple simulations for different values of the DC bias current.

B. Methodology for Superconducting Fault Current Limiter modelling based on reluctance method

A methodology for SFCL modelling, based on its constitutive and electrical parameters was presented. This is based on a reduced reluctance model which is able to describe the non-linearity magnetic properties of the SFCL cores and return the $\Psi - i$ magnetic characteristic. The methodology was validated through FEM simulation, which shows good agreement between magnetic characteristics obtained by FEM and by the proposed methodology.

C. Methodology for Superconducting Fault Current Limiter modelling based on FEM

A methodology to obtain the $\Psi - i$ characteristic of the SFCL based on FEM method is presented. The methodology receives the constitutive parameters of the SFCL as input, carries out an auxiliary parametric sweep and returns the respective $\Psi - i$ characteristic.

4

Saturated Cores Superconducting Fault Current Limiter: Design Optimisation

In this chapter, a design methodology that allows modelling and optimising saturated cores fault current limiters considering the characteristics of each constitutive element of the SFCL, while addressing utility requirements and power grid characteristics is introduced. Genetic algorithms are heuristic optimisation algorithms that mimic the process of natural evolution in order to solve optimisation problems. Therefore, it is possible to optimise either a constitutive element of the limiter or its behaviour in the power grid, using genetic algorithms.

4.1 Formulation of the Design Optimisation by Genetic Algorithms

Genetic algorithms (GA) are a subclass of evolutionary algorithms. GA mimics natural evolution to find an optimal solution to solve a problem by recombining the decision variables. The purpose of using genetic algorithms is to optimise some aspects of the SFCL (the goals), such as the minimization of the volume of the limiter. The GA toolbox of MATLAB is used to optimise the SFCL design.

Three different simulation/modelling methodologies that can describe the behaviour of the SFCL were developed and presented in CHAPTER 3.

- The first methodology was developed to simulate the behaviour of SC-SFCL based on the magnetic characteristic of the device.

- The second methodology is based on a reluctance circuit that describes approximately the magnetic behaviour of the SC-SFCL. This methodology will be used to provide an initial optimal solution for the problem solved by GA and it is used in a multi-objective optimisation approach, in order to generate a Pareto front (set of nondominated optimal solutions).
- The last methodology is based on finite elements method (FEM) simulations and gives the final optimal solution.

The process used to obtain an optimal solution for the proposed problem starts by setting decision variables, objectives, and constraints. Next, the optimisation process is divided into two steps:

- First-step optimisation: Multi-objective optimisation

  The first step consists of running the optimisation process using the reluctance methodology and multi-objective approach in order to find an approximate optimal solution through analysing the Pareto-front. After that, a decision task to select a solution from the obtained Pareto-front is performance (performed by the designer).
- Final-Step optimisation: Single-objective optimisation

  The final optimal solution uses FEM methodology in the optimisation process which starts from the approximate solution given by the first step.

Using two optimisation steps, an optimal solution is found with a reduced number of iterations by FEM, reducing the time of optimisation because FEM is only used locally, that is to tune the approximate solution to achieve the final optimal solution.

Next is shown and described the decision variables used to describe the SC-SFCL and its constraints, as well as the fitness function.

4.1.1 Optimisation Criteria and Decision Variables

4.1.1.1 Possible Optimisation Criteria

The purpose of using GA is to optimise design aspects of the SC-SFCL (the goals) which need to be maximized or minimized. In the SFCL under consideration, several optimisation criteria are possible, as following:

- Low core volume.

- Minimum length of HTS tape for DC bias coil.
- Maximum fault current limitation.
- Low manufacturing cost or low material cost.
- Low losses.
- Etc.

4.1.1.2 Decision Variables (or Input Variables) Possible

Several decision variables may be identified for the SFCL under study, therefore, choosing appropriate decisions variables that describe the behaviour of the SFCL is required. In CHAPTER 3.3.2 was identified the SFCL electrical and geometrical parameters that are able to describe the SFCL completely.

Decision variables chosen are listed in TABLE 4.1 and are related to the constitutive parts of the SFCL (see FIGURE 3.27).

Table 4.1 – Decision variables chosen for the optimisation process.

Decision Variable	Parameter	Description
DV 1	$\mathrm{N_{AC}}$	Number of turns of the AC coil
DV 2	l_l	Mean magnetic length of limbs
DV 3	l_y	Mean magnetic length of yokes
DV 4	S_{DC}	Cross-section area of the DC limb

The remaining parameters are defined with a fixed value or related to other decision variables.

- $\mathrm{I_{DC}}$ (DC bias current) is set with a fixed value, according to the HTS tape specification.
- $\mathrm{N_{DC}}$ (Number of turns of the DC coil) is chosen from the optimal bias *mmf*, which saturates the DC and AC limbs with the same magnetic induction values (see CHAPTER 2.3.2.2).
- $S_{AC} = 0.6 \times S_{DC}$ (AC cross-section of limbs)
- $S_{AC} = 0.8 \times S_{DC}$ (cross-section of yokes)

Having several goals to be optimised, a multi-objective approach is considered to find the optimal solutions and, after that, to choose an appropriate solution.

4.1.2 Fitness Function (Objective Function)

The fitness function is a function or procedure which assesses the performance of each chromosome (candidate solutions of the optimisation problem). FIGURE 4.1 shows the fitness function diagram.

Decision variables are used in order to obtain the number of turns of the DC bias coil and the $\Psi - i$ characteristic through the SFCL methodology used for the optimisation process (reluctance methodology or FEM simulation). The behaviour of the SFCL is simulated through the power grid simulating model. If it meets the grid requirements, the fitness value is returned, if not a penalty function is applied to penalize the fitness value in order to discard that solution later.

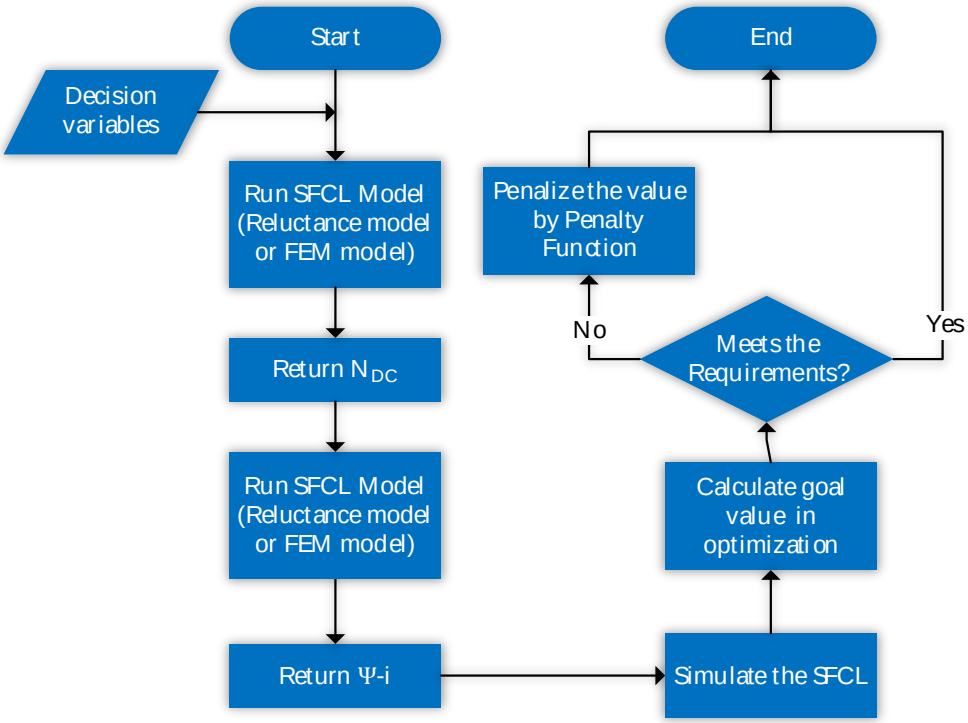

Figure 4.1 - Diagram of the fitness function.

4.1.3 Parameters

The population size directly affects the overall performance and efficiency of GA. A population with few individuals provides a small coverage of the problem search space, which reduces algorithm performance. In the case of a high population, coverage of the

problem domain is assured and the probability that the algorithm converges to local instead of global solutions is reduced. However, these high populations consume more time and resources, which can deteriorate the performance of the optimisation process. Typical values are between 20 and 200 individuals. The parameters of GA and multi-objective optimisation are the default used by MATLAB.

The number of generations is related to the size of the population and the computational time available for the execution of the algorithm.

Parameters of GA and multi-objective optimisation are the default used by MATLAB and are resumed in TABLE 4.2.

Table 4.2 – Parameters used for GA and Multi-objective optimisation.

Parameter	Value
Population size	50 when number of decision variables <= 5; 200 otherwise
Number of generations	100 x (number of decision variables). 200 x (number of decision variable) for GA multi-objective.
Elite count	0.05 x (Population Size)
Elite function	Gaussian function
Crossover fraction	80%
Pareto fraction	0.60 (only for GA multi-objective)

4.1.4 Constraints

In this work four physical restrictions are imposed:

- $l_l > l_y$ that is, the length of limbs must be higher than the length of yokes.
- $N_{AC} < N_{max}$ that depends on the allowed maximum voltage per turn.
- Minimum core window dimensions in order to accommodate the coils and cryostat.
- $S_{AC} = 0.6 \cdot S_{DC}$ and $S_y = 0.8 \cdot S_{DC}$.

Two electrical restrictions are imposed (peak values):

- $i_{fault} < 50\%$ of $i_{prospective}$, under a fault event, short-circuit current must be lower than 50% of prospective short-circuit current (steady-state).

- $i_{fault\_1^{o}peak} < 75\%$ of $i_{prospective}$, the first peak of the fault current should be lower than 75% of the prospective current in steady-state.
- $\Delta U_{normal} < 5\%$, the voltage drop of the limiter during normal regime must be lower than 5% of the grid voltage.

4.1.5 Penalty Function and Stopping Criteria

If the goal value does not meet the requirements, it needs to be penalized in order to be discarded later. Thus, the value of fitness function takes the penalized value which is calculated by EQUATION (4.1).

$$Penalized_{VALUE} = Max\_Goal_{VALUE} + Goal_{VALUE} \cdot (g_1 + g_2) \quad (4.1)$$

where Max_Goal_{VALUE} is the maximum fitness value obtained during the optimised process, g_1 and g_2 are coefficients associated with the requirements for the SFCL (how higher they are, further away is the SFCL to meet the requirements) and $GOAL_{VALUE}$ is the fitness value obtained in this iteration.

4.1.6 Graphical User Interface

A graphical user interface (GUI) was developed due to the need of giving a friendly way to perform the optimisation process, step by step. FIGURE 4.2 shows the GUI, divided into several steps, as follows:

1. Power Grid Definition: this block allows to define the parameters of the equivalent power grid used for the optimisation process.
2. Constraints: constraints regarding the SFCL voltage drop and current limitation are defined here.
3. Coils Electrical Properties: Electrical properties for AC and DC coils are defined in this block.
4. GA Multi-objective Optimisation: In this block are defined the bound constraints, GA parameters and goals in optimisation. The multi-objective optimisation can be started here.
5. GA Final Optimisation: The single-objective optimisation is started in this block where the point chosen from the previous step is defined as well as the GA parameters.

FIGURE 4.3 (A) shows the GUI window where the stopping criteria are shown as well as the Pareto front for the case of multi-objective optimisation. FIGURE 4.3 (B) shows one of the Pareto front graphs used for the decision process. All points are numbered in order to be defined as the point chosen in the previous step 5.

At the end of the optimisation process is retuned the SFCL dimensions obtained by optimisation.

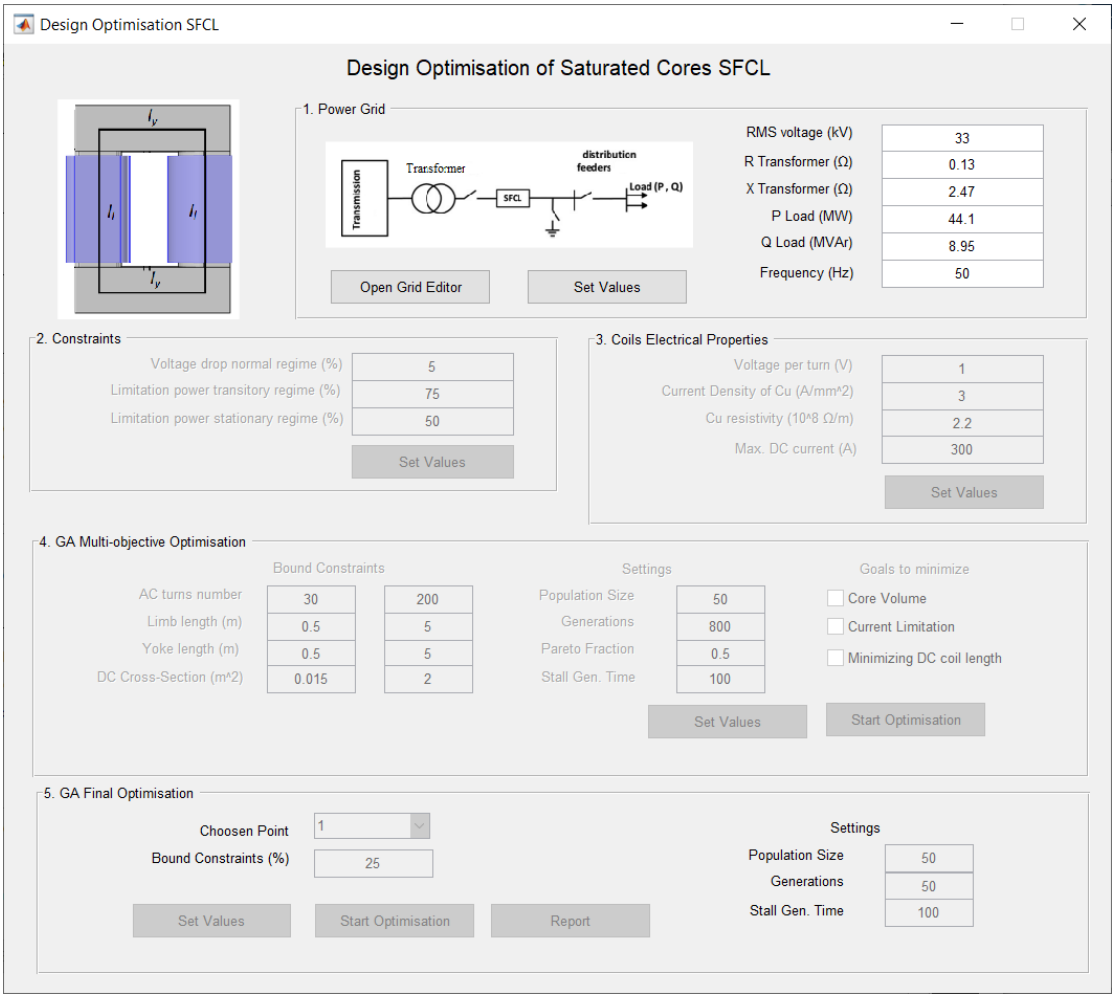

Figure 4.2 – Developed GUI for the optimisation process of the SC-SFCL.

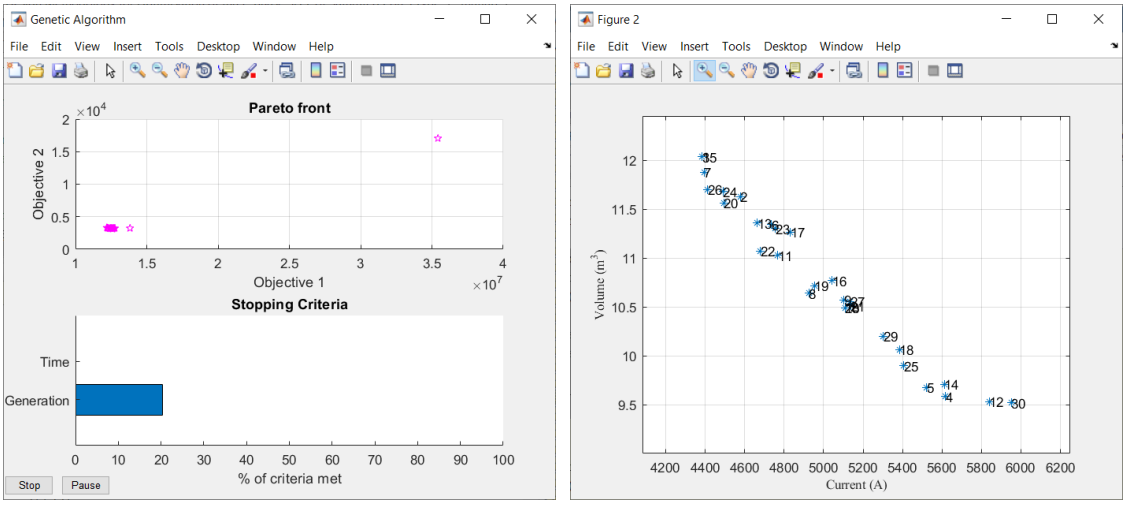

(a) (b)

Figure 4.3 – GUI windows. (a) window where is shown the Pareto front (in the case of multi-objective optimisation) and the stopping criteria. (b) windows where is shown the Pareto front from the multi-objective optimisation.

4.1.7 Optimisation of a Three-phase Saturated Cores Superconducting Fault Current Limiter

To verify the application of this design methodology to model an SC-SFCL for a specific grid, some simulations were carried out.

At first, a multi-objective simulation is carried out in order to relate the different goal with each other. After that, a final optimisation is performed, minimizing the three previous goals simultaneously. In the end, a FEM simulation is carried out for simulating the optimal SFCL and verify if its behaviour during normal and fault operations meets the optimisation criteria and objectives.

4.1.7.1 Optimisation Criteria

Three minimization goals were chosen:

1. Core volume: $S_{DC} \cdot l_l + S_{AC} \cdot l_l + 2 \cdot S_y \cdot l_y$
2. Length of the HTS tape for the DC bias coil: $N_{DC} \cdot 2\pi\sqrt{S_{DC}/\pi}$
3. Maximum limited fault current (peak value).

The optimisation constraints for the optimisation process are shown in CHAPTER 4.1.4.

4.1.7.2 Power Grid Characterisation

The power grid circuit used in simulations is shown in FIGURE 4.4. It should be a generic representation of the real grid to which the SFCL is designed. To simulate the behaviour of the SFCL in a specific three-phase power grid, the simulation methodology described in CHAPTER 3.2 is used.

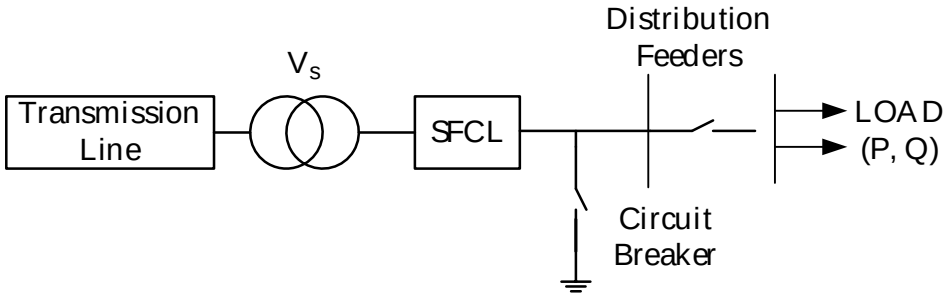

Figure 4.4 - Power grid diagram. It is composed of a voltage source and its impedance, a load impedance, a circuit breaker (phase-earth fault maker) and the SFCL.

TABLE 4.3 shows the parameters of the power grid (FIGURE 4.4).

Table 4.3 – Power grid parameters values.

Parameter	Parameter	Description
V_S	$33\ kV_{rms}$	Voltage source
Z_{Source}	$0.13 + j2.47\Omega$	Source impedance
P_{Load}	$44.10\ MW$	Load Active Power
Q_{load}	$8.95\ MVA_r$	Load Reactive Power
f	$50\ Hz$	Frequency

Analysing the grid, current under normal conditions should be around 1 kA and current under fault conditions (prospective current) should be around 10 kA.

4.1.7.3 Magnetic Core Characterisation

The $B-H$ characteristic for the magnetic cores used in the optimisation process is shown in FIGURE 3.24, in CHAPTER 3.3.1. The $B-H$ curve needs to be parameterised to be used in previous modelling models. Therefore, the $B-H$ curve is parametrised by curve

fitting process by EQUATION (3.11), following the steps described in CHAPTER 3.3.1. The fitted curve shows a good agreement with the original $B-H$ curve where the fitted coefficient are $k_1 = 4.5$, $k_2 = 2.4$ and $k_3 = 50.0$.

4.1.7.4 First-step: Multi-objective Optimisation

A multi-objective simulation was carried out in order to assess each goal in the optimisation and decide for the approximate optimal solution.

For the simulation, a population with 50 individuals was used and the algorithm run along 800 generations or until maximum stall generations of 100 is achieved.

Bound constraints defined for decision variables are as follow:

- $30 < N_{AC} < 200$
- $0.5 < l_l < 5\ (m)$
- $0.5 < l_y < 5\ (m)$
- $0.015 < S_{DC} < 2\ (m^2)$

For the proposed optimisation problem, the best obtained Pareto-front using the reluctance model is decomposed into two 2D planes, which are represented in FIGURE 4.5. FIGURE 4.5 (A) shows the volume of each core versus the maximum limited current under a fault and FIGURE 4.5 (B) relates the volume of each core by the length of the HTS tape for the DC bias coil. Analysing those results, it is possible to confirm that there are no dominant solutions.

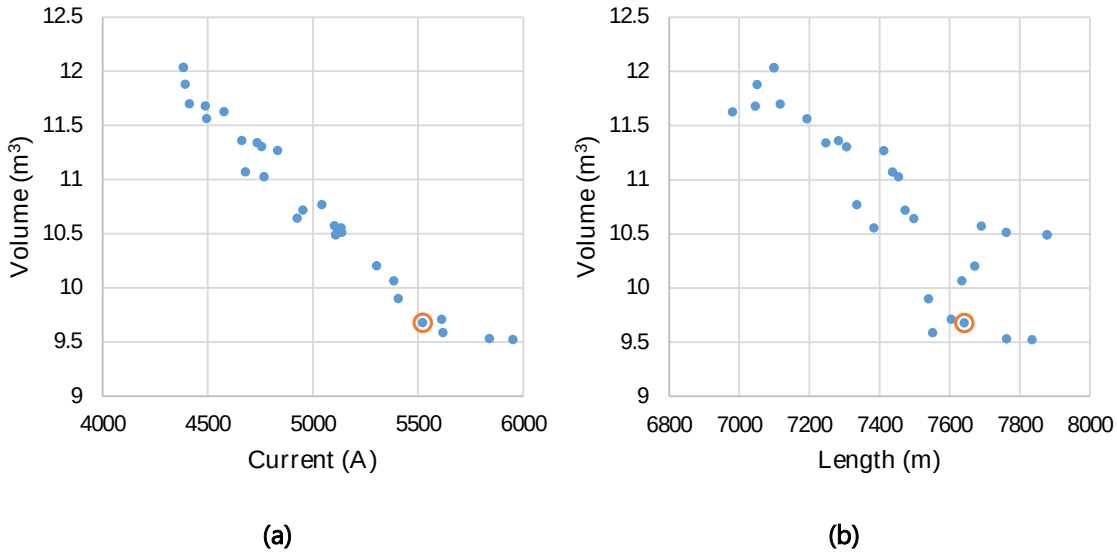

(a) (b)

Figure 4.5 - Pareto-front graphs obtained by the multi-objective optimisation. (a) Volume of each core vs Maximum limited fault current. (b) Volume of each core vs Quantity of HTS tape.

Considering those results, a decision strategy must be applied. Analysing FIGURE 4.5 (A), it was decided to choose the knee point identified by an orange circle, because after this the maximum volume of each core increases significantly. FIGURE 4.5 (B) shows dispersed points but which took a linear distribution. The chosen point minimizes the quantity of DC tape used while assuring a good fault reduction. The optimised point chosen in the decision process takes the values present in TABLE 4.4 (orange circle in previous figures) and the decision variables are shown in TABLE 4.6.

Table 4.4 – The optimised point from the multi-objective simulation.

Maximum limited current	Volume of each core	Quantity of HTS tape
5522 A	9.68 m^3	7640 m

4.1.7.5 Final-Step: Single-objective Optimisation

The last step is to refine the optimal solution found previously, using the FEM model. For this simulation, a population with 50 individuals was used and the algorithm run along 100 generations or until maximum stall generations of 50 is achieved. Bound constraints are defined from the approximate solution, within a range of ±20 % (this value will be changed automatically if the solution is approaching its bounds). The default configuration for genetic algorithm simulation on MATLAB is used. TABLE 4.5 shows the final solution.

Table 4.5 – The optimised point from the single-objective simulation.

Maximum limited current	Volume of each core	Quantity of HTS tape
5110 A	8.59 m^3	73.00 m

4.1.7.6 Optimised Limiter

TABLE 4.6 shows the approximate solution given by GA multi-objective simulation and the final optimal solution.

Table 4.6 – Decision Variables OF the Optimised Solution from The Multi-objective Simulation and Final Simulation.

Decision Variable	Approximate solution	Final Solution
DV 1	69	74
DV 2	3.20 m	3.11 m
DV 3	1.48 m	1.44 m
DV 4	1.29 m^2	1.18 m^2

According to conversion equations in CHAPTER 3.3.2.1, dimensions of each core (in meter) of the optimised SFLC are $W = 2.04$, $H = 3.51$, $T_{AC} = 0.62$, $T_{DC} = 1.04$, $T_y = 0.83$ and $D = 1.04$. The number of turns of DC bias coil is $N_{DC} = 1896$.

FIGURE 4.6 shows the $\psi - i$ characteristic of the limiter, associated with the final optimal solution. When the line current is low, $d\psi/di$ is also low, thus the limiter voltage drop is negligible and the line current is unlimited. When a fault occurs, current enters in high $d\psi/di$ regions, and the high inductive voltage drop at the limiter terminals, limits the fault current.

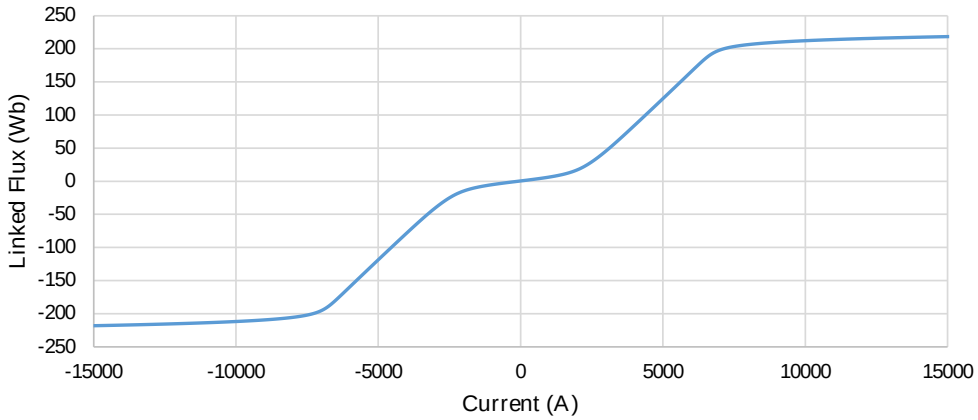

Figure 4.6 - $\psi - i$ characteristic of the optimised SFCL.

4.1.7.7 Evaluation of the Dynamic Behaviour of Optimised Limiter

In order to validate the specifications of the limiter optimised by present methodology, a FEM simulation was carried out. The simulation considered the power grid previously defined. A short-circuit was applied at 0.1 s and simulation run along 0.4 s.

FIGURE 4.7 (A) shows the evolution of line current and FIGURE 4.7 (B) shows the voltage drop of the limiter. As shown in these figures, when a fault occurs the voltage drop of the SFCL increases, and the line current is thus limited.

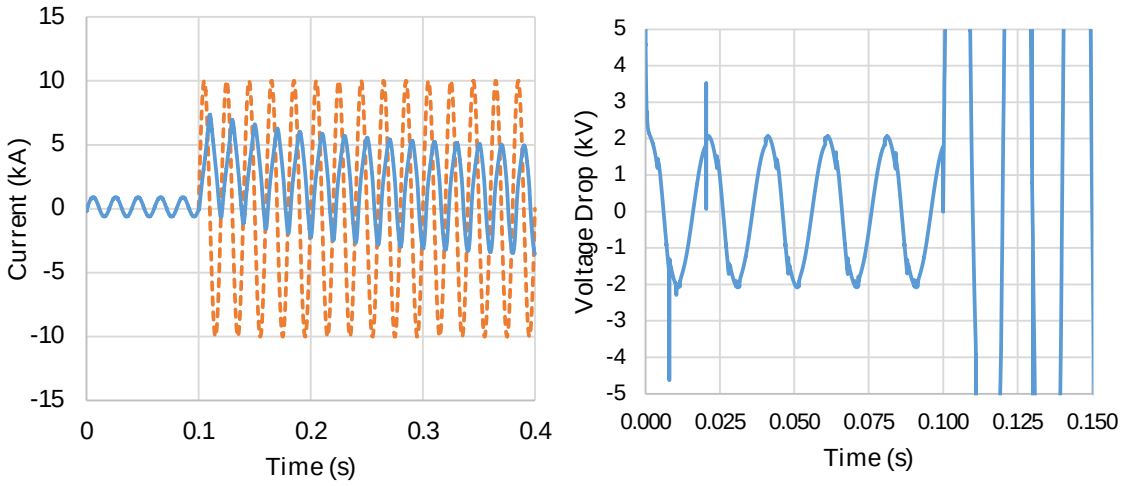

(a) (b)

Figure 4.7 – Line current evolution and SFCL voltage drop under a fault. (a) line current evolution under a fault and the prospective current (dashed curve) as a function of time. (b) SFCL voltage drop at its terminals.

The voltage drop across the SFCL, during the normal regime, is about 2000 V, thus less than 5% of the voltage source. Limited current peak was as about 4.4 kA in the stationary state, a reduction of 56% of the prospective current (10 kA). The optimised SFCL meets the defined requirements for the grid.

4.2 Optimisation of the Design of a Laboratory Scale Three-phase Saturated Cores Superconducting Fault Current Limiter

The proposed optimisation methodology is used to optimise a three-phase SC-SFCL for a laboratory-scale power grid. FIGURE 4.8 shows the topology of the device which is set to be assembled. It is composed of three single-phase topologies, placed side by side in a hexagonal configuration, where the HTS bias coil embraces all inner limb cores.

The aim of building this prototype is to validate the optimisation tool, testing the limiter to check if it meets the defined requirements, as well as to build an SFCL prototype.

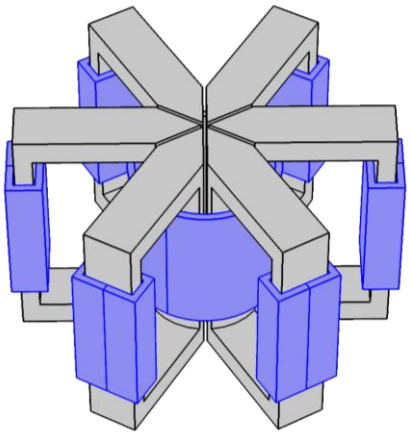

Figure 4.8 – Topology of the three-phase SFCL. AC coils are represented in blue and placed in the outer limbs. DC coil is represented in blue and embraces the inner limbs of the cores.

4.2.1 Optimisation Criteria

The goals chosen for optimisation are the following:

1. Core volume:

   To minimize the core volume.

   $Volume = S_{DC} \cdot l_l + S_{AC} \cdot l_l + 2 \cdot S_y \cdot l_y$

2. Length of the HTS tape for the DC bias coil:

   To minimize the HTS tape material used.

   $Length = N_{DC} \cdot 2\pi\sqrt{S_{DC}/\pi}$

3. Maximum limited fault current.

   With the aim of maximizing the limitation power of the device.

Also, the optimisation constraints for the optimisation process are described in CHAPTER 4.1.4, which remain the same. The applied DC bias current is 285 A (5% less than the critical current of the superconducting tape to be used in the prototype).

4.2.2 Power Grid Characterisation

The laboratory-scale SFCL is built with the aim to be installed in a low voltage three-phase laboratory-scale power grid, shown in FIGURE 4.9. The power source is considered ideal and the load is balanced. The faults are caused by closing the respective switch S_1 to S_5, depending on the type of fault. In TABLE 4.7 is depicted the parameter values of the power grid.

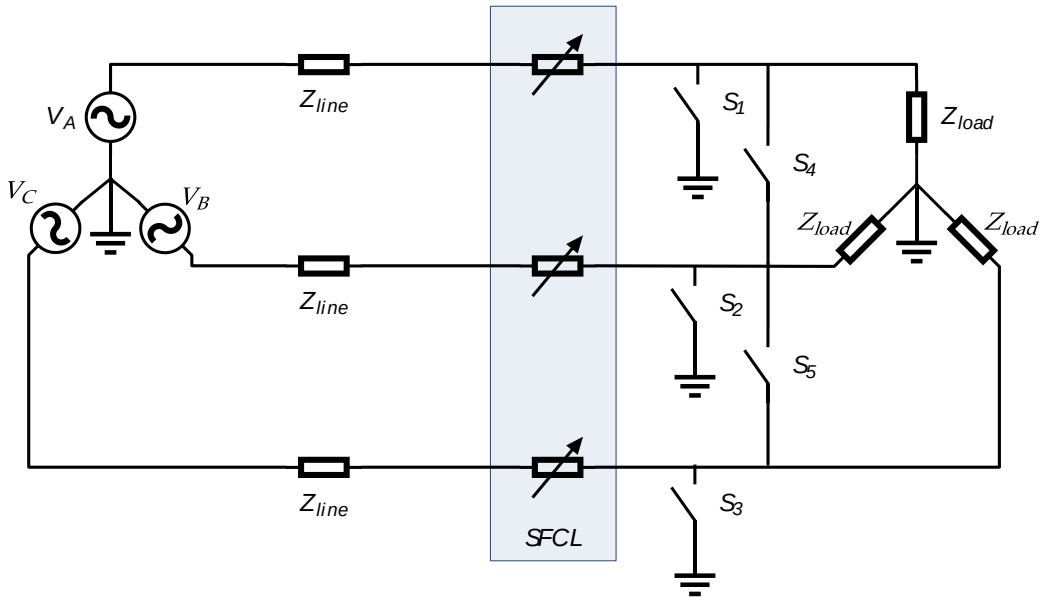

Figure 4.9 – Laboratory scale power grid.

Table 4.7 – Power grid parameters values.

Parameter	Parameter	Description
V_{LL}	$400\ kV_{rms}$	Voltage source
Z_{Line}	$1.2\ \Omega$	Source and Line impedance
P_{Load}	$3.17\ kW$	Load Active Power
Q_{load}	$0\ VA_r$	Load Reactive Power
f	$50\ Hz$	Frequency

4.2.2.1 Prospective Fault Currents

To analyse the prospective fault current of the most common types of faults, some simulations were carried out in MATLAB/SIMULINK for three types of faults and depicted in TABLE 4.8. As can be seen, for the laboratory grid and considering the voltage source as ideal, the maximum prospective current is 272 A.

Table 4.8 – Amplitude of prospective fault currents of each fault type.

Type of fault	Prospective fault current
Phase-to-earth fault	270 A
Phase-to-phase fault	235A
Three-phase-to-earth fault	272A

4.2.3 Magnetic Core Characterisation

The electrical steel material used for the optimisation process, as well as to manufacture the SFCL prototype, is a non-oriented grain steel material with 0.5 mm of thickness, whose properties are depicted in TABLE 4.9.

Table 4.9 – Characterization of the electrical steel material used for the magnetic cores.

Property	Value
Reference	M 330-50 A Steel material Non-oriented grain
Thickness (mm)	0.5
Indicative Max loss (W/Kg)	1.35 at 50 Hz at 1T
Guaranteed Min polarisation (T)	1.49 at 2500 A/m 1.60 at 5000 A/m
Density (Kg/m^3)	7850

The $B-H$ characteristic of the steel material was measured by an Epstein frame device, which is shown in FIGURE 4.10. The $B-H$ curve needs to be parameterised in order to be used in previous modelling models. Therefore, the original $B-H$ curve is parametrised by curve fitting process through EQUATION (3.11), following the steps described in chapter 3.3.1, which is also depicted in FIGURE 4.10. As can be seen, the fitted curve shows a good agreement with the original $B-H$ curve where the fitted coefficient are $k_1 = 1$, $k_2 = 2.6$ and $k_3 = 150$.

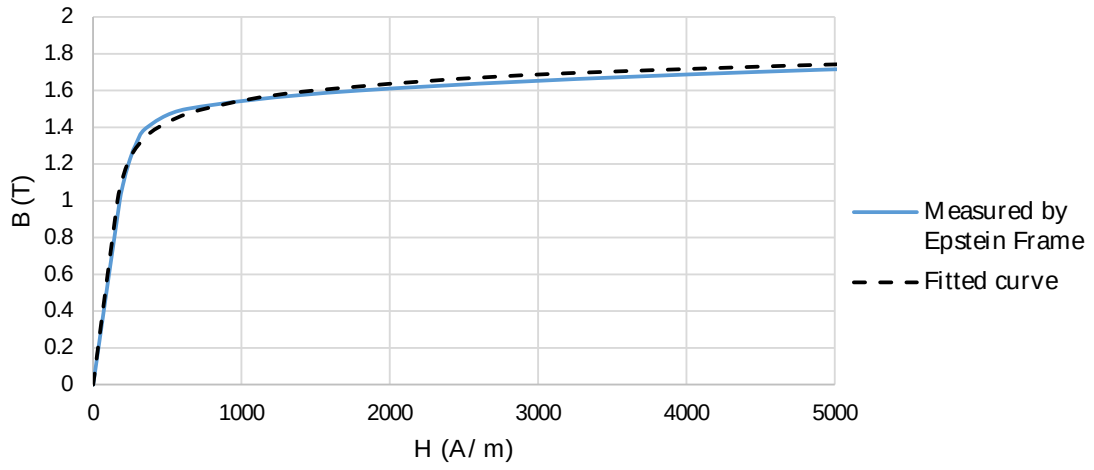

Figure 4.10 – $B-H$ curve of the magnetic material used in the SFCL cores.

4.2.4 Multi-objective Decision Process for Approximate Optimal Solution

The first step of the optimisation process is to carry out a multi-objective optimisation in order to decide which optimised point is preferable.

For the simulation, a population with 50 individuals was used and the algorithm run along 800 generations or until maximum stall generations of 100 is achieved.

Bound constraints defined for decision variables are as follow:

- $100 < N_{AC} < 200$
- $0.01 < l_l < 0.5\ (m)$
- $0.01 < l_y < 0.5\ (m)$
- $0.001 < S_{DC} < 0.01\ (m^2)$

FIGURE 4.11 and FIGURE 4.12 show the Pareto-front obtained by the multi-objective optimisation. Considering the results, the chosen optimised point was identified by the red arrow because it represents the minimisation of the three goals in optimisation.

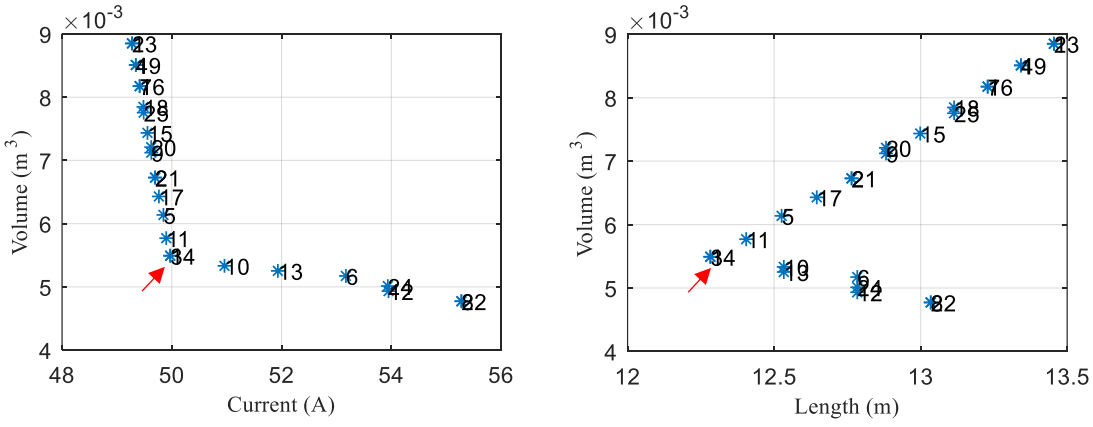

(a) (b)

Figure 4.11 – Pareto-front graph from multi-objective optimisation. (a) Volume of each core vs fault current limitation. (b) Volume of each core vs Quantity of HTS tape.

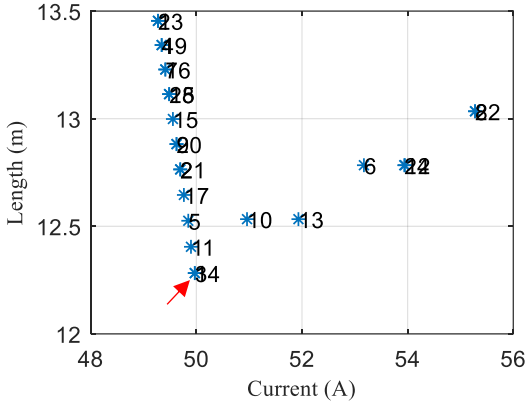

Figure 4.12 - Pareto-front graph from multi-objective optimisation: Quantity of HTS tape vs fault current limitation.

The optimisation process was terminated by the average change in the spread of Pareto solutions less than the defined tolerance. The number of generations was 116. The optimised point chosen in the decision process takes the values present in TABLE 4.10 (orange circle in previous figures) and the decision variables are shown in TABLE 4.12.

Table 4.10 – The optimised point from the multi-objective simulation.

Maximum limited current	Volume of each core	Quantity of HTS tape
49.90 A	0.00549 m^3	12.30 m

4.2.5 Final Optimal Solution

The last step is to refine the optimal solution chosen in the decision process in the multi-objective optimisation process, using the FEM model. For this simulation, a population with 50 individuals was used and the algorithm runs along 100 generations or until maximum stall generations of 50 is achieved. Bound constraints are defined from the approximate solution, within a range of ±5 % (this value will be changed automatically if the solution is approaching its bounds). Default configuration for genetic algorithm simulation on MATLAB is used. TABLE 4.11 shows the final solution.

Table 4.11 – The optimised point from the single-objective simulation.

Maximum limited current	Volume of each core	Quantity of HTS tape
48.19 A	0.0048 m^3	12.03 m

4.2.6 Optimised Limiter

The final design SFCL, particularly optimised for the laboratory test grid previously presented, is achieved by the proposed methodology. TABLE 4.12 shows the approximate solution given by GA multi-objective simulation and the final optimal solution.

Table 4.12 – Decision Variables of the Optimised Solution from The Multi-objective Simulation and Final Simulation (listed in TABLE 4.1).

Decision Variable	Approximate solution	Final Solution
DV 1	197	206
DV 2	0.34 m	0.34 m
DV 3	0.29 m	0.28 m
DV 4	0.0050 m^2	0.0048 m^2

According to conversion equations in CHAPTER 3.3.2.1, dimensions of each core (in meter) of the optimised SFLC are $W = 0.335$, $H = 0.395$, $T_{AC} = 0.042$, $T_{DC} = 0.069$, $T_y = 0.055$ and $D = 0.069$. The number of turns of DC bias coil is $N_{DC} = 49$ for an applied DC bias current of $I_{DC} = 285$. The copper wire of the AC coils has a cross-section of 2 mm^2 and $R_{FCL} = 0.01\ \Omega$.

4.2.6.1 Validation of the Optimal Limiter Design by FEM

The previous optimal SC-SFCL design is simulated by FEM in order to prove compliance with the imposed restrictions. FIGURE 4.13 shows the FCL implemented in FEM software meeting the previous dimensions of the optimal design.

A phase-to-earth fault on phase A was caused at 0.05 s. FIGURE 4.14 shows the voltage drop of the SFCL in normal regime and fault regime. As can be seen, the voltage drop is less than 5% of the voltage source, in normal regime, meeting the requirement for this parameter. FIGURE 4.15 shows the fault current behaviour where the faulty phase is limited to 82% of the prospective fault current, once again, the requirement is fulfilled. FIGURE 4.16 (A) shows the linked flux as a function of time and FIGURE 4.16 (B) shows the $\Psi - i$ excursion of the SFCL which can be seen that the limiter does not achieve the reverse saturation zone, during the fault limitation.

For this optimisation design, all requirements have been met, limiting efficiently the fault current and not affecting healthy phases.

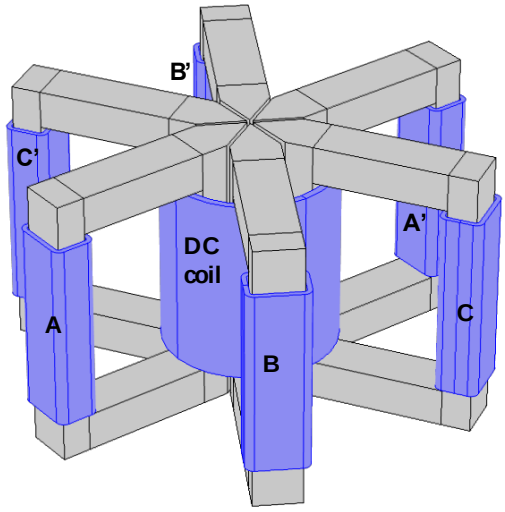

Figure 4.13 – FEM implementation of the optimal SC-SFCL design. It is shown the pair coils of each phase A, B and C, as well as the DC bias coil involving the inner limbs of each core.

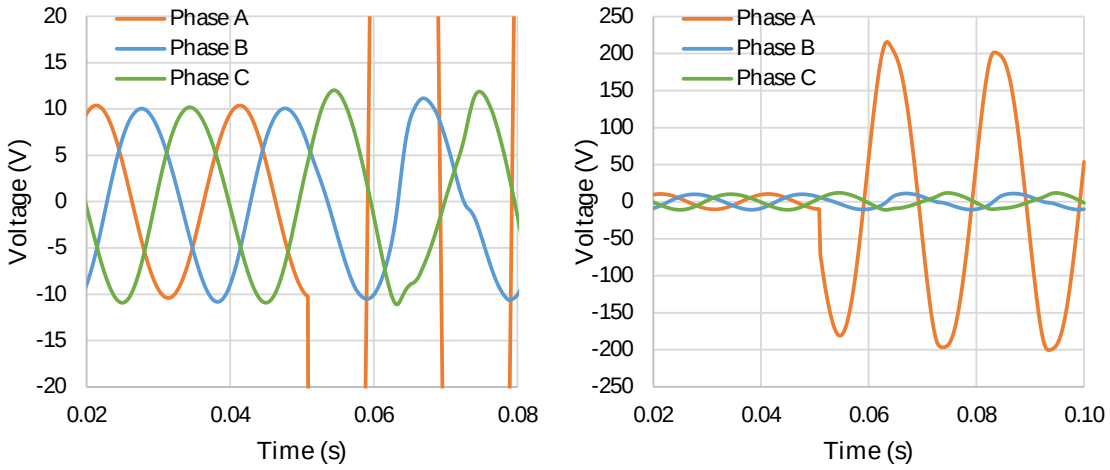

(a) (b)

Figure 4.14 – Drop voltage of the SFCL as a function of time, of each phase, under a phase-to-earth fault in phase A. (a) Voltage drop in detail, during normal regime. (b) Voltage drop of the SFCL, under a fault

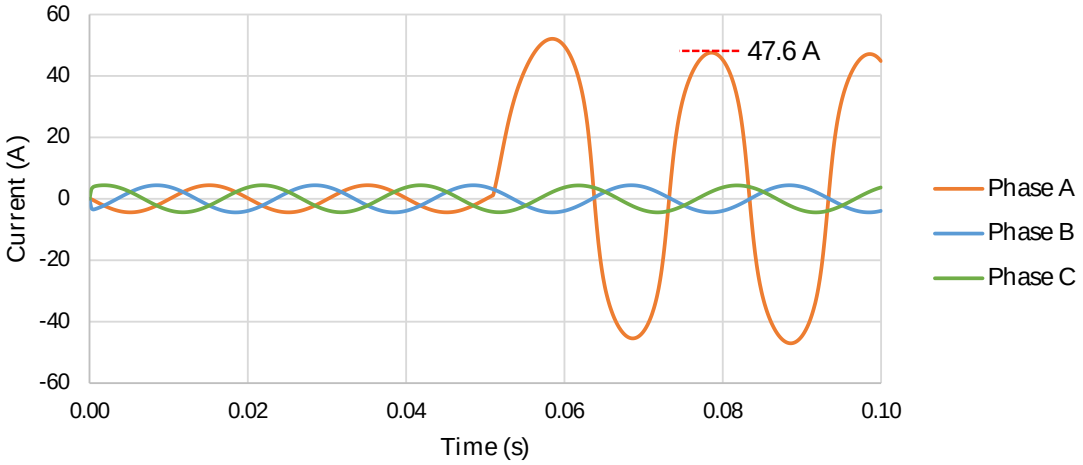

Figure 4.15 - Line currents under a phase-to-earth fault in phase A as function of time.

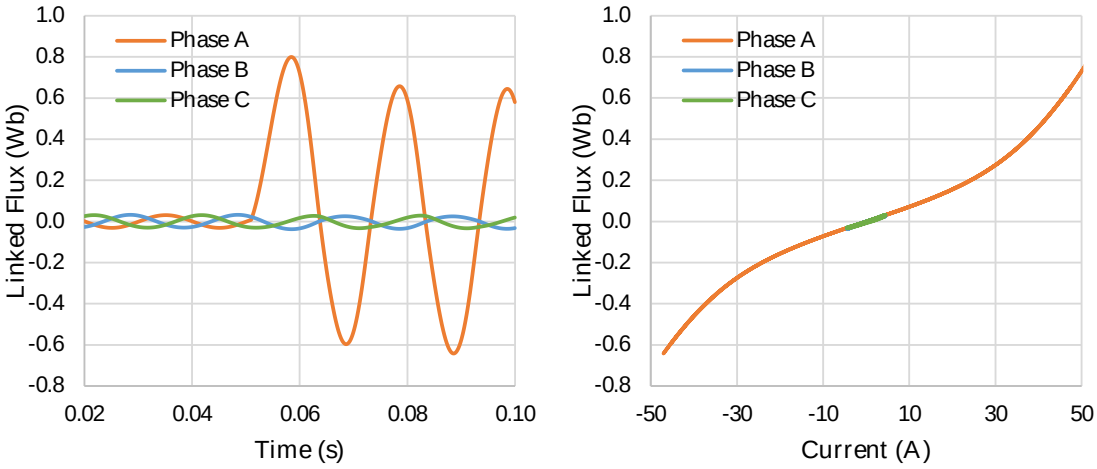

(a) **(b)**

Figure 4.16 - Linked flux of each phase, as a function of time, under a phase-to-earth fault condition. (a) Linked flux as a function of time. (b) $\Psi - i$ excursion of each phase.

4.3 Assembly and Testing of the Laboratory Scale Saturated Cores Superconducting Fault Current Limiter

In CHAPTER 4.2 was optimised the design of the SC-SFCL to be built which its optimal dimensions and electrical characteristics are depicted in CHAPTER 4.2.6.

However, due to the need to use pre-existing magnetic cores, it was not possible to ensure that they had the optimised dimensions. Therefore, a new optimised process was done where only the number of turns of AC and DC coils were optimised, keeping the core dimensions fixed and ensuring all constraints described before.

FIGURE 4.17 shows the dimensions of the pre-existing cores. The cross-section of each limb and yokes are $S_{DC} = 0.002965$ m^2, $S_{AC} = 0.001820$ m^2 and $S_{yoke} = 0.002450$ m^2 respectively.

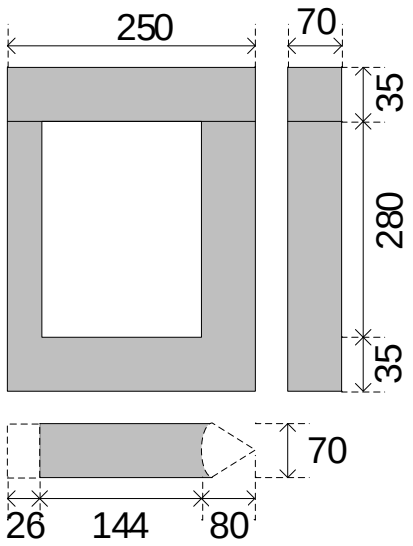

Figure 4.17 – Dimensions of each magnetic core (in millimetres)

TABLE 4.13 shows the decision variable of the optimal solution founded, according to conversion equations in CHAPTER 3.3.2.1, due to the fact the dimensions of the cores are fixed. The number of turns of the DC bias coil is $N_{DC} = 42$ for an applied DC bias current of $I_{DC} = 285$. The copper wire of the AC coils has a cross-section of 2 mm^2 and $R_{FCL} = 0.008\ \Omega$.

Table 4.13 – Decision Variables of the Optimised Solution from the final optimisation process (listed in TABLE 4.1).

Decision Variable	Optimal Solution
DV 1	150
DV 2	0.325 m
DV 3	0.206 m
DV 4	0.002965 m^2

FIGURE 4.18 shows the $\psi - i$ characteristic of the limiter, associated with the optimal solution.

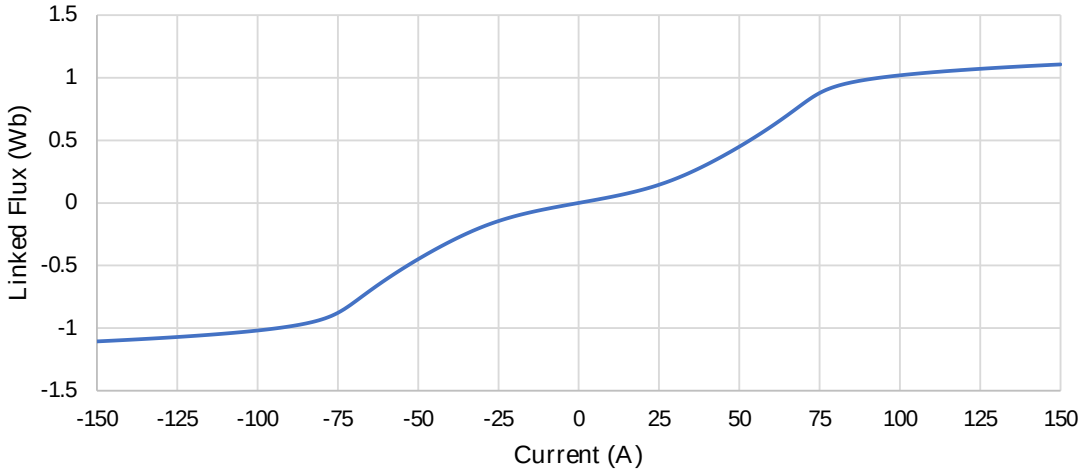

Figure 4.18 - $\psi - i$ characteristic of the optimised SC-SFCL.

4.3.1 Validation of the Optimal Limiter Design by FEM

The optimised SC-SFCL design is simulated by FEM to prove compliance with the imposed restrictions. FIGURE 4.13 shows the SFCL implemented in FEM software meeting the previous dimensions of the optimal design.

A phase-to-earth fault on phase A was caused at 0.05 s. The voltage drop of the SFCL is shown in FIGURE 4.22 where can be seen that the voltage drop is less than the 5% of the power source. FIGURE 4.20 shows the line current evolution under fault conditions where can be seen that the fault current was limited in 70%. In FIGURE 4.21 is shown the linked flux of the limiter as well as its $\Psi - i$ excursion. As can be seen, during fault regime, the limitation capability of the SFCL is ensured.

For this optimisation design, all requirements have been met, limiting efficiently the fault current and not affecting healthy phases.

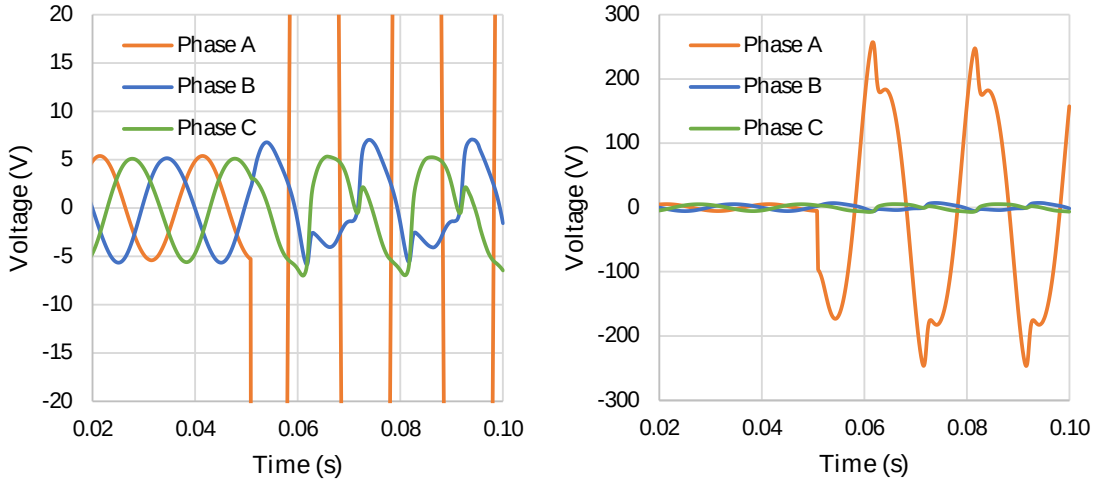

(a) (b)

Figure 4.19 – Drop voltage of the SFCL as a function of time, of each phase, under a phase-to-earth fault in phase A. (a) Voltage drop in detail, during normal regime. (b) Voltage drop of the SFCL, under a fault.

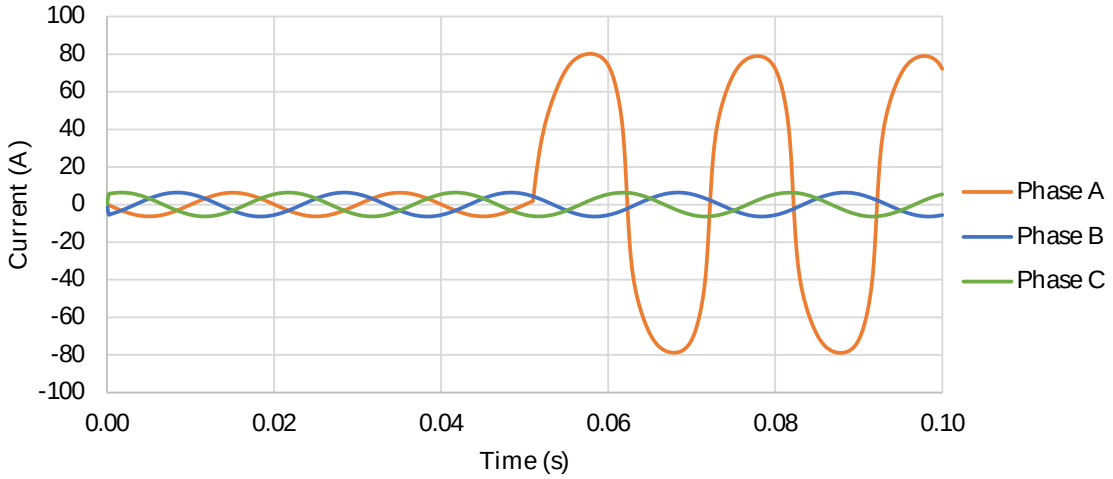

Figure 4.20 - Line currents under a phase-to-earth fault in phase A as function of time.

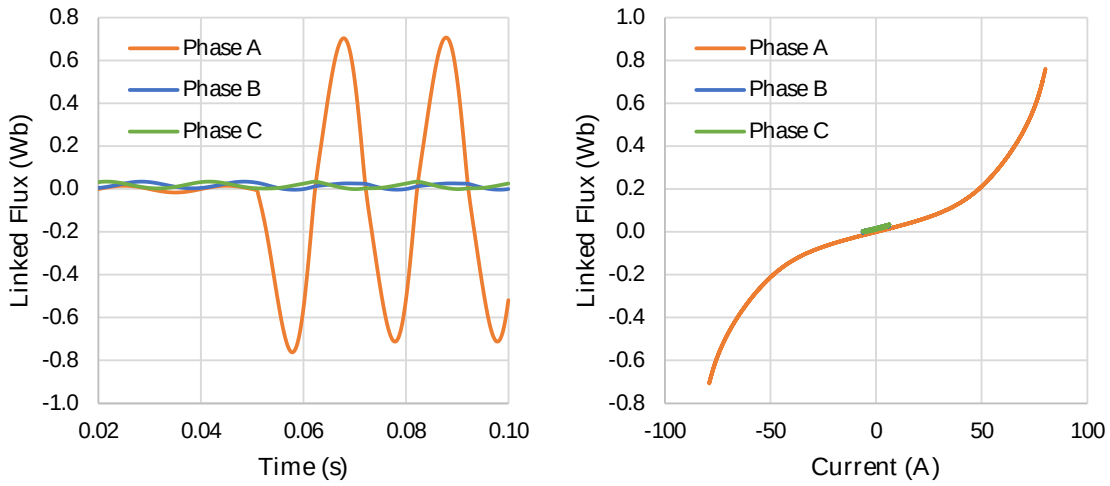

(a) (b)

Figure 4.21 - Linked flux of each phase, as a function of time, under a phase-to-earth fault condition. (a) Linked flux as a function of time. (b) $\Psi - i$ excursion of each phase.

4.3.2 Magnetic Cores

FIGURE 4.22 shows the magnetic cores used to assembly the SC-SFCL. The magnetic characteristics of the cores were described in CHAPTER 4.2.3. As said before, the cores are placed in a hexagonal form, symmetrically distributed, as can be seen in FIGURE 4.22 (B).

(a) (b)

Figure 4.22 – Magnetic cores used to assembly the SC-SFCL. (a) Magnetic cores assembled in a hexagonal format. (b) Top view of the SC-SFCL.

4.3.3 Coils

The SC-SFCL is composed of 6 conventional AC coils, connected in pairs to each phase of the three-phase power grid. These coils are made of copper and their characteristics are depicted in TABLE 4.14. The coils have two separate windings, the power winding, connected to the power line, and an auxiliary winding used to measure the linked flux with the main winding.

The DC bias coil is made of superconducting tape and embraces the inner limbs of all magnetic cores. Its characteristic is depicted in TABLE 4.15. FIGURE 4.23 shows the built DC coil in its support made of G11 material.

Table 4.14 – Characteristics of each AC coil.

Parameter	
Turns of each coil number	150
Turns of the auxiliary winding	100
Height of the coil (mm)	200
Length x width (mm)	74 x 28
Cross-section of the copper wire (mm^2)	2.5

Table 4.15 – Characteristics of DC coil.

Parameter	
Turns of the coil	42 turns in 4 layers
Height of the coil (mm)	200
Diameter (mm)	183
Conductor material	2nd generation HTS tape from SuperOx Ref.: 12-30Ag-05Cu-60H-PI Critical current: 300 A at 77 K Width: 12 mm
Support material	G11

Figure 4.23 – DC bias coil and its support made of G11 material.

4.3.4 Final Assembly

The SC-SFCL is assembled in a hexagonal configuration, as can be seen in FIGURE 4.25. The cryostat for the DC coil was manufactured in stainless steel and is shown in FIGURE 4.24.

(a) (b)

Figure 4.24 – Cryostat made of stainless steel. (a) Cryostat inserted into the inner limbs. (b) The cryostat.

Figure 4.25 – Final assembly of the SC-SFCL.

4.3.5 Data Acquisition System

The NI-6210 data acquisition (DAQ) board (FIGURE 4.26) is used to acquire all needed signals from the SC-SFCL prototype, which are line currents, linked fluxes, SFCL voltage drops and power source voltages. This board also allows digital control for the switches used to simulate the faults. The board has 4 digital output and 4 digital input channels, and 16 analogue input channels (16 bits, 250 kS/s).

Figure 4.26 – NI USB-6210

The previous signals are measured through LEM transducers, which are based on the hall effect, except the linked flux which is measured directly by the DAQ board after a conditioning circuit that integrates the signal from auxiliary winding, with a time constant of 1 s.

Table 4.16 – Sensors used in the prototype to measure the signals.

To measure	Sensor
Power source voltage	LEM LV-25P in range [-400 , 400] V
SFCL voltage drop	LEM LV-25P in range [-267, 267] V
Line current	LEM LA 100-P/SP13 in range [-122 , 122] A
DC bias current	LEM LF-305 S in range [0 , 357] A

4.3.6 Evaluation of the Dynamic Behaviour of the Optimised Limiter

The built three-phase SC-SFCL was tested under short-circuited conditions in order to analyse its behaviour. Three types of faults were tested, which are the phase-to-earth fault, the phase-to-phase fault, and the three-phase-to-earth fault. For each test was analysed the SFCL behaviour in normal operation and operation under a fault.

The SC-SFCL was installed in a laboratory-scale power grid described in CHAPTER 4.2.2. The faults were caused by closing the right combination of switches S_1 to S_5. The switches were activated remotely by the control system which applied a fault with a 500 ms of duration. Due to limitations of the DC power source, the DC bias current was limited to 200 A instead of the 285 A initially defined.

The test apparatus is shown in FIGURE 4.27.

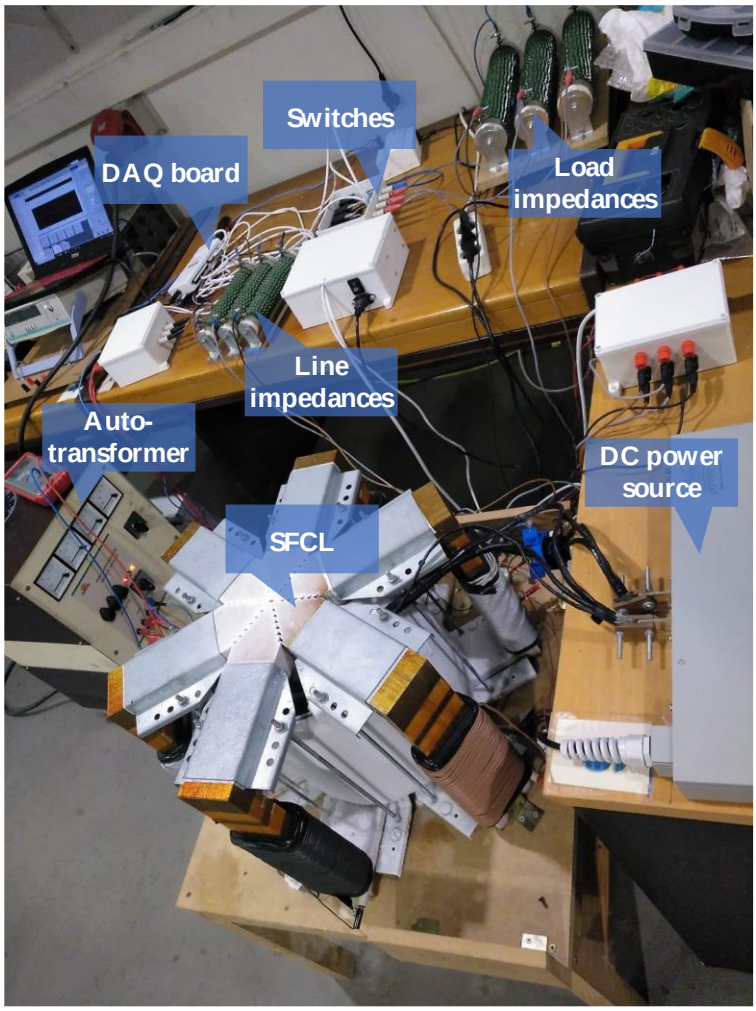

Figure 4.27 – Laboratory apparatus during tests.

4.3.6.1 Phase-to-Earth Fault

Switch S_2 (FIGURE 4.9) is closed to cause a phase-to-earth fault in phase B. Following, line current of each phase, voltage source and voltage drop of the limiter and the $\Psi - i$ excursion are analysed.

A. Line Current Analysis

FIGURE 4.28 shows the line current evolution as a function of time, of each phase and FIGURE 4.29 shows the line current of the heathy phases in detail. In normal regime the line current is sinusoidal with a value of 6 A for each phase. In fault conditions, from $t = 4.5$ s approximately, the fault current is limited to 65 A which represents a fault reduction of 76% of the prospective fault current. The healthy phases are not affected by the fault, therefore slight asymmetries can be observed, probably caused by imbalances at the source, as these already occur under normal conditions.

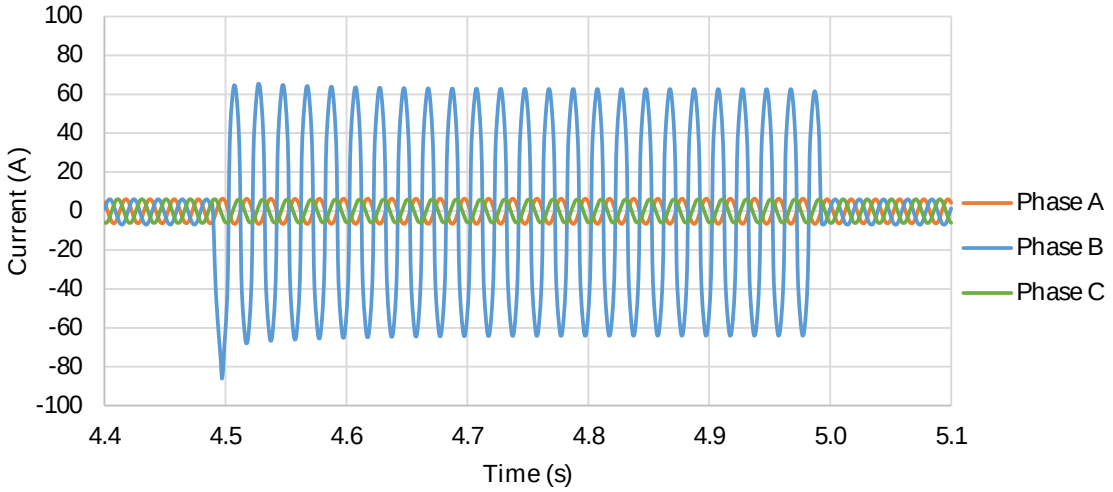

Figure 4.28- Line currents under a phase-to-earth fault in phase B as a function of time.

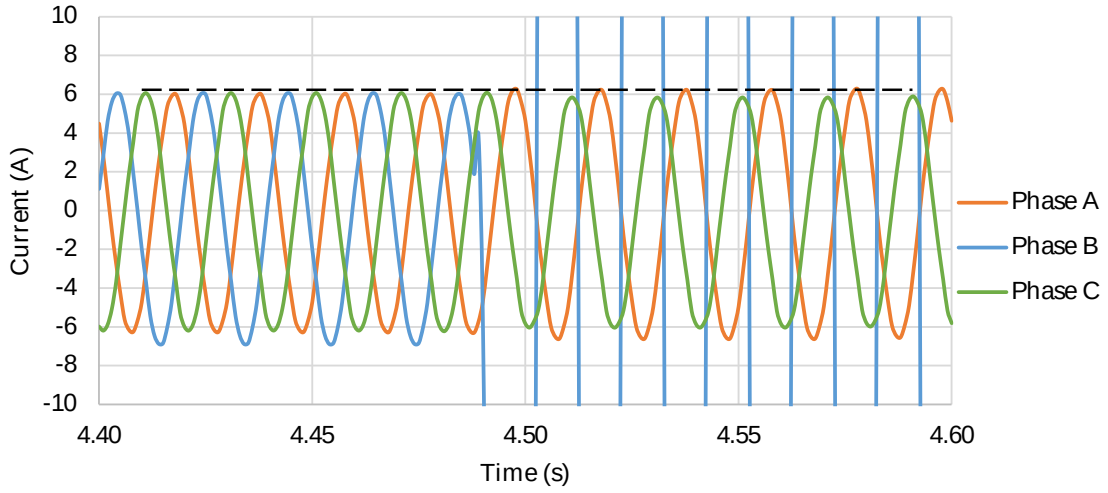

Figure 4.29 - Line currents under a phase-to-earth fault in phase B as a function of time, in detailed for healthy phases.

FIGURE 4.30 shows the line currents under a phase-to-earth fault in phase B, simulated by FEM. As can be seen, in normal regime the current is around 6 A, according to the laboratory results. In fault conditions, the fault current was similarly limited for both results, to around 60 A.

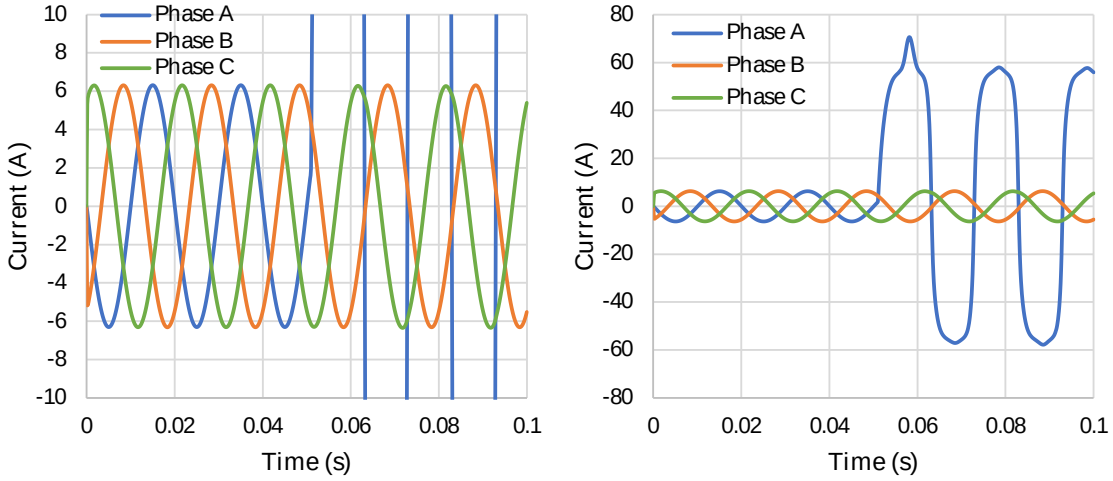

(a) (b)

Figure 4.30 – Line current under a phase-to-earth fault in phase B as a function of time, by FEM simulation. (a) normal regime. (b) fault regime.

B. Linked Flux Analysis

FIGURE 4.31 (A) shows the linked flux associated with each phase coil under fault conditions as a function of time. As can be seen, the magnetic flux, in healthy phases, does not increase its amplitude, which means the healthy phases does not suffer from the faulted phase. FIGURE 4.31 (B) shows the $\Psi - i$ excursion of each phase. As can be seen, under fault condition, the full limitation capability is assured due to the fact the limiter does not achieve the saturation zone, when in fault regime.

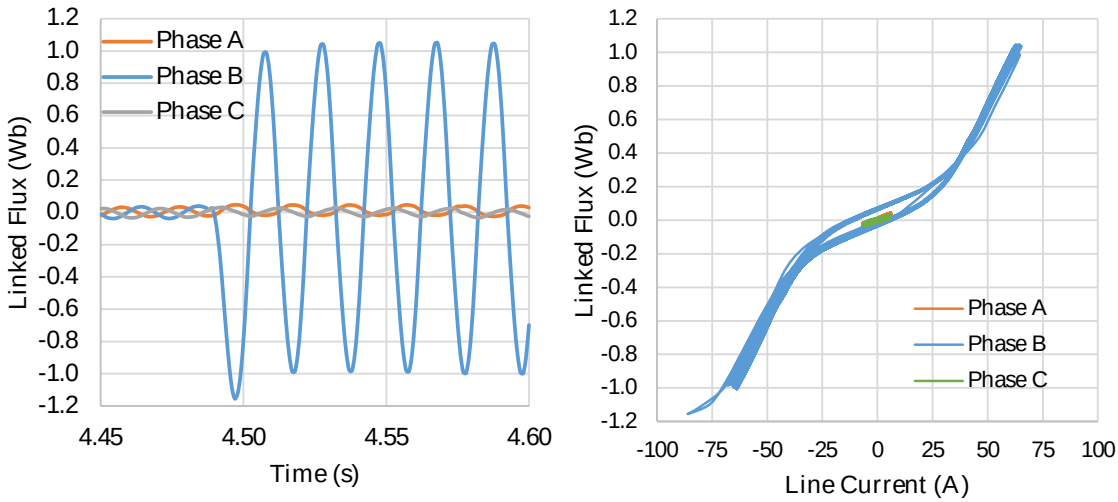

(a) (b)

Figure 4.31 – Linked flux of each phase, as a function of time, under a phase-to-earth fault condition. (a) Linked flux as a function of time. (b) $\Psi - i$ excursion of each phase.

In FIGURE 4.32 is depicted the $\Psi - i$ excursion of the SC-SFCL, for phase B, by experimental test and simulated by FEM, the last step of the optimisation methodology. As can be seen, both curves show good agreement.

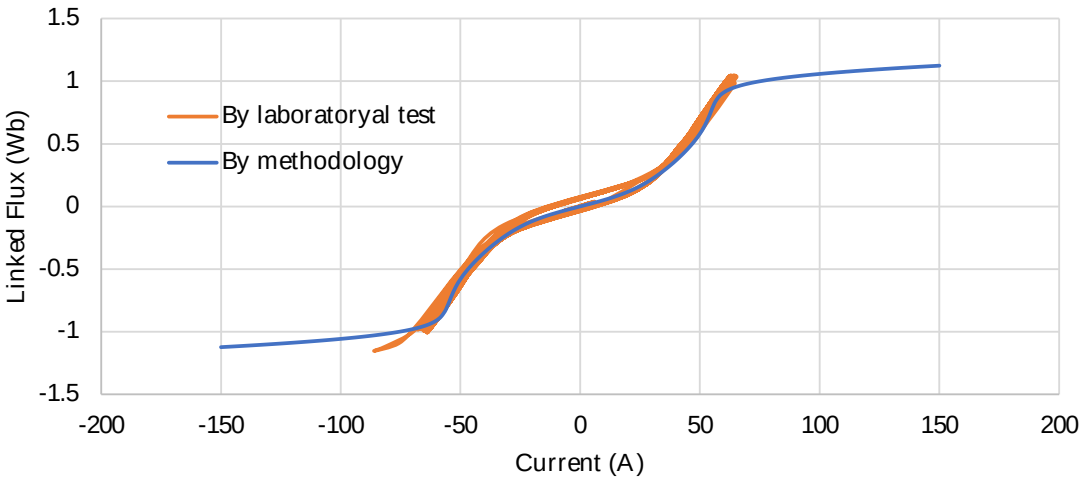

Figure 4.32 - $\Psi - i$ excursion of affected phase B, by real test and methodology.

C. DC Bias Current Analysis

FIGURE 4.33 shows the DC bias current applied to the HTS bias coil. As can be seen, the current ripple in normal operation is high, about 20 A of peak-to-peak amplitude, which is about 15% of the nominal bias current. This is due to the fact the cores are not properly saturated. Note that the bias current should be 290 A instead of the 200 A applied. Recovery time is approximately 150 ms (green zone).

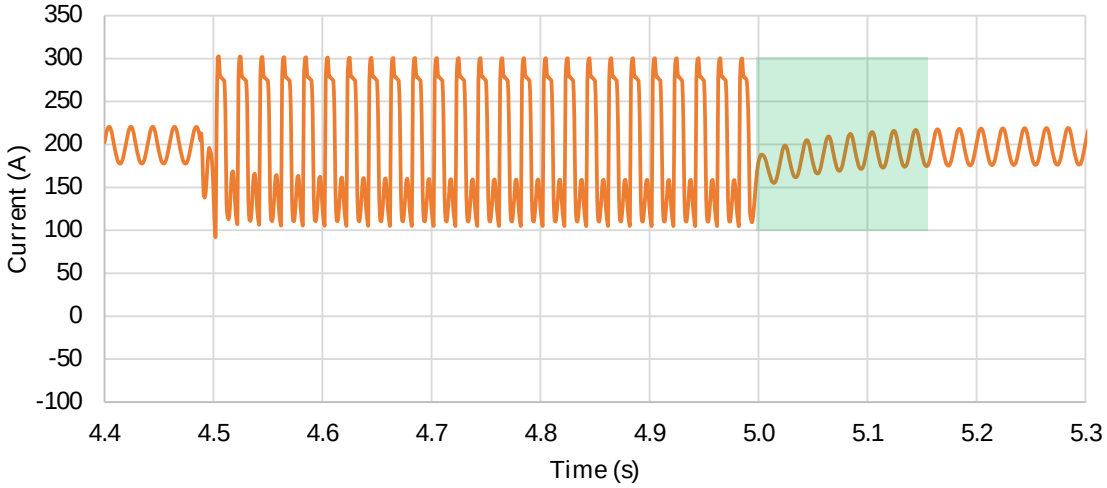

Figure 4.33 – DC bias current as a function of the time, under a phase-to-earth fault condition.

D. Voltages Analysis

In FIGURE 4.34 is show the voltage of the power source. As can be seen, in normal regime, the voltage of each phase is balanced, however when the fault occurs, the voltage of the faulted phase decrease by 7%. The healthy phases also experience a change in voltage. The voltage of phase C decreases by 4% approximately and voltage of phase A increases 2% approximately.

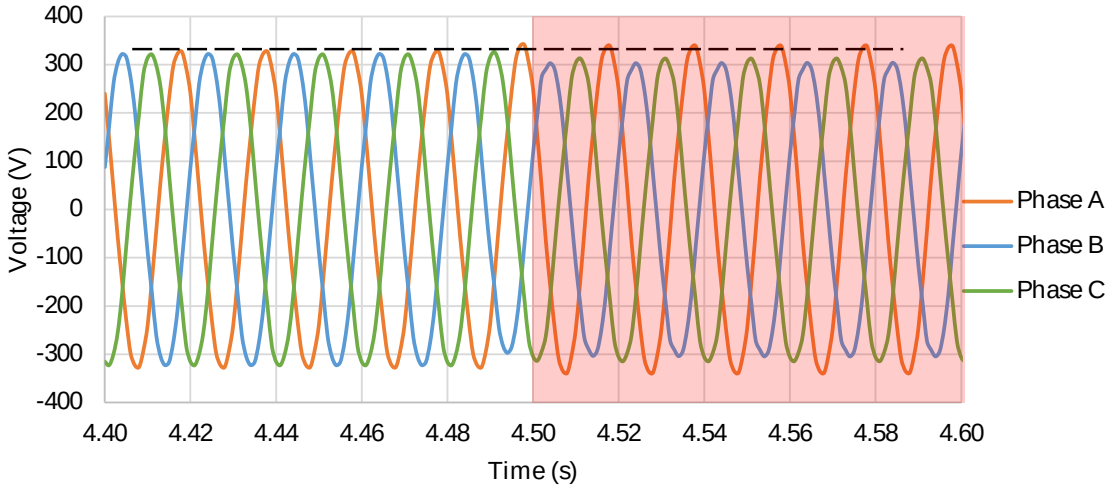

Figure 4.34 – Voltage of the power source for each phase, under a phase-to-earth fault condition.

FIGURE 4.35 shows the voltage drop of the SC-SFCL. During normal regime, the voltage drop is less than 10 V, which means 3% of the power source voltage. In fault regime, 76 % of the power source voltage drops in the SFCL, assuring an effective fault current limitation.

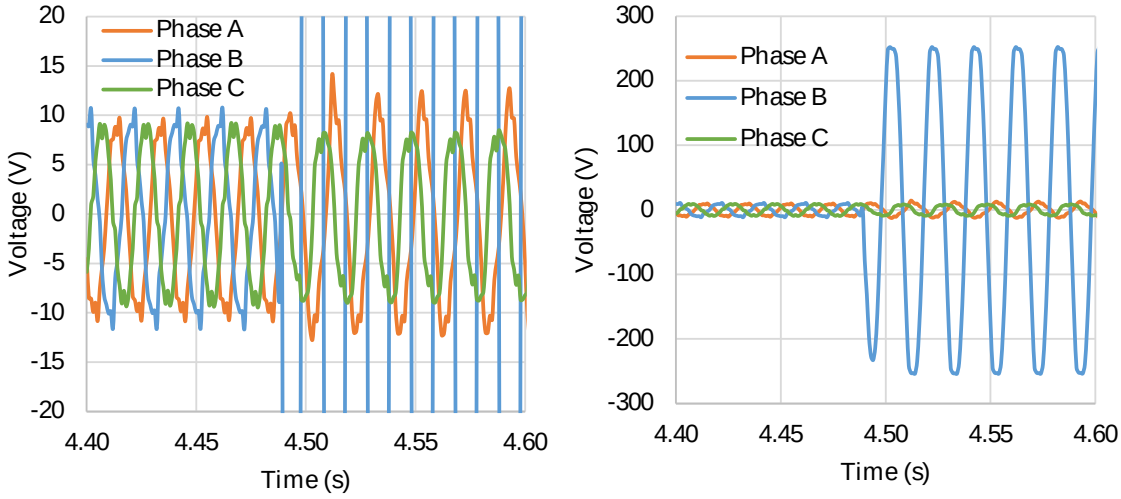

(a) (b)

Figure 4.35 – Voltage drop of the SC-SFCL as a function of time, of each phase, under a phase-to-earth fault condition. (a) Voltage drop in detail, during normal regime. (b) Voltage drop of the SFCL, under a fault.

4.3.6.2 Phase-to-Phase Fault

Switch S_5 is closed to cause a phase-to-phase fault between phase B and C. Following, line current of each phase, voltage source and voltage drop of the limiter and the $\Psi - i$ excursion are analysed.

A. Line Current Analysis

FIGURE 4.36 (A) shows the line current evolution as a function of time, for each phase and FIGURE 4.36 (B) shows the line current of the heathy phases in detail. In normal regime, the line current shows the same waveform for phase-to-earth fault, which is expectable. In fault conditions, from $t = 3.6$ s approximately, the fault current is limited to 72 A for phase B and to 69 A for phase C, which represents a fault reduction of 70% of the prospective fault current. The healthy phase A is not affected by the fault.

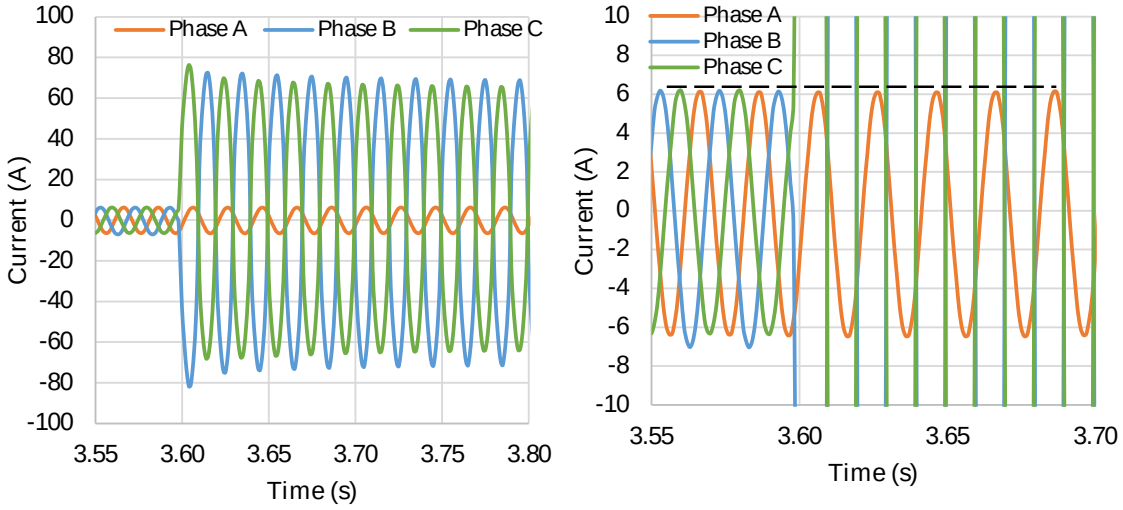

(a) (b)

Figure 4.36 - Line currents under a phase-to-phase fault between phase B and C. (a) Line currents as a function of time. (a) Line currents as a function of time.

B. Linked Flux Analysis

FIGURE 4.37 (A) shows the linked flux associated with each phase coil under fault condition as a function of time. The magnetic flux in healthy phase A does not increase

its amplitude, which means it does not suffer from the faulted phases. FIGURE 4.37 (B) shows the $\Psi - i$ excursion of each phase. Phase B is more affected by the fault phase C, which means there is some asymmetry either in the power grid or in the limiter (probably the number of turns of AC coils are not equal).

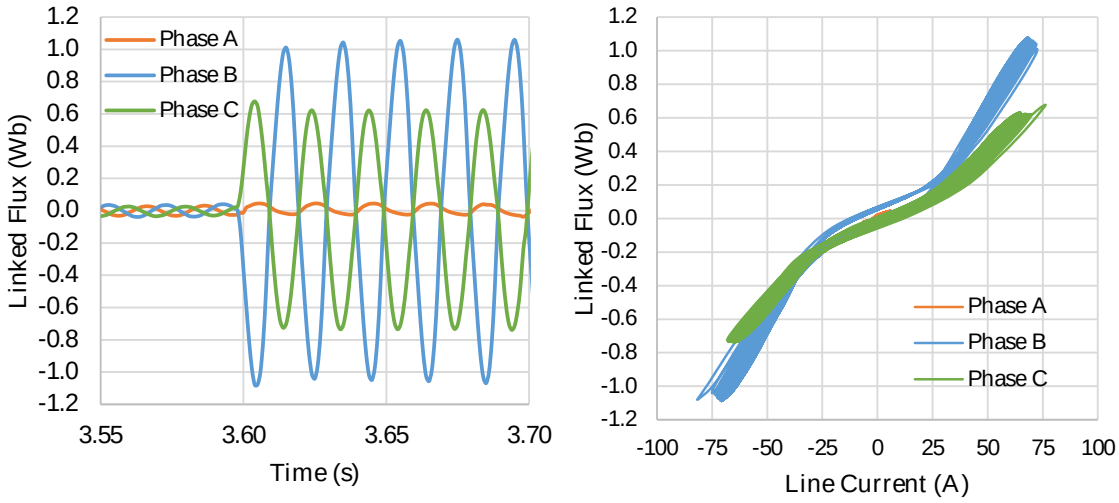

(a) (b)

Figure 4.37 - Linked flux of each phase, as a function of time, under a phase-to-earth fault condition. (a) Linked flux as a function of time. (b) $\Psi - i$ excursion of each phase.

C. DC Bias Current Analysis

FIGURE 4.38 shows the DC bias current applied to the HTS bias coil. As can be seen, the current ripple in normal operation shows the same waveform as in phase-to-earth fault. Recovery time is approximately 200 ms.

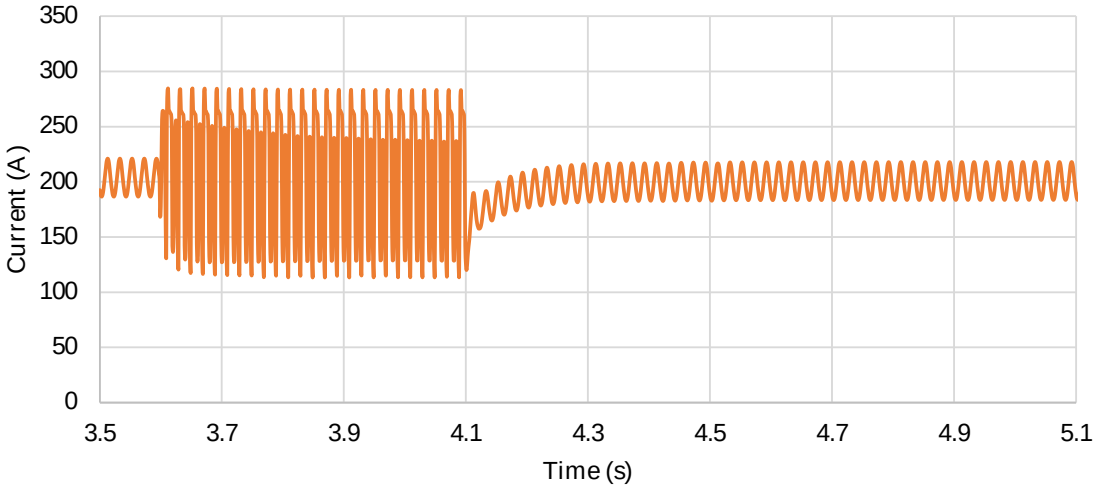

Figure 4.38 - DC bias current as a function of the time, under a phase-to-phase fault condition.

D. Voltages Analysis

In FIGURE 4.39 is show the voltage of the power source. As can be seen, in fault regime the voltage of the healthy phase does not suffer any attenuation. However, the faulty phases experience a slight variation.

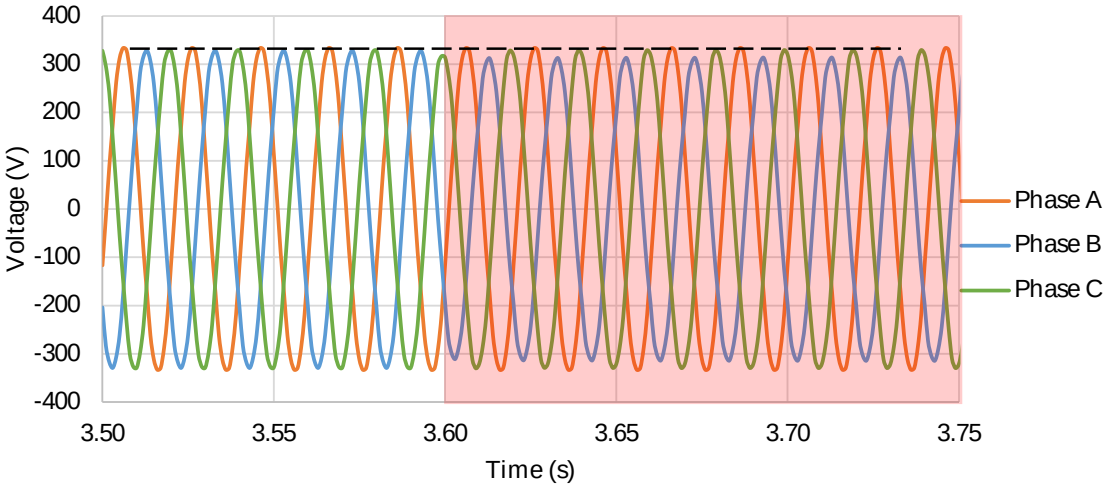

Figure 4.39 - Voltage of the power source for each phase, under a phase-to-phase fault condition

FIGURE 4.40 shows the voltage drop of the SC-SFCL. During normal regime, the voltage drop is approximately 3% of the power source voltage. In fault regime, 75% of the power source voltage drops in the SFCL, assuring an effective fault current limitation.

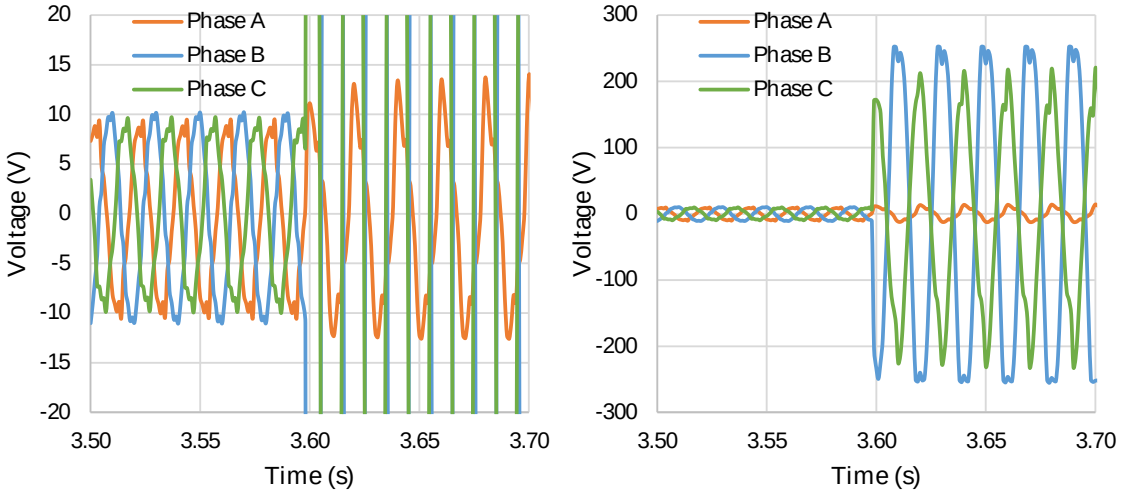

(a) (b)

Figure 4.40 - Voltage drop of the SC-SFCL as a function of time, of each phase, under a phase-to-phase fault condition. (a) Voltage drop in detail, during normal regime. (b) Voltage drop of the SFCL, under a fault.

4.3.6.3 Three-Phase-to-Earth-Fault

Switches S_1, S_4 and S_5 are closed to cause a three-phase-to-earth fault. Following, the line current of each phase, voltage source and voltage drop of the limiter and the psi-I excursion are analysed.

A. Line Current Analysis

FIGURE 4.41 shows the line current evolution as a function of the time, of each phase. In fault conditions, from $t = 7.24$ s approximately, the fault current is limited to 60 A in stationary regime, which represents a fault reduction of 78% of the prospective fault current. The waveform of each phase looks symmetrical during the fault, ensuring a symmetric fault reduction.

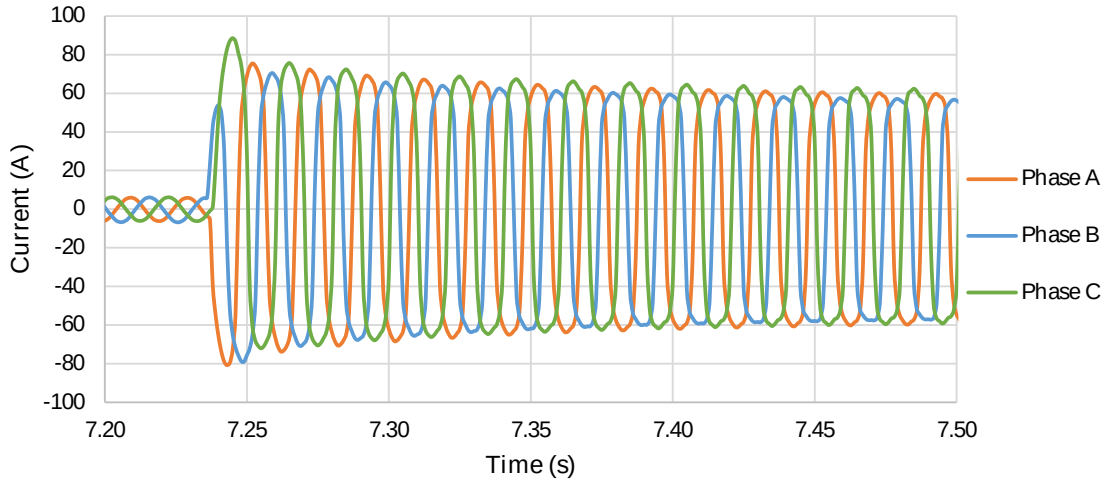

Figure 4.41 - Line currents under a three-phase-to-earth fault, as a function of time.

B. Linked Flux Analysis

FIGURE 4.42 (A) shows the linked flux associated with each phase coil under fault condition as a function of time and FIGURE 4.42 (B) shows the $\Psi - i$ excursion of each phase. As can be seen, under fault condition, the full limitation capability is assured due to the fact the limiter does not achieve the saturation. The $\Psi - i$ characteristic of each phase is similar, but phase C achieve a lower maximum linked flux, showing the same behaviour of previous faults.

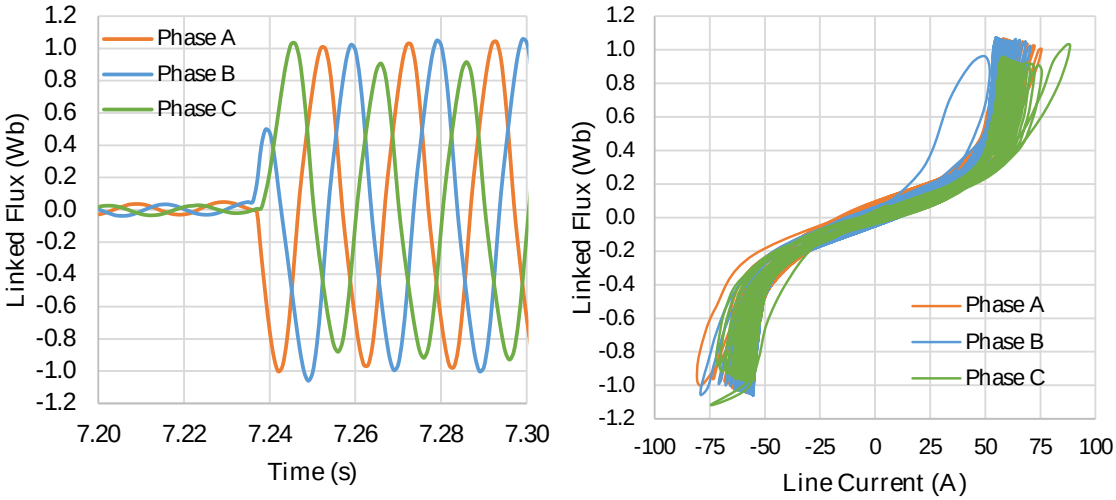

Figure 4.42 - Linked flux of each phase, as a function of time, under a three-phase-to-earth fault condition. a) Linked flux as a function of time. (b) $\Psi - i$ excursion of each phase.

C. DC Bias current Analysis

FIGURE 4.43 shows the DC bias current applied to the HTS bias coil. The current behaviour is the same as previous faults. Recovery time is approximately 250 ms.

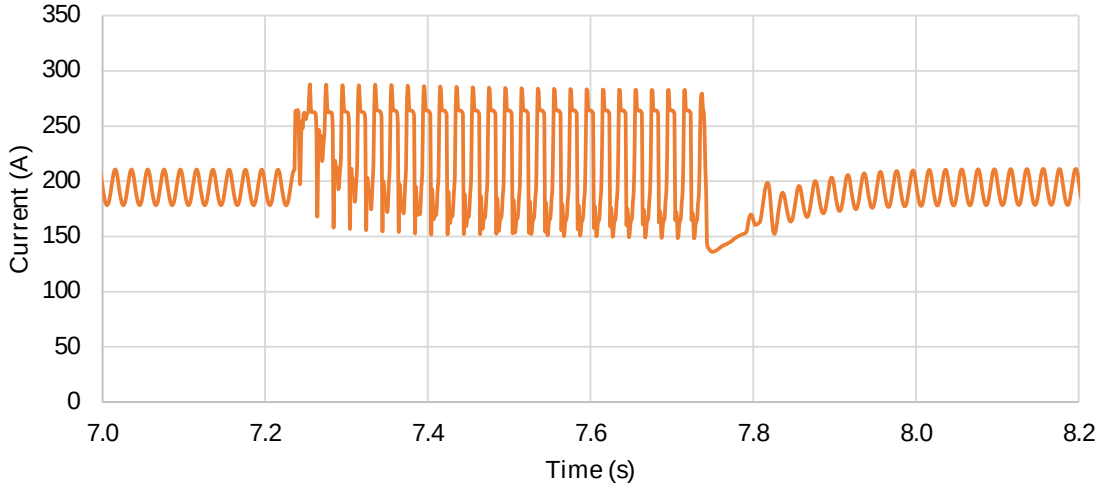

Figure 4.43 - DC bias current as a function of the time, under a three-phase-to-earth fault condition

D. Voltages Analysis

In FIGURE 4.44 is show the voltage of the power source. As can be seen, in fault conditions the voltage of each phase decrease by 7.8%.

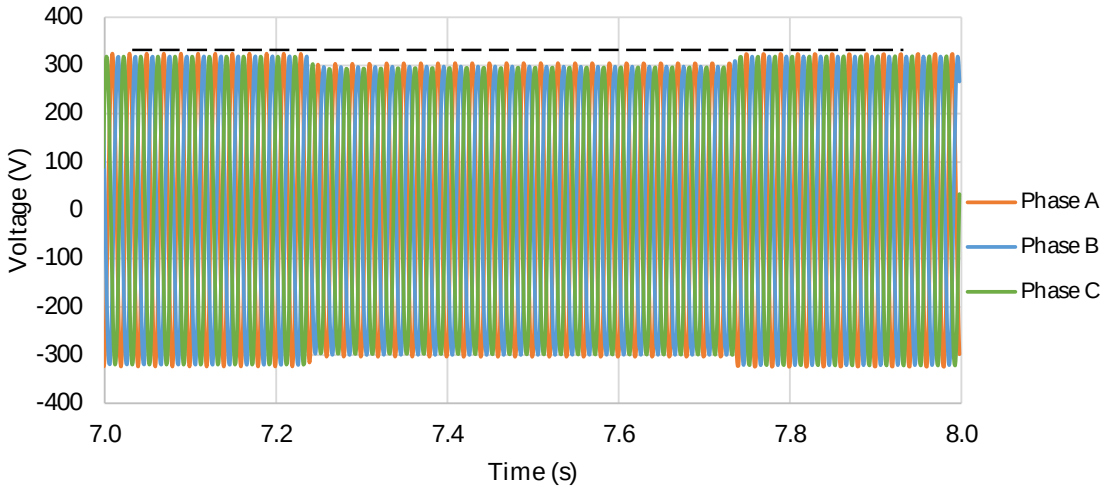

Figure 4.44 - Voltage of the power source for each phase, under a three-phase-to-earth fault condition.

FIGURE 4.45 shows the voltage drop of the SC-SFCL. In fault regime, 76% of the power source voltage drops in the SFCL, assuring an effective fault current limitation for each phase.

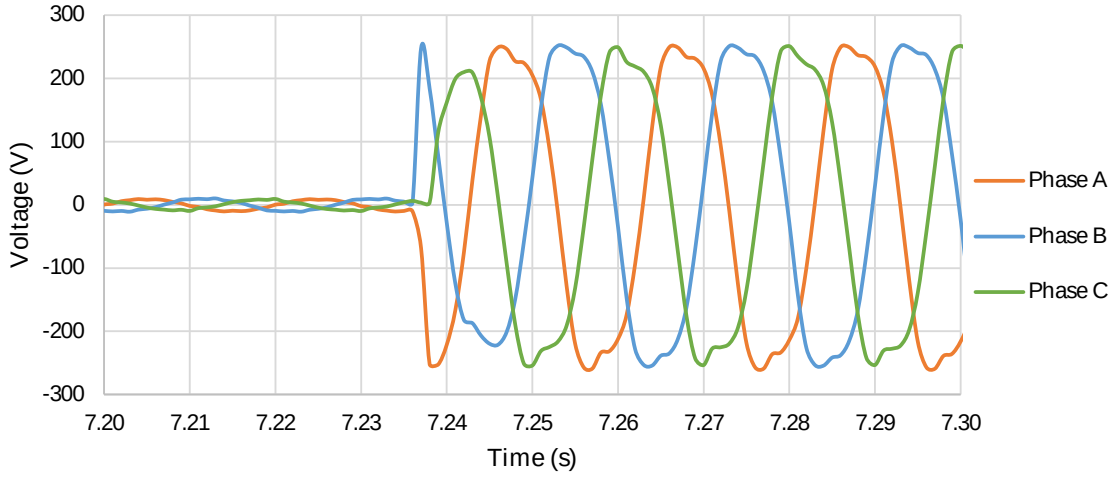

Figure 4.45 - Voltage drop of the SC-SFCL as a function of time, of each phase, under a three-phase-to-earth fault condition.

4.3.6.4 $\Psi - i$ Excursion for Different DC Bias Current Values

The appropriated magnetisation of the magnetic cores is essential for an effective fault current limitation. FIGURE 4.46 shows the $\Psi - i$ excursion of the limiter under tests for different DC bias current values. As can be seen, the SFCL begins limiting the fault current to around 30 A for all curves. However, the limitation capability varies with the DC bias current applied. The slope of the curve, in the limitation zone, decreases inversely with the DC bias current, which means a reduction in the limitation capability of the limiter. In TABLE 4.17 is depicted the fault current reduction for each DC bias current applied to the limiter which is also shown in FIGURE 4.47. As can be seen, there is a linear relationship between the fault current limitation of the SFCL and its applied DC bias current. Of course, this relation is not linear for all DC bias current values due to the fact the SFCL do not assure a 100% fault current limitation. This curve is only valid for the interval where the saturation of the cores is assured.

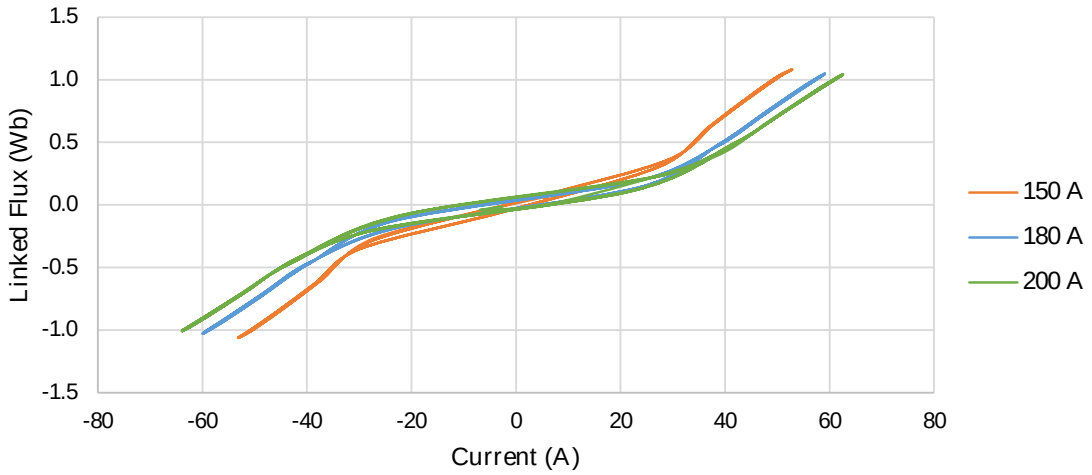

Figure 4.46 – $\Psi - i$ excursion for different DC bias current values.

Table 4.17 – Fault limitation for different DC bias current values.

DC bias current	Fault Limitation
150 A_{DC}	53 A (80.4 %)
180 A_{DC}	59 A (78.1 %)
200 A_{DC}	63 A (76.7 %)

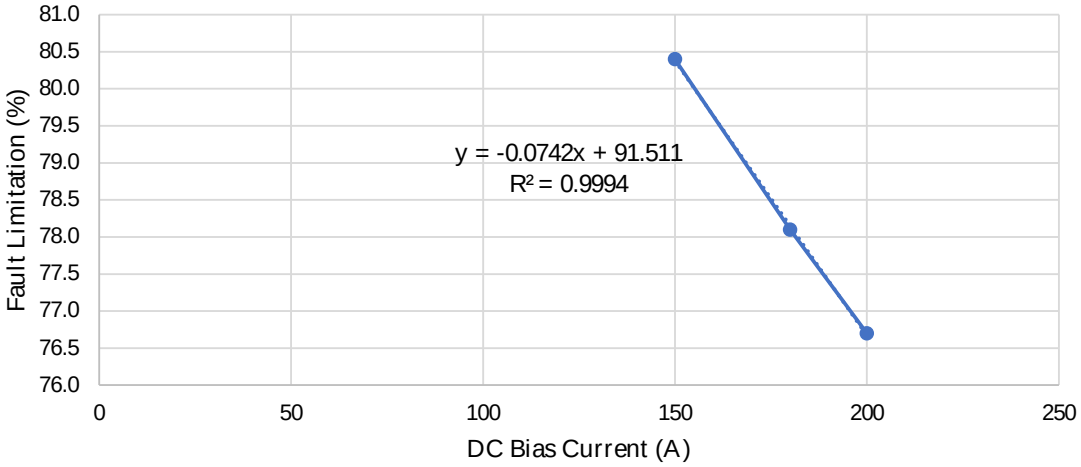

Figure 4.47 – Relation between the fault current limitation and the applied DC bias current.

4.4 Summary

A design methodology to optimise an SC-SFCL for a specific electrical grid was presented in this chapter. It uses genetic algorithms to find the optimal solutions of the SFCL design.

The optimisation process is performed in two stages:

1. Using reluctance model during the first stage, in a multi-objective solution, has the advantage of achieving a swift approximated solution for the problem (after the decision process from Pareto front).
2. The last stage is to find the final solution by FEM simulations, which is faster in this stage due to the fact that the searching interval is concentrated around the solution found in stage 1 and is more accurate.

The SC-SFCL optimised by this methodology meets the restrictions imposed for the prospective fault current and voltage drop during normal regime.

A laboratory prototype of a SC-SFCL was optimised considering a laboratory-scale power grid, and built. However, due to the fact, the magnetic cores have already been manufactured and due to power limitation of the DC power source, which cannot supply the desired DC bias current, the built prototype does not meet the optimal design obtained in CHAPTER 4.2. Therefore, a new optimisation process was done taking into account the pre-existent magnetic cores, optimising only the coils of the device.

Several laboratory tests were carried out to analyse the performance and behaviour of the optimised SC-SFCL. For the three types of faults tested, the SFCL has limited the fault current effectively. In normal regime, the voltage drop of the limiter is negligible. The results from a phase-to-earth fault, in phase B, by laboratory test and by FEM simulation was compared in order to check the agreement between the FEM model used in the optimisation process and real tests. Both results show good agreement. The relation between the DC bias current and the limitation capability was also analysed, which conclude that there is a linear relation between them.

5

Transformer Type Superconducting Fault Current Limiter: Analysis of the Electromechanical Forces Developed Under Faults

During fault conditions, the line current can increase up to several times higher than its rated value, therefore SFCL windings can experience substantial forces. The consequences of these forces can be the destruction of windings, particularly if these are made of HTS material, which is less mechanically robust than copper windings. To ensure the integrity of HTS windings, the mechanical design must be carefully defined in order to avoid the permanent deformations of windings or fracture from resulting stresses *(Soika et al., 2007)*.

Stress tests performed on YBCO tape have shown that the tape has excellent mechanical resistance due to its axial strength, therefore maintaining superconducting performance under these types of forces *(Osamura et al., 2010)*.

The effects of transverse stresses on the performance of the YBCO tape has been studied showing that the critical current of YBCO tapes degrades significantly under transverse stress before delamination, causing low delamination strength of less than 15 MPa *(Laan et al., 2007; Takao et al., 2007)*.

Since tape joints are crucial to superconducting power applications, YBCO tape lap joints submitted to mechanical stresses have also been tested showing good results for their strength and electrical resistance *(Duckworth et al., 2010)*.

In this chapter, the analysis of electromechanical forces developed in the inductive TT-SFCL under such extreme conditions is performed, based on finite elements method (FEM) and experimental tests.

5.1 Description of the Goals and Specifications

The study of electromechanical forces developed on the superconducting windings is essential to ensure their integrity and that of the device in which they are used.

The working principle of a TT-SFCL was described in CHAPTER 2.3.3. In normal operation, the limiter acts as a transformer with its secondary short-circuited, where *mmf* created by the primary coil is nullified by the HTS secondary winding, therefore, magnetic flux changes in the core are almost null and the voltage drop at the terminals of the limiter is negligible. However, when a fault occurs, the AC current in the primary coil increases abruptly and the secondary rings achieve their limited ability to nullify the *mmf* created by the primary. Thus, magnetic flux changes through the core appear to steeply increase the line impedance and allow current limitation.

The secondary winding of the limiter can be made of HTS short-circuited tapes, called HTS rings, where the number of rings defines the limitation ability of the device *(Arsénio, 2017)*. The HTS rings are placed in the same core limb of the primary coil and can be distributed axially or radially, as can be seen in FIGURE 5.1.

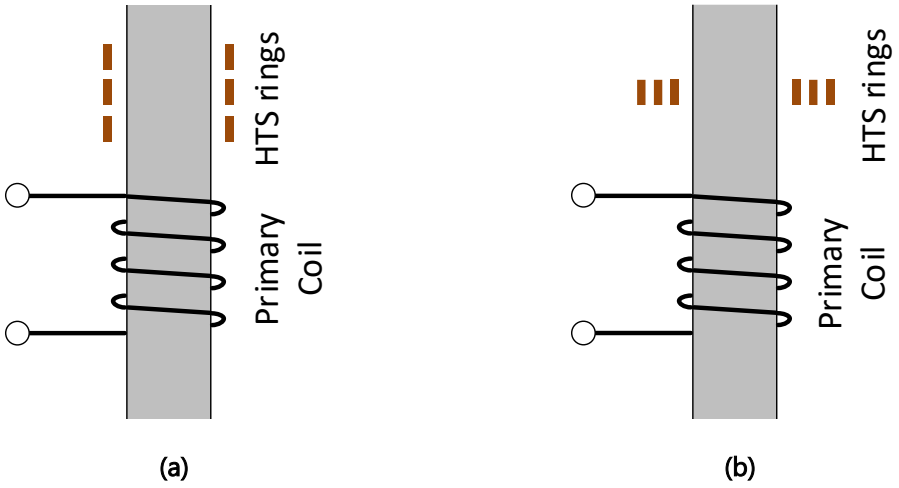

Figure 5.1 – Distribution of 3 HTS rings on the magnetic core limb. (a) Axial distributed. (b) Radial distributed.

The main objectives of this study are:

- Study of the best secondary winding configuration that provides good fault current reductions while minimizing the electromechanical forces on the winding.
- Measure the electromechanical forces developed on the secondary windings, under fault conditions, in order to better understand their mechanical integrity.

5.2 Description of the Prototypes Under Tests

Two prototypes of a TT-SFCL (laboratory scale) were used, a single-phase SFCL and a three-phase SFCL. Both prototypes have been designed and built previously. The single-phase device in *(Arsénio, 2017)* can be seen in FIGURE 5.2, and the three-phase device in *(Barroso, 2014)* can be seen in FIGURE 5.4.

The prototypes are composed of a magnetic core, a primary and secondary winding and their holders and a cryostat.

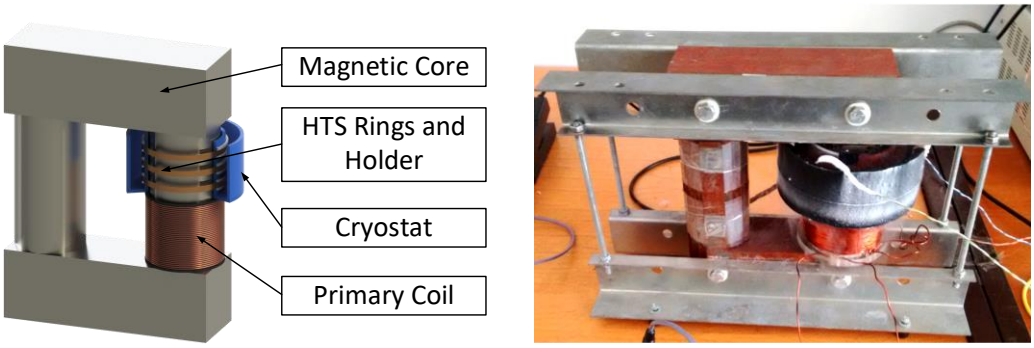

(a) (b)

Figure 5.2 – Single-phase transformer type TT-SFCL. (a) Schematic of the SFCL. b) Prototype.

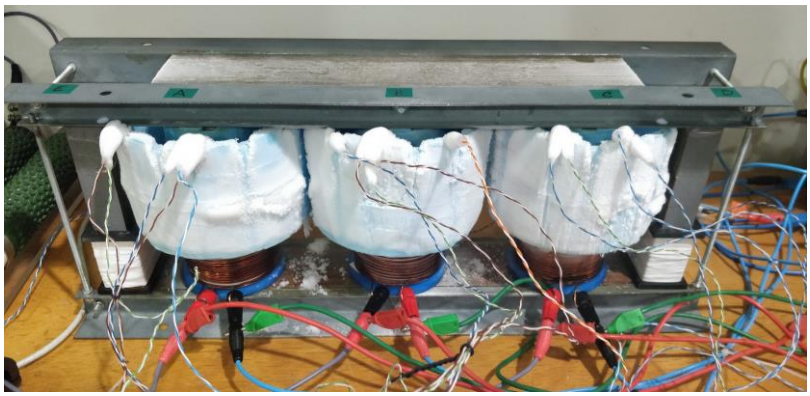

Figure 5.3 – Three-phase TT-SFCL prototype.

5.2.1 Magnetic Cores

The prototypes are built by a closed-core configuration, which allows better current limitation during a fault event *(Janowski et al., 2003)*, among other advantages. The magnetic cores were manufactured using non-oriented grain electrical steel, with a thickness of 0.5 mm and a stacking factor of 0.97.

The single-phase device uses a UI core configuration, where its limbs have a circular shape. FIGURE 5.4 (A) shows the limiter dimensions. Otherwise, the three-phase device is built using an EI core configuration (dimensions presented in FIGURE 5.4 (B). There are two different top yokes for the three-phase limiter, which are used for two distinct topologies. Traditional topology uses the short yoke that magnetically closes the three internal limbs where the AC coils are placed. To provide an alternative path for the magnetic flux, two external limbs are used through the long top yoke. This topology is called shell topology.

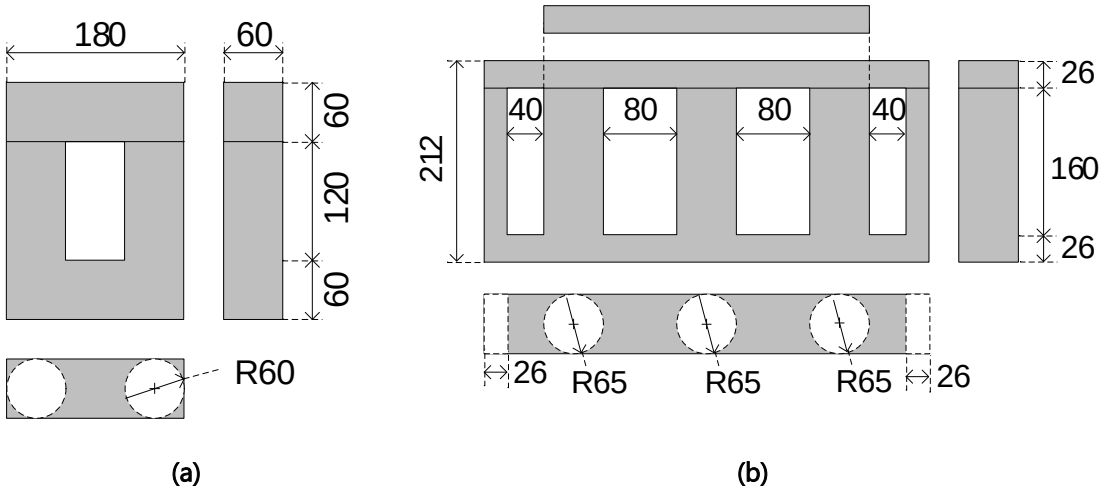

Figure 5.4 – Dimensions of cores for each prototype. (a) Single-phase magnetic core. (b) Three-phase magnetic core.

5.2.2 Windings

The prototypes are composed of the primary and secondary windings. Primary windings are connected in series with the AC line and are made of copper, a typical conductor for power devices. TABLE 5.1 summarises the properties of primary windings.

Table 5.1 – Characteristics of the primary winding and its holder.

Parameter	
Material of the electrical conductor	Copper
Cross-section area of the conductor (mm^2)	1.5
Number of turns	50
Holder medium radius (mm)	34
Holder height (mm)	40

The secondary winding of the limiter is composed of one or more short-circuited rings of superconducting tape. 2G tape, from Superpower, was used and its characteristic is shown in TABLE 5.2. In FIGURE 5.5 is shown the secondary winding, with one ring in its holder.

Table 5.2 - Characteristics of the secondary winding and its holder.

Parameter	
Reference	Superpower SCS4050
Cross-section area of the tape (mm^2)	4x0.1
Minimum critical current density at 77.3 K (A/mm^2)	250
Minimum n-value at 77.3 K	30
Holder medium radius (mm)	34
Holder height (mm)	15

Figure 5.5 – Secondary winding (one HTS ring inserted into the winding holder).

5.3 Analysis of Electromechanical Forces by FEM

The secondary winding of a TT-SFCL can be assembled by one or more HTS rings. To determine the optimal distribution of the HTS rings along the limb the analysis of electromagnetic forces developed on the secondary winding is essential. Therefore, the SFCL prototype, previously described, was modelled in FEM software Flux2D from Cedrat company *(Vilhena et al., 2016)*.

5.3.1 TT-SFCL Specification and Modelling

The single-phase prototype was modelled in FEM software according to the specifications presented in CHAPTER 5.2. FIGURE 5.6 shows the test grid used in the simulations where the values of each component are shown in TABLE 5.3.

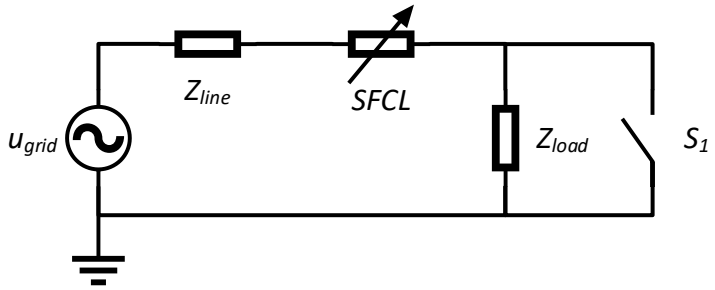

Figure 5.6 – Simulation test grid.

Table 5.3 - Characteristics of simulation test grid.

Parameter	
Voltage source u_g (V_{rms})	50
Frequency f (Hz)	50
Line impedance (Ω)	1 + i0.31
Load impedance (Ω)	25 + i3.14

Four different distributed configurations for the HTS rings were defined as shown in FIGURE 5.7. The configurations are radially distributed (R), radially distributed concentric with the primary (RC), axially distributed (A) and axially distributed concentrically with the primary (AC).

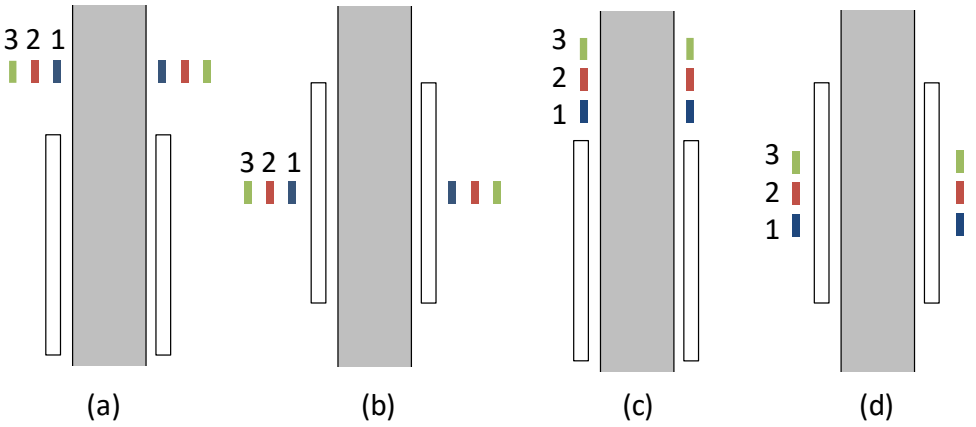

Figure 5.7 - Distribution of superconducting windings on the core limb. The limb of the core is shown in grey, the primary is shown in white and the secondary winding are shown in blue for the first HTS ring, in red for the second and in green for the third. (a) Radial distributed. (b) Radial distributed concentrically with the primary. (c) Axial distributed. (d) Axial distributed concentrically with the primary.

FIGURE 5.8 shows the middle line where the forces were calculated along with the superconducting tape, from top to bottom.

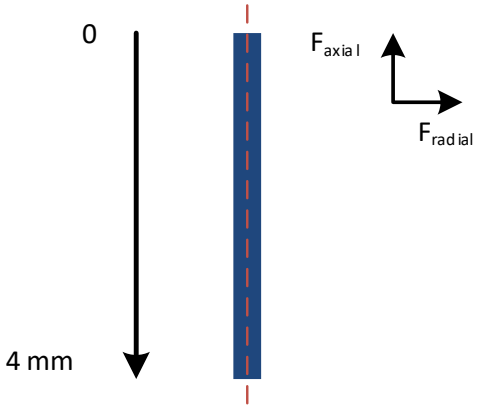

Figure 5.8 – Middle line (dashed red line) and direction (from top to bottom) where axial and radial forces were calculated by FEM.

5.3.2 Performance Analysis of the TT-SFCL

In order to compare the performance of the TT-SFCL under fault conditions in the four distributions, a simulation for each configuration of HTS rings was carried out.

5.3.2.1 Line Current

The analysis of the line current behaviour under fault conditions for all different distribution configurations is important in order to take this into account when the

design and optimisation of the SFCL are done because the limitation power must be maximized.

FIGURE 5.9 shows line current evolution as a function of time. For each case, the current was limited to around 12% of the prospective short-circuit value (70.7 A). Analysing the graph, it can be concluded that the configuration of the HTS rings does not influence the limitation capacity of the limiter.

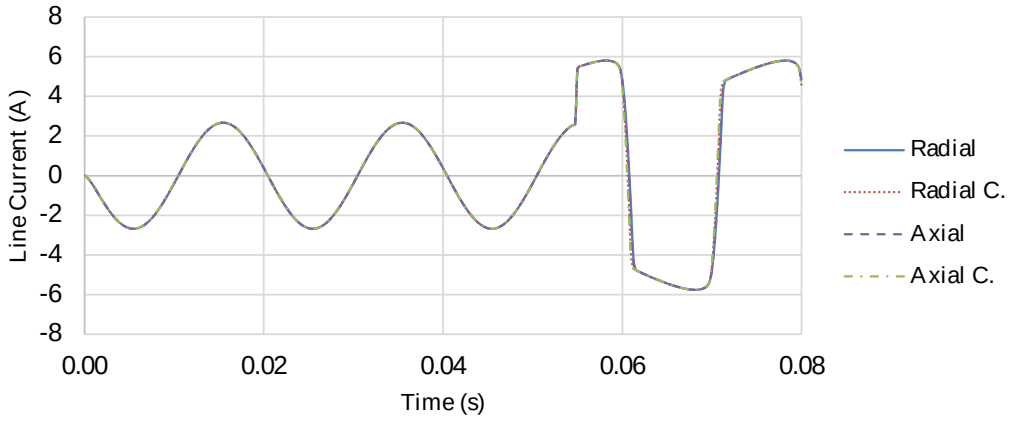

Figure 5.9 – TT-SFCL line current time evolution under fault conditions.

5.3.2.2 Current in Superconducting Rings

The electromagnetic forces developed in the rings are directly related to their current. FIGURE 5.10 shows the current in each HTS ring for the radial distribution configuration. It can be observed that the ring current has the same behaviour in all rings under fault conditions but, at regular operation conditions, the current flows through the rings with different amplitudes.

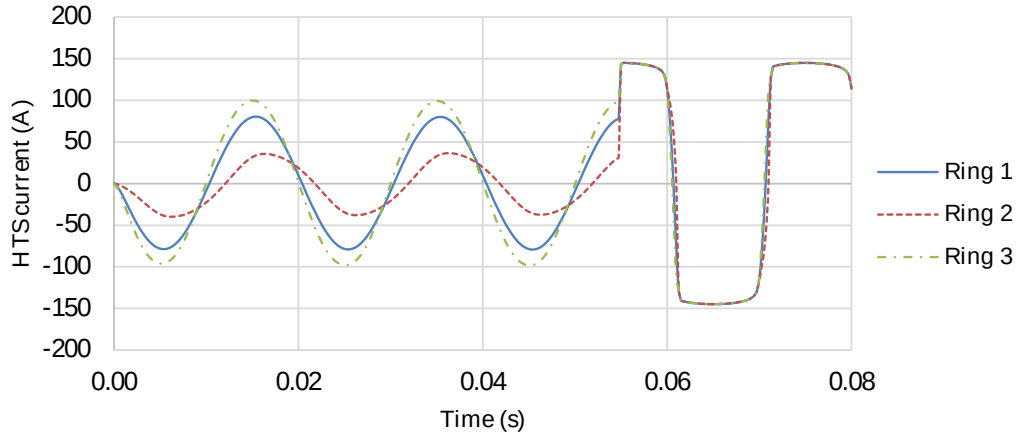

Figure 5.10 - HTS rings current time evolution for the radial distributed configuration (R).

FIGURE 5.11 shows the amplitude of HTS rings current at normal operating conditions. Therefore, the HTS rings will experience different electromagnetic forces because the force magnitude is directly related to current density of the rings (CHAPTER 2.3.3.3).

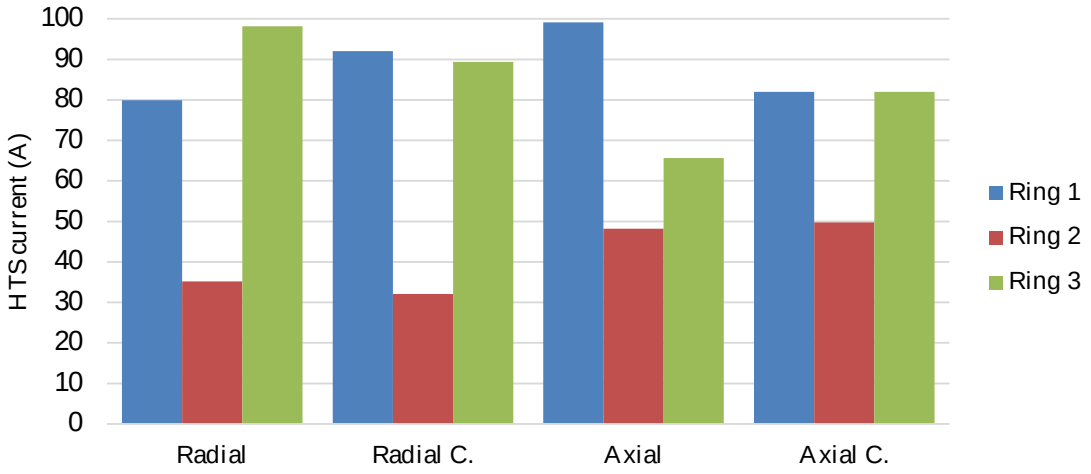

Figure 5.11 - Amplitude of current in rings for each configuration, at normal state of the SFCL.

5.3.3 Forces Analysis on HTS Rings under Short-circuit Conditions

The HTS rings of the TT-SFCL are immersed in a magnetic field. Due to the interaction between the magnetic field and the current density, the rings will experience electromagnetic forces that can mechanically damage them. As described in CHAPTER 2.3.3.3, forces in axial direction tend to compress the HTS rings axially, and forces in radial direction cause compressive and bending stresses or tensile stress (hoop stress) acting over the length of the rings. The hoop stress can compress or pull depending on whether the radial pressure acts inward or outward.

FIGURE 5.12 shows force vectors through the rings in radially distributed (a) and axially distributed (b) topologies. FIGURE 5.12 (A) shows that radial forces cause an attraction between rings number 1 and 3 which cause high hoop stress on those rings. The magnetic flux density in ring number 2 is very small because it is the sum of the leakage flux of Rings 1 and 3, which cancel each other out. Therefore, no significant stress should be on ring number 2. FIGURE 5.12 (B) shows the existence of compressive effects in the rings.

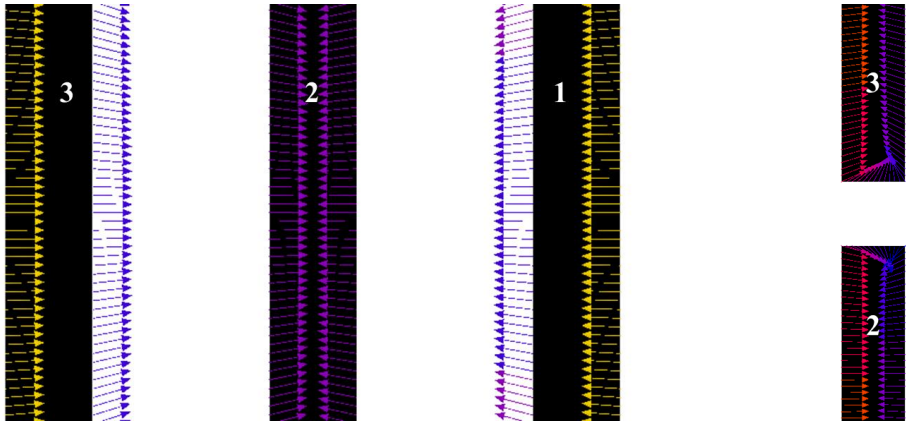

Figure 5.12 – Lorentz force density vectors through HTS rings in (a) radial distribution and (b) axial distribution. The sections of the rings show in (a) and (b) are the left sections of the winding.

5.3.3.1 Radial Forces Analysis

Radial forces result from the interaction between current flowing in the HTS ring and axial component of the leakage flux density. These forces are responsible for hoop stresses on the rings. This happens because the ring has a cylindrical profile where normal forces create tangential stresses (hoop stresses, σ_H) and axial stresses (σ_a) *(Vecchio et al., 2010)*.

The values due to radial forces can be seen in FIGURE 5.13, FIGURE 5.14, FIGURE 5.15 and FIGURE 5.16 for each ring distribution along the core limb. In each graph, positive values represent that the radial component of the Lorentz force forces the ring towards its limb (compressive force) and negative values in the opposite direction (tensile force).

It is important to notice that a tensile force in the rings causes axial compressive force and vice versa, due to the hoop stress effect on the rings.

FIGURE 5.17 shows the maximum radial forces for each distribution simulated where negative values represent compressive forces and positive values represent tensile forces. As can be observed, radial forces are stronger in the radial distribution of the rings.

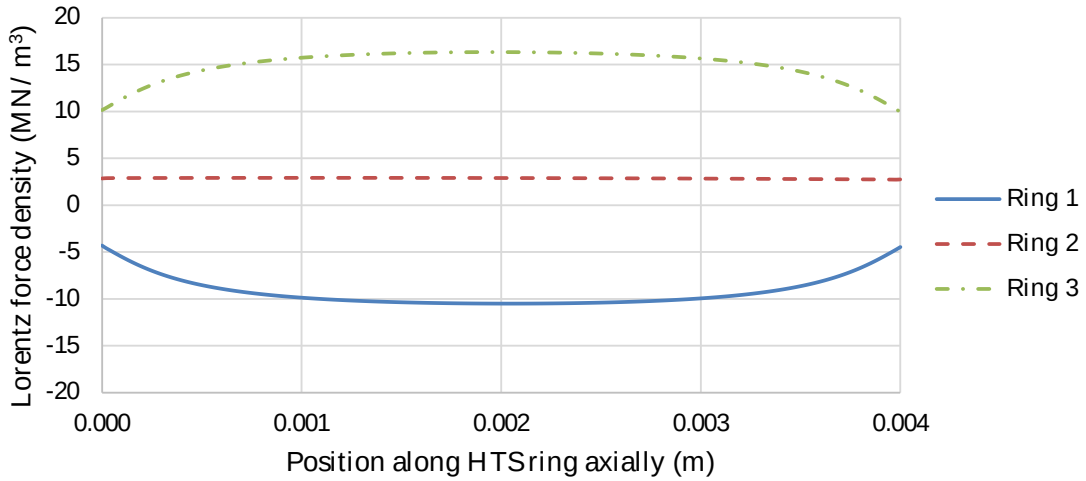

Figure 5.13 Radial component of the Lorentz force on the HTS rings radially distributed.

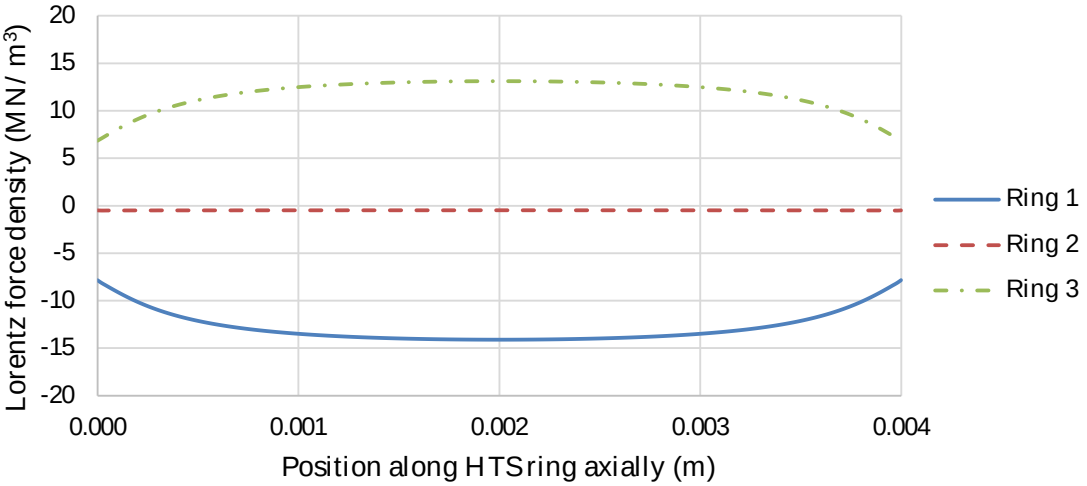

Figure 5.14 Radial component of the Lorentz force on the HTS rings radially distributed and concentric with primary.

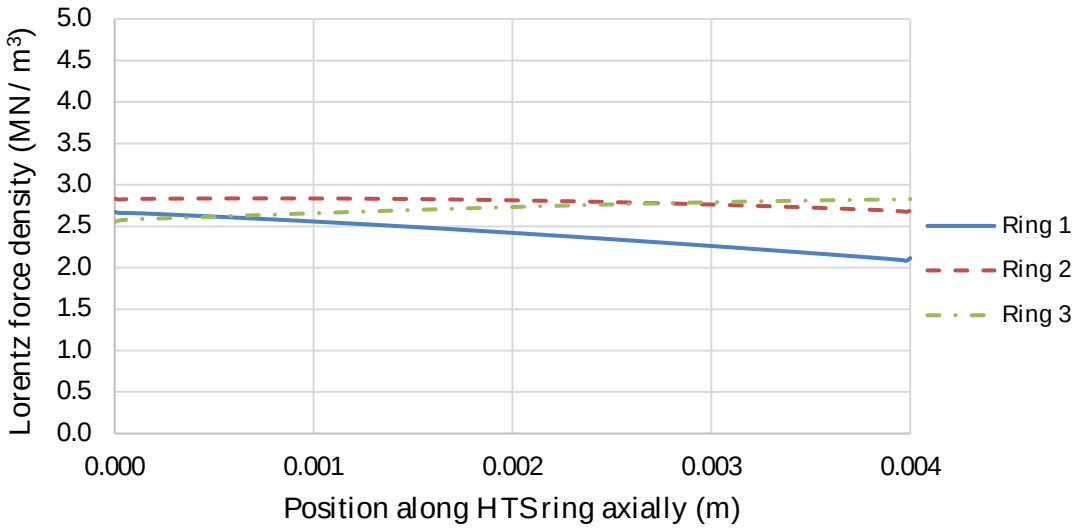

Figure 5.15 - Radial component of the Lorentz force on the HTS rings axially distributed.

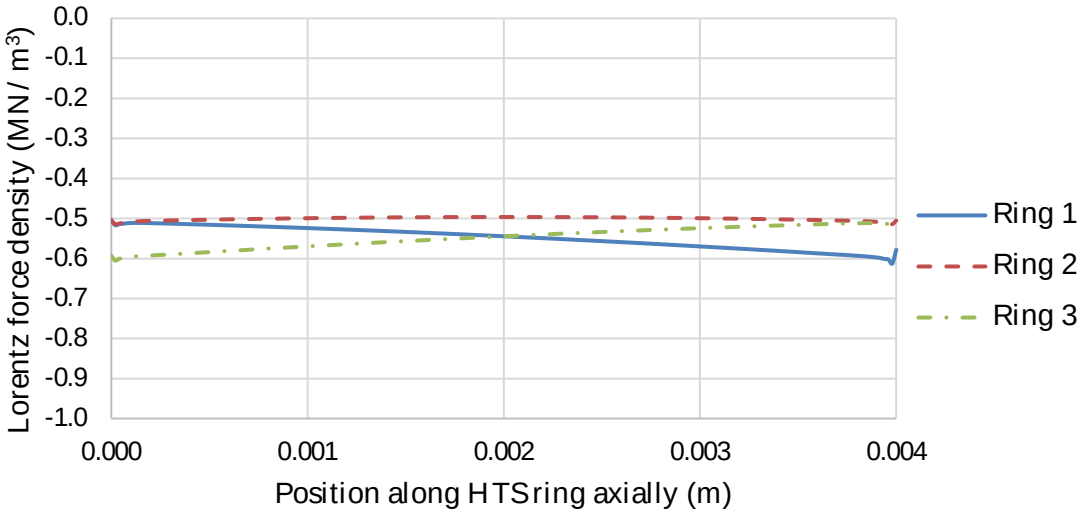

Figure 5.16 – Radial component of the Lorentz force on the HTS rings axially distributed and concentric with primary.

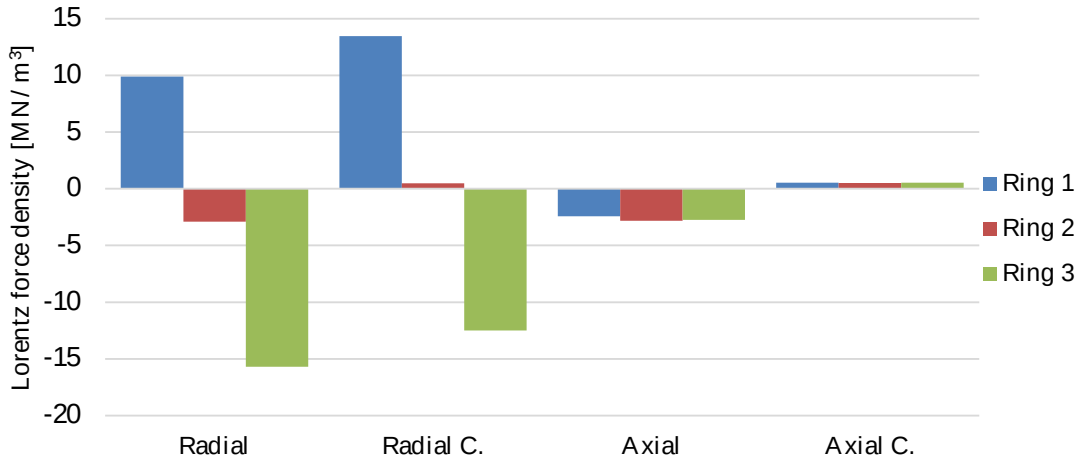

Figure 5.17 - Maximum radial forces on HTS rings for each ring distribution.

5.3.3.2 Axial Forces Analysis

Axial forces caused by the radial component of magnetic induction on the rings are shown in FIGURE 5.18, FIGURE 5.19, FIGURE 5.20 and FIGURE 5.21 for each ring distribution along the limb. FIGURE 5.22 shows the maximum cumulative axial forces for each distribution simulated (represented as negative values for compressive forces). As can be observed, axial forces along the ring length are not constant which means that, in general, the axial forces compress the rings axially. In some cases, axial forces along the ring take always the same direction, a situation that needs to be taken into account when dimensioning the ring holders.

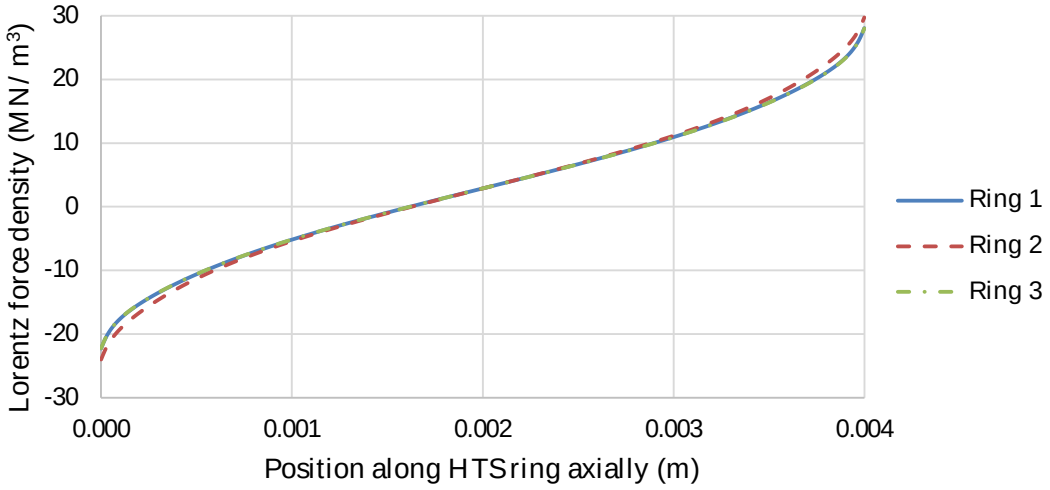

Figure 5.18 – Axial component of the Lorentz force on the HTS rings radially distributed.

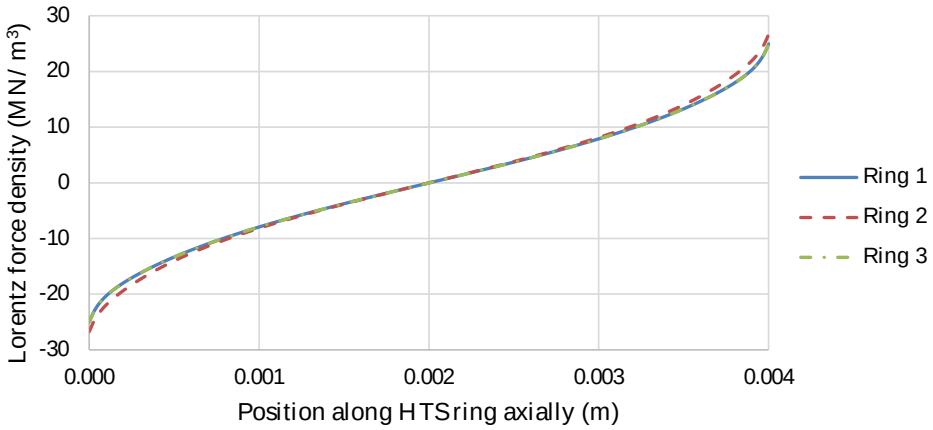

Figure 5.19 – Axial component of the Lorentz force on the HTS rings radially distributed and concentric with primary.

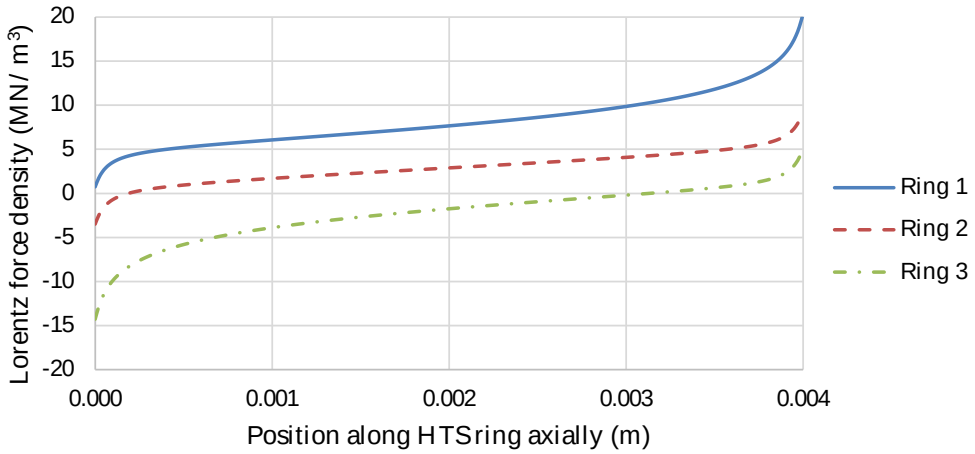

Figure 5.20 - Axial component of the Lorentz force on the HTS rings axially distributed.

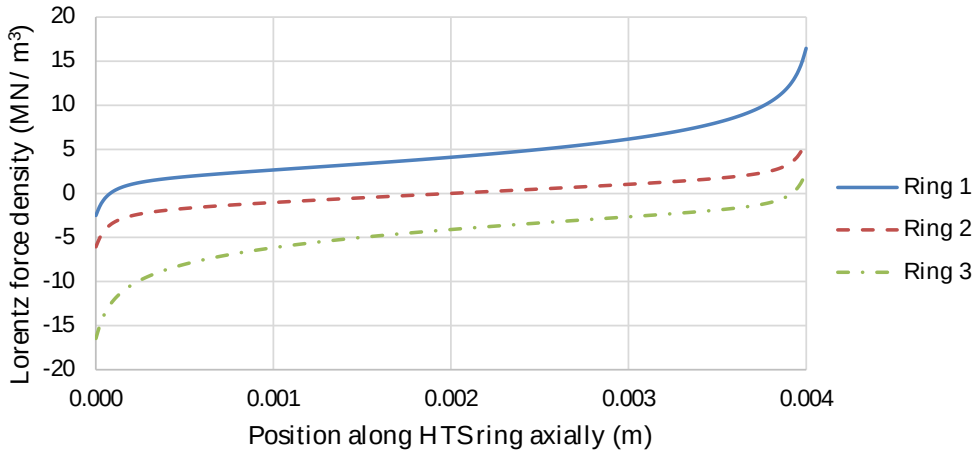

Figure 5.21 - Axial component of the Lorentz force on the HTS rings axially distributed and concentric with primary.

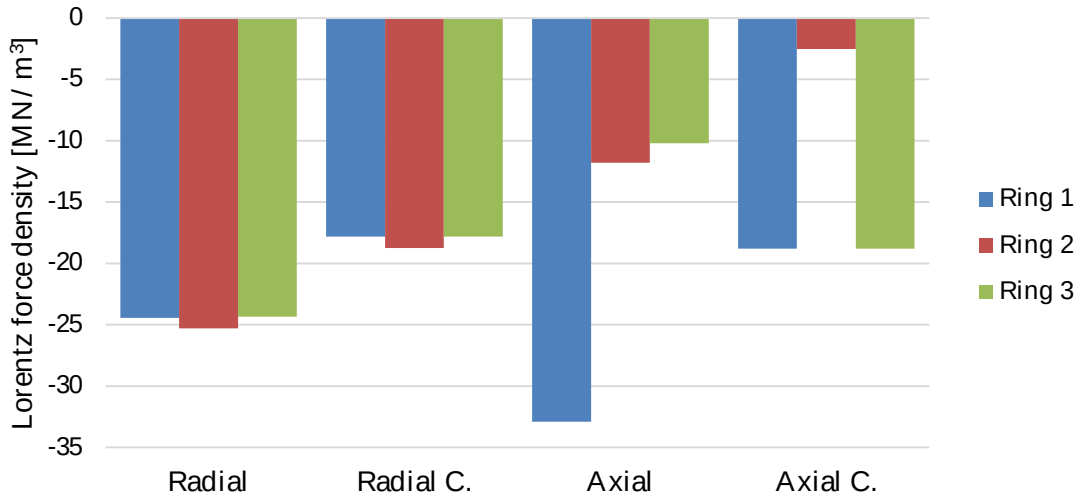

Figure 5.22 – Cumulative axial forces on HTS rings for each ring distribution.

5.3.3.3 Magnetic Induction Field Analysis

Concerning the magnetic induction field normal component to the YBCO tape, the radial configuration is less suitable. FIGURE 5.23 shows the normal component of magnetic induction on the rings. As can be seen, the normal magnetic induction field is higher in radial configuration, which makes radial configurations less adequate.

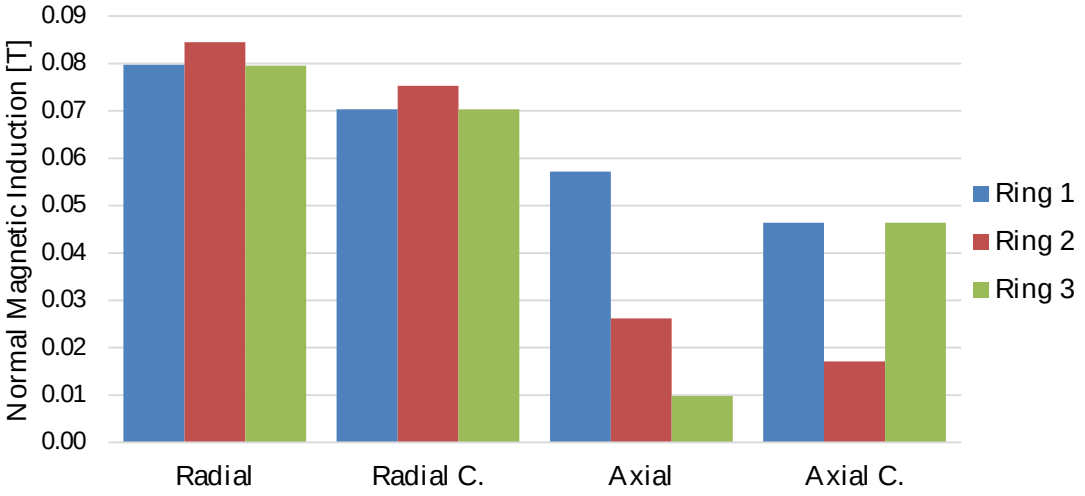

Figure 5.23 - Maximum normal magnetic induction field on the rings.

5.4 Measurement of Electromechanical Forces using Strain Gauges

In order to experimentally measure the mechanical stresses experienced by the HTS rings, laboratory tests of the TT-SFCL were performed.

Strain gauges were used as measure devices (as described in CHAPTER 2.3.3.4) to quantify the mechanical stresses that superconductive tapes suffer during the fault event. These measurements were intended to contribute to the study and optimisation of power devices, especially the ones using HTS materials.

The present problem is characterized by a biaxial state of stresses, thus calculation of mechanical stresses is not linear. Two strain gauges are placed on each HTS rings with their axes coincident with the main directions of deformation, allowing for the measurement of the axial and radial strain in the ring.

The mechanical stress is calculated from EQUATION (5.1) where x represents radial direction, y represents axial direction, υ represents the Poisson's ratio and E represents the Young's modulus of the material.

$$\begin{cases} \sigma_x = \dfrac{E}{1-\upsilon^2}\left(\varepsilon_x + \upsilon \cdot \varepsilon_y\right) \\ \sigma_y = \dfrac{E}{1-\upsilon^2}\left(\varepsilon_y + \upsilon \cdot \varepsilon_x\right) \end{cases} \tag{5.1}$$

5.4.1 Measurement Procedure

In order to measure and analyse the mechanical forces in the HTS rings, the apparatus described below was used with strain gauges. During test conditions, these devices change their electrical resistance as an image of the developed strain in the material, according to EQUATION (5.2).

$$\frac{\Delta R}{R} = \varepsilon \cdot K \tag{5.2}$$

where R is the resistance of the strain gauge without deformation, ΔR is the change in resistance caused by strain, K is the gauge factor and ε is the strain. R and K are constants that can characterize the strain gauge, this means that the strain is calculated by measuring ΔR, for instance, through a Wheatstone bridge circuit.

5.4.1.1 Data Acquisition System

A Wheatstone bridge is an electrical circuit used to measure an unknown electrical resistance by balancing two legs of a bridge output, as shown in FIGURE 5.24. This type of

circuit is used to acquire signals from the strain gauges. The R_{SG1} represents the strain gauge attached to the HTS ring. However, because of working in a cryogenic environment, a second strain gauge R_{SG2} was used, immersed in the cryogenic liquid, in order to compensate the temperature difference. The potentiometer R_{POT} is essential to adjust the bridge. As the output voltage of this circuit is very small, the signal is amplified and filtered before its acquisition and analysis. The measured voltage will be directly related to the developed stress on the rings.

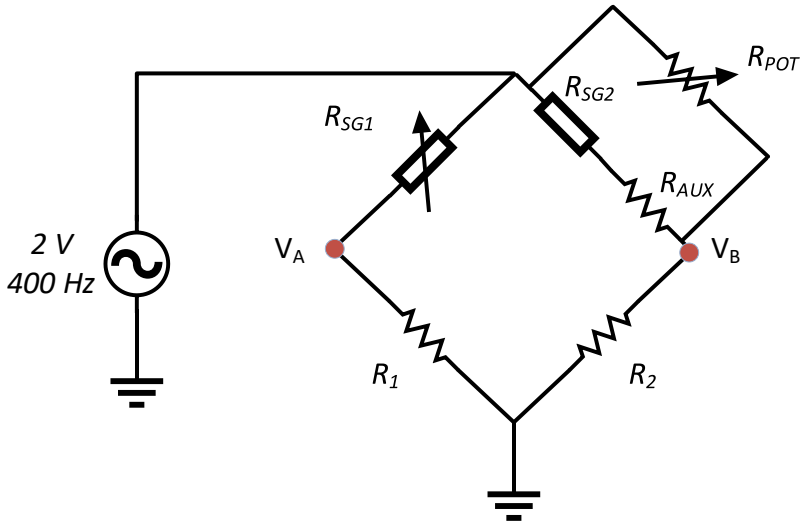

Figure 5.24 - Wheatstone bridge used on the measurement circuit.

One Wheatstone bridge in a half-bridge configuration is used to measure each signal being acquired. The circuit is excited by an AC voltage source because this allows eliminating the DC offset and it is a better approach for noise rejection. The AC voltage must not exceed 3 V due to the power dissipation capability of the strain gauges *(Kitchin & Counts, 2006)*.

The schematic of the circuit used for signal conditioning is shown in FIGURE 5.25. Graph A shows the AC voltage signal given to the Wheatstone bridge; graph B shows the output differential signal ($V_A - V_B$) of the bridge; graph C shows the signal after being amplified; graph D shows the signal after being rectified by the synchronous demodulator, and graph E shows the filtered DC signal output. The output signal V_{out} is measured by a data acquisition board (NI6001 from Texas Instruments).

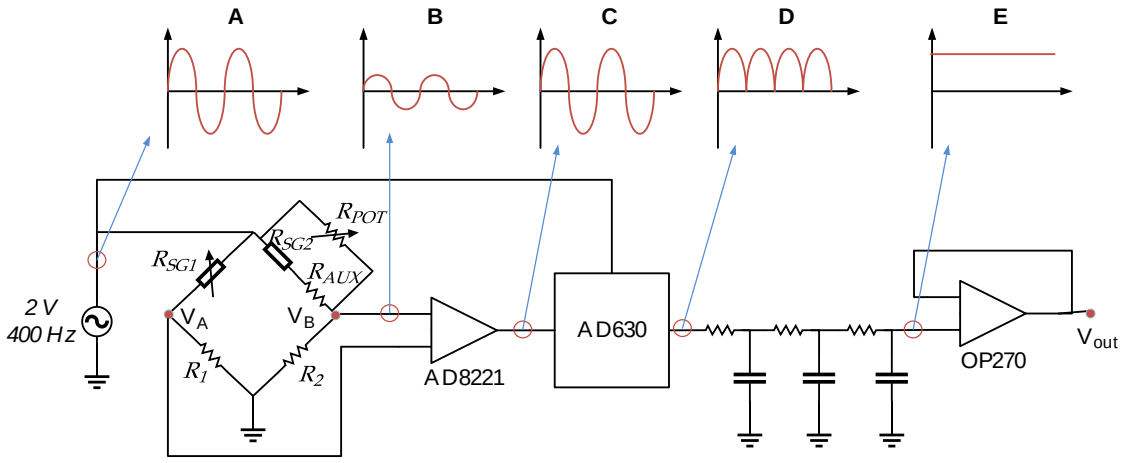

Figure 5.25 – Schematic of the circuit used for signal conditioning.

5.4.1.2 Measuring HTS Current

The electromagnetic forces developed in HTS rings are directly related to their current. In order to study the rings current behaviour, a Rogowski coil was developed (shown in FIGURE 5.26). Each Rogowski coil is built in a flexible and open-ended non-magnetic core where 75 turns are wounded. The signal in the output of the coil is integrated and amplified through a signal conditioning circuit so that its output is an image of the electrical current in the ring. Each coil is also calibrated before the tests.

Figure 5.26 – Rogowski coil involving the HTS ring

5.4.1.3 Test Apparatus

The schematic of the test bench used to test the single-phase TT-SFCL is represented in FIGURE 5.27. It is composed of the following elements:

- Autotransformer: An autotransformer is used to regulate the voltage applied to the test grid.
- Insulation transformer: This transformer provides galvanic isolation between the utility grid and the test grid. Its rated power is 2 kVA.
- R_{LINE}: This element represents the line resistance.
- R_{LOAD}: This element represents the load resistance.
- S_1: To cause a fault, a breaker is used, in parallel with the load, allowing the load to be short-circuited.
- $SFCL$: The fault current limiter prototype under test.
- Hall probe: Hall effect current probe, from Tektronix (A622). This probe is used to measure the line current.
- Rogowski coil: Current probe used to measure the HTS ring current.
- Auxiliary winding and integrator: This is an open winding used to measure the primary linked flux. The output integrated signal is an image of the linked flux with the primary winding.
- Data acquisition system: As described previously, this device is used to measure the forces developed on the HTS rings, under a fault event. The signals from this device are sent to the data acquisition board.
- Data acquisition board: This board allows data acquisition from all sensors and send those data to the computer. This device is from National Instruments (NI-6001) and communicates with the computer through USB interface.

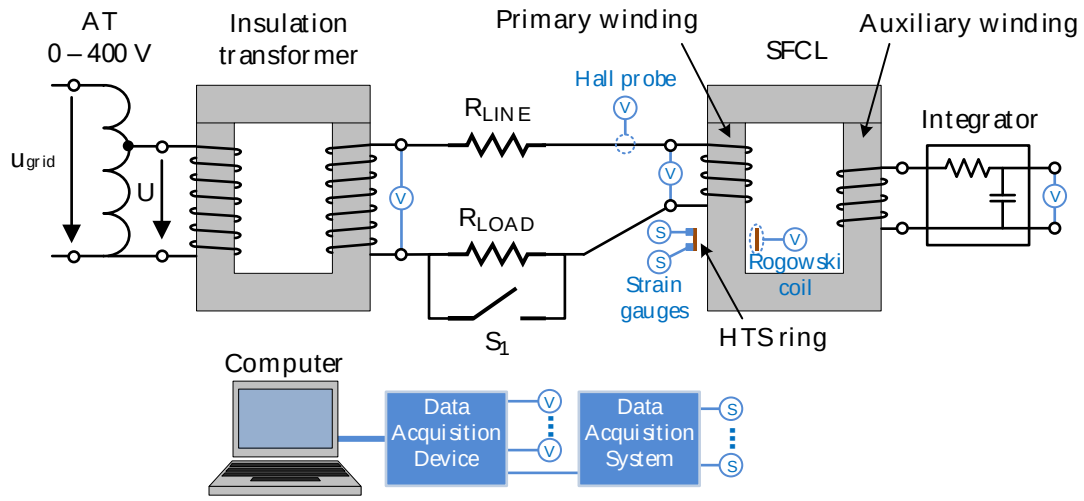

Figure 5.27 – Schematic of the test bench used for the experiments. The auxiliary winding is represented on a different limb of the primary winding only for diagram simplification purpose, both windings are concentric.

The test bench for the three-phase TT-SFCL is very similar to the previous one. A three-phase insulation transformer is used connected to a three-phase line resistor, to the three-phase SFCL and a three-phase load resistor in star connection.

To perform the tests, some main steps must be considered:

1. Cooldown the HTS ring with liquid nitrogen and wait until they reach the superconducting state.
2. Calibrate the Wheatstone bridges so that the output signals are centred at zero.
3. Turn on the autotransformer and regulate it to the desired voltage.
4. Start recording the signals from the data acquisition board.
5. The breaker is activated in order to short-circuit the load and thus simulate a fault in the test grid.

5.4.2 Single-Phase TT-SFCL: Electromagnetic Forces Under Short-Circuit Conditions

A single-phase TT-SFCL laboratory prototype is submitted to mechanical stresses caused by faults in the test grid. Three different HTS ring distributions, along the SFCL limb, were chosen as can be seen in FIGURE 5.28. In distribution a), only one HTS ring was tested, with the purpose of verifying if its strength limit is not exceeded. In distribution b) and c), two HTS rings axially and radially distributed, respectively, were tested in order to check which configuration is more advantageous. No configuration with concentric

HTS rings with the primary winding was considered due to the fact that the prototype used did not allow this configuration.

In FIGURE 5.29 is shown the schematic of test grid used for the test. Its parameter values are depicted in TABLE 5.4. In normal conditions, the line current is approximately 1.44 A while the prospective fault current is approximately 84.9 A.

The fault condition is imposed by closing the breaker, which is activated remotely, ensuring a fault time of 700 ms.

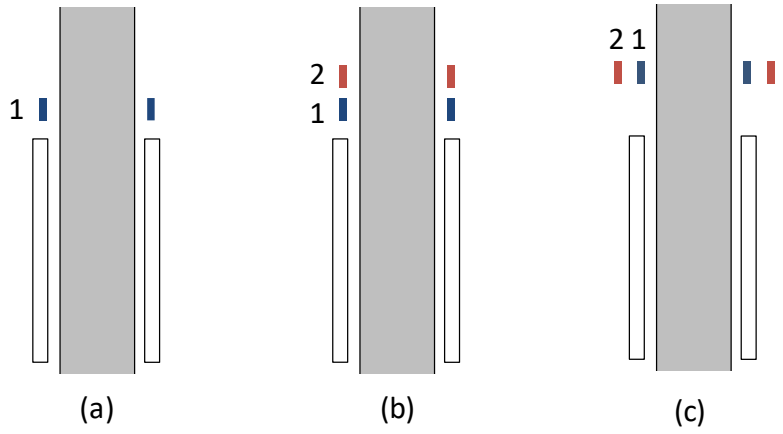

Figure 5.28 – HTS ring distributions used for the single-phase TT-SFCL tests.

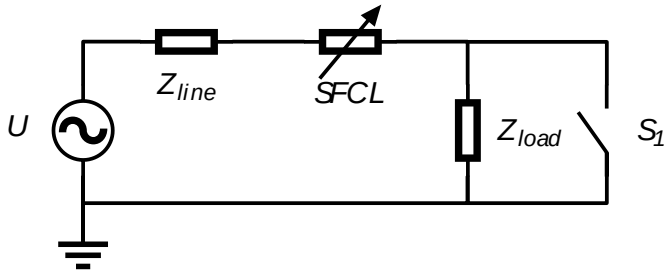

Figure 5.29 – Test grid for single-phase TT-SFCL

Table 5.4 - Characteristics of single-phase test grid.

Parameter	
Applied voltage U (V_{rms})	60
Frequency (Hz)	50
Line impedance (Ω)	1
Load impedance (Ω)	58

5.4.2.1 Forces Measurement and Analysis in Distribution a)

For this test, the secondary is composed of only one HTS ring.

Line current was measured using a hall probe embracing the power wire which is connected to the TT-SFCL. FIGURE 5.30 shows the magnitude of the line current under fault conditions. The line current was limited to, approximately, 14% of the prospective fault current (84.9 A), around 11.9 A.

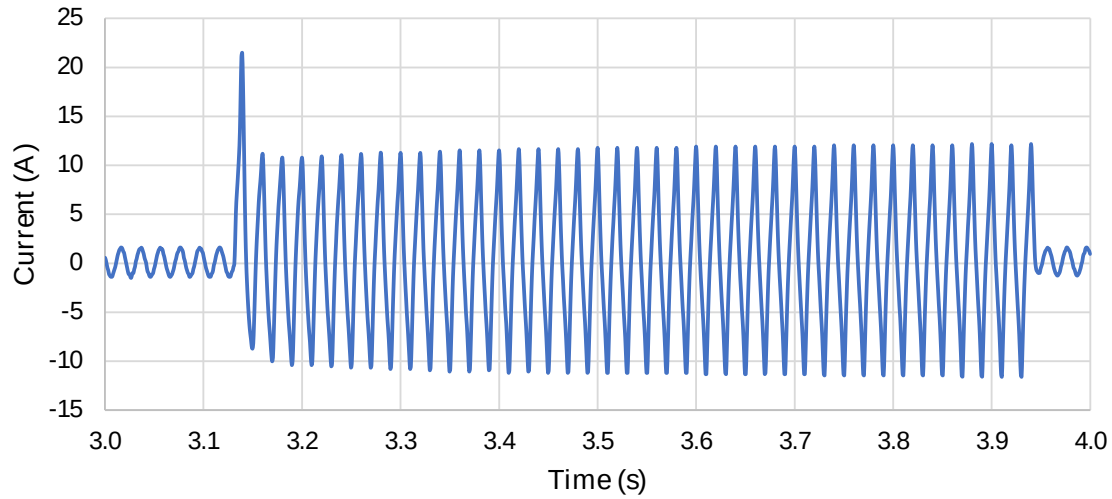

Figure 5.30 - Line current evolution under a fault as a function of time, for a secondary configuration of one HTS ring.

FIGURE 5.31 shows the HTS ring current under fault conditions, as well as the mechanical stresses suffered by the ring.

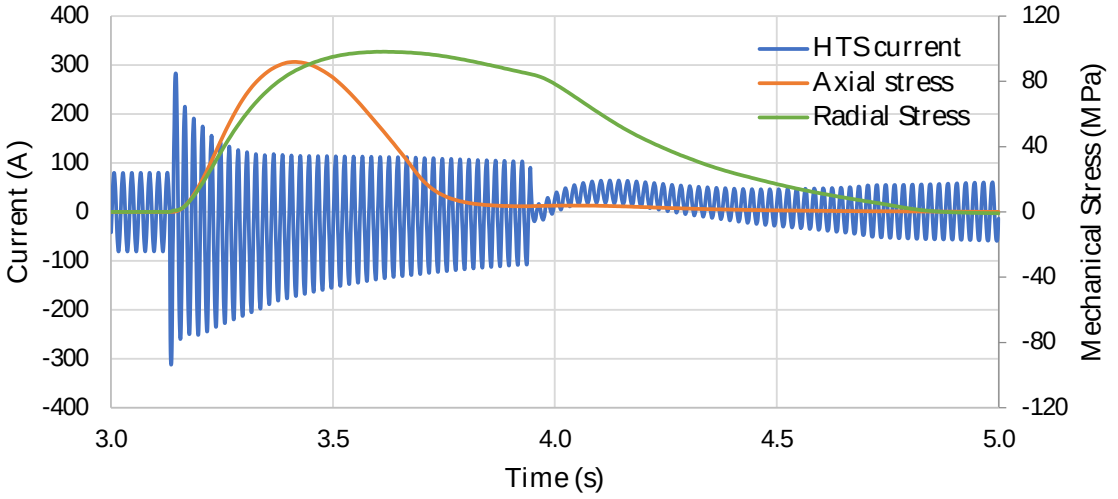

Figure 5.31 – HTS ring current and radial and axial stresses under a fault as a function of time, for a secondary configuration of one HTS ring.

During the fault, the transient response of current achieved approximately 300 A, decreasing exponentially until stabilizes in the critical current value of the superconducting tape (100 A). When the fault ends, the recovery time of the HTS ring (restores its full superconducting properties and deduced when its current normalizes) is approximately 1.5 s.

Both mechanical stresses response immediately when the fault occurs, reaching their maximum when HTS current steady-state is achieved. Axil stress reaches its peak and drops immediately, while radial stress maintains a high magnitude value for longer before starting to decrease after the fault ends. Axial stress value is lower than radial stress value (92 MPa and 98 MPa, respectively).

5.4.2.2 Forces Measurement and Analysis in Distribution b)

The secondary is composed of two HTS rings axially distributed, for the test of rings distribution b).

FIGURE 5.32 depicted the line current that shows a current limitation of 86% of the prospective fault current (84.9 A).

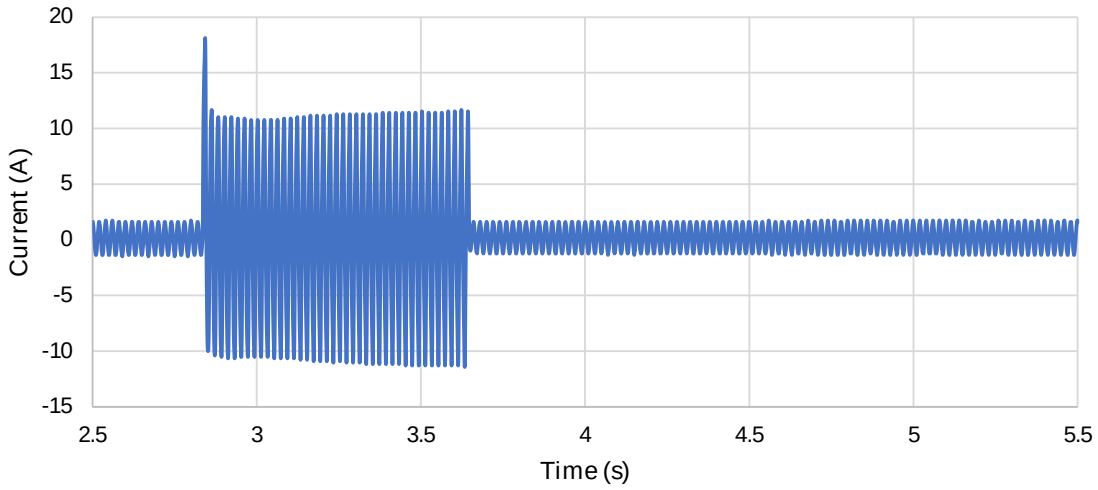

Figure 5.32 - Line current evolution under a fault as function of time, for a secondary configuration of two HTS ring in axial distribution.

Axial and radial mechanical stresses are higher in ring 1, which is closer to the primary coil, than ring 2 (28.5% and 14% higher respectively), as can be seen in FIGURE 5.33. This is because the leakage magnetic flux is more intense in the vicinity of the primary winding. Their behaviour is similar to the previous test.

Regarding the current of each ring, in normal state, its magnitude is half when compared to the previous test of one HTS ring, which is expected because the test grid did not change its parameter values, thus the produced *mmf* is shared by two rings. In fault conditions, the current behaviour is similar, however, the recovery time has increased to approximately 2 s.

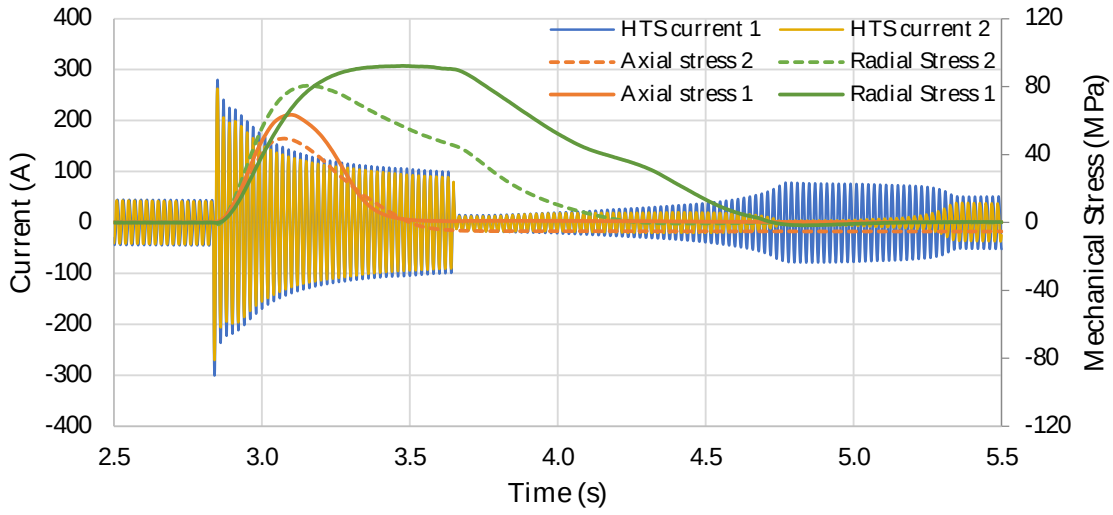

Figure 5.33 - HTS ring current and radial and axial stresses under a fault as function of time, for a secondary configuration of two HTS ring in axial distribution.

5.4.2.3 Forces Measurement and Analysis in Distribution c)

In the last test, 2 HTS rings were arranged radially.

FIGURE 5.34 depicted the line current that shows a current limitation of 87% of the prospective fault current (84.9 A), similar behaviour of previous tests.

FIGURE 5.35 shows the mechanical stresses and HTS ring currents. Once again, the current behaviour in each ring is identical, however, its value is higher because only one Rogowski coil is used, embracing both HTS rings, so measuring the sum of the two currents. Recovery time is approximately 2 s.

Axial mechanical stresses in ring 2 are higher than in ring 1. The results for radial stress in ring 2 must be despised because, during the test, the strain gauge was damaged and could not be replaced, however ring 1 is as expected.

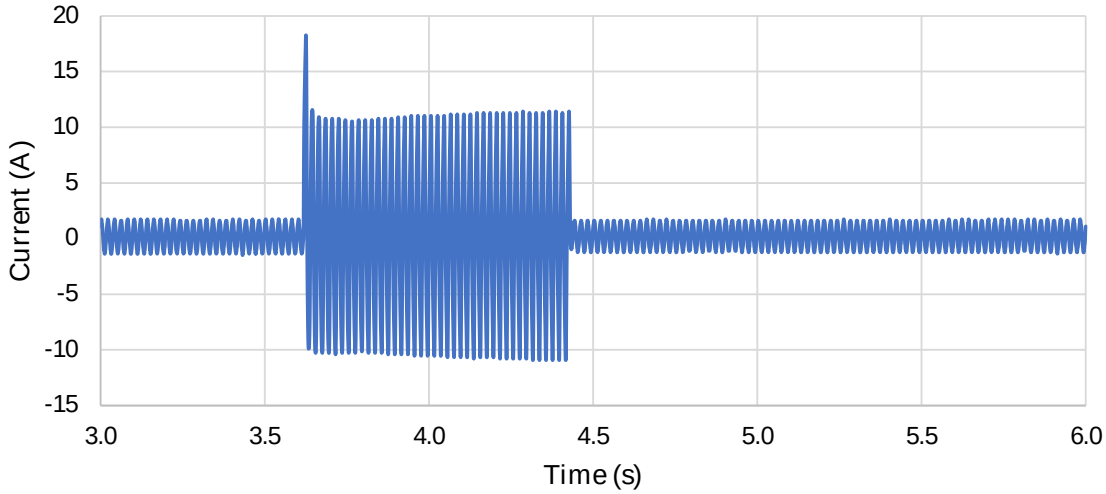

Figure 5.34 - Line current evolution under a fault as a function of time, for a secondary configuration of two HTS ring in radial distribution.

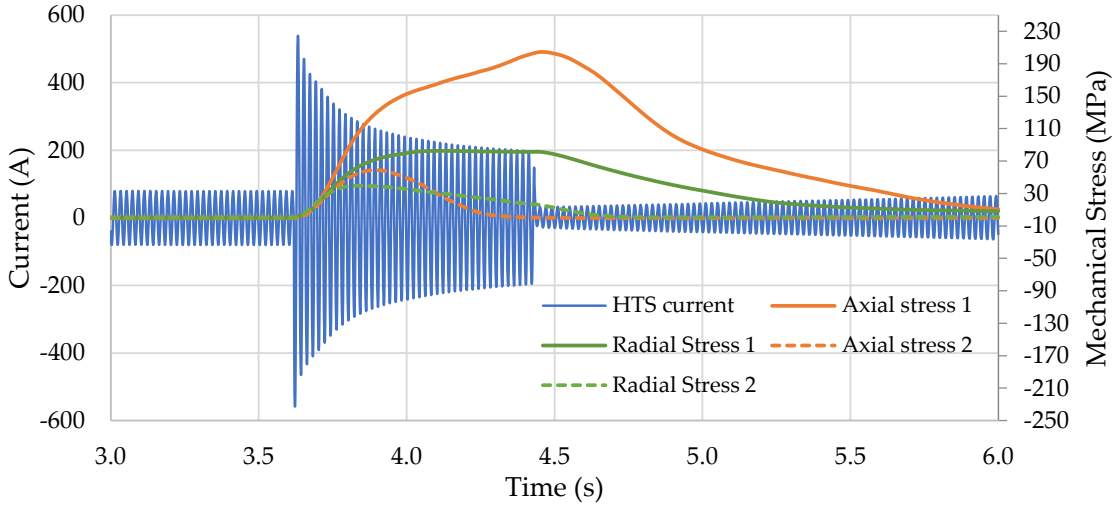

Figure 5.35 - HTS ring current and radial and axial stresses under a fault as a function of time, for a secondary configuration of two HTS ring in radial distribution.

5.4.2.4 Summary of single-phase TT-SFCL tests

In all tests, strain gauges detected the mechanical stresses while short-circuit fault occurred. For the three tests, radial tensile stresses were detected reaching the maximum value after half a second and started to decrease gradually until the fault condition ends. This decrease during the fault is according to the current decay on the HTS ring. The delay between the two measured signals is due to the different response time of electrical and mechanical instrumentation. The higher initial slope of radial stress curve results

from the local heating of the strain gauge which corresponds to an increase of its electrical resistance that contributes to reinforcing the increase resulting from tensile stresses.

The axial forces occur in the transverse direction of the coils. These forces are more intense at the ends of the windings where the magnetic field induction is stronger. For all the experiments were observed axial tensile stresses on the HTS rings.

TABLE 5.5 shows the maximum mechanical stress measured for each ring distribution which is presented graphically in FIGURE 5.36. YBCO tape has a stress limit of around 864 MPa *(Ilin et al., 2015)* until its critical current starts to degrade, under tensile stresses. Considering the obtained results, there was no risk regarding superconducting material integrity. Recovery time increased when more than one HTS ring is in use, due to the influence of one HTS ring on the other.

Table 5.5 – Test values of the main parameters for each ring distribution.

Parameter	Distribution a)	Distribution b)	Distribution c)
Max. axial stress ring 1 (MPa)	92	64	40
Max. axial stress ring 2 (MPa)	-	49	59
Max. radial stress ring 1 (MPa)	98	92	83
Max. radial stress ring 2 (MPa)	-	81	*
Faulted Line current steady-state (A)	12.1	11.6	11.2
Recovery Time (s)	1.5	2.0	2.0

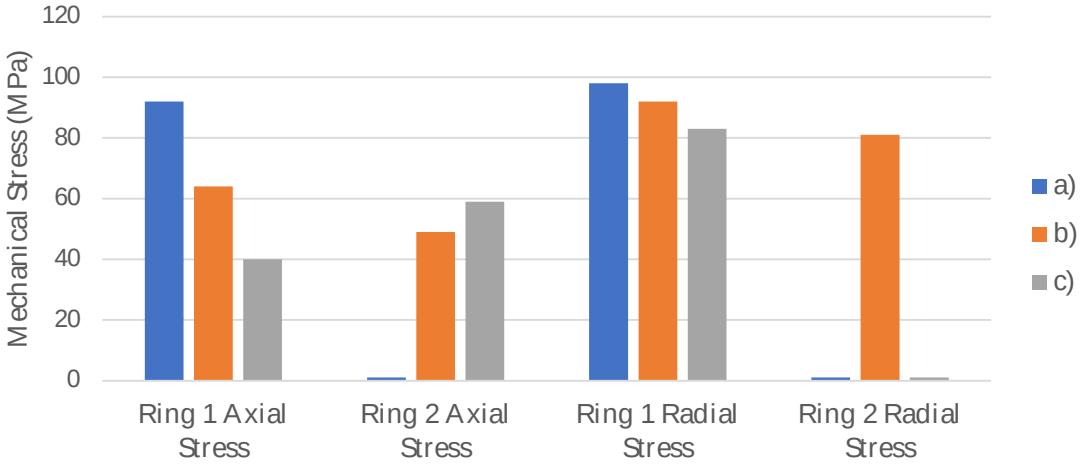

Figure 5.36 – Maximum axial and radial mechanical stress values for each HTS ring according the ring distribution in test.

5.4.3 Three-Phase TT-SFCL: Electromagnetic Forces Under Short-Circuit Conditions

The transmission and distribution are mainly done in three-phase networks, therefore the study of a three-phase SFCL is essential. A three-phase TT-SFCL prototype is submitted to mechanical forces due to the most common types of network faults (CHAPTER 2.1.1), which are the single-phase-to-earth, the phase-to-phase fault and the three-phase-to-earth fault, in order to study and analyse the effect of these different faults in terms of mechanical forces, in the HTS material. Two distinct topologies are also used, traditional and shell topologies, to study which topology minimizes the mechanical forces on the HTS rings, and which one has better performance. It was used one ring per phase.

FIGURE 5.37 shows the schematic of the three-phase test grid used for the tests. Its parameter values are depicted in TABLE 5.6. In normal conditions, the line current is approximately 1.44 A while the prospective fault current is approximately 84.9 A for the single-phase fault.

The fault condition is imposed by closing the breaker S_n $(n = 1\ to\ 5)$, which is activated remotely, ensuring a fault time of 700 ms.

The test apparatus is shown in FIGURE 5.38.

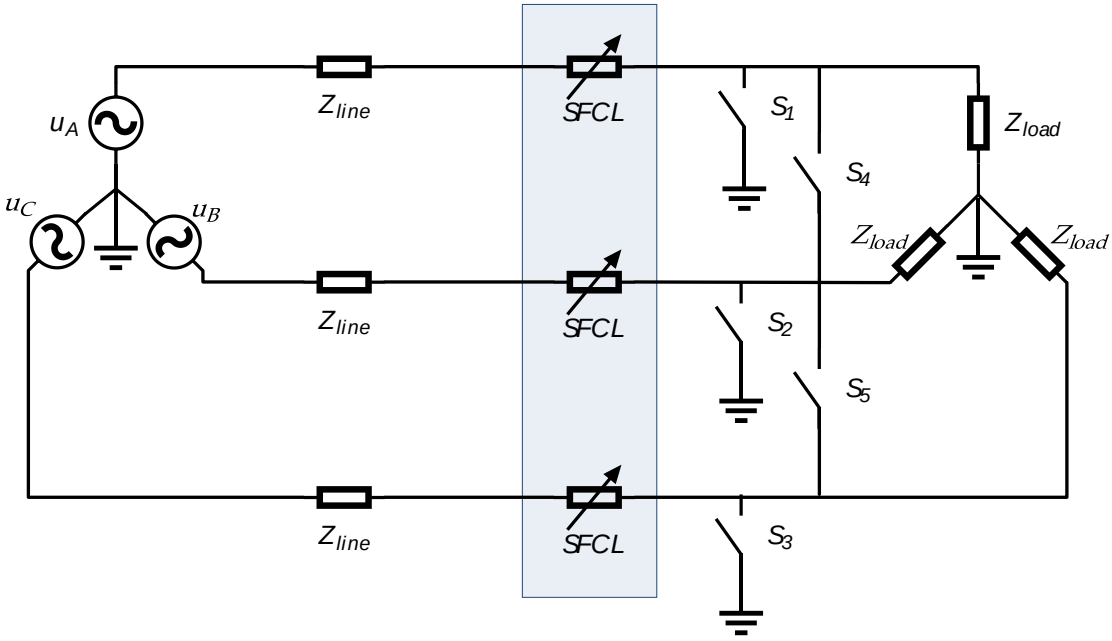

Figure 5.37 – Test grid for the three-phase TT-SFCL.

Table 5.6 - Characteristics of three-phase test grid.

Parameter	
Line-to-neutral voltage U (V_{rms})	60
Frequency (Hz)	50
Line impedance (Ω)	1+i0
Load impedance (Ω)	58+i0

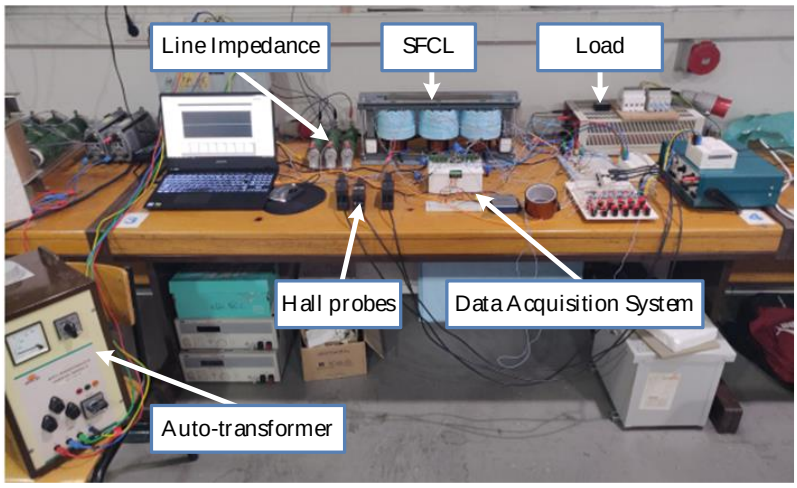

Figure 5.38 – Laboratory apparatus for the three-phase TT-SFCL tests.

5.4.3.1 Forces Measurement and Analysis for Phase-to-earth Fault

To cause a phase-to-earth fault in phase B, switch S_2 (FIGURE 5.37) is closed during the duration of the fault. Following, the line current of each phase, HTS ring currents associated with each phase, as well as the linked flux of each phase coil are analysed. In the end, the mechanical forces are also discussed.

A. Line Current Analysis

FIGURE 5.39 and FIGURE 5.40 show the line current evolution as a function of time, of each phase, for a traditional or shell core topology, respectively. For each core topology, the current was limited to around 85% of the prospective short-circuit value (60 Arms). The topology of the magnetic core does not influence the limitation capacity of the limiter.

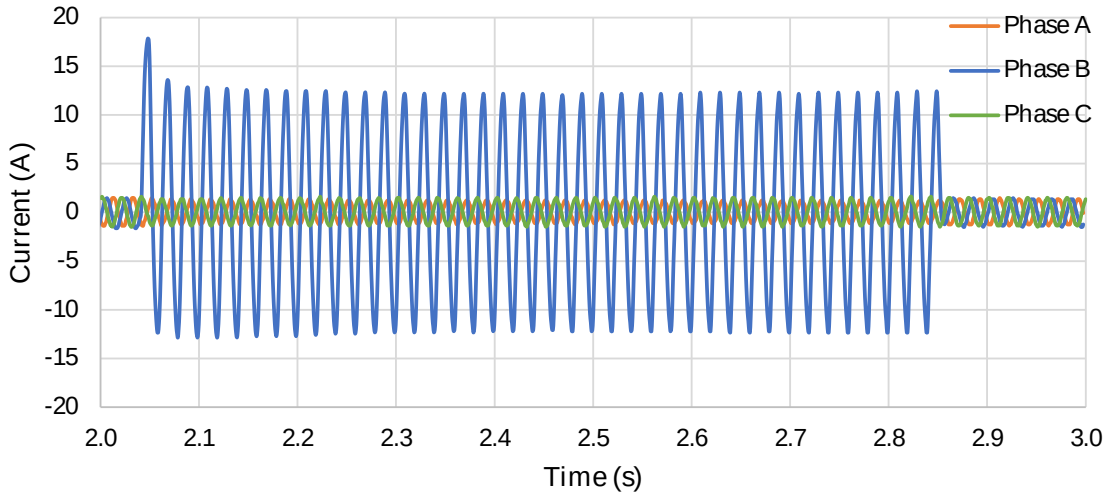

Figure 5.39 - Line currents under a phase-to-earth fault as a function of time, for the magnetic core traditional topology of the TT-SFCL.

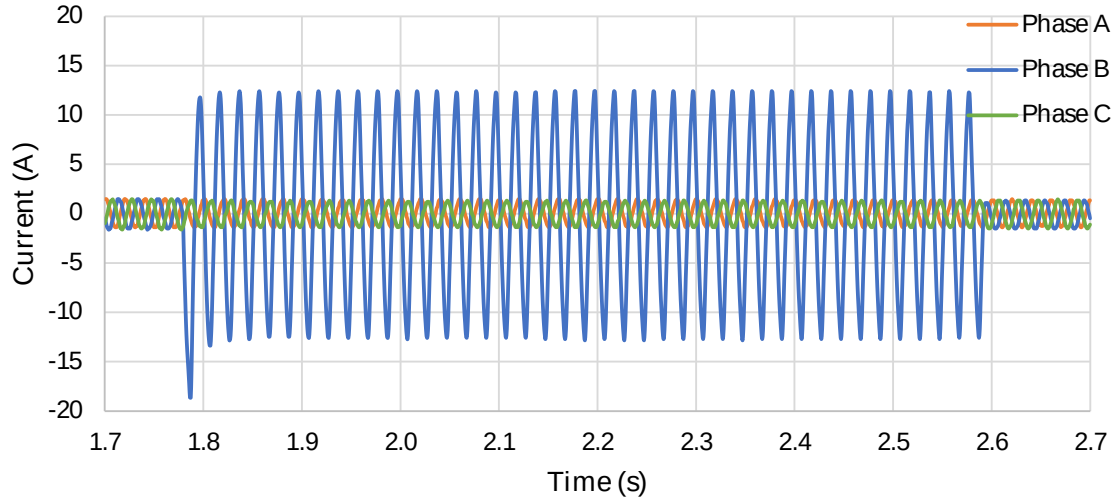

Figure 5.40 - Line currents under a phase-to-earth fault as a function of time, for the magnetic core-shell topology of the TT-SFCL.

FIGURE 5.41 (A) and FIGURE 5.41 (B) show the three-phase line currents in detail, for the moment when the fault is started, for traditional and shell core topology, respectively. As can be seen, the healthy phases are affected by the fault in phase B, for the traditional topology, which is not verified for the shell topology. This behaviour was expected due to the fact the shell topology has an alternative magnetic path that will provide a bypass for the magnetic flux from faulty phase B. Apparently, the recovery time is similar for both core topologies.

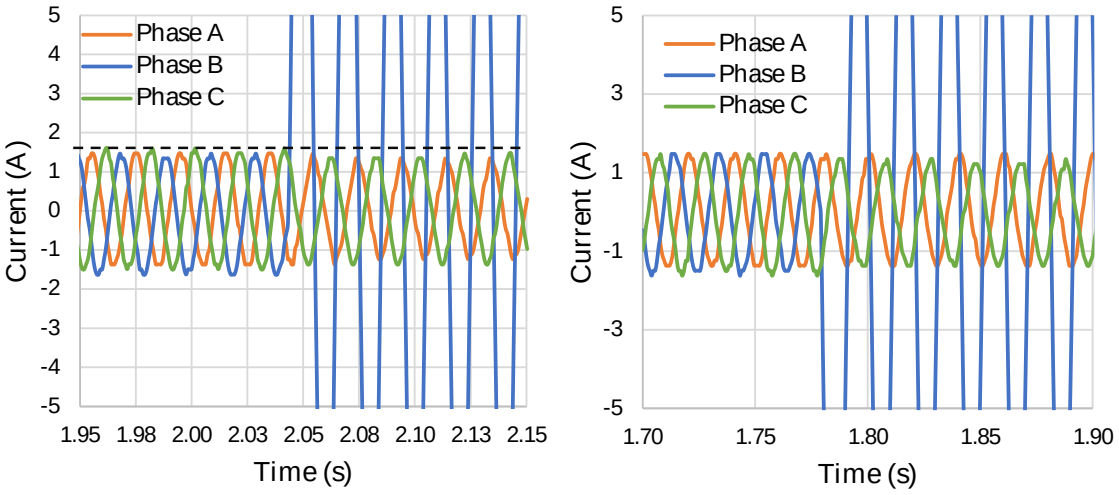

(a) (b)

Figure 5.41 - Line currents detailed for the moment when the phase-to-earth fault is started as a function of time, for each magnetic core topology of the TT-SFCL. (a) Traditional topology (b) Shell topology.

B. Current Analysis on HTS Rings

FIGURE 5.42 and FIGURE 5.43 show the HTS ring currents for each phase under a fault as a function of time, for a traditional or shell core topology, respectively. It can be observed that the HTS ring current has the same behaviour in all phases under fault, either for traditional topology or shell topology, however, the HTS rings in the shell topology show a half recovery time comparing to the traditional topology.

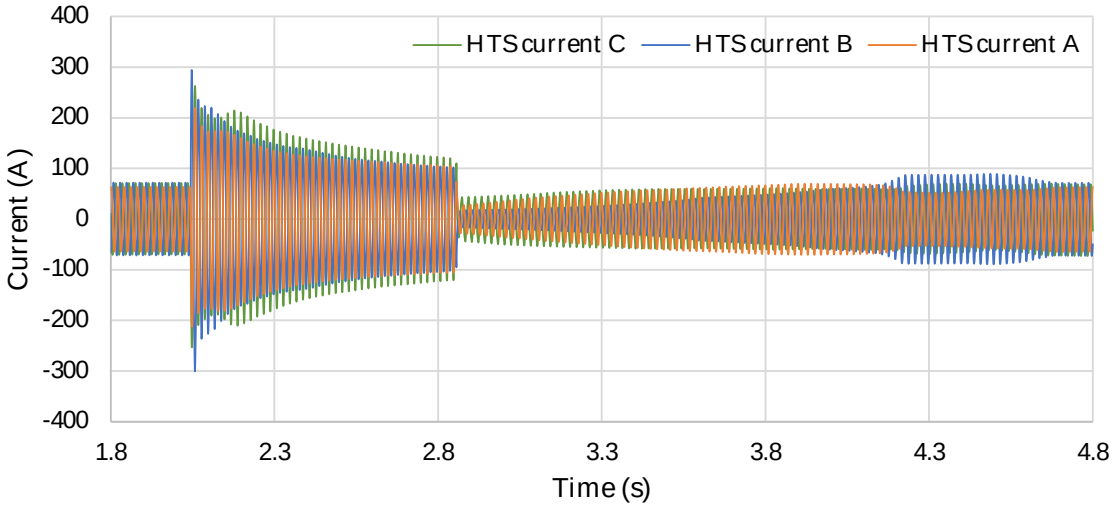

Figure 5.42 - HTS ring currents under a phase-to-earth fault as a function of time, for the magnetic core traditional topology of the TT-SFCL.

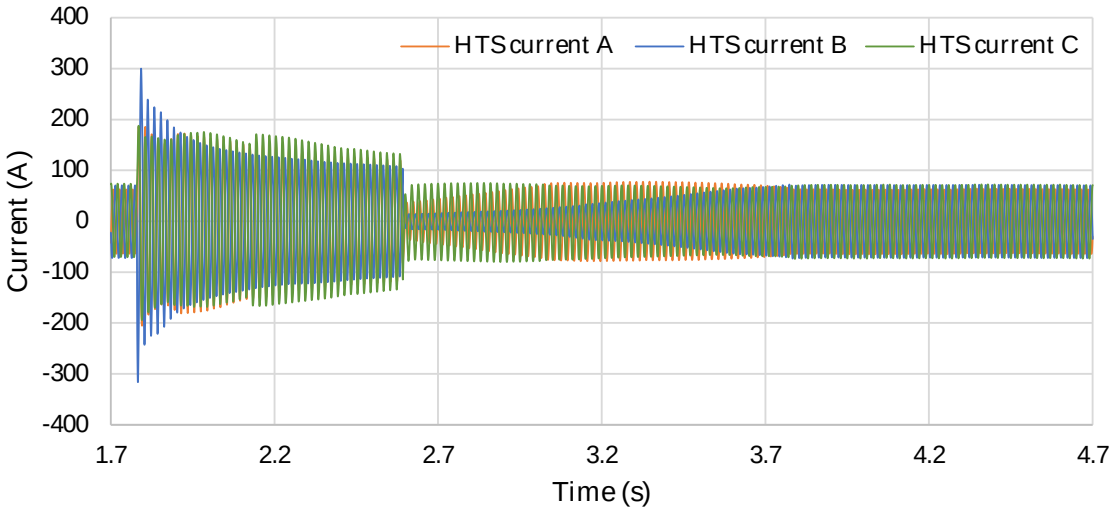

Figure 5.43 - HTS ring currents under a phase-to-earth fault as a function of time, for the magnetic core shell topology of the TT-SFCL.

FIGURE 5.44 (A) and FIGURE 5.44 (B) show the detailed HTS ring currents for each phase at the moment the fault started, for a traditional or shell core topology, respectively. During transient state, the HTS current of the non-faulty phases is more affected by the traditional topology. It should be noted that during the fault, HTS currents of the non-faulty phases are in phase.

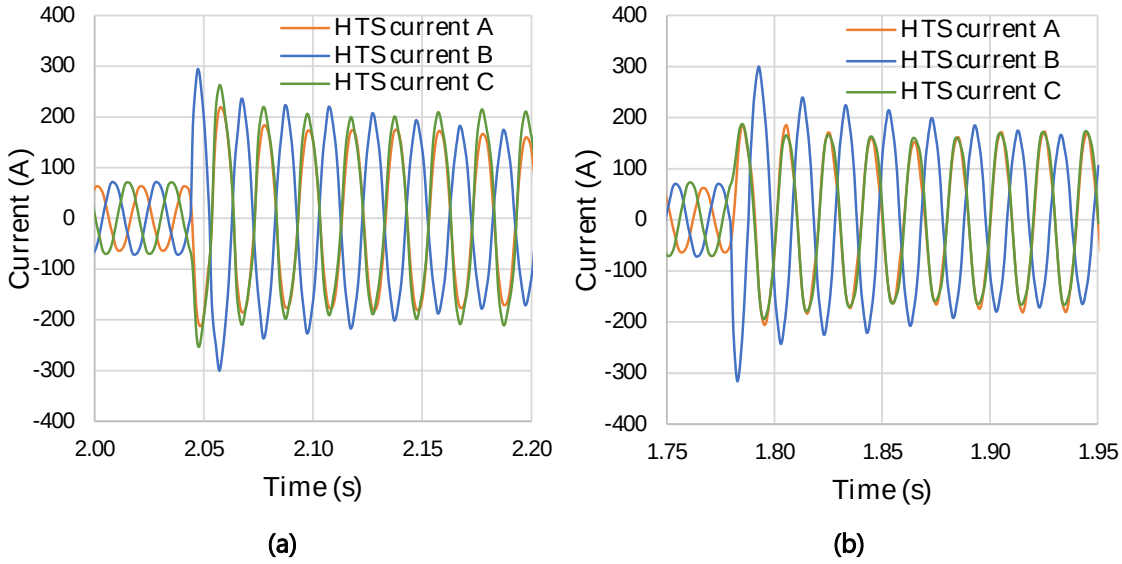

Figure 5.44 – HTS ring currents detailed for the moment when the phase-to-earth fault started as a function of time, for each magnetic core topology of the TT-SFCL. (a) Traditional topology. (b) Shell topology.

C. Linked Flux Analysis

FIGURE 5.45 and FIGURE 5.46 show the linked flux associated with each phase coil under a fault, as a function of time, for a traditional or shell core topology, respectively. The penetration of magnetic flux in the healthy phase limbs is higher for traditional topology than for shell topology (a reduction of 25% approximately), as well as the recovery time.

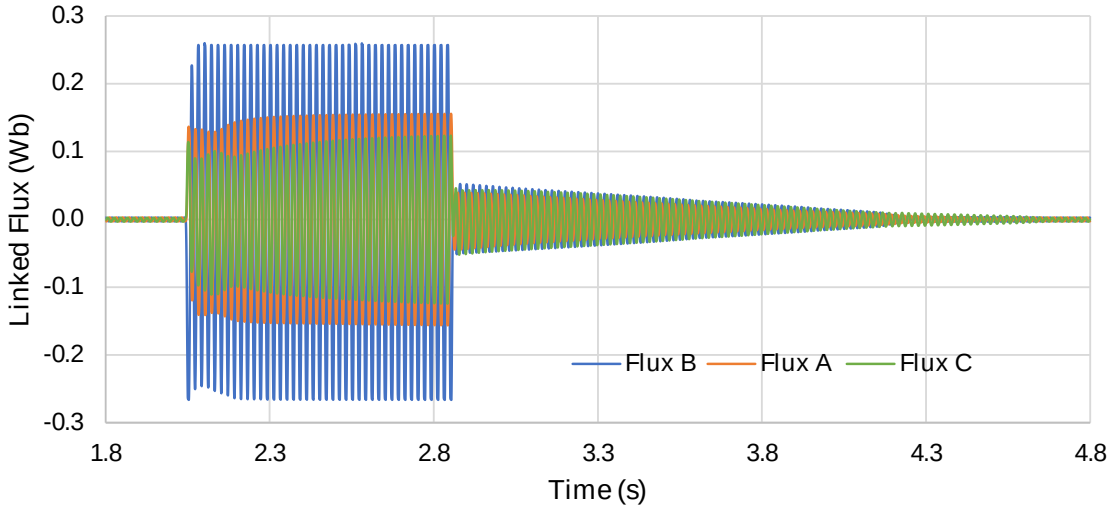

Figure 5.45 – Primary linked flux under a phase-to-earth fault as a function of time, for the magnetic core traditional topology of the TT-SFCL.

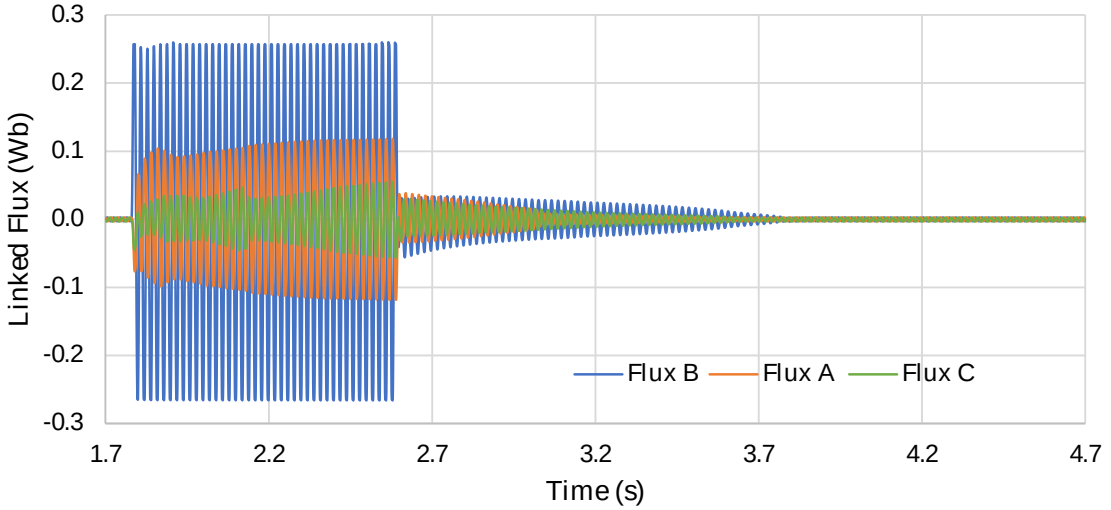

Figure 5.46 - Primary linked flux under a phase-to-earth fault as a function of time, for the magnetic core shell topology of the TT-SFCL.

D. Forces Analysis on HTS rings

FIGURE 5.47 shows the HTS ring current of phase B and the radial and axial stresses on the HTS rings associated with each phase, for the TT-SFCL using the traditional magnetic core. FIGURE 5.48 shows the same parameter but for the SFCL using the shell magnetic core topology. It is also shown the fault signal which represents the moment that the fault started and finished. TABLE 5.7 shows the maximum value of the developed

stress in the HTS rings for the traditional and shell topology. A much lower stress is obtained for the shell topology.

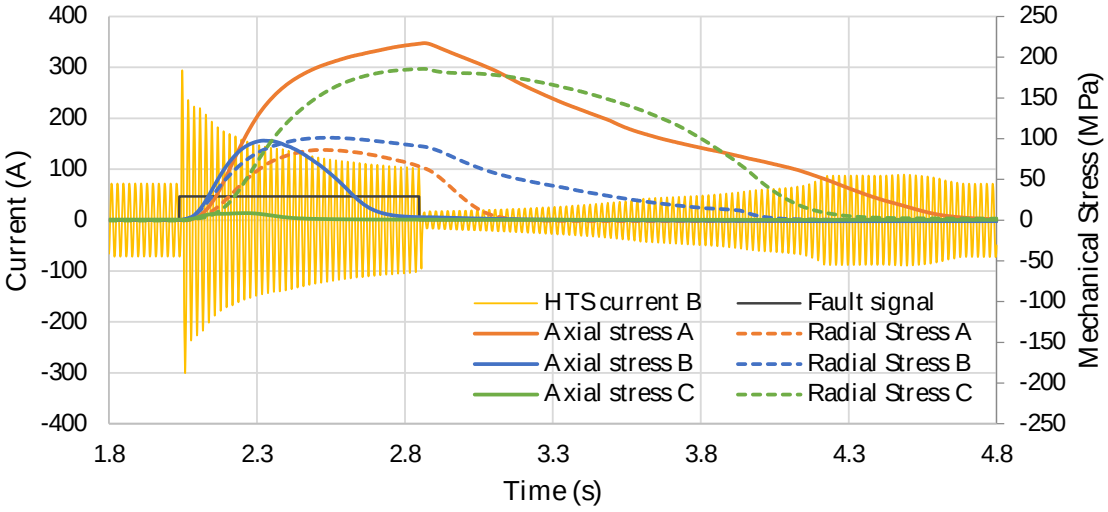

Figure 5.47 - HTS ring current and radial and axial stresses under a phase-to-earth fault as a function of time, for the magnetic core traditional topology of the TT-SFCL.

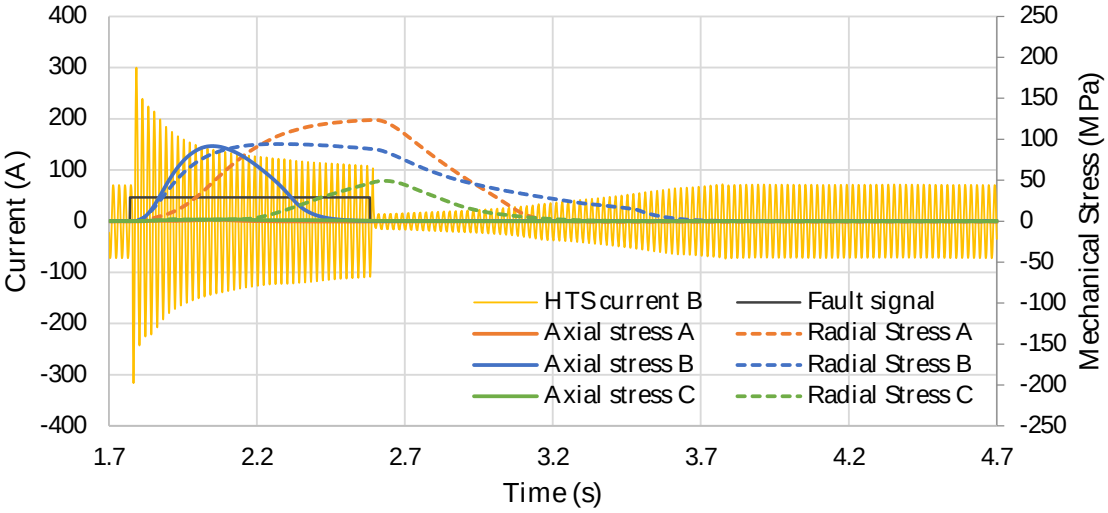

Figure 5.48 - HTS ring current and radial and axial stresses under a phase-to-earth fault as a function of time, for the magnetic core shell topology of the TT-SFCL.

Table 5.7 – Maximum values for the phase-to-earth fault for each topology.

Parameter	Traditional Topology	Shell Topology
Max. axial stress ring A (MPa)	217.3	1.7
Max. axial stress ring B (MPa)	97.7	91.8
Max. axial stress ring C (MPa)	8.6	2.3
Max. radial stress ring A (MPa)	86.2	123.7
Max. radial stress ring B (MPa)	101.3	94.2
Max. radial stress ring C (MPa)	185.8	49.4
Line current stead-state phase A (A)	12.4	12.4
Line current stead-state phase B (A)	1.5	1.5
Line current stead-state phase C (A)	1.6	1.5
Recovery Time (s)	1.8	1.0

5.4.3.2 Forces Measurement and Analysis for Phase-to-phase Fault

To cause a phase-to-phase fault between phase A and B, switch S_4 (FIGURE 5.37) is closed during the duration of the fault. Following, the line current of each phase, HTS ring currents associated with each phase, as well as the linked flux of each phase coil are analysed. In the end, the mechanical forces are discussed.

A. Line Current Analysis

FIGURE 5.49 (A) and FIGURE 5.49 (B) show the line current evolution as a function of time, of each phase, for a traditional or shell core topology, respectively. For each core topology, the current was limited to around 92% of the prospective short-circuit value (104 Arms) for the traditional topology and around 93% for shell topology. The topology of the magnetic core influences the limitation capacity of the limiter, where the shell topology is more effective. FIGURE 5.50 shows line current in detail, where can be verified that the line current of the healthy phase is not affected, during the fault.

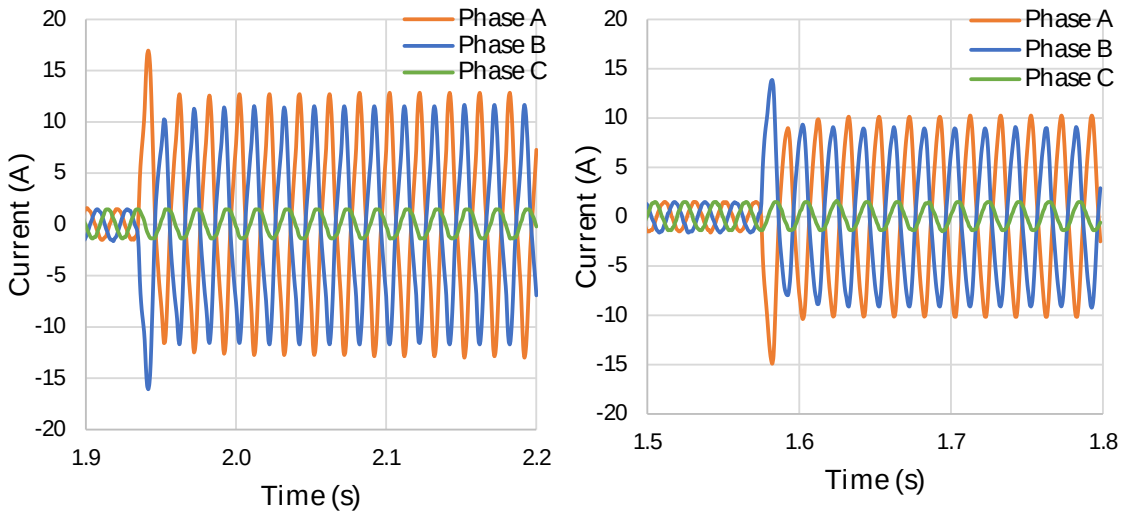

(a) (b)

Figure 5.49 - Line currents under a phase-to-phase fault as a function of time, for each magnetic core topology of the TT-SFCL. (a) Traditional topology. (b) Shell topology.

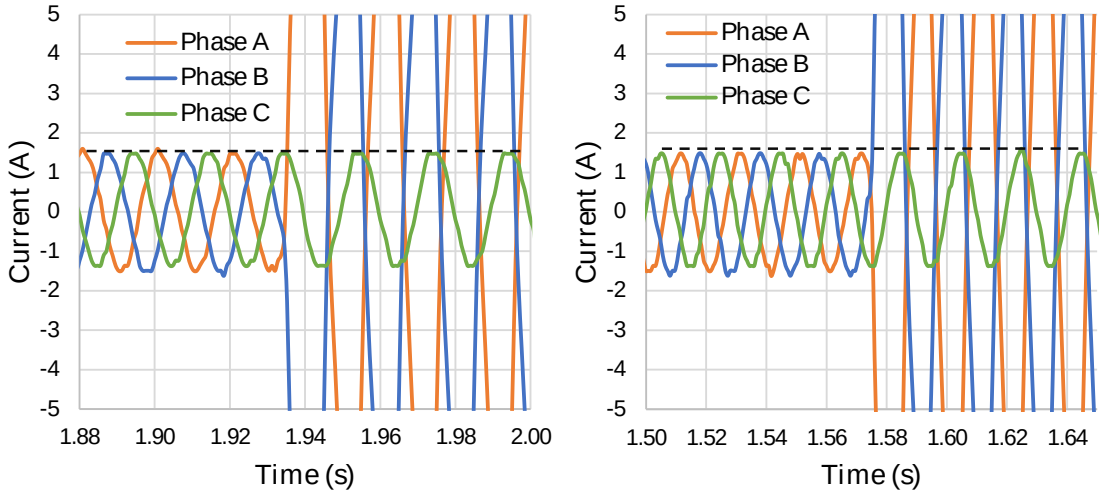

(a) (b)

Figure 5.50 - Line currents detailed for the moment when the phase-to-phase fault started as a function of time, for each magnetic core topology of the TT-SFCL. (a) Traditional topology. (b) Shell topology.

B. Current Analysis on HTS Rings

FIGURE 5.51 (A) and FIGURE 5.51 (B) show the HTS ring currents for each phase under a fault as a function of time, for a traditional or shell core topology, respectively. The HTS ring current has the same behaviour for the affected phases, either for traditional topology or shell topology, however, the HTS rings recovery is smoother in the shell

topology. The recovery time of the non-affected phase is instantaneous, as in the previous test, but is more affected for the traditional topology. Recovery time is similar for both core topology.

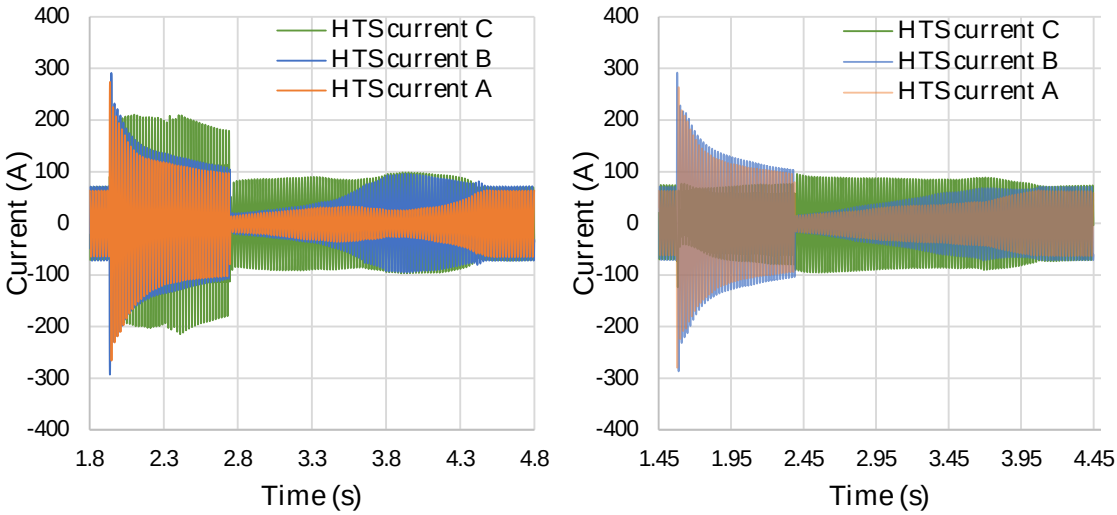

Figure 5.51 - HTS ring currents under a phase-to-phase fault as a function of time, for each magnetic core topology of the TT-SFCL. (a) Traditional topology. (b) Shell topology.

In FIGURE 5.52 (A) and FIGURE 5.52 (B) can be seen the HTS ring current in detail. HTS current of faulty phases are in phase opposition during the fault and the total harmonic distortion of HTS ring current of the non-affected phase is high.

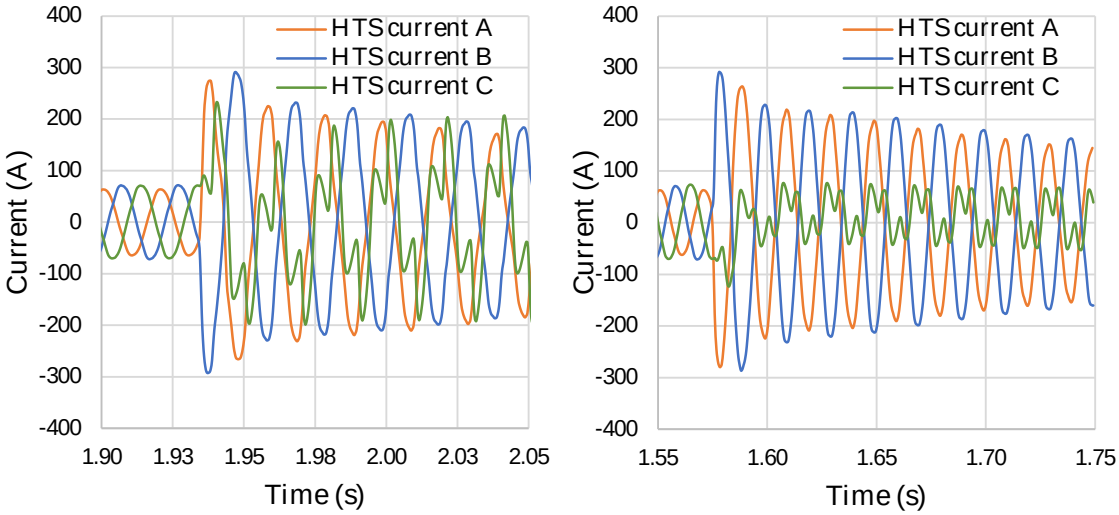

Figure 5.52 - HTS ring currents detailed for the moment when the phase-to-phase fault started as a function of time, for each magnetic core topology of the TT-SFCL. (a) Traditional topology. (b) Shell topology.

C. Linked Flux Analysis

FIGURE 5.53 (A) and FIGURE 5.53 (B) shows the linked flux associated with each phase coil under a fault as a function of time, for a traditional or shell core topology, respectively. The penetration of magnetic flux in the healthy phase limb is higher for traditional topology than for shell topology which has almost no magnetic flux penetration.

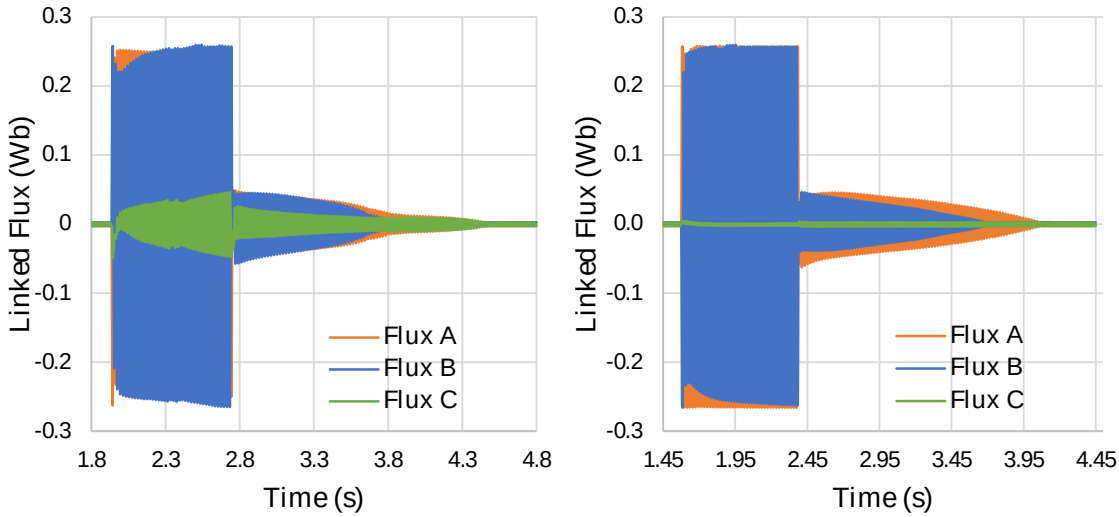

(a) (b)

Figure 5.53 - Primary linked flux under a phase-to-phase fault as a function of time, for each magnetic core topology of the TT-SFCL. (a) Traditional topology. (b) Shell topology.

D. Forces Analysis on HTS rings

FIGURE 5.54 shows the HTS ring current of phase B and the radial and axial stresses on the HTS rings associated with each phase, for the TT-SFCL using the traditional magnetic core. FIGURE 5.55 shows the same parameter but for the SFCL using the shell magnetic core topology. It is also shown the fault signal which represents the moment the fault started and finished. For the present case, the healthy phase is almost no affected by mechanical forces, mainly for the shell topology.

TABLE 5.8 shows the maximum value of the developed stress in the HTS rings for the traditional and shell topology.

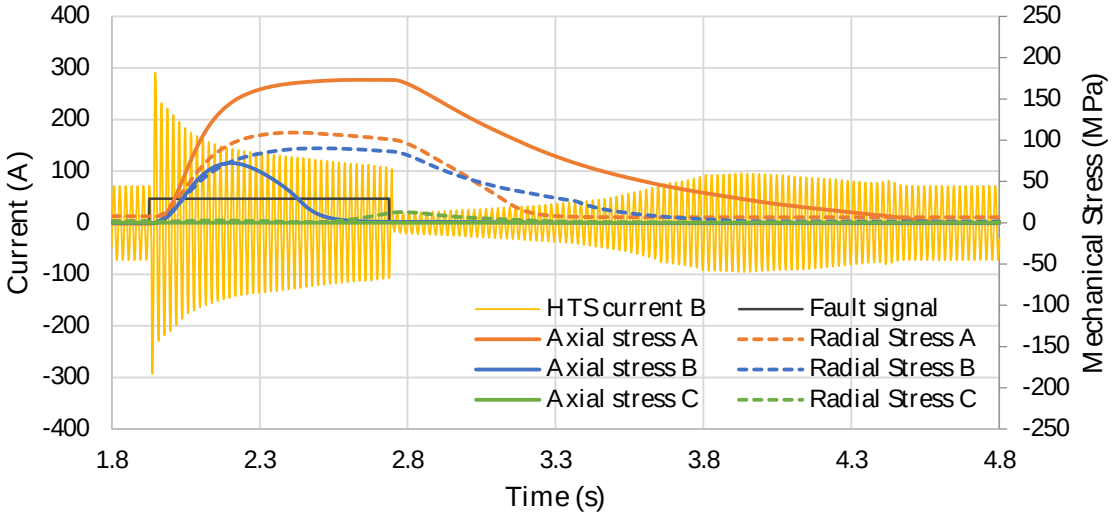

Figure 5.54 - HTS ring current and radial and axial stresses under a phase-to-phase fault as a function of time, for the magnetic core traditional topology of the TT-SFCL.

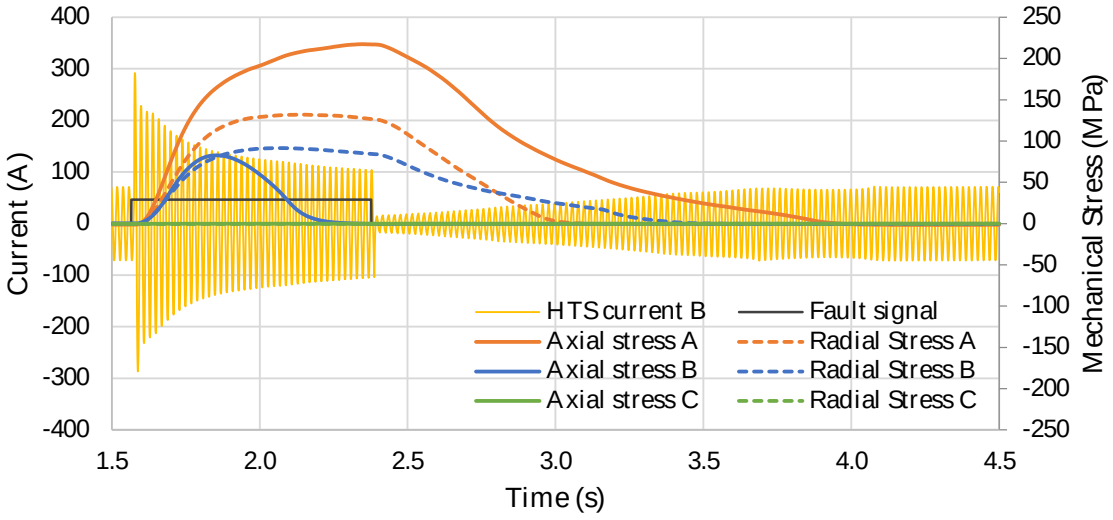

Figure 5.55 - HTS ring current and radial and axial stresses under a phase-to-phase fault as a function of time, for the magnetic core shell topology of the TT-SFCL.

Table 5.8 – Maximum values for the phase-to-phase fault for each topology.

Parameter	Traditional Topology	Shell Topology
Max. axial stress ring A (MPa)	173.2	217.4
Max. axial stress ring B (MPa)	72.4	82.7
Max. axial stress ring C (MPa)	5.8	1.0
Max. radial stress ring A (MPa)	109.4	132.0
Max. radial stress ring B (MPa)	90.3	91.5
Max. radial stress ring C (MPa)	13.0	1.0
Line current stead-state phase A (A)	12.8	10.5
Line current stead-state phase B (A)	11.6	9.2
Line current stead-state phase C (A)	1.5	1.5
Recovery Time (s)	1.8	1.5

5.4.3.3 Forces Measurement and Analysis for Three-phase-to-earth Fault

The last case in study is the three-phase-to-earth fault. To cause the fault in phase, switches S_1, S_2 and S_3 (FIGURE 5.37) are closed during the duration of the fault. Following, the line current of each phase, HTS ring currents associated with each phase, as well as the linked flux of each phase coil are analysed and also the mechanical forces developed in the HTS rings.

A. Line Current Analysis

FIGURE 5.56 (A) and FIGURE 5.56 (B) show the line current evolution as a function of time, of each phase, for a traditional or shell core topology, respectively. For traditional core topology, the current was limited in around 85%, 86% and 77%, for phase A, B and C respectively, of the prospective short-circuit value (60 Arms). For shell core topology, the current was limited in around 87%, 86% and 83%, for phase A, B and C. The topology of the magnetic core influences the limitation capacity of the limiter, where the shell topology has better limitation performance. It is also important to notice that the current limitation is not similar for each phase. This behaviour is caused probably by a non-symmetric magnetic path or due to AC coils differences.

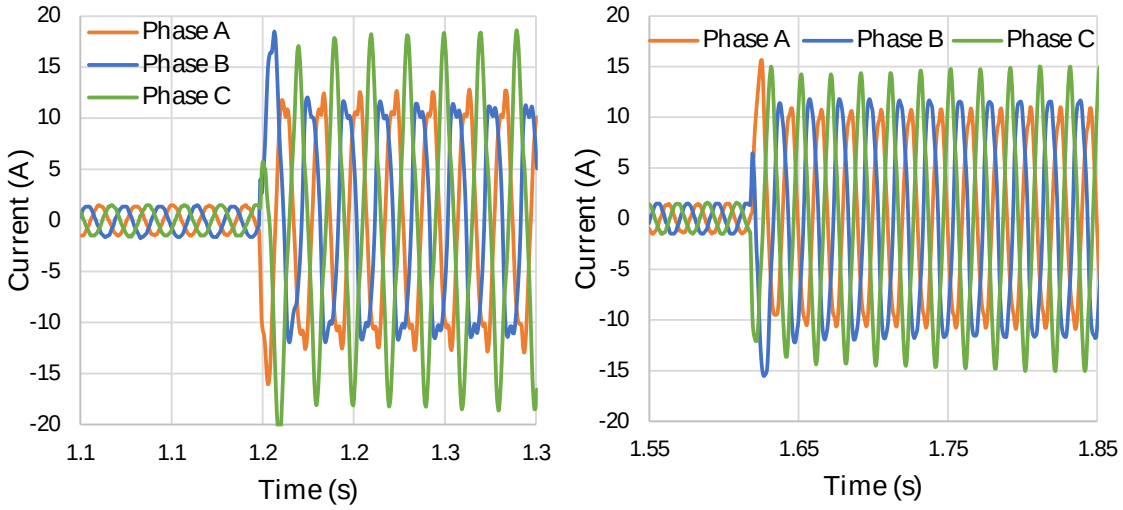

Figure 5.56 - Line currents under a three-phase-to-earth fault as a function of time, for each magnetic core topology of the TT-SFCL. (a) Traditional topology. (b) Shell topology.

B. Current Analysis on HTS Rings

FIGURE 5.57 (A) and FIGURE 5.57 (A) show the HTS ring currents for each phase under a fault as a function of time, for a traditional or shell core topology, respectively. It can be observed that the HTS ring current behaviour in like each phase under fault, either for traditional topology or for shell topology, and according to last cases. However, the HTS rings current, in the shell topology, show now a recovery time higher comparing to the traditional topology.

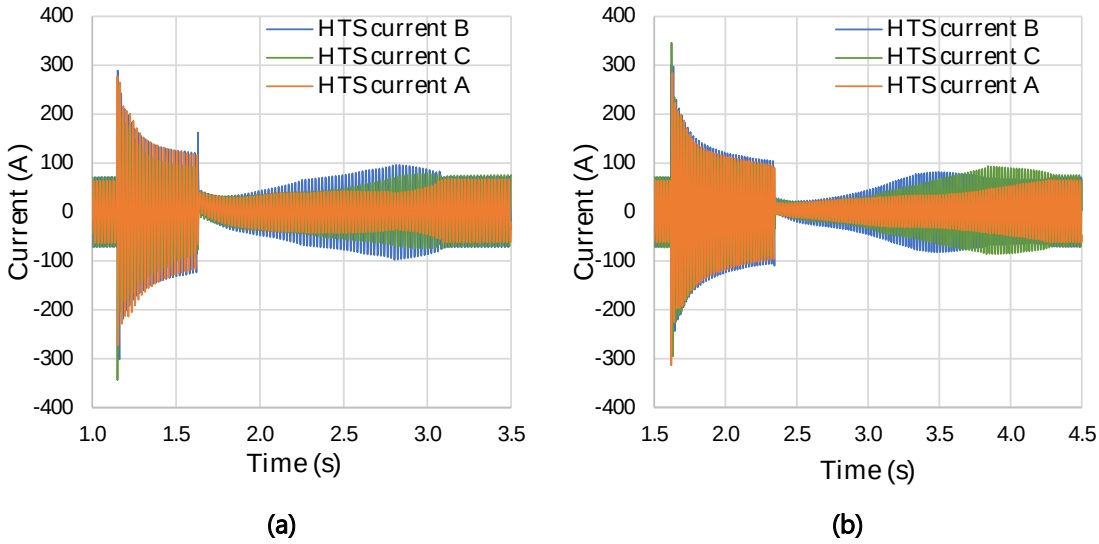

Figure 5.57 - HTS ring currents under a three-phase-to-earth fault as a function of time, for each magnetic core topology of the TT-SFCL. (a) Traditional topology. (b) Shell topology.

FIGURE 5.58 shows the HTS ring currents in detail where can be seen that all currents are a 120º out of phase with each other.

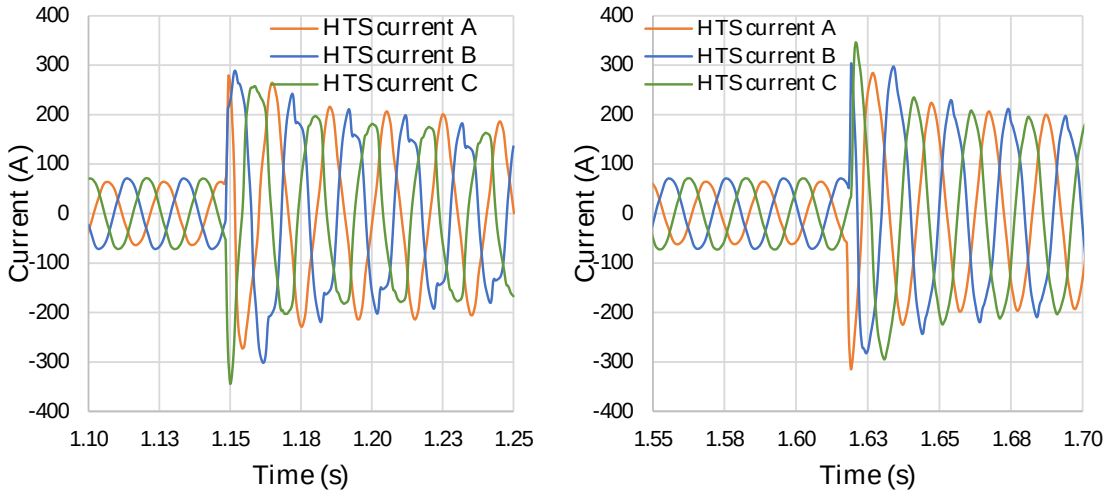

(a) (b)

Figure 5.58 - HTS ring currents detailed for the moment when the three-phase-to-earth fault started as a function of time, for each magnetic core topology of the TT-SFCL. (a) Traditional topology. (b) Shell topology.

C. Linked Flux Analysis

FIGURE 5.59 (A) and FIGURE 5.59 (B) show the linked flux associated with each phase coil under a fault as a function of time, for a traditional or shell core topology, respectively.

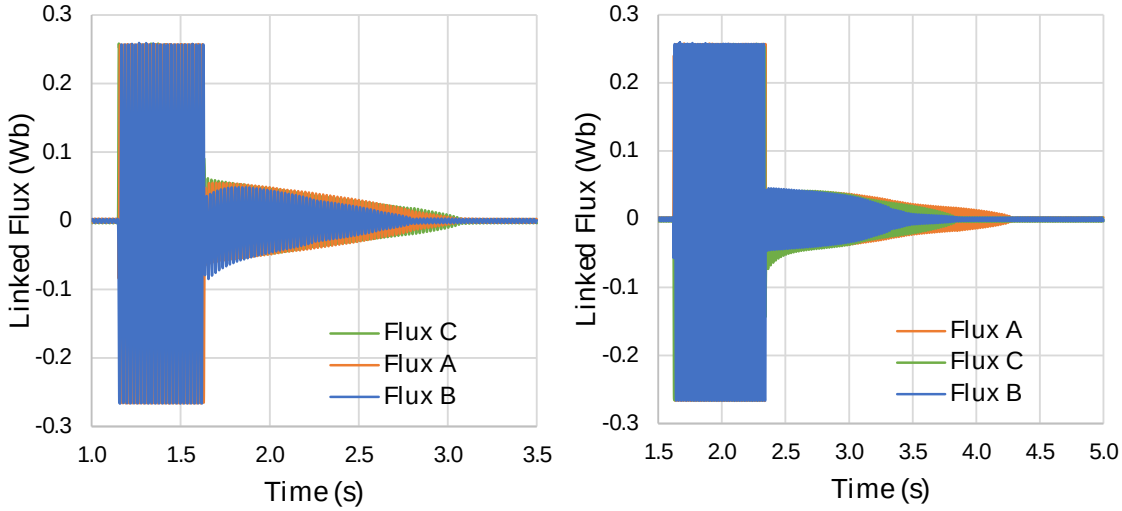

(a) (b)

Figure 5.59 - Primary linked flux under a three-phase-to-earth fault as a function of time, for each magnetic core topology of the TT-SFCL. (a) Traditional topology. (b) Shell topology.

The penetration of magnetic flux in faulty phases limbs shows the same behaviour. Total recovery time is higher for the shell topology, with different recovery time for each phase.

D. Forces Analysis on HTS rings

FIGURE 5.60 shows the HTS ring current of phase B and the radial and axial stresses on the HTS rings associated with each phase, for the SFCL using the traditional magnetic core. FIGURE 5.61 shows the same parameter but for the SFCL using the shell magnetic core topology. For the present case, phase A is the most affected by mechanical forces, mainly for the shell topology. As discussed before, this happens due to the non-symmetric magnetic paths of the SFCL core.

TABLE 5.9 shows the maximum value of the developed stress in the HTS rings for the traditional and shell topology.

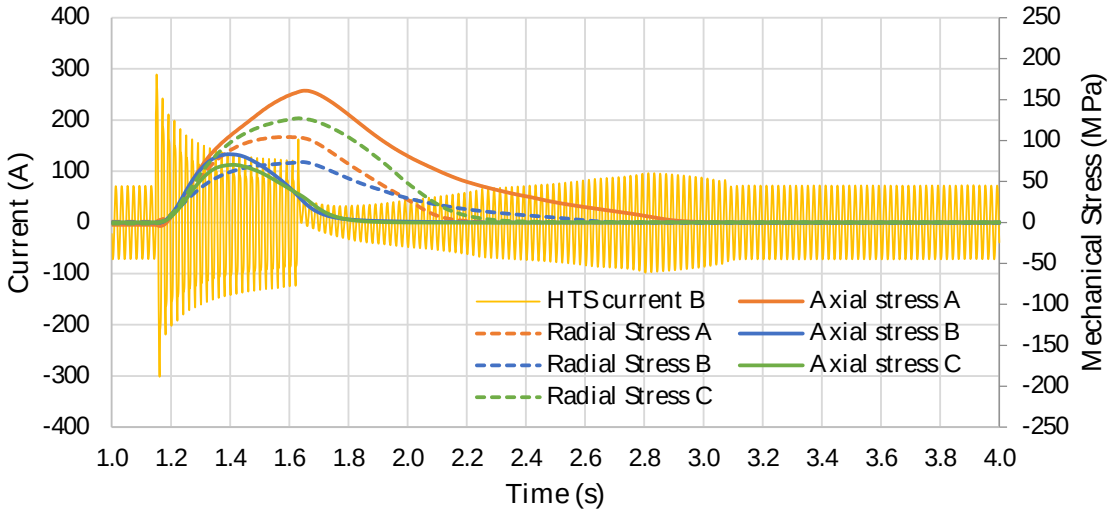

Figure 5.60 - HTS ring current and radial and axial stresses under a three-phase-to-earth fault as a function of time, for the magnetic core traditional topology of the TT-SFCL.

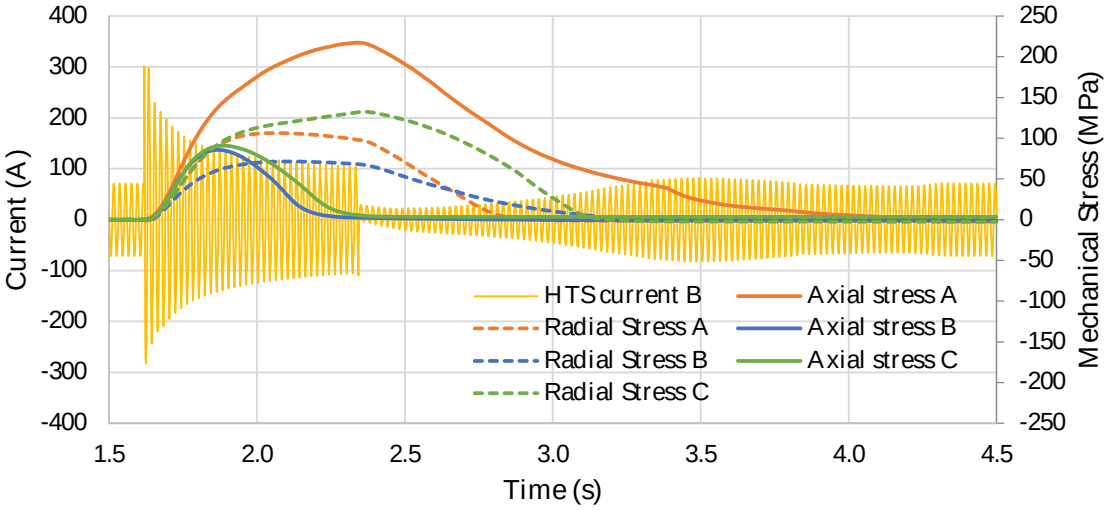

Figure 5.61 - HTS ring current and radial and axial stresses under a three-phase-to-earth fault as a function of time, for the magnetic core shell topology of the TT-SFCL.

Table 5.9 – Maximum values for the three-phase-to-earth fault for each topology.

Parameter	Traditional Topology	Shell Topology
Max. axial stress ring A (MPa)	224.0	110.1
Max. axial stress ring B (MPa)	83.3	83.9
Max. axial stress ring C (MPa)	75.9	92.5
Max. radial stress ring A (MPa)	108.5	56.2
Max. radial stress ring B (MPa)	73.8	69.3
Max. radial stress ring C (MPa)	158.5	159.1
Line current stead-state phase A (A)	13.0	10.1
Line current stead-state phase B (A)	11.7	11.8
Line current stead-state phase C (A)	18.9	14.6
Recovery Time (s)	1.6	2.0

5.4.3.4 Summary of three-phase TT-SFCL tests

The three-phase TT-SFCL was tested for the three most common faults that occur in the power grid.

Regarding the limitation capability of the limiter, there is no big difference between the traditional topology to shell topology. In both topologies, the current limitation was above 85%, although the shell topology shows slightly superior performance.

Analysing the HTS rings current, it can be concluded that their behaviour is similar, in both topologies, for faulty phases. However, the healthy phase is less affected in shell topology. The recovery time is lower for shell-type SFCL under asymmetric faults, specially on phase-to-ground fault, the most common type in electrical grids. This can be verified by analysing the linked flux graphs, where the magnetic flux penetration in healthy phases is much lower in shell topology than traditional topology.

In all tests, strain gauges detected the mechanical stresses while short-circuit fault occurred. The behaviour of the axial and radial stresses is similar to what was analysed and discussed and CHAPTER 5.4.2. In healthy phases, electromechanical forces, axial and radial, are lower in shell type topology. In faulty phases, electromechanical forces are usually lower in shell-type topology, except for phase-to-phase fault.

FIGURE 5.62 (A), FIGURE 5.62 (B) and FIGURE 5.63 show the maximum mechanical stress measured for each HTS ring in phases A, B and C for the three types of faults tested. YBCO tape has a stress limit of around 864 MPa *(Ilin et al., 2015)* until its critical current starts to degrade, under tensile stresses. Considering the obtained results, there was no risk regarding superconducting material integrity. For non-affected phases, the shell topology allows lower stresses on the HTS rings.

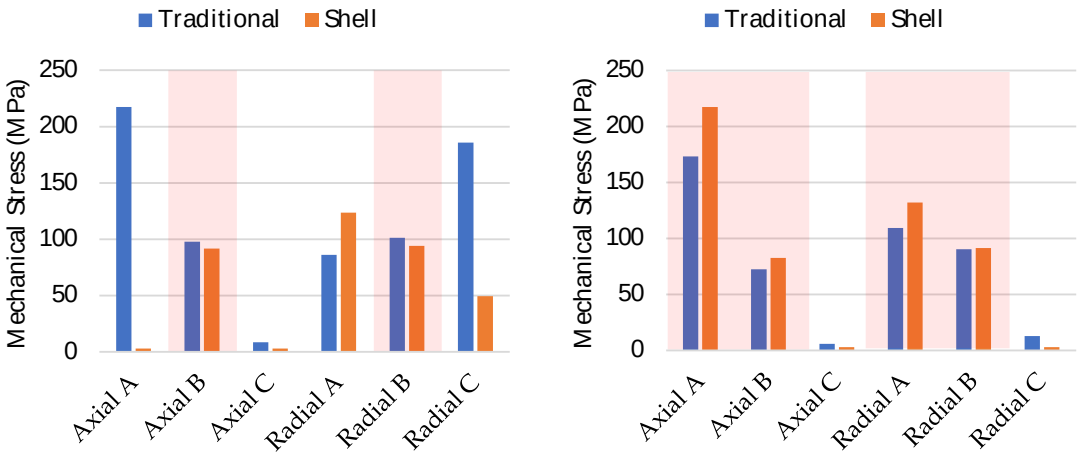

Figure 5.62 – Maximum axial and radial mechanical stress values for the HTS rings of each phase according to the type of fault under study. (a) PhaseB to earth fault. (b) PhaseA to PhaseB fault.

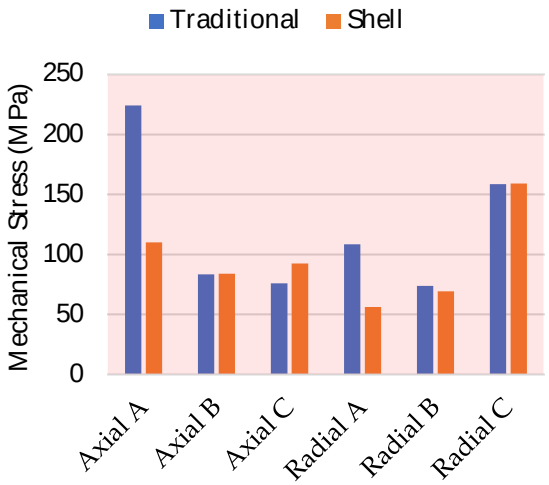

Figure 5.63 - Maximum axial and radial mechanical stress values for the HTS rings of each phase for the three-phase-to-earth fault.

5.5 Summary

In this chapter, the electromechanical forces developed on a TT-SFCL under short-circuit conditions was simulated by FEM and measured by real tests in order to be analysed and compared.

A. FEM simulations

Concerning the FEM simulation, four different configurations of HTS rings were analysed: radial and axial distributions, concentric with the primary coil or aligned with it. Regarding the SFCL behaviour, it is possible to conclude that the limitation capacity of SFCL is not affected by ring distribution configurations. In normal operation conditions, current on ring number 2 is always smaller than ring number 1 and number 3. In short-circuit conditions, currents are equal in all rings. Regarding the electromagnetic forces developed on HTS rings, axial forces compress the rings in all scenarios, however, these are more balanced in radial rings configuration. Contrariwise, radial forces are more balanced in axial configuration, their effect on the rings (compression or tensile) is the same and they are weaker. Simulation analysis of normal magnetic induction field in SFCL rings shows higher values in radial configuration (around 0.08 T in rings top).

According to achieved results, axially concentric configuration seems to be the most adequate architecture for TT-SFCL, whether to build a secondary with short-circuited ring or through a solenoid coil. The advantages are as following:

- Balanced and minimum radial forces intensity, and the same effect on the rings, allows for easier manufacturing of the holder.
- Outer rings (ring number 1 and 3) suffer higher axial forces, however, those forces are lower in comparison with radial configuration. The inner rings suffer less from the effect of these forces.
- The normal component of the magnetic induction field is also lower in axial configuration.

B. Laboratory tests

Concerning the laboratory tests, the most common types of faults in the power grid were tested in a laboratory-scale TT-SFCL, which are the phase-to-earth fault, the phase-to-phase fault and the three-phase-to-earth fault.

Analysing the results, it is possible to conclude that the measurement procedure using strain gauges was able to detect mechanical forces as soon as the short-circuit failure started. The measurement procedure based on strain gauges allows a quick and reliable method to obtain mechanical stresses developed on HTS power devices, mainly in the short-circuited HTS tapes of the TT-SFCL, making it a viable method to be used in the prevention of possible damages. Nevertheless, further measurements with strain

gauge local heating compensation and including a second strain gauge, to eliminate the bending effect, will be needed to accurate the process.

Tests on the single-phase device concluded that for the chosen configurations and under fault conditions, both radial and axial forces develop tensile stresses. The values obtained are all below the critical limits for YBCO tapes integrity. It was observed a delay between the time response of the electrical and mechanical signals. This could result from two aspects: (a) the increase in the temperature of strain gauges during the short-circuit conditions, as a result of higher currents (b) the fact that the electrical signals are faster detected than mechanical deformations (changes).

The tests performed with the three-phase device concluded that in general, the shell topology allows a lower magnetic flux penetration in the healthy phase limbs, a reduced recovery time of the faulty phase, as well as a better current behaviour of the healthy phases, is possible. The previous topology is the better choice for this type of SFCL.

According to *(Ilin et al., 2015)*, YBCO tapes have stress and strain limits around 864 MPa and 0.67%, respectively, until their critical current starts to degrade (under tensile stresses). Considering the obtained results, for this type of fault, there was no risk regarding superconducting material integrity. So, the TT-SFCL will maintain its mechanical integrity after the fault.

6

Conclusions and Future Work

The contribution of this thesis for the study of the integration of superconducting fault current limiters in electrical distribution grids is based on the development of modelling and simulation design tools for the SC-SFCL, the development of an optimisation method for the SC-SFCL which could be adapted for other types of SFCL, and the implementation of a measurement procedure to determine the mechanical forces on a TT-SFCL as well as the study of the effects of such forces.

At the end of each chapter, relevant conclusions were presented and discussed. Following, a general summary is performed:

- The modelling methodology based on reluctance approach allowed the obtention of an approximate $\Psi - i$ characteristic of the SFCL, essential to be used in the first stage of the optimisation process. The magnetic characteristic is obtained faster using this methodology.
- The simulation methodology, based on the $\Psi - i$ characteristic of the SFCL, appeared as a faster simulation tool to predict the transient behaviour of the SFCL under a fault event. This methodology was validated by FEM simulation and experimental tests, which resulted in good and accurate results.
- The optimisation method uses the previous modelling and simulation methodologies to carry out an optimisation through genetic algorithms to find the optimal SFCL design. The optimisation method consists of two steps. The first step gives an approximated optimal solution by a multi-objective approach

and a decision process. The final step gives the final optimal solution, refined by a more accurate simulation method (based on FEM simulations).

- A prototype of an SFCL of saturated cores was optimised, built, and tested. Different types of faults were caused in order to analyse the behaviour of the SC-SFCL and verify if it meets the proposed requirements for the optimisation process. The $\Psi - i$ characteristic of the SC-SFCL obtained by the optimisation process and by laboratory test shows good agreement, validating the methodologies used for the optimisation.
- The measurement procedure presented in this work allows a quick and reliable method to obtain mechanical stresses developed on HTS power devices making it a viable method to be used in the prevention of possible damages.
- For the tested prototypes (both single-phase and three-phase devices), the developed mechanical stresses were not strong enough to put the integrity of the limiter at risk.

6.1 Future Work

Future work should consider the following aspects:

6.1.1 Modelling, Simulation and Test

- Consider the effect of magnetic coupling between DC bias coil and AC coils.
- Improve the reluctance methodology in order to include more magnetic paths to increase the accuracy of the method.

6.1.2 Design Optimisation

- Instead of using the constitutive parts of the limiter, i.e. dimensions and electrical parameters, to obtain the $\Psi - i$ characteristic of the SFCL for the optimisation process, the $\Psi - i$ characteristic could be modelled by a mathematical expression and used directly in the optimisation process. After an optimal $\Psi - i$ characteristic is found, the appropriated dimensions and electrical parameters of the SFCL could be obtained by studying the relation between the parameters used in the $\Psi - i$ parameterisation and the constitutive parts of the limiter.

6.1.3 Analysis of Electromechanical Forces Developed under Faults

- Study of the effect of electromechanical forces in high power ratings SFCL of transformer type.
- Improve the measurement procedure for mechanical forces with extra strain gauges to nullify the bending effect and develop a better strategy for local heating compensation.

C

Contributions and Publications

During this work, 4 master dissertations were done in collaboration and co-supervised by the author, to contribute and implement the objectives of this work.

- 2014 - Amanda Taillacq Cabrera, "Estudo das forças electrodinâmicas desenvolvidas em limitadores de corrente supercondutores" (" Study of the electromechanical forces in superconducting fault current limiters").
- 2016 - Ricardo Manuel Machado dos Santos Mateus, "Medição dos esforços eletromecânicos desenvolvidos em dispositivos de potência que utilizam materiais supercondutores" ("Measurements of electromechanical forces in superconducting power devices").
- 2019 – Filipe Miguel França Saldanha do Vale, "Desenvolvimento de um dispositivo de medida para determinação dos esforços eletromecânicos em limitadores de corrente supercondutores" ("Development of a measuring device for determining electromechanical forces in superconducting fault current limiters").
- 2020 – Ivo Diogo David, "Construção e ensaio de um limitador de corrente supercondutor trifásico do tipo indutivo de núcleos saturados" ("Built and test af a three-phase superconducting fault current limiter of saturated cores type").

During this work, several scientific papers were published, which are listed below.

A. Journal Papers

- Vilhena, N., Murta-Pina, J., Pronto, A., Alvarez, A., "A design methodology for the optimisation of three-phase SFCL of saturated cores type", *IEEE Transactions on Applied Superconductivity*, 28, 4, 5601505, June 2018. DOI: 10.1109/TASC.2018.2806001
- Murta-Pina, J., Vilhena, N., Arsenio, P., Pronto, A., Alvarez, A., "Preliminary Design and Test of Low-Resistance High Temperature Superconducting Short-Circuited Coils", *IEEE Transactions on Applied Superconductivity*, 28, 4, 4604105, June 2018. DOI: 10.1109/TASC.2018.2820726
- Vilhena, N., Taillacq, A., Pronto, A., Murta-Pina, J., Alvarez, A., "Analysis of electromagnetic forces in superconducting fault current limiters under short-circuit condition", *IEEE Transactions on Applied Superconductivity*, 26, 3, 5601704, April 2016. DOI: 10.1109/TASC.2016.2548482
- Vilhena, N., Arsénio, P., Murta-Pina, J., Pronto, A., Álvarez, A., "A Methodology for modelling and simulation of Saturated Cores Fault Current Limiters", *IEEE Transactions on Applied Superconductivity*, 25, 3, 5600704, June 2015. DOI: 10.1109/TASC.2014.2374179
- Arsénio, P., Silva, T., Vilhena, N., Pina, J. M., Pronto, A., "Analysis of characteristic hysteresis loops of magnetic shielding inductive fault current limiters", *IEEE Transactions on Applied Superconductivity*, 23, 3, pp. 5601004, June 2013. DOI: 10.1109/TASC.2012.2235896

B. Conference Proceedings

- Mateus, R., Vilhena, N., Pronto, A., Igreja, R., "Measurements of electromechanical forces in superconducting fault current limiters tapes under short circuit conditions", *2019 International Young Engineers Forum (YEF-ECE)*, May 2019. DOI: DOI: 10.1109/YEF-ECE.2019.8740820
- Vilhena, N., Arsénio, P., Murta-Pina, J., Pronto, A., Álvarez, A., "Development of a Simulink Model of a Saturated Cores Superconducting Fault Current Limiter ",

Camarinha-Matos L., Baldissera T., Di Orio G., Marques F. (eds) Technological Innovation for Cloud-Based Engineering Systems. DoCEIS 2015. IFIP Advances in Information and Communication Technology, vol 450. Springer, Cham, March 2015. DOI: 10.1007/978-3-319-16766-4_44

- Figueira, P., Pronto, A., Vilhena, N., Pina, J., "Electric and magnetic properties measurement and analysis of a conventional and a superconducting power transformer", *Journal of Physics: Conference Series*, 507, 3, 032015, May 2014. DOI: 10.1088/1742-6596/507/3/032015
- Ferreira, R., Murta-Pina, J., Vilhena, N., Arsenio, P., Pronto, A., Martins, J., " Analysis of the effects of asymmetric faults in three-phase superconducting inductive fault current limiters", *Journal of Physics: Conference Series*, 507, 3, 032036, May 2014. DOI: 10.1088/1742-6596/507/3/032036
- P. Arsénio, N. Vilhena, J. Murta-Pina, A. Pronto, and A. Álvarez, "Design Aspects and Test of an Inductive Fault Current Limiter", *Electrical, Control and Communication Engineering*, vol. 5, no. 1, pp. 40–45, Jan. 2014. DOI: 10.2478/ecce-2014-0006

R

References

Abramovitz, A., & Ma Smedley, K. (2012). Survey of Solid-State Fault Current Limiters. *IEEE Transactions on Power Electronics*, *27*(6), 2770–2782. https://doi.org/10.1109/TPEL.2011.2174804

Akhmatov, V., & Eriksen, P. Bø. (2007). A Large Wind Power System in Almost Island Operation - A Danish Case Study. *IEEE Transactions on Power Systems*, *22*(3), 937–943. https://doi.org/10.1109/TPWRS.2007.901283

Amaran, S., Sahinidis, N. V., Sharda, B., & Bury, S. J. (2016). Simulation optimization: a review of algorithms and applications. *Annals of Operations Research*, *240*(1), 351–380. https://doi.org/10.1007/s10479-015-2019-x

Arsénio, P. (2017). *Contribution for the Study of Inductive Fault Current Limiters in Electrical Distribution Grids* [Universidade NOVA de Lisboa]. http://hdl.handle.net/10362/26673

Arsenio, P., Silva, T., Vilhena, N., Pina, J. M., & Pronto, A. (2013). Analysis of Characteristic Hysteresis Loops of Magnetic Shielding Inductive Fault Current Limiters. *IEEE Transactions on Applied Superconductivity*, *23*(3), 5601004–5601004. https://doi.org/10.1109/TASC.2012.2235896

Arsénio, P., Vilhena, N., Murta-Pina, J., Pronto, A., & Álvarez, A. (2014). Design Aspects and Test of an Inductive Fault Current Limiter. *Electrical, Control and Communication Engineering*, *5*(1), 40–45. https://doi.org/10.2478/ecce-2014-0006

Bahramian Habil, H., Azad-Farsani, E., & Askarian abyaneh, H. (2015). A novel method for optimum fault current limiter placement using particle swarm optimization algorithm. *International Transactions on Electrical Energy Systems*, *25*(10), 2124–2132. https://doi.org/10.1002/etep.1952

Barroso, P. (2014). *Projeto, ensaio e comparação de limitadores de corrente supercondutores trifásicos indutivos* [Universidade NOVA de Lisboa]. http://hdl.handle.net/10362/14097

Bäuml, K., & Kaltenborn, U. (2012). Possibilities of integrating renewable generation to the distribution grid by fault current limiters. *CIRED 2012 Workshop: Integration of Renewables into the Distribution Grid*, *137*, 137–137. https://doi.org/10.1049/cp.2012.0768

Bednorz, J. G., & Müller, K. A. (1986). Possible high Tc superconductivity in the Ba-La-Cu-O system. *Zeitschrift Für Physik B Condensed Matter*, *64*(2), 189–193. https://doi.org/10.1007/BF01303701

Bekhaled, M. (1987). *Superconductive AC current limiter* (Patent No. US4700257A).

Bertsimas, D., & Tsitsiklis, J. N. (1997). *Introduction to Linear Optimization*. Athena Scientifi.

Boenig, H., & Paice, D. (1983). Fault current limiter using a superconducting coil. *Magnetics, IEEE Transactions On*, *19*(3), 1051–1053. https://doi.org/10.1109/TMAG.1983.1062396

Brauer, J. (1975). Simple equations for the magnetization and reluctivity curves of steel. *IEEE Transactions on Magnetics*, *11*(1), 81–81. https://doi.org/10.1109/TMAG.1975.1058555

Buckel, W., & Kleiner, R. (2004). *Superconductivity: Fundamentals and Applications* (2nd ed.). Wiley - VCH.

Cave, J., Willen, D., Nadi, R., & Brissette, Y. (1999). Development of inductive fault current limiters up to 100 kVA class using bulk HTS materials. *IEEE Transactions on Appiled Superconductivity*, *9*(2), 1335–1338. https://doi.org/10.1109/77.783549

Chang, K.-H. (2015). Multiobjective Optimization and Advanced Topics. In *e-Design* (pp. 1105–1173). Elsevier. https://doi.org/10.1016/B978-0-12-382038-9.00019-3

Chen, B., Huang, A. Q., Baran, M., Han, C., & Song, W. (2006). Operation Characteristics of Emitter Turn-Off Thyristor (ETO) for Solid-State Circuit Breaker and Fault Current Limiter. *Twenty-First Annual IEEE Applied Power Electronics Conference and Exposition, 2006. APEC '06.*, 174–178. https://doi.org/10.1109/APEC.2006.1620535

Commins, P. A., & Moscrop, J. W. (2013). Analytical Nonlinear Reluctance Model of a Single-Phase Saturated Core Fault Current Limiter. *IEEE Transactions on Power Delivery*, *28*(1), 450–457. https://doi.org/10.1109/TPWRD.2012.2214404

Dalessandro, R. B., Bocchi, M., Rossi, V., & Martini, L. F. (2007). Test Results on 500 kVA-Class ${\rm MgB}_{2}$-Based Fault Current Limiter Prototypes. *IEEE Transactions on Applied Superconductivity*, *17*(2), 1776–1779. https://doi.org/10.1109/TASC.2007.899034

Dey, A., & Choudhury, A. B. (2016). A comparative study between scalarization approach and Pareto approach for multi-objective optimization problem using Genetic Algorithm (MOGA) formulated based on superconducting fault current limiter. *2016 IEEE 1st International Conference on Power Electronics, Intelligent Control and Energy Systems (ICPEICES)*, 1–4. https://doi.org/10.1109/ICPEICES.2016.7853238

Didier, G., Bonnard, C. H., Lubin, T., & Lévêque, J. (2015). Comparison between inductive

and resistive SFCL in terms of current limitation and power system transient stability. *Electric Power Systems Research*, *125*, 150–158. https://doi.org/10.1016/j.epsr.2015.04.002

Duckworth, R. C., Zhang, Y., Gouge, M. J., Rey, C. M., van der Laan, D. C., Clickner, C., & Balachandran, U. (Balu). (2010). VOLTAGE DISTRIBUTION AND MECHANICAL STRENGTH IN SPLICE JOINTS MADE FROM AS-MANUFACTURED YBCO COATED CONDUCTORS. *Icmc*, *370*, 370–379. https://doi.org/10.1063/1.3402325

Fleming, P. ., & Purshouse, R. . (2002). Evolutionary algorithms in control systems engineering: a survey. *Control Engineering Practice*, *10*(11), 1223–1241. https://doi.org/10.1016/S0967-0661(02)00081-3

Garrity, T. (2008). Getting Smart. *IEEE Power and Energy Magazine*, *6*(2), 38–45. https://doi.org/10.1109/MPE.2007.915181

Gunawardana, S. M., Commins, P. A., Moscrop, J. W., & Perera, S. (2015). Applicability of nonlinear reluctance model to a closed core Fault Current Limiter. *2015 IEEE Eindhoven PowerTech*, 1–6. https://doi.org/10.1109/PTC.2015.7232797

Hazelton, D. W. (2011). Application of SuperPower 2G HTS Wire to High Field Devices Demands on conductor for high field applications. *MT22 Conference*. http://www.superpower-inc.com/system/files/2011_0913+MT22+2CO-3+Hazelton.pdf

Hazelton, D. W., Selvamanickam, V., Duval, J. M., Larbalestier, D. C., Markiewicz, W. D., Weijers, H. W., & Holtz, R. L. (2009). Recent Developments in 2G HTS Coil Technology. *IEEE Transactions on Applied Superconductivity*, *19*(3), 2218–2222. https://doi.org/10.1109/TASC.2009.2018791

He, H., Wu, Y., Yang, Z., Zhao, P., Zhu, X., Niu, C., & Rong, M. (2018). Study of Liquid Metal Fault Current Limiter for Medium-Voltage DC Power Systems. *IEEE Transactions on Components, Packaging and Manufacturing Technology*, *8*(8), 1391–1400. https://doi.org/10.1109/TCPMT.2018.2791435

Hekmati, A. (2015). Multiobjective Design of Tunable Shield-Type Superconducting Fault Current Limiter. *IEEE Transactions on Applied Superconductivity*, *25*(5), 1–8. https://doi.org/10.1109/TASC.2015.2461622

Heydari, H., & Faghihi, F. (2010). Mechanical Force Analysis in Heavy-Current HTS Transformers Based on Field and Current Nonuniformity Coupled Analysis. *IEEE Transactions on Applied Superconductivity*, *20*(4), 2276–2282. https://doi.org/10.1109/TASC.2010.2049356

Holland, J. H. (1992). *Adaptation in Natural and Artificial Systems*. University of Michigan Press.

Hong, H., Cao, Z., Zhang, J., Hu, X., Wang, J., Niu, X., Tian, B., & Wang, Y. (2009). DC Magnetization System for a 35 kV/90 MVA Superconducting Saturated Iron-Core Fault Current Limiter. *IEEE Transactions on Applied Superconductivity*, *19*(3), 1851–1854. https://doi.org/10.1109/TASC.2009.2019292

Hoshino, T., Muta, I., Nakamura, T., Salim, K. M., & Yamada, M. (2005). Non-Inductive

Variable Reactor Design and Computer Simulation of Rectifier Type Superconducting Fault Current Limiter. *IEEE Transactions on Appiled Superconductivity*, *15*(2), 2063–2066. https://doi.org/10.1109/TASC.2005.849452

Hyung-Chul Jo, Sung-Kwan Joo, & Kisung Lee. (2013). Optimal Placement of Superconducting Fault Current Limiters (SFCLs) for Protection of an Electric Power System with Distributed Generations (DGs). *IEEE Transactions on Applied Superconductivity*, *23*(3), 5600304–5600304. https://doi.org/10.1109/TASC.2012.2232958

Ichikawa, M., & Okazaki, M. (1995). A magnetic shielding type superconducting fault current limiter using a Bi2212 thick film cylinder. *IEEE Transactions on Appiled Superconductivity*, *5*(2), 1067–1070. https://doi.org/10.1109/77.402736

Ilin, K., Yagotintsev, K. A., Zhou, C., Gao, P., Kosse, J., Otten, S. J., Wessel, W. a J., Haugan, T. J., van der Laan, D. C., & Nijhuis, A. (2015). Experiments and FE modeling of stress–strain state in ReBCO tape under tensile, torsional and transverse load. *Superconductor Science and Technology*, *28*(5), 055006. https://doi.org/10.1088/0953-2048/28/5/055006

Janowski, T., Kozak, S., Malinowski, H., Wojtasiewicz, G., Kondratowicz-Kucewicz, B., & Kozak, J. (2003). Properties comparison of superconducting fault current limiters with closed and open core. *IEEE Transactions on Appiled Superconductivity*, *13*(2), 2072–2075. https://doi.org/10.1109/TASC.2003.812991

Jiles, D. C., & Atherton, D. L. (1984). Theory of ferromagnetic hysteresis. *Journal of Applied Physics*, *55*(6), 2115. https://doi.org/10.1063/1.333582

Jiles, D. C., & Thoelke, J. B. (1989). Theory of ferromagnetic hysteresis: determination of model parameters from experimental hysteresis loops. *IEEE Transactions on Magnetics*, *25*(5), 3928–3930. https://doi.org/10.1109/20.42480

Karady, G. G. (1992). Principles of fault current limitation by a resonant LC circuit. *IEE Proceedings C Generation, Transmission and Distribution*, *139*(1), 1. https://doi.org/10.1049/ip-c.1992.0001

Kitchin, C., & Counts, L. (2006). *A Designer's Guide to Instrumentation Amplifiers 3*. https://www.analog.com/media/en/training-seminars/design-handbooks/designers-guide-instrument-amps-complete.pdf

Kojima, H., Kotari, M., Kito, T., Hayakawa, N., Hanai, M., & Okubo, H. (2011). Current Limiting and Recovery Characteristics of 2 MVA Class Superconducting Fault Current Limiting Transformer (SFCLT). *IEEE Transactions on Applied Superconductivity*, *21*(3), 1401–1404. https://doi.org/10.1109/TASC.2010.2089413

Kovalsky, L., Yuan, X., Tekletsadik, K., Keri, A., Bock, J., & Breuer, F. (2005). Applications of Superconducting Fault Current Limiters in Electric Power Transmission Systems. *IEEE Transactions on Appiled Superconductivity*, *15*(2), 2130–2133. https://doi.org/10.1109/TASC.2005.849471

Kozak, J., Janowski, T., Kozak, S., Malinowski, H., Wojtasiewicz, G., & Kondratowicz-Kucewicz, B. (2005). Design and Testing of 230 V Inductive Type of Superconducting

Fault Current Limiter With an Open Core. *IEEE Transactions on Appiled Superconductivity*, *15*(2), 2031–2034. https://doi.org/10.1109/TASC.2005.849444

Kozak, Janusz, Majka, M., Janowski, T., & Kozak, S. (2012). Design and Development of the First Polish Superconducting Fault Current Limiter For MV Distribution Systems. *Physics Procedia*, *36*, 845–848. https://doi.org/10.1016/j.phpro.2012.06.138

Kudymow, A., Elschner, S., Maeder, O., & Goldacker, W. (2011). Optimization of 2G YBCO Wires for Resistive Fault Current Limiters. *IEEE Transactions on Applied Superconductivity*, *21*(3), 1311–1314. https://doi.org/10.1109/TASC.2010.2086410

Kunche, P., & Reddy, K. V. V. S. (2016). Metaheuristic Applications to Speech Enhancement. In *SpringerBriefs in Speech Technology*. Springer International Publishing. https://doi.org/10.1007/978-3-319-31683-3

Kyowa. (2016). *Strain gauges*. http://www.kyowa-ei.com/eng/support/download/manual/strain_gage/index.html

Laan, D. C. Van Der, Ekin, J. W., Clickner, C. C., & Stauffer, T. C. (2007). Delamination strength of YBCO coated conductors under transverse tensile stress. *Superconductor Science and Technology*, *20*(8), 765–770. https://doi.org/10.1088/0953-2048/20/8/007

Leung, E. M., Rodriguez, I., Albert, G. W., Burley, B., Dew, M., Gurrola, P., Madura, D., Miyata, G., Muehleman, K., Nguyen, L., Pidcoe, S., Ahmed, S., Dishaw, G., Nieto, C., Kersenbaum, I., Gamble, B., Russo, C., Boenig, H., Peterson, D., … Haldar, P. (1997). High temperature superconducting fault current limiter development. *IEEE Transactions on Appiled Superconductivity*, *7*(2), 985–988. https://doi.org/10.1109/77.614670

Leupold, H., & Potenziani, E. (1996). A Permanent Magnet Circuit Design Primer. *US Army Research Laboratory*, *July*. http://oai.dtic.mil/oai/oai?verb=getRecord&metadataPrefix=html&identifier=ADA311457

Li, F., Qiao, W., Sun, H., Wan, H., Wang, J., Xia, Y., Xu, Z., & Zhang, P. (2010). Smart Transmission Grid: Vision and Framework. *IEEE Transactions on Smart Grid*, *1*(2), 168–177. https://doi.org/10.1109/TSG.2010.2053726

Li, Q., Xu, J., Zou, L., & Lou, J. (2012). Modelling methodology and experimental verification of the permanent-magnet-biased saturation-based fault current limiter. *IET Electric Power Applications*, *6*(8), 504. https://doi.org/10.1049/iet-epa.2012.0032

Li, Y., Liu, B., Zhu, Y., Hou, J., Liu, R., & Guo, L. (2019). High-Impedance Transformer Parameter Determination Method for Limiting Short-Circuit Current of Power System. *2019 22nd International Conference on Electrical Machines and Systems (ICEMS)*, 1–5. https://doi.org/10.1109/ICEMS.2019.8921810

Magnusson, J., Martinez-Velasco, J. A., Bissal, A., Engdahl, G., & Liljestrand, L. (2014). Optimal design of a medium voltage hybrid fault current limiter. *2014 IEEE International Energy Conference (ENERGYCON)*, 431–438. https://doi.org/10.1109/ENERGYCON.2014.6850463

Malhotra, R., Singh, N., & Singh, Y. (2011). Genetic Algorithms: Concepts, Design for Optimization of Process Controllers. *Computer and Information Science*, *4*(2), 39–54. https://doi.org/10.5539/cis.v4n2p39

Metz-Noblat, B. De, Dumas, F., & Poulain, C. (2005). Cahier technique no 158. Calculation of short-circuit currents. *Schneider Electric, Updated*, *158*. http://scholar.google.com/scholar?hl=en&btnG=Search&q=intitle:Cahier+technique+no+.158.+Calculation+of+short-circuit+currents#0

Meyer, C., Kollensperger, P., & De Doncker, R. W. (2004). Design of a novel low loss fault current limiter for medium-voltage systems. *Nineteenth Annual IEEE Applied Power Electronics Conference and Exposition, 2004. APEC '04.*, *3*, 1825–1831. https://doi.org/10.1109/APEC.2004.1296114

Morandi, A. (2013). State of the art of superconducting fault current limiters and their application to the electric power system. *Physica C: Superconductivity*, *484*, 242–247. https://doi.org/10.1016/j.physc.2012.03.004

Moriconi, F., De La Rosa, F., Darmann, F., Nelson, A., & Masur, L. (2011). Development and Deployment of Saturated-Core Fault Current Limiters in Distribution and Transmission Substations. *IEEE Transactions on Applied Superconductivity*, *21*(3), 1288–1293. https://doi.org/10.1109/TASC.2011.2104932

Moriconi, F., De La Rosa, F., Singh, A., Chen, B., Levitskaya, M., & Nelson, A. (2010). An innovative compact saturable-core HTS Fault Current Limiter - development, testing and application to transmission class networks. *IEEE PES General Meeting*, 1–8. https://doi.org/10.1109/PES.2010.5590090

Moriconi, F., Koshnick, N., De La Rosa, F., & Singh, A. (2010). Modeling and test validation of a 15kV 24MVA Superconducting Fault Current Limiter. *IEEE PES T&D 2010*, 1–6. https://doi.org/10.1109/TDC.2010.5484412

Moscrop, J. W. (2013). Experimental Analysis of the Magnetic Flux Characteristics of Saturated Core Fault Current Limiters. *IEEE Transactions on Magnetics*, *49*(2), 874–882. https://doi.org/10.1109/TMAG.2012.2214396

Moscrop, Jeff, & Darmann, F. (2009). Design and development of a 3-Phase saturated core High Temperature Superconducting Fault Current Limiter. *Electric Power and Energy Conversion Systems, 2009. EPECS '09. International Conference On*, 1–6. http://ieeexplore.ieee.org/xpls/abs_all.jsp?arnumber=5415730

Moscrop, JW, & Hopkins, S. (2009). Development and performance analysis of a saturated core high temperature superconducting fault current limiter. *19th Australasian Universities Power Engineering Conference*, 1–6. http://ro.uow.edu.au/engpapers/1083/

Murta-Pina, J., Vilhena, N., Arsenio, P., Pronto, A., & Alvarez, A. (2018). Preliminary Design and Test of Low-Resistance High Temperature Superconducting Short-Circuited Coils. *IEEE Transactions on Applied Superconductivity*, *28*(4), 1–5. https://doi.org/10.1109/TASC.2018.2820726

Nelson, A., Moriconi, F., De La Rosa, F., Masur, L., & Kirsten, D. (2011). Saturated-core fault

current limiter field experience at a distribution substation. *CIRED - 21st International Conference on Electricity Distribution*, 0680.

Nikulshin, Y., Wolfus, S., Friedman, A., Yeshurun, Y., Rozenshtein, V., Landwer, D., & Garbi, U. (2016). Saturated Cores Fault Current Limiters in a Live Grid. *IEEE Transactions on Applied Superconductivity*, *2*, 1–1. https://doi.org/10.1109/TASC.2016.2524444

Noe, M, Steurer, M., Eckroad, S., & Adapa, R. (2008). Progress on the R&D of fault current limiters for utility applications. *2008 IEEE Power and Energy Society General Meeting - Conversion and Delivery of Electrical Energy in the 21st Century*, 1–4. https://doi.org/10.1109/PES.2008.4596267

Noe, Mathias, & Steurer, M. (2007). High-temperature superconductor fault current limiters: concepts, applications, and development status. *Superconductor Science and Technology*, *20*(3), R15–R29. https://doi.org/10.1088/0953-2048/20/3/R01

Oberbeck, G., Stanton, W., & Stewart, A. (1979). Saturable Reactor Limiter For Current. In *US Patent 4,152,637*. http://www.google.com/patents?hl=en&lr=&vid=USPAT4152637&id=mGcuAAAAEBAJ&oi=fnd&dq=Saturable+reactor+limiter+for+current&printsec=abstract

Osamura, K., Machiya, S., Tsuchiya, Y., & Suzuki, H. (2010). Internal Strain and Mechanical Properties at Low Temperatures of Surround Cu Stabilized YBCO Coated Conductor. *IEEE Transactions on Applied Superconductivity*, *20*(3), 1532–1536. https://doi.org/10.1109/TASC.2010.2042437

Paul, W., & Chen, M. (1998). Superconducting control for surge currents. *IEEE Spectrum*, *35*(5), 49–54. https://doi.org/10.1109/6.669977

Pellecchia, A., Klaus, D., Masullo, G., Marabotto, R., Morandi, A., Fabbri, M., Goodhand, C., & Helm, J. (2017). Development of a Saturated Core Fault Current Limiter With Open Magnetic Cores and Magnesium Diboride Saturating Coils. *IEEE Transactions on Applied Superconductivity*, *27*(4), 1–7. https://doi.org/10.1109/TASC.2016.2642147

Raju, B. P., Parton, K. C., & Bartram, T. C. (1982). A Current Limiting Device Using Superconducting D.C. Bias Applications and Prospects. *IEEE Power Engineering Review*, *PER-2*(9), 34–35. https://doi.org/10.1109/MPER.1982.5519468

Ramachandran, A., Rustum, R., & Adeloye, A. J. (2019). Review of Anaerobic Digestion Modeling and Optimization Using Nature-Inspired Techniques. *Processes*, *7*(12), 953. https://doi.org/10.3390/pr7120953

Razzaghi, R., & Niayesh, K. (2011). Current limiting reactor allocation in distribution networks in presence of distributed generation. *2011 10th International Conference on Environment and Electrical Engineering*, 1–4. https://doi.org/10.1109/EEEIC.2011.5874615

Rozenshtein, V., Friedman, A., Wolfus, Y., Kopansky, F., Perel, E., Yeshurun, Y., Bar-Haim, Z., Ron, Z., Harel, E., & Pundak, N. (2007). Saturated Cores FCL - A New Approach. *IEEE Transactions on Applied Superconductivity*, *17*(2), 1756–1759. https://doi.org/10.1109/TASC.2007.898153

Schmitt, H., Amon, J., Braun, D., Camescasse, F., & Collet, G. (2003). Fault Current Limiters

Report on the Activities of CIGRE WG A3.10 CIGRE. *Working Group*, *10*.

Shahbazi, Y., Niayesh, K., & Mohseni, H. (2011). Finite element methode analysis of performance of inductive saturable-core fault current limiter. *2011 1st International Conference on Electric Power Equipment - Switching Technology*, *3*, 352–355. https://doi.org/10.1109/ICEPE-ST.2011.6123006

Shuki, W., Yeshurun, Y. ., Friedman, A., Rozenshtein, V., & Bar-Haim, Z. . (2011). *Improved fault current limiter with saturated core*. https://doi.org/WO2011024179A3

Sivanandam, S. N., & Deepa, S. N. (2008). *Introduction to Genetic Algorithms* (1st ed.). Springer Berlin Heidelberg. https://doi.org/10.1007/978-3-540-73190-0

Soika, R., Schmidt, F., & Allais, A. (2007). Mechanical Requirements for Superconducting Tapes in HTS Power Cable Applications. *IEEE Transactions on Applied Superconductivity*, *17*(2), 1730–1733. https://doi.org/10.1109/TASC.2007.899060

Strumpler, R., Skindhoj, J., Glatz-Reichenbach, J., Kuhlefelt, J. H. W., & Perdoncin, F. (1999). Novel medium voltage fault current limiter based on polymer PTC resistors. *IEEE Transactions on Power Delivery*, *14*(2), 425–430. https://doi.org/10.1109/61.754084

Subramanyam, G., & Boolchand, P. (2001). *HTS Processing: Bulk, Thin Film, and Wires* (P. J. Lee (ed.)). John Wiley & Sons.

Sung-Hun Lim, & Jae-Chul Kim. (2012). Analysis on Protection Coordination of Protective Devices With a SFCL Due to the Application Location of a Dispersed Generation in a Power Distribution System. *IEEE Transactions on Applied Superconductivity*, *22*(3), 5601104–5601104. https://doi.org/10.1109/TASC.2011.2179509

Sung-Hun Lim, Jin-Seok Kim, Jong-Fil Moon, Jae-Chul Kim, Sang-Bong Rhee, Chul-Hwan Kim, & Ok-Bae Hyun. (2009). Quench and Recovery Characteristics of a SFCL Applied Into Neutral Line of a Three-Phase Power System. *IEEE Transactions on Applied Superconductivity*, *19*(3), 1835–1838. https://doi.org/10.1109/TASC.2009.2017754

Superpower. (2016). *2G HTS Wire Specification*. http://www.superpower-inc.com/content/2g-hts-wire

Takao, T., Koizuka, S., Oi, K., Ishiyama, A., Kato, J., Machi, T., Nakao, K., & Shiohara, Y. (2007). Characteristics of Compressive Strain and Superconducting Property in YBCO Coated Conductor. *IEEE Transactions on Applied Superconductivity*, *17*(2), 3517–3519. https://doi.org/10.1109/TASC.2007.899654

Teng, J.-H., & Lu, C.-N. (2010). Optimum fault current limiter placement with search space reduction technique. *IET Generation, Transmission & Distribution*, *4*(4), 485. https://doi.org/10.1049/iet-gtd.2009.0340

van der Laan, D. C., Ekin, J. W., Douglas, J. F., Clickner, C. C., Stauffer, T. C., & Goodrich, L. F. (2010). Effect of strain, magnetic field and field angle on the critical current density of Y Ba 2 Cu 3 O 7−δ coated conductors. *Superconductor Science and Technology*, *23*(7), 072001. https://doi.org/10.1088/0953-2048/23/7/072001

Vecchio, R. M. Del, Feeney, M.-E. F., Feghali, P. T., Poulin, B., Shah, D. M., Ahuja, R., & Shah, D. M. (2010). *Transformer Design Principles: With Applications to Core-Form Power*

Transformers (2nd edit.). Taylor & Francis Group. http://books.google.com/books?id=Lzjs0LNHhVYC&pgis=1

Venter, G. (2010). Review of Optimization Techniques. In *Encyclopedia of Aerospace Engineering* (pp. 1–12). John Wiley & Sons, Ltd. https://doi.org/10.1002/9780470686652.eae495

Vilhena, N. (2012). *Construção e Ensaio de Um Limitador de Corrente Supercondutor de Núcleos Saturados* [Universidade NOVA de Lisboa]. http://hdl.handle.net/10362/8516

Vilhena, N., Arsenio, P., Murta-Pina, J., Pronto, A., & Alvarez, A. (2015). A Methodology for Modeling and Simulation of Saturated Cores Fault Current Limiters. *IEEE Transactions on Applied Superconductivity*, *25*(3), 1–4. https://doi.org/10.1109/TASC.2014.2374179

Vilhena, N., Arsénio, P., Murta-Pina, J., Pronto, A. G., & Álvarez, A. (2015). Development of a Simulink Model of a Saturated Cores Superconducting Fault Current Limiter. In *IFIP Advances in Information and Communication Technology* (Vol. 450, pp. 415–422). https://doi.org/10.1007/978-3-319-16766-4_44

Vilhena, N., Murta-Pina, J., Pronto, A., & Alvarez, A. (2018). A Design Methodology for the Optimization of Three-Phase SFCL of Saturated Cores Type. *IEEE Transactions on Applied Superconductivity*, *28*(4), 1–5. https://doi.org/10.1109/TASC.2018.2806001

Vilhena, N., Taillacq, A., Pronto, A., Murta-Pina, J., & Alvarez, A. (2016). Analysis of Electromagnetic Forces in Superconducting Fault-Current Limiters Under Short-Circuit Condition. *IEEE Transactions on Applied Superconductivity*, *26*(3), 1–4. https://doi.org/10.1109/TASC.2016.2548482

Wojtasiewicz, G., Janowski, T., Kozak, S., Kozak, J., Majka, M., & Kondratowicz-Kucewicz, B. (2014). Experimental Investigation of a Model of a Transformer-Type Superconducting Fault Current Limiter With a Superconducting Coil Made of a 2G HTS Tape. *IEEE Transactions on Applied Superconductivity*, *24*(3), 1–5. https://doi.org/10.1109/TASC.2013.2295117

Wolfus, Y., Nikulshin, Y., Friedman, A., & Yeshurun, Y. (2014). Double storey three phase saturated cores fault current limiter. *Journal of Physics: Conference Series*, *507*(3), 032058. https://doi.org/10.1088/1742-6596/507/3/032058

Xin, Y., Gong, W. Z., Sun, Y. W., Cui, J. B., Hong, H., Niu, X. Y., Wang, H. Z., Wang, L. Z., Li, Q., Zhang, J. Y., Wei, Z. Q., Liu, L., Yang, H., & Zhu, X. H. (2013). Factory and Field Tests of a 220 kV/300 MVA Statured Iron-Core Superconducting Fault Current Limiter. *IEEE Transactions on Applied Superconductivity*, *23*(3), 5602305–5602305. https://doi.org/10.1109/TASC.2012.2234205

Xin, Y., Zhang, J. Y., & Gong, W. Z. (2010). Voltage Surge Protection Circuit for Superconducting Bias Coil. *IEEE Transactions on Applied Superconductivity*, *20*(3), 1118–1121. https://doi.org/10.1109/TASC.2010.2045363

Yang, H.-T., Tang, W.-J., & Lubicki, P. R. (2018). Placement of Fault Current Limiters in a Power System Through a Two-Stage Optimization Approach. *IEEE Transactions on*

Power Systems, *33*(1), 131–140. https://doi.org/10.1109/TPWRS.2017.2693390

Yazawa, T., Yoneda, E., Matsuzaki, J., Shimada, M., Kuriyama, T., Nomura, S., Ohkuma, T., Sato, Y., & Takahashi, Y. (2001). Design and test results of 6.6 kV high-Tc superconducting fault current limiter. *IEEE Transactions on Appiled Superconductivity*, *11*(1), 2511–2514. https://doi.org/10.1109/77.920376

Yin Xin, Gong, W. Z., Niu, X. Y., Gao, Y. Q., Guo, Q. Q., Xiao, L. X., Cao, Z. J., Hong, H., Wu, A. G., Li, Z. H., Hu, X. M., Tian, B., Zhang, J. Y., He, Y., Wang, Y., Cui, J., Ding, S. Z., Wang, J. Z., Ren, A. L., & Ye, F. (2009). Manufacturing and Test of a 35 kV/90 MVA Saturated Iron-Core Type Superconductive Fault Current Limiter for Live-Grid Operation. *IEEE Transactions on Applied Superconductivity*, *19*(3), 1934–1937. https://doi.org/10.1109/TASC.2009.2018510

Ying Xin, Weizhi Gong, Xiaoye Niu, Zhengjian Cao, Jingyin Zhang, Bo Tian, Haixia Xi, Yang Wang, Hui Hong, Yong Zhang, Bo Hou, & Xicheng Yang. (2007). Development of Saturated Iron Core HTS Fault Current Limiters. *IEEE Transactions on Applied Superconductivity*, *17*(2), 1760–1763. https://doi.org/10.1109/TASC.2007.898181

Zalzala, A. M., & Fleming, P. J. (1997). *Genetic Algorithms in Engineering Systems*. Institution of Electrical Engineers.

Zhang Xuhong, Zhou Youqing, & Zhang Zhifeng. (2005). Design of saturated iron core superconducting fault current limiter based on numerical calculation. *2005 IEEE/PES Transmission & Distribution Conference & Exposition: Asia and Pacific*, 1–5. https://doi.org/10.1109/TDC.2005.1546761

Zhengyu Lu, Daozhuo Jiang, & Zhaolin Wu. (2003). A new topology of fault-current limiter and its parameters optimization. *IEEE 34th Annual Conference on Power Electronics Specialist, 2003. PESC '03.*, *1*, 462–465. https://doi.org/10.1109/PESC.2003.1218335

Zobolas, G. I., Tarantilis, C. D., & Ioannou, G. (2008). *Exact, Heuristic and Meta-heuristic Algorithms for Solving Shop Scheduling Problems* (pp. 1–40). Springer, Berlin, Heidelberg. https://doi.org/10.1007/978-3-540-78985-7_1